PARAMETRIC DEPENDENCIES OF AEROENGINE FLUTTER FOR FLUTTER CLEARANCE APPLICATIONS

by

Asif Khalak

GTL Report #231

August 2000

GAS TURBINE LABORATORY
MASSACHUSETTS INSTITUTE OF TECHNOLOGY
CAMBRIDGE, MASSACHUSETTS

PARAMETRIC DEPENDENCIES OF AEROENGINE FLUTTER FOR FLUTTER CLEARANCE APPLICATIONS

by

Asif Khalak

GTL Report #231 August 2000

This research was supported by a National Science Foundation Fellowship and the Air Force Office of Scientific Research, Grant #F49620-00-1-0014, Tom Beutner, Contract Monitor.

Parametric dependencies of aeroengine flutter for flutter clearance applications

by

Asif Khalak

Abstract

This thesis describes the effects of operational parameters upon aeroengine flutter stability. The study is composed of three parts: theoretical development of relevant parameters, exploration of a computational model, and analysis of fully scaled test data. Results from these studies are used to develop a rational flutter clearance methodology—a test procedure to ensure flutter-free operation.

It is shown, under conditions relevant to aeroengines, that four nondimensional parameters are necessary and sufficient for flutter stability assessment of a given rotor geometry. We introduce a new parameter, termed the reduced damping, g/ρ^*, which collapses the combined effects of mechanical damping and mass ratio (blade mass to fluid inertia). Furthermore, the introduction of the compressible reduced frequency, K^*, makes it possible to uniquely separate the corrected performance map from the non-dimensional operating environment (including inlet temperature and pressure). Simultaneous plots of the performance map of corrected mass flow and corrected speed, $(\dot{m}_c, N_c)$, with the $(K^*, g/\rho^*)$ map provide a dimensionally complete and fully integrated view of flutter stability, as demonstrated in the context of a historic multimission engine.

A parametric, computational study was conducted using a 2D, linearized unsteady, compressible, potential flow model of a vibrating cascade. This study showed the independent effects of Mach number, inlet flow angle, and reduced frequency upon flutter stability in terms of critical reduced damping, which corroborates the 4D view of flutter stability.

Test data from a full-scale transonic fan, spanning the full 4D parameter space, were also analyzed. A novel boundary fitting tool was developed for data processing, which can handle the generic case of sparse, multidimensional, binary data. The results indicate that the inlet pressure does not alone determine the flight condition effects upon flutter, which necessitates the use of the complete 4D parameter set. Such a complete view of the flutter boundary is constructed, and sensitivities with respect to various parameters are estimated.

A rational flutter clearance procedure is proposed. Trends in K^* and g/ρ^* allow one to rapidly determine the worst-cases for testing a given design. One may also use sensitivities to extend the results of sea level static (SLS) testing, if the worst case is relatively close to the SLS condition.

Acknowledgments

Bismillah Ar-Rahman Ar-Rahim

I would first like to thank my thesis advisor, Prof. Jack Kerrebrock, who was uniquely empowering and encouraging, who directed me towards the real issues, and whose independent thinking and unassuming nature are examples from which to learn.

Thanks are also due the other members of my thesis committee. Prof. Edward Greitzer helped in finding and obtaining the rare, sufficiently complete data needed for this effort. Prof. Kenneth Hall contributed his aeroelastic code to get the work started in a meaningful direction. Prof. Wai Cheng provided a helpful perspective, and filled a much needed role on short notice. Furthermore, I would like to thank Dr. Choon Tan and Dr. James Paduano for giving their feedback, and generally being supportive.

Instrumental help came from practioners from the aircraft engine industry. I would like to thank the Volvo Corporation, and Mr. Lennart Kjellen in particular, for providing us with their data. I would also like to thank GE Aircraft Engines for sharing their flutter experience data with us, and for the continued interest with this work. Dr. Robert Kielb from GEAE, in particular, was extremely helpful in several discussions on turbomachinery flutter. Finally, I would like to acknowledge the help of Pratt and Whitney, and Mr. Carl Meece in particular, in sharing some of their results with us.

There are many friends who have made MIT a pleasant place to live and work. Thank you all. Most of all, to my wife Nan, who I met and married while working on this project. I had not suspected, coming in, that a doctorate would be only the second best thing that I would get at MIT.

This thesis is dedicated to my parents, who have been unwaveringly supportive. And, of course, all praise and thanks is ultimately due to God.

Contents

1 **Introduction** **21**

1.1 Previous Work 22

1.2 Focus of the Present Work 24

1.3 Thesis Contributions 25

2 **Complete set of parameters for flutter stability** **27**

2.1 Stability Analysis 30

2.1.1 Fluid Dynamical Conditions 32

2.1.2 Development of Stability Conditions 33

2.2 Summary 36

3 **A new technique for representing flutter boundaries** **37**

3.1 Uniqueness of Parameters 38

3.2 Reduced damping and compressible reduced frequency 39

3.2.1 Reduced damping parameter 39

3.2.2 Compressible Reduced Frequency 43

3.2.3 Remarks 49

3.3 Fully specified flutter boundaries 51

3.3.1 Special Case: Incompressible limit and the "Flutter Map" 55

3.4 Stability of a design 57

3.4.1 Example: Application to early multimission engine 63

3.5 Summary 67

4 Exploratory study of aeroelastic computational model 69

4.1 Description of Study 70

4.1.1 Parameter Space Description 70

4.1.2 Description of Dynamic Model 72

4.1.3 Code Verification 72

4.1.4 Cascade Geometry 74

4.1.5 Range of Parameters 75

4.2 Metric for Stability Assessment 79

4.3 Results for torsional and bending stability 81

4.3.1 Bending vibrations 81

4.3.2 Torsional vibrations 86

4.3.3 Separation of subresonant and superresonant regions 90

4.3.4 Torsional stability in region A 92

4.3.5 Torsional stability in region B 97

4.4 Reduction of mach number trend 100

4.4.1 General trends of phase with Mach number 100

4.4.2 Effects of varying frequency on trends of fluid force phase 104

4.4.3 Effect of varying geometry on trends of fluid force phase 106

4.4.4 Effect of varying inlet flow angle on trends of fluid force phase 107

4.4.5 Break down of Mach number "collapse" in superresonant regime 108

4.5 Summary 109

5 Technique for Analysis of Full-Scale Engine Data 111

5.1 Overview 111

5.1.1 Analysis Process 113

5.1.2 Range of Sampled Data 113

5.2 Reduction of Raw Data 115
5.3 Centrifugal Stiffening 118
5.4 Rule for Selecting Data Subsets 121
5.5 Fitting the Stability Boundary using Sampled Data 124
    5.5.1 Error Estimates 129
5.6 Summary 131

6 Results of Experimental Data Analysis 133

6.1 Trends in Flutter Stability 135
    6.1.1 Trends with varying reduced damping 136
    6.1.2 Trends of varying compressible reduced frequency 138
6.2 Effect of Pressure 140
    6.2.1 Static Deformations 140
    6.2.2 Effect of temperature at constant pressure 141
6.3 Effects of K_0^* and g/ρ^* 144
    6.3.1 Speedline/Flutter Boundary Intersections 146
    6.3.2 Trends with respect to changes in reduced damping 146
    6.3.3 Comparison of g/ρ^* effects at $K_0^* = 0.685$ and $K^* = 0.705$ 148
    6.3.4 Trends with respect to changes in K_0^* 152
6.4 Flutter boundary on frequency-damping map 154
6.5 Summary 160

7 Flutter Clearance 161

7.1 Design of Experimental Tests 161
    7.1.1 Requirements for Flutter Clearance 163
    7.1.2 Mission Requirements 163
7.2 Examples 165
    7.2.1 Case 1: Low Speed Aircraft 166

7.2.2 Case 2: High Speed Aircraft 168
7.3 Summary 170

8 Conclusions 173

8.1 Thesis Summary 173
8.2 Conclusions 176
8.3 Future Work 177

A Derivation of the Non-dimensional Fluid Operator 179

A.1 Equations for the pressure field 179
A.1.1 Boundary Conditions 182
A.1.2 Summary of Dependence 184
A.2 Alternate, equivalent formulation 187

B Uniqueness of operability parameters 189

B.1 Primitive Variables 190
B.2 Derivation of the Parameter Set 191
B.3 Generalization to the Case of Centrifugal Stiffening 194

C Boundary fitting using Support Vector Machines 197

C.1 Description of Aeroelastic Stability Data 198
C.2 Data Classification using Support Vector Machines 200
C.2.1 Optimal Separating Hyperplane 200
C.2.2 Extension to non-separable data 203
C.2.3 Non-linear boundary characterization 206
C.3 Performance of Procedure on Test Cases 210
C.3.1 3D Paraboloid 210
C.3.2 2D Ellipse 212

D Flutter boundary fits 215

List of Figures

2-1 Temperature sensitivity of flutter boundary on Performance Map 28

2-2 Stagnation quantities (T_t, p_t, ρ_t) as a function of flight Mach number at sea level and at 12km. 29

2-3 Schematic model of fluttering rotor 31

2-4 Example of real and imaginary parts of generalized coordinate, q. 31

3-1 Collapse of computations of Försching(1994) with reduced damping, g/ρ^* 42

3-2 Diagram depicting three relevant time scales: inertial, acoustic, and vibrational 44

3-3 Fan test results of Stargardter (1979) 45

3-4 Effect of reduced frequency on aerodynamic work coefficient in Fifth Standard Configuration 46

3-5 Schematic relationship between K^* and unsteady fluid phase lag, ϕ_f. 47

3-6 Effect of reduced frequency on phase between unsteady fluid forces and torsional oscillations in Fifth Standard Configuration. 48

3-7 A family of boundaries, each for a particular g/ρ^* and K^*. 51

3-8 Map of compressible reduced frequency, K^*, versus mass-damping, g/ρ^* 52

3-9 Dual view of performance map and (K^*,g/ρ^*) map 53

3-10 Boundaries from computational model on (K^*,g/ρ^*) map 54

3-11 Classical flutter map of reduced velocity, U^*, versus incidence, i, should work for incompressible (low-speed) compressors, neglecting damping. 57

3-12 Typical flight envelopes for subsonic and supersonic aircraft 58

3-13 Envelope of inlet states 59

3-14 Typical flight envelopes on (K^*,g/ρ^*) map 61

3-15 Regions of desired operation and flutter boundaries on performance map, and $(K^*, g/\rho^*)$ map 62

3-16 Performance map of early multimission engine. Flutter problem occurred at part-speed . . 64

3-17 Fan data on $(K^*, g/\rho^*)$ map. 66

3-18 Fan data on $(K^*, g/\rho^*)$ map, with flight envelope for "generic" supersonic aircraft. 67

4-1 Comparison of Hall's linearized potential code with LINSUB 73

4-2 Geometry of the Tenth Standard Configuration 75

4-3 Geometry of First and Fifth Standard Configuration 76

4-4 Region of steady code convergence 10th Standard Configuration 77

4-5 Schematic of regions of study in parameter space for 10th Standard Config. 78

4-6 Typical case of bending for 10th Standard Configuration 82

4-7 Overall results for bending vibrations 83

4-8 Bending instability of a flat plate cascade at negative incidence. 85

4-9 Instability in Bending. Trends with interblade phase, σ 87

4-10 Instability in Bending. Trends with reduced frequency, k 88

4-11 Trend of critical reduced damping versus interblade phase, σ, in torsion. 89

4-12 Separation of acoustic wave effects in torsional vibrations 91

4-13 Depiction of stability boundary in region A. 93

4-14 Trends of flutter stability, $(g/\rho^*)_{\rm cr}$, with reduced frequency, k, in the case of torsion for different flow angles. 94

4-15 Trends of flutter stability, $(g/\rho^*)_{\rm cr}$, with reduced frequency, k, in the case of torsion for different Mach numbers. 96

4-16 Torsional stability, 10th Standard Configuration. 98

4-17 Trend of $(g/\rho^*)_{\rm cr}$, with reduced frequency, k, for torsional vibrations near the acoustic wave instability "lobes" 99

4-18 Trend of work-per-cycle with reduced frequency, k, for torsional vibrations near the acoustic wave instability "lobes" 101

4-19 Fluid force phase as a function of Mach number, 10th Standard Config 102

4-20 Collapse of fluid force phase in 10th Standard Configuration 105

4-21 Fluid force phase vs. Mach number, several geometries 106

4-22 Effect of inlet flow angle on fluid force phase 107

4-23 Fluid force phase in the superresonant region 108

5-1 Schematic of Data Analysis Process 112

5-2 Measured data on Performance Map 114

5-3 Histogram of Measured Stress Level 118

5-4 Schematic of suspended spring-mass system 119

5-5 Campbell diagram of experimental data 120

5-6 Data spread on (K_0^*, $(g/\rho^*)_{\text{rel}}$) map 122

5-7 Flutter data for a specific (K_0^*,$(g/\rho^*)_{\text{rel}}$) cluster 123

5-8 Schematic of subset selection rule 125

5-9 Use of "assumed data" in boundary fits 126

5-10 Optimal Separating Hyperplane 127

5-11 Commutation Diagram for non-linear SVM fitting 128

5-12 Range of uncertainty in boundary fits 130

6-1 Analysis boxes on the (K_0^*,g/ρ^*) map 134

6-2 Flutter boundaries on performance map for $K_0^* = 0.685$, and varying g/ρ^* 136

6-3 Flutter boundary on performance map for $K_0^* = 0.705$, and varying g/ρ^* 137

6-4 Flutter boundaries on performance map for $g/\rho^* = 1$, and varying K_0^* 139

6-5 Effect of inlet pressure on pressure correlation 142

6-6 Graph of inlet pressure versus deviation from pressure correlation 143

6-7 Effect of temperature at a constant pressure 145

6-8 Schematic of intersection between speed line and flutter boundary 146

6-9 Critical mass flow and pressure ratio at flutter for $K_0^* = 0.685$, and varying g/ρ^* 147

6-10 Critical π comparison between $K_0^* = 0.685$ and $K_0^* = 0.705$ 150

6-11 Critical $\dot{m}_c$ comparison between $K_0^* = 0.685$ and $K_0^* = 0.705$ 151

6-12 Critical mass flow and pressure ratio at flutter for $g/\rho^* = 1$, and varying K_0^* 153

6-13 Example of flutter boundary on $(K_0^*, g/\rho^*)$ map, for a specific point on the performance map 155

6-14 Family of flutter boundaries on $(K_0^*, g/\rho^*)$ map, for 63% corrected speed 157

6-15 Family of flutter boundaries on $(K_0^*, g/\rho^*)$ map, for 70% corrected speed 157

6-16 Family of flutter boundaries on $(K_0^*, g/\rho^*)$ map, for 74% corrected speed 158

6-17 Family of flutter boundaries on $(K_0^*, g/\rho^*)$ map, for 78% corrected speed 158

6-18 Family of flutter boundaries on $(K_0^*, g/\rho^*)$ map, for 83% corrected speed 159

7-1 Schematic of data sampling rule 164

7-2 SLS Flutter boundary, estimated minimum stability boundary, and desired operating line for Case 1 167

7-3 Flight requirements and minimal clearance region on $(K_0^*, (g/\rho^*)_{\text{rel}}$ map 169

7-4 Flutter boundaries for various points in Case 2 171

A-1 Typical compressor performance at constant corrected speed, N_c. 183

C-1 Picture of abstract operating space, $\mathcal{V}$, with lines of constant damping, δ. 198

C-2 Schematic of boundary fitting procedure 199

C-3 Distinction between optimal and non-optimal separating hyperplanes 202

C-4 Optimal Hyperplane lies between the supporting hyperplanes 203

C-5 Diagram of paraboloid oriented on z-axis 211

C-6 Schematic view of ellipse in the plane. 213

D-1 Flutter boundary on performance map, for $K_0^* = 0.685$ and $(g/\rho^*)_{\text{rel}} = 0.60$ 216

D-2 Flutter boundary on performance map, for $K_0^* = 0.684$ and $(g/\rho^*)_{\text{rel}} = 0.85$ 216

D-3 Flutter boundary on performance map, for $K_0^* = 0.685$ and $(g/\rho^*)_{\text{rel}} = 0.98$ 217

D-4 Flutter boundary on performance map, for $K_0^* = 0.684$ and $(g/\rho^*)_{\text{rel}} = 1.06$ 217

D-5 Flutter boundary on performance map, for $K_0^* = 0.705$ and $(g/\rho^*)_{\text{rel}} = 0.63$ 218

D-6 Flutter boundary on performance map, for $K_0^* = 0.747$ and $(g/\rho^*)_{\text{rel}} = 0.97$ 218

D-7 Flutter boundary on performance map, for $K_0^* = 0.728$ and $(g/\rho^*)_{\text{rel}} = 0.75$ 219

D-8 Flutter boundary on performance map, for $K_0^* = 0.671$ and $(g/\rho^*)_{\text{rel}} = 0.89$ 219

D-9 Flutter boundary on performance map, for $K_0^* = 0.685$ and $(g/\rho^*)_{\text{rel}} = 0.69$ 220

D-10 Flutter boundary on performance map, for $K_0^* = 0.706$ and $(g/\rho^*)_{\text{rel}} = 0.93$ 220

D-11 Flutter boundary on performance map, for $K_0^* = 0.705$ and $(g/\rho^*)_{\text{rel}} = 0.80$ 221

D-12 Flutter boundary on performance map, for $K_0^* = 0.706$ and $(g/\rho^*)_{\text{rel}} = 0.70$ 221

List of Tables

3.1 Cascade flutter studies with damping effect included 41

4.1 List of non-dimensional parameters in study 72
4.2 Flat plate cascade runs for code verification 73
4.3 Cascade geometries used in parametric runs 74
4.4 Definition of unsteady force coefficent, various studies 79

5.1 Raw variables measured in engine tests 115
5.2 Similarity variables determined from measurements 116

6.1 Flutter boundary sensitivity estimates. 148
6.2 Estimate and upper bound of flutter boundary sensitivity using point data. 154

A.1 List of fundamental fluid dynamic scales. 180
A.2 List of non-dimensional flow variables 181

C.1 Listing of some commonly used Kernels and the function classes to which they refer 207
C.2 Results from boundary fitting of paraboloid test case 212
C.3 Results from boundary fitting of 2D ellipse test case 214

Nomenclature

Roman

A_d	Annular cross-sectional area
c	blade chord
C_x	axial velocity
F_b	force on a blade in cascade
F_j	vibration-induced fluid forces on blade j
g	modal damping
g/ρ^*	reduced damping
$(g/\rho^*)_{\mathrm{cr}}$	critical reduced damping
l_j	vibration-induced fluid force coeff. based on inlet pressure
l'_j	vibration-induced fluid force coeff. based on inlet dynamic head
k	classical reduced frequency
K^*	compressible reduced frequency
K_0^*	centrifugally-corrected compressible reduced frequency
m_0	modal mass
$\dot{m}$	mass flow
$\dot{m}_c$	corrected mass flow
M_{tang}	tangential Mach number
M_{ax}	axial Mach number
M_f	flight Mach number
M_b	moment on a blade in cascade
M	Mach number in rotating coordinate frame
N_c	corrected speed
N_{raw}	raw rotor speed
p_t	stagnation pressure
p	pressure at inlet
Δp	pressure rise
p_{ref}	reference pressure
Pr	Prandtl number
q_j	generalized coordinate for mode j
ρ_t	stagnation density
ρ	density at inlet
R	gas constant $[kJ/kgK]$
Re	Reynolds number
s	southwell coefficient
t	time
T	temperature at inlet
T_t	stagnation temperature

T_{ref}	reference temperature
U	characteristic flow velocity in rotating coordinate frame
U^*	reduced velocity

Greek

α	inlet flow angle
δ	system damping
η	non-dimensional modal coordinate
ϕ_j	modeshape of blade j
ϕ	phase lag between motions and fluid forces
ϕ_{f0}	phase lag at zero frequency (quasi-steady lag)
γ	ratio of specific heats
μ	mass ratio
ω_0	modal frequency
ω_{rest}	frequency of vibration with no centrifugal effects
Ω'	Rossby number
Ψ	pressure rise coefficient
π	pressure ratio
ρ^*	fluid inertia parameter
σ	inter blade phase angle
σ_b	blade stress
τ'	fluid dynamic lag
τ	shear stress tensor
θ_{IGV}	inlet guide vane angle
ζ	viscous damping

Notation for Appendix B

$\mathcal{V}$	parameter space
$\mathbf{w}$	directed normal of trial hyperplane
$\mathbf{v}$	vector in parameter space
s_i	binary input data
d_i	distance from point i to the boundary
$\mathbf{e}$	slack variable vector
ξ_j	slack variable for data point j
Q	Quadratic optimization function
L	Lagrangian function
α, β	Lagrange multipliers
$\mathbf{w}^*$	optimal hyperplane normal
Q_d	Objective function of dual optimization problem
$\mathbf{H}$	Hessian matrix
$K(\mathbf{v}_i, \mathbf{v}_j)$	Kernel function
Φ	non-linear map from $\mathbf{v}$ to $F(\mathbf{v})$

Chapter 1

Introduction

To assure reliability and safety of jet propulsion, designers must mitigate possible blade vibrations in the turbomachinery stages. The cyclical strains associated with blade vibration can rapidly accrue to promote high cycle fatigue (HCF) failure, greatly diminishing blade life. The current work deals with blade flutter in turbomachinery, a vibrational instability.

Flutter involves an interaction between the unsteady fluid mechanics, and the unsteady structural mechanics in which there is a net energy transfer from the flow to the structure. This leads to unstable vibrations. The physical interactions involved are sophisticated enough that they do not reduce to an easily solved limiting case. Therefore, predictive models for this phenomenon are typically computationally intensive, and it is difficult to ensure high fidelity. A contributor to the complexity of this problem is that there are a large number of relevant physical parameters.

Rig and engine testing are therefore necessary in any engine development program. In general, the parameters describing the system can be divided into those which are fixed for a particular engine and those which vary during the operation of an engine, that therefore define the *operating space* of the engine. The point of experimental engine flutter testing is to ensure that flutter does not occur throughout the operating space.

The operating space relevant to performance in terms of pressure ratio and efficiency is typically measured in terms of corrected mass flow, $\dot{m}_c$, and corrected speed. For a given machine, these are equivalent to the axial and tangential blade relative Mach number, respectively. Flutter stability, however, is not solely described by these variables, but requires other variables as well. In particular, the flight condition in terms of inlet temperature and pressure is known to influence flutter stability. In the present research, we address the effects upon flutter stability from the full (nondimensional) set of operating space variables.

1.1 Previous Work

Aeroelastic problems in turbomachines have been studied for almost 50 years. The AGARD Manual on Aeroelasticity (Sisto and Carta, editors, 1987) summarizes the accomplishments in the field through the late 1980s. Since then there has been considerable further research, particularly in the area of computational flow simulations. More recent reviews include Verdon (1993), Försching (1994), and Srinivasan (1997).

The analysis techniques have tended towards numerical simulations of the unsteady flow, starting from the early work of Whitehead (1960, 1962) on 2-D, incompressible, inviscid, flat plate cascades. These have been developed to the current 3-D, unsteady, viscous flow methods currently used. A number of parametric studies have been performed using simplified flow simulations to gain insight into the parameter dependencies of the flutter phenomenon (including Srinivasan and Fabunmi (1984), Kielb and Ramsey (1989), Smith and Kadambi (1993), Försching (1994), Panovsky and Kielb (1998)).

The problem of flight condition effects upon flutter stability was first identified by Jeffers and Meece (1975) in the context of a fan flutter problem during the development of the F100 Engine. Rig testing conducted at sea-level ambient conditions initially indicated that the engine was clear of flutter instabilities. However, a flutter problem was found during subsequent flight testing. Later simulated flight condition testing confirmed the effects of inlet temperature and density upon flutter stability. Further work on this problem with the F100 was taken up at NASA (Mehalic et. al. (1977)), confirming the trends identified by Jeffers and Meece (1975).

Another study of the effects of flight condition was included in the experimental parameter study on an annular cascade (Jutras, Stallone, and Bankhead, 1980) which focused upon choke flutter in mid-stage compressors. This study also showed temperature effects to be a significant contributor to stability. This study, unlike the F100 development testing, did not find any effects of inlet density on flutter stability at a constant temperature. Later in the thesis, we suggest why the experimental setup, as described in Rutowski et. al. (1978), might be expected to exhibit such behavior since it was carefully designed to tightly clamp the blade to its supports, eliminating any frictional damping.

In general, the experimental approach in flutter is hampered by the fact that test data for fully-scaled rigs are expensive and, therefore, scarce. Other publically available experimental flutter tests include the studies of Stargardter (1979) and Jutras, et. al. (1981), which varied the corrected speed, N_c, and corrected mass flow, $\dot{m}_c$, but did not explore the effects of flight condition. Stargardter showed the classical procedure of correlating flutter onset with respect to reduced velocity, U^*, and incidence was not valid in his tests. Since Stargardter's tests were taken at a constant inlet condition, increases in reduced velocity also entailed increases in Mach number. This mixing of Mach number effects and reduced velocity effects is an important element of Stargardter's results, which underscores the need to account for *all* the relevant parameters in assessing aeroengine flutter stability.

Although flight condition effects are understood to be relevant to flutter stability, the understanding to date is still incomplete as noted by Jeffers (1988) in the AGARD Manual:

> "The adverse effect of increasing temperature on the stability of turbomachinery airfoils has long been recognized but remains today one that is not fully understood.... The effects of increasing temperature on the parameters that comprise reduced frequency, i.e., the frequency of the unsteady airfoil motion and relative flow velocity, are well known. Unfortunately, the resulting effect on aeroelastic stability, particularly for 'stall' flutter, is not."

This view is corroborated in Srinivasan (1997), who also makes the following general observation:

> "One important scientific element that is conspicuously absent in our pursuit to improve structural integrity is similitude. As blades operate in a harsh thermal and centrifugal environment, successful laboratory modeling would imply that we can develop scaling laws that can be used to interpret data. There is an opportunity here for academia to assess the scope of needed research and provide guidelines"

The concept of similitude and its application to aeroengine flutter is at the essence of the current work.

1.2 Focus of the Present Work

The focus of the current work is to develop a rational methodology for *flutter clearance*; that is, for ensuring that the boundary of the flutter instability for a particular engine lies outside the engine's operating envelope. An analysis of the basic fluid and structural equations is conducted to identify the non-dimensional system parameters. We formulate the parameters in a manner uniquely suited for operability assessment. This set of parameters is discussed in relation to previously published results, as well as a computational parameter study to identify dominant parametric trends. We incorporate data, provided by the Volvo Corporation, from extensive, experimental flutter tests on a full-scale test rig. These data, coupled with the current analysis, can provide new insight into the effects of flight condition in the context of flutter clearance. Relevant engineering questions include:

- What is a minimal, but complete, set of non-dimensional parameters relevant to describe flutter stability of a given machine?
- What is the best choice of parameters for the purpose of engine flutter operability assessment?
- What is the role of the flight condition with respect to the non-dimensional description and how can this be physically interpreted? Are there distinct effects of temperature and density or can these be summarized by a single parameter?
- What is the sensitivity of flutter stability with respect to the non-dimensional variables specifying the flight condition for a typical machine?

The thesis is laid out as follows: Chapter 2 develops a set of four non-dimensional parameters that is necessary and sufficient for flutter stability; Chapter 3 integrates these parameters into a new technique for representing flutter boundaries, and interprets this technique in the light of previous work; Chapter 4 explores the role of the non-dimensional parameters influencing the unsteady fluid forces on the basis of a 2-D compressible, potential model with real airfoils in bending and in torsional vibrations; Chapter 5 describes the procedure used in analyzing a set of full-scale test data in which the full parameter dependence was measured; Chapter 6 discusses the results from this full-scale engine testing; Chapter 7 presents a flutter clearance test procedure; and Chapter 8 summarizes the work and conclusions which may be drawn from it.

1.3 Thesis Contributions

The key contributions of the thesis are the following:

1. It is shown, on the basis of the fundamental (Navier-Stokes) fluid and (linear) structural equations, that a four dimensional parameter space is necessary and sufficient to assess linear aeroelastic stability for a given geometric design, under conditions relevant to aeroengine operation. Furthermore, under these circumstances, the parameter space of the vibration-induced fluid forces is three dimensional.

2. A representation for flutter stability boundaries has been developed for operability assessment. This technique extends the commonly used performance map with a second map which, for given structural parameters, spans the flight envelope in terms of inlet temperature and density. It is shown that the particular choice of four parameters associated with this new technique uniquely separates the effects of performance from the effects of flight condition. To the author's knowledge, this is the first description to include all of the relevant non-dimensional parameters for a given machine in an integrated manner.

3. It is demonstrated that the effects of mechanical damping and mass ratio (between blade mass and fluid mass) can be collapsed into a single parameter, which we term the reduced damping, g/ρ^*, for the high mass ratios found in aeroengines. This combination is novel in the context of turbomachinery aeroelasticity.

4. A computational study using a linearized-unsteady, compressible, potential flow model shows that the primary instability mechanism in this model both for bending and for torsion was local (i.e. a length scale of the same order as the blade chord). That is, the instability arises from the effect of a vibrating blade upon itself and its neighboring blades.

5. A data analysis procedure has been constructed for data which span the four-dimensional parameter space to assess the flutter boundary. In this context, a novel, generic boundary-fitting technique using

Support Vector Machines was developed to fit boundaries between stable and unstable data.

6. Stability boundaries that account for the full 4D parameter space were assessed from experimental test data of a full-scale fan. Sensitivities of the flutter boundary were quantitatively assessed. These parameter sensitivities can be used to extend data from ambient tests on similar geometries to estimate the effects of flight condition.

7. A rational methodology is developed for *flutter clearance*. Using this methodology, the most sensitive points in the parameter space can be quickly identified for rig testing, or for computational simulation.

Chapter 2

Complete set of parameters for flutter stability

The current methodology of designating flutter regions on the performance map of pressure ratio in terms of corrected mass flow and corrected speed (see Figure 2-1) is useful, but incomplete. In particular, the corrected quantities do not eliminate the dependence of inlet temperature and pressure on the flutter boundary, although they do remove these dependencies upon compressor performance parameters (pressure ratio, corrected speed, and corrected weight flow). Therefore, the boundary may "shift" depending upon the inlet conditions as depicted for raised temperature in Figure 2-1, which occurred in the case of the F100 fan, as described in the introduction.

The thermodynamic conditions at the rotor inlet, the temperature, the pressure, and the density, are dependent upon the flight conditions (altitude and flight Mach number), and the upstream geometry in the engine. The stagnation quantities (temperature, T, density, ρ, and pressure, p) of the outside air are defined as

$$T_t = T_0 \left(1 + \frac{\gamma - 1}{2} \mathrm{M}_f^2\right)$$

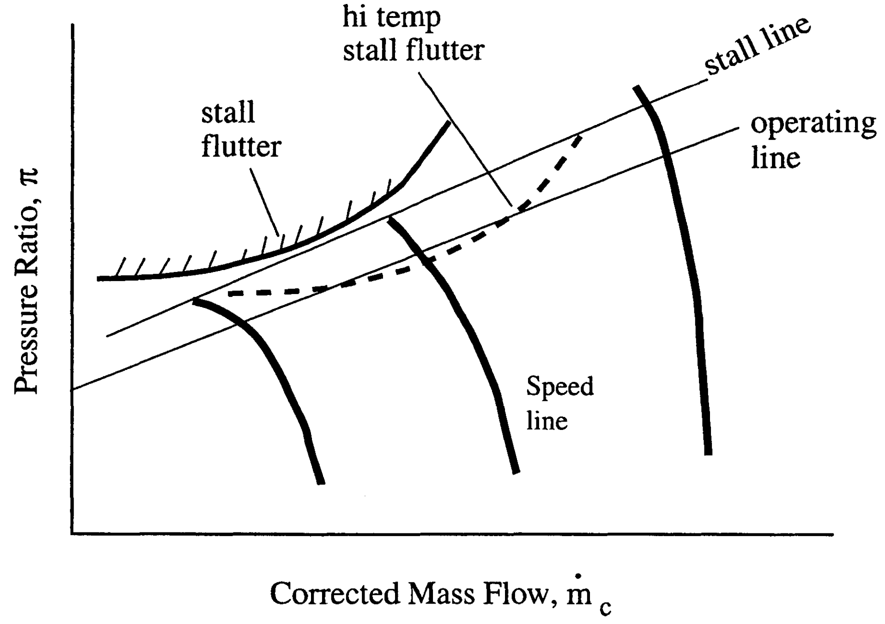

Figure 2-1: Schematic of performance map with stall flutter boundary shown. Changes in the thermodynamic conditions can move the boundary, as shown.

$$
\begin{aligned}
p_t &= p_0 \left(1 + \frac{\gamma - 1}{2} \mathrm{M}_f^2\right)^{\gamma/(\gamma-1)} \\
\rho_t &= \rho_0 \left(1 + \frac{\gamma - 1}{2} \mathrm{M}_f^2\right)^{1/(\gamma-1)}
\end{aligned}
$$

where the subscript 0 represents ambient quantities, and t represents stagnation (or "total") quantities, M_f is the flight Mach number, and γ is the ratio of specific heats. Figure 2-2 shows the effect of flight Mach number, M_f on the stagnation quantities.

With an ideal diffuser, these stagnation quantities can be recovered as the air travels into the engine, raising the static temperature, pressure and density at the rotor inlet to the front stage compared to ambient conditions. For latter stages, these quantities will be further increased due to the work transfer from the compressor to the fluid.

In this chapter, the problem of constructing a complete set of non-dimensional parameters for the stall flutter problem is addressed, which goes beyond the classical performance map, and can account for the inlet thermodynamic conditions. Precise conditions are described under which a set of four non-dimensional parameters that are necessary and sufficient for flutter stability assessment.

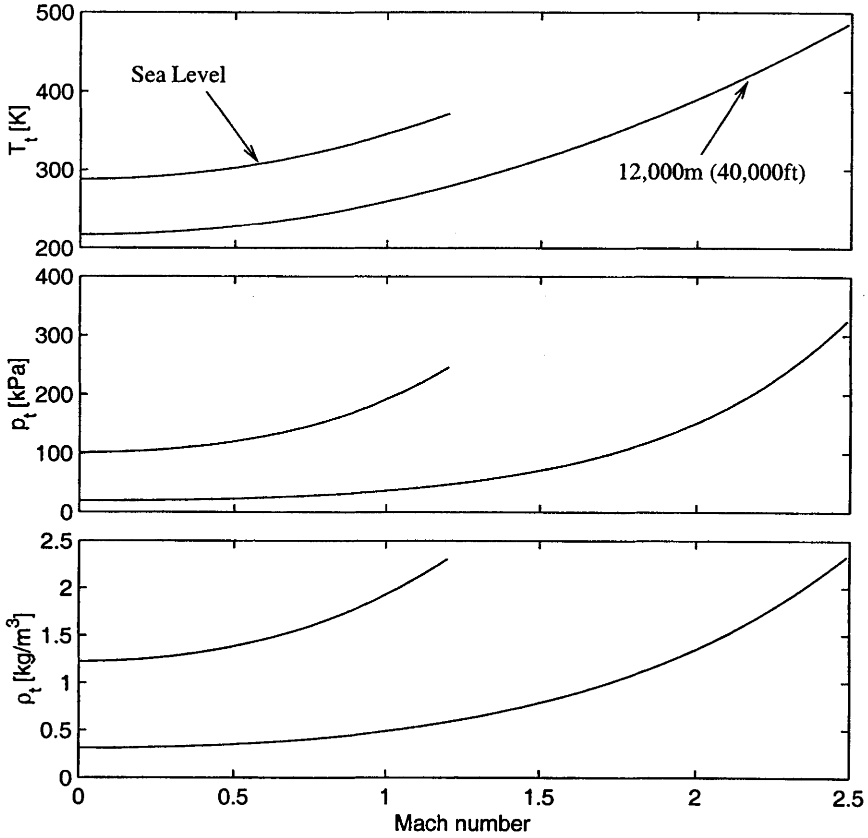

Figure 2-2: Ambient stagnation temperature, T_t, pressure, p_t, and density, ρ_t, as a function of flight Mach number for two altitudes: Sea level and at 12km. Ideal diffusers are able to recover these conditions for the first stage.

2.1 Stability Analysis

Although we have noted the incompleteness of the performance map due to the dependency on flight condition, the problem remains of constructing a set of parameters that does provide a complete description. To approach this question, we begin with an idealization of the system as shown in Figure 2-3. Here, we consider a single blade vibrational mode, with a given modal mass, m_0, modal frequency, ω_0, and modal (structural) damping g. The blade-to-blade coupling occurs as a consequence of the fluid dynamic forces.

A general form of the aeroelastic equation for a particular blade, j, is

$$m_0\ddot{q}_j + m_0\omega_0^2(1+ig)q_j = F_j \tag{2.1}$$

where q is the generalized coordinate, F_j is the unsteady fluid forcing, and the structural damping is added as an imaginary stiffness. This aeroelastic formulation (see Crawley, 1988) uses a complex-valued generalized coordinate such that the imaginary part of q is phase-shifted from the real part by 90°. The real part of complex-valued quantities are said to be "in-phase" with the vibration, and the imaginary part is "out-of-phase." If the vibrations are sinusoidal with frequency ω_0 (which occurs at resonance), then $q_j = \bar{q}_j e^{i\omega_0 t}$, and equation (2.1) is equivalent to the familiar forced, damped, harmonic oscillator, where the forcing function comes from the flow:

$$m_0\ddot{q}_j + 2m_0\omega_0\zeta\dot{q}_j + m_0\omega_0^2 q_j = F_j \tag{2.2}$$

where $\zeta = g/2$. We consider solutions of equation (2.1) that are harmonic, with a complex frequency, ω, (see Figure 2-4). For cases near the stability boundary, the amplitude is small, and the frequency has an imaginary part near zero. One might deduce from Figure 2-4 that the complex frequency is related to stability. In fact, one can form an "aeroelastic eigenvalue", namely $s = i\omega$, which follows the same trends as linear system eigenvalues do (Crawley, 1988). For example, if the real part of s is negative, then the system is stable[1]. Correspondingly, if the imaginary part of ω is positive, then the system is stable.

The unsteady fluid forces, F_j, however are still unspecified. We presume the following form:

---

[1] Note that the substitution for q is essentially a Laplace transform, when viewed in this way

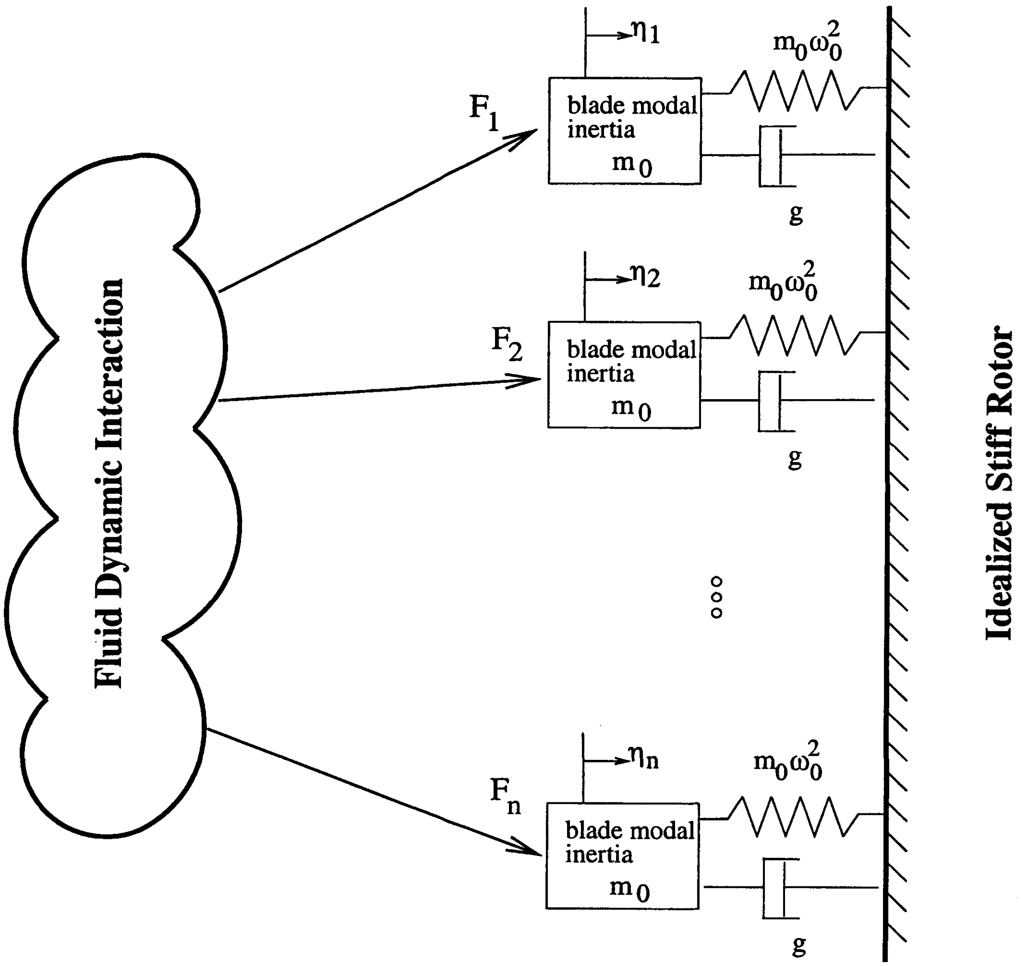

Figure 2-3: Schematic model of the fluttering rotor for a specific mode of vibration. The blades are modeled as second-order systems (corresponding to the structural mode being analyzed). The blades are subject to fluid forcing, which generates an aerodynamic coupling between blades.

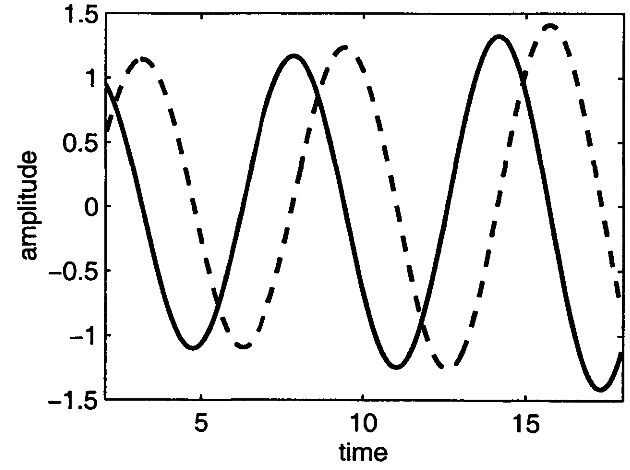

Figure 2-4: Example of real (solid) and imaginary (dashed) parts of generalized coordinate, q. The imaginary part is 90° out of phase from the real part, and the frequency has a small imaginary part.

$$F_j = \gamma c^2 p_0 \; l_j(\bar{\eta}_1, \ldots, \bar{\eta}_n; M, \alpha, \tilde{K}^*) \tag{2.3}$$

where c is the blade chord, γ is the ratio of specific heats, p_0 is the inlet pressure, and l_j is the non-dimensional fluid force coefficient for forces on blade j which depends upon $\bar{\eta}$, the complex blade amplitude of $\eta = q/c$, upon M, the inlet relative Mach number, α the inlet flow angle, and upon $\tilde{K}^*$, the "compressible reduced frequency" based on the oscillating frequency, $\mathrm{Re}(\omega)$,

$$\tilde{K}^* = \frac{\mathrm{Re}(\omega)c}{\sqrt{\gamma R T_0}}.$$

This compressible reduced frequency is a new parameter, which will be discussed further in the next chapter. The $\sim$ above the K^* indicates that the oscillating frequency, $\mathrm{Re}(\omega)$ is used in computing $\tilde{K}^*$, rather than the natural frequency, ω_0, used in computing K^*.

One should note that the inlet pressure in (2.3) can be written in terms of the inlet Temperature and density, by the ideal gas law

$$p_0 = \rho_0 R T_0. \tag{2.4}$$

It is shown in Appendix A, that an alternate, but equivalent, expression for the forces, (2.3), is

$$F_j = c^2 \rho_0 U^2 \; l'_j(\bar{\eta}_1, \ldots, \bar{\eta}_n; M, \alpha, \tilde{k}) \tag{2.5}$$

where $\rho_0 U^2$ is the inlet dynamic pressure and $\tilde{k} = \mathrm{Re}(w)c/U$ is the classical reduced frequency based on $\mathrm{Re}(w)$.

2.1.1 Fluid Dynamical Conditions

The conditions under which equation (2.3) describes the vibration-induced fluid forces are derived in Appendix A, and are as follows:

1. (a) fixed nominal flow path geometry,

(b) structure with linear dynamics and a single blade mode, (m_0, g, ω),

(c) Prandtl number of unity, $Pr \approx 1$, and high Reynolds number, Re

(d) Adiabatic Blades

2. We assume that M and α act independently. This implies that we avoid the "unique incidence" region (i.e. vertical speedlines on the performance map, see Cumpsty, 1989). In the case of unique incidence, we must use the pressure ratio, π, to replace either M or α.

3. Existence of a steady flow solution (about which the unsteady flow may be linearized), which implies that there are no large scale oscillations such as rotating stall or surge.

4. Inlet characteristic Mach number, M, and flow angle, α, captures the inlet flow distribution. This implies an axisymmetric flow, with an inlet radial velocity distribution specified by a single characteristic Mach number, M, and flow angle, α. That a single quantity is sufficient is a reasonable assumption if the inlet guide vane (IGV) angles are scheduled with the corrected parameters (i.e. the corrected mass flow, m_c, and corrected speed, N_c).

2.1.2 Development of Stability Conditions

Substituting the form for the fluid forces, (2.3), into the aeroelastic equation, (2.1), and non-dimensionalizing, we obtain

$$-\left(\frac{\omega}{\omega_0}\right)^2 \left(\frac{1}{\rho^*}\right) \bar{\eta}_j + \left(\frac{1}{\rho^*}\right) \bar{\eta}_j + i \left(\frac{g}{\rho^*}\right) \bar{\eta}_j = \frac{1}{(K^*)^2}\, l_j(\bar{\eta}_1, \ldots, \bar{\eta}_n; M, \alpha, \tilde{K}^*) \tag{2.6}$$

where ρ^* is the non-dimensional air mass/fluid mass ratio defined in the following manner:

$$\rho^* = \frac{\rho c^2}{m_0},$$

if m_0 is given as a sectional mass, or $\rho c^3/m_0$ if m_0 is given as a total mass. This is related to the typically defined blade mass ratio, μ,

$$\rho^* = \frac{4}{\pi \mu}.$$

For our purposes, we prefer using ρ^* to highlight the role of the flight condition (i.e. inlet density). In the context of assessing linear stability, we linearize for small amplitude vibrations, $\bar{\eta}$. Although the pressure field is not necessarily linear with respect to small perturbations (due to shock motion), the integrated fluid force does behave linearly. Furthermore, it can be shown that in the tuned (identically bladed), linear case, switching to interblade phase coordinates (Lane, 1954), decouples the equations for the blades in (2.6). Each interblade phase, σ_j, corresponds to a case in which all of the blades undergo vibrations with a fixed phase shift, σ_j, between neighboring blades. The discrete interblade phase angles correspond to periodic circumferential modes in the duct, the most unstable of which is relevant for stability assessment. The aeroelastic equation for harmonic motions in interblade phase σ_j is

$$-\left(\frac{\omega}{\omega_0}\right)^2\left(\frac{1}{\rho^*}\right)\bar{\eta}_{\sigma_j}+\left(\frac{1}{\rho^*}\right)\bar{\eta}_{\sigma_j}+i\left(\frac{g}{\rho^*}\right)\bar{\eta}_{\sigma_j}=\frac{1}{(K^*)^2}\,l_{\sigma_j}(M,\alpha,\tilde{K}^*)\,\bar{\eta}_{\sigma_j} \tag{2.7}$$

Substituting $\omega = \mathrm{Re}(\omega) + i\,\mathrm{Im}(\omega)$, and taking the real and imaginary parts gives the following pair of equations,

$$-\frac{1}{\rho^*}\left(\frac{1}{\omega_0^2}\right)\left(\mathrm{Re}(w)^2+\mathrm{Im}(w)^2\right)+\frac{1}{\rho^*} = \frac{1}{(K^*)^2}\mathrm{Re}(l_{\sigma_j}(M,\alpha,\tilde{K}^*)) \tag{2.8}$$

$$-\frac{2\mathrm{Re}(w)\mathrm{Im}(w)}{\rho^*}+\frac{g}{\rho^*} = \frac{1}{(K^*)^2}\mathrm{Im}(l_{\sigma_j}(M,\alpha,\tilde{K}^*)) \tag{2.9}$$

As mentioned before, stability depends upon the imaginary part of complex frequency. In particular, a positive $\mathrm{Im}(\omega)$ is stable.[2]

Combining the mass and mechanical damping parameters

Since $Re(\omega)/\rho^*$ is always positive, the stability condition can be framed in terms of the right hand side of equation (2.9). Furthermore, we consider the worst case (i.e. the least stable) interblade phase angle, σ_j. This produces the stability condition

---

[2] Using the "aeroelastic eigenvalue" concept, this corresponds to $\mathrm{Im}(-si) > 0$, or $\mathrm{Re}(s) < 0$, which is more familiar for linear systems

$$g/\rho^* > \frac{1}{(K^*)^2} \max_{\sigma_j} \mathrm{Im}(l_{\sigma_j}(M, \alpha, \tilde{K}^*)) \tag{2.10}$$

Notice that a parameter reduction has occurred in this step. The damping, g, and the aerodynamic mass ratio, ρ^*, can be combined into a single parameter, g/ρ^*, which we term the reduced damping.

Case of massive blades

We can now use the real part of the equation to find the condition such that $\tilde{K}^* \approx K^*$. Since we are most interested in neutrally stable solutions, it is reasonable to set $\mathrm{Im}(\omega) = 0$ in equation (2.8). This implies that

$$\mathrm{Re}(\omega)^2 = \omega_0^2 \left(1 - \frac{\rho^*}{(K^*)^2} \mathrm{Re}(l_{\sigma_j}(M, \alpha, \tilde{K}^*))\right) \tag{2.11}$$

It therefore follows that $\mathrm{Re}(\omega) \approx \omega_0$, or that $\tilde{K}^* \approx K^*$ if

$$1 \gg \frac{\rho^*}{(K^*)^2} \mathrm{Re}(l_{\sigma_j}(M, \alpha, \tilde{K}^*)). \tag{2.12}$$

Since ρ^* is typically small for blades in aeroengines, $O(0.01)$, this condition is usually a good approximation.

Stability Condition

The stability condition can be written as

$$g/\rho^* > \frac{1}{(K^*)^2} \max_{\sigma_j} \mathrm{Im}(l_{\sigma_j}(M, \alpha, K^*)) \tag{2.13}$$

Overall, there are four parameters that are necessary and sufficient for the assessment of flutter stability of a given machine: the Mach number, M, the flow angle, α, the compressible reduced frequency, K^*, and the reduced damping, g/ρ^*.

Alternate Stability Condition

A similar argument using the equivalent form, (2.5), results in the following, similar stability criterion:

$$g/\rho^* > \frac{1}{k^2}\max_{\sigma_j}\mathrm{Im}(l_{\sigma_j}(M, \alpha, k)) \tag{2.14}$$

where k is the classical reduced frequency, $k = \omega_0 c/U$.

2.2 Summary

The environment of high Mach number flight can significantly alter the inlet thermodynamic conditions to an aeroengine from the sea level static point. Such changes influence flutter stability in a manner not accounted by the corrected performance map.

Under specified conditions, the aeroelastic stability of a bladed rotor of a given design depends upon a four variable parameter space, which is spanned by $(M, \alpha, K^*, g/\rho^*)$, where M is the Mach number, α is the inlet flow angle, K^* is a new parameter termed the compressible reduced frequency, and g/ρ^* is a new parameter termed the reduced damping.

The introduction of the reduced damping, g/ρ^*, indicates that the effects of mechanical damping and the fluid inertia parameter have coupled effects in the non-dimensional parameter space. Equivalent formulations exist using either the compressible reduced frequency parameter, K^*, or the classical reduced frequency parameter, k. The new parameters, g/ρ^*, and K^*, are discussed in further detail in Chapter 3.

A flutter stability condition, (2.13), is derived in terms of the four non-dimensional parameters. This involves an unsteady aerodynamic coefficent, l_σ, which depends upon three of the four parameters: (M, α, K^*).

Chapter 3

A new technique for representing flutter boundaries

In this chapter, a new technique is introduced for representing flutter stability. This technique continues our focus upon the operability issues for a particular design. There are many ways to pick four nondimensional parameters to span the parameter space described in the previous chapter as being necessary and sufficient to describe flutter stability of a design. However, for operability issues, we show that a particular set uniquely[1] separates the influence of performance conditions, ($\dot{m}_c$, N_c) from the influence of flight conditions, in terms of inlet temperature, T_0, and inlet density, ρ_0. This unique set includes two parameters not in common usage: a reduced damping parameter, g/ρ^*, and a compressible reduced frequency parameter, K^*. The role that these two parameters play in flutter stability is discussed.

A methodology is constructed, using this unique set of parameters, by which flutter boundaries may be fully specified. A complementary plot to the performance map completes the parameter space. For given structural parameters, this plot has a one-to-one correlation with the flight condition (inlet temperature, T_0, and inlet density, ρ_0). This methodology can be used to look at the stability of a design throughout its intended flight envelope.

---

[1] The sense in which the set is unique is discussed precisely in Appendix B. For example, multiples of these parameters also have these properties.

Finally, these concepts are illustrated in the context of a multimission engine, which encountered problems with flutter at the flight test stage, due to temperature and density effects.

3.1 Uniqueness of Parameters

In this section, we address the question of how to choose a set of parameters to span the parameter space. For the current purposes, we are concerned with describing the operability of a machine in a convienient way.

We consider the chord, c, to be fixed, which is in keeping with the previous assumption of fixed, nominal flowpath geometry. In this case, the Mach number, M, and flow angle, α, can be shown to be equivalent to the corrected mass flow, $\dot{m}_c$, and the corrected speed, N_c. Since the map of $\dot{m}_c$ and N_c is the standard way to represent performance, we reserve two of the four parameters for ($\dot{m}_c$, N_c).

We would like the two parameters left to describe the location on the flight envelope. This would make it possible to separate the effect of flight condition from the performance point, described by ($\dot{m}_c$, N_c). More precisely, we impose the condition that if the structural variables, (ω_0, m_0, g), are constant, then the flight condition, in terms of inlet temperature and inlet density, is solely described in terms of the two free parameters.

Another desireable property is related to the functional form of the stability condition, (2.13). Here, it is shown that the vibration-induced fluid coefficient is only a function of three of the four parameters. It is beneficial to define our parameters such that this is the case, to avoid describing the fluid forces in a manner that is more complicated than necessary.

It is shown in Appendix B that the aforementioned conditions establish a unique[2] set of four parameters.

$$(\dot{m}_c, N_c, K^*, g/\rho^*)$$

where K^* is a parameter that we introduced in Chapter 2, the compressible reduced frequency defined as

---

[2] The parameters are unique within a continuous monotonic transformation of any of the parameters (e.g. $x \to x^2$)

$$K^* = \frac{\omega_0 c}{\sqrt{\gamma R T_0}}. \tag{3.1}$$

The remainder of this section discusses the properties of this four parameter space and how a flutter description based on these four parameters can complete the flutter boundary description, drawn solely upon the performance map.

3.2 Reduced damping and compressible reduced frequency

Generally speaking, increases of the reduced damping, g/ρ^*, and the compressible reduced frequency parameter, K^*, have ***stabilizing influences*** on the rotor. In this section, the physical interpretation of these two parameters is discussed, as well as their effect on stability.

3.2.1 Reduced damping parameter

In previous literature concerning turbomachinery flutter (see reviews by Srinivasan, 1997, and Förschng, 1994) the mechanical damping, g, and the mass ratio, μ (or, equivalently, ρ^*), are treated as separate parameters. Our use of a combined reduced damping, g/ρ^*, is therefore novel in the current context. However, the concept of a combined reduced damping parameter has been used in other areas, notably for bluff-body fluid-structure interactions (Vickery and Watkins (1964), Scruton (1965), and Skop and Griffin (1973)).

The roles of the damping, g, and fluid inertia parameter, ρ^* (or, equivalently, mass ratio μ), are often neglected in discussions of turbomachinery flutter. Often, it is assumed that since g and ρ^* are individually small compared to unity (or, equivalently, $\mu \gg 1$), the effects of the fluid inertia and mechanical damping are, likewise, individually negligible. More specifically, the ***sign*** of $Im(l_\sigma)$ which is often used as a flutter criterion in predictive schemes, is not necessarily conservative for analysis of data from real machines.

Unfortunately, it is notoriously difficult to accurately estimate the mechanical damping. This problem was extensively studied by Srinivasan (1981) (see also Srinivasan, 1997) who characterized the effects due to material damping, and friction at the shroud and root attachment. According to the ***in vacuo*** tests of

Srinivasan, material damping of a typical titanium blade is of order $g = O(0.0002)$, while damping on the same blade due to frictional effects at the root is of order $g = O(0.01)$ for bending modes, and of order $g = O(0.01)$ for torsional modes.

There has also been extensive work, on design of platform dampers, (Griffin (1979), Cardinale, Bankhead, and McKay (1980), Srinivasan (1981)), to the more recent work of Sanliturk, Ewins, and Stanbridge (1999)), and specialized blade inserts (El-Aini, 1996) which have been used to increase damping in turbine stages. Furthermore, recent work has shown that significant material damping is possible using viscoelastic material in interior cavities (Gordon, 1997), and in layers within composite blades (Kosmatka and Mehmed, 1998). These can potentially provide an increase in the damping of order $g = O(0.01)$.

The fluid inertia parameter, ρ^*, is dependent on the air density, the blade size (chord), and the modal mass, m_0. The modal mass, m_0, depends on the modeshape and the blade density. For a typical fan blade (taken from Fan-C, a NASA research transonic fan) at sea level static, the value of ρ^* is approximately 0.009, based on the blade sectional mass and sea level conditions.

Combining these estimates, we find that for inserted metal blades,

$$g/\rho^* \approx \frac{0.01}{0.009} \approx 1. \tag{3.2}$$

For metallic blisks (integrally bladed disks), if the frictional damping is negligible, then the reduced damping estimate changes dramatically to

$$g/\rho^* \approx \frac{0.0001}{0.009} \approx 0.01. \tag{3.3}$$

For blades with dampers, the associated g/ρ^* may be substantially higher. However, roughly speaking, the reduced damping is O(1) for inserted blades. Thus, damping may not always be ignored in the stability criterion (2.13). Those studies which account for damping and fluid inertia typically yield reduced damping parameters on the order of unity, as those listed in Table 3.1.

Among these studies, Försching's parametric study using an inviscid, incompressible model particularly focuses on the effects of mass ratio and damping. He describes the "interdependent effects" of these two

Study	g	ρ^*	g/ρ^*
Kielb and Ramsey [1989]	0, 0.001, 0.002	0.0028	0, 0.36, 0.71
Kaza and Kielb [1982]	0.004	0.0031	1.27
Bendikson Friedmann [1980]	0.005, 0.02	0.004	1.23, 5
Försching [1994] (review paper)	0, 0.005, 0.01, 0.02, 0.03, 0.05	0.0010, 0.0014, 0.0016, 0.0018, 0.0025, 0.0064	0, 0.781, 2, 2.78, 3.125, 3.57, 4, 5, 5.5, 7.14, 8, 10, 12, 12.5, 20
Srinivasan and Fabunmi [1984]	0.4, 0.8, 1.2	1.4	0.28, 0.57, 0.85

Table 3.1: Cascade flutter studies with damping effect included

parameters, noting that the level of mechanical damping strongly influences the sensitivity to mass ratio. These effects are neatly encapsulated into the current description which uses a single reduced damping parameter, g/ρ^*.

In fact, the single g/ρ^* parameter collapses the results of Försching's (1994) 2-D, inviscid, incompressible parametric study of the 4th standard configuration (Bölcs and Fransson, 1986). Försching lists the results as curves of critical reduced velocity, $U^* = 1/k$ versus interblade phase, for each combination of damping, g, and mass ratio, μ (equivalent to ρ^*). Since the flow is modeled as incompressible, the classical reduced velocity, $U^* = 1/k$, is used.

Figure 3-1a shows the critical reduced velocity versus the reduced damping parameter for Försching's simulations in a combined bending-torsion mode. Each data point on the plot corresponds to a separate curve of Försching (1994), with the value at the least stable interblade phase angle selected. The $\circ$, $\Box$, and $\diamond$ symbols denote different mass ratios, μ, of 500, 700, and 900, respectively. As the reduced damping increases, the critical reduced velocity, U^*, increases linearly, as shown. The dashed line is a least-squares linear fit. The effects of mass ratio (i.e. density parameter, ρ^*) and damping, g, are very well captured by the reduced damping, g/ρ^*.

The Figure 3-1b shows this movement in least stable interblade phase, σ_{min}, with reduced damping, g/ρ^*. This shows that the least stable interblade phase, in this case, has a weak trend with the reduced

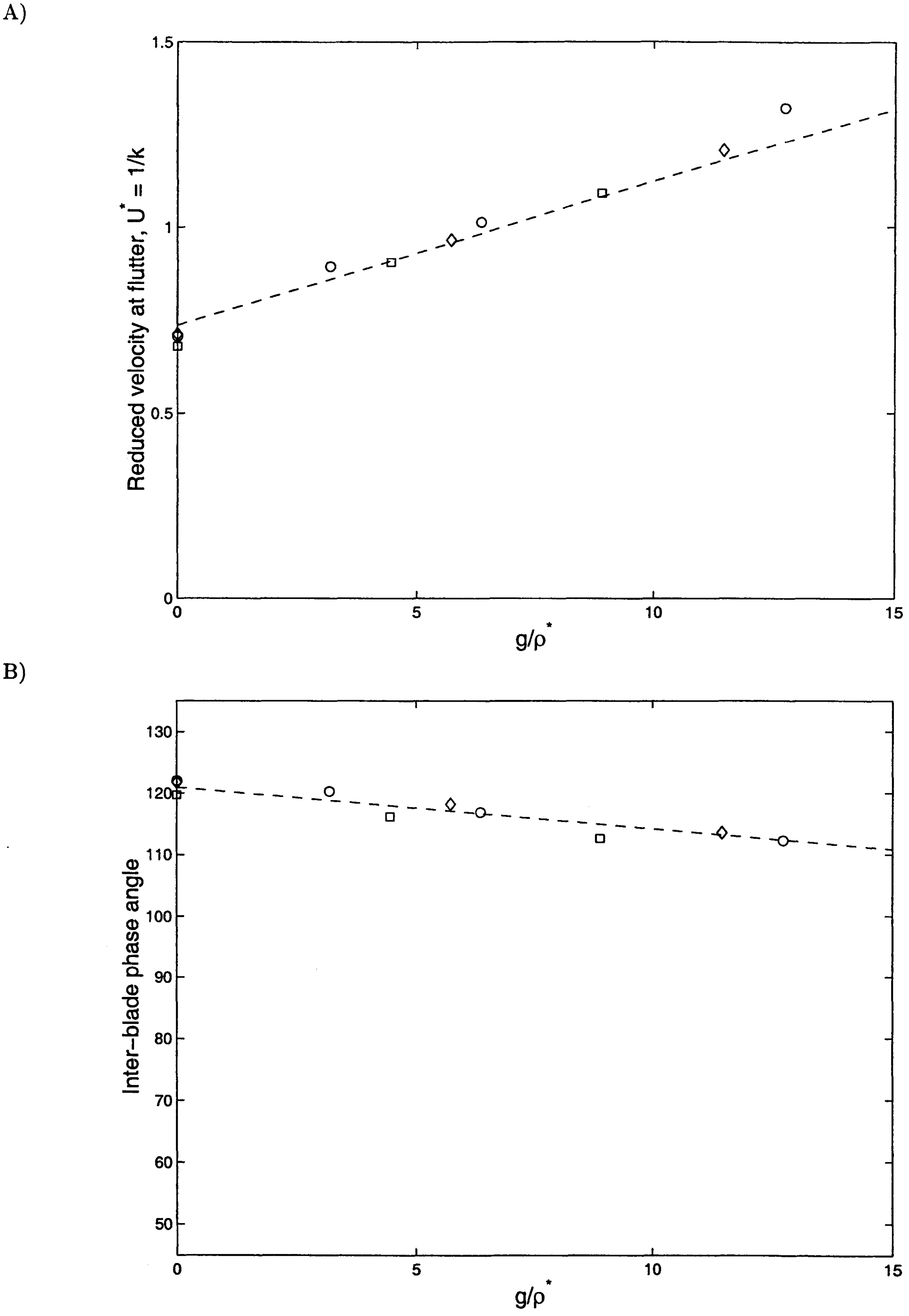

Figure 3-1: Collapse of computations of Försching (1994) with reduced damping, g/ρ^* for a combined bending-torsion mode. The parameters g and ρ^* are individually varied. A ○ represents $\rho^* = 0.87 \times 10^{-3}$, ($\mu = 900$), a ◊ represents $\rho^* = 1.12 \times 10^{-3}$, ($\mu = 700$), and a □ represents $\rho^* = 1.57 \times 10^{-3}$, ($\mu = 500$). Two plots are shown: (a) Critical reduced frequency as a function of g/ρ^*, and (b) Interblade phase at stability point. The single parameter, g/ρ^*, summarizes the combined effects of damping and fluid inertia.

damping.

This example shows that previous work in the flutter literature may be usefully reinterpreted using the reduced damping, g/ρ^*. The *justification* for the reduced damping, however, comes directly from a rigorous mathematical development of the linear stability. Therefore, such a collapse is not dependent on the details of unsteady aerodynamic modeling.

An important property, which is utilized later in the thesis, is that increasing the reduced damping has a stabilizing effect on flutter stability. This is intuitive since an increase in damping typically mitigates the occurance of vibrations. Furthermore, inspection of the flutter stability condition, equation (2.13), makes it clear that increasing g/ρ^* is beneficial to stability.

3.2.2 Compressible Reduced Frequency

The compressible reduced frequency, K^*, is particularly convenient for use with the performance map, as discussed in the next section. Here, we discuss in more detail the relationship of the reduced frequency parameter, K^*, to the classical reduced frequency, k, and to flutter stability.

It is helpful to consider the physical interpretation of the reduced velocity, k, and the compressible reduced velocity, K^*. They both can be interpreted as ratios of time scales between the unsteady fluid and vibrating structure. In particular,

$$\begin{aligned} k = \frac{\omega_0 c}{U} &= \frac{\text{flow-through time}}{\text{vibration time}} \\ K^* = \frac{\omega_0 c}{\sqrt{\gamma R T_0}} &= \frac{\text{acoustic time}}{\text{vibration time}} \end{aligned}$$

The "flow-through" time is the time required for a particle of fluid to pass through the blade passage, and the "acoustic" time is the time required for a fluid pressure disturbance to pass through the blade passage. Including the "vibration" time for one radian of the cycle to elapse, there are three relevant time scales. These three time scales relevant to the problem are shown schematically in Figure 3-2.

If the Mach number is specified, the relationship between the two fluid time scales is likewise set. In this case, *either* a further specification of the compressible reduced frequency, K^*, or the classical reduced

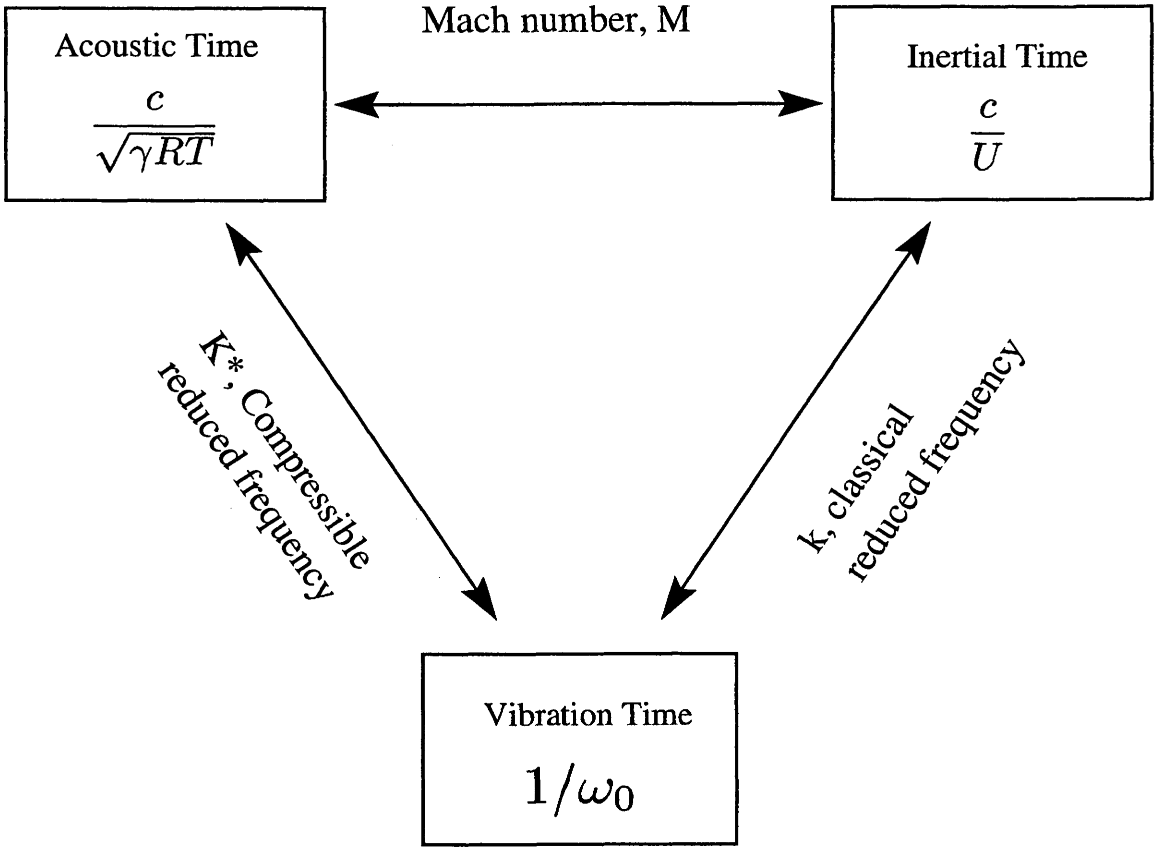

Figure 3-2: Diagram depicting three relevant time scales: inertial, acoustic, and vibrational, and relationships between these using Mach number, M, classical reduced frequency, k, and compressible reduced frequency, K^*.

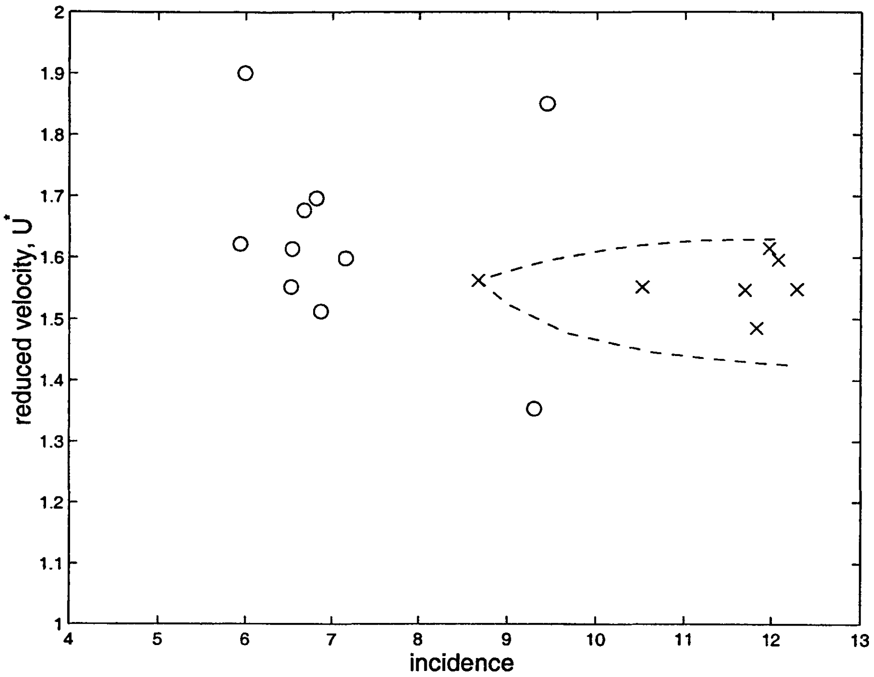

Figure 3-3: Fan test results of Stargardter(1979). Stable points are plotted as o symbols and flutter points are plotted as × symbols. Since the data are taken with ambient air, the effects of Mach number and reduced frequency are mixed.

frequency, k, determines the relationship among these three time scales.

Consider the "critical" reduced velocity, U^*_{cr}, of the y-axis of Figure 3-1. This is the maximum reduced velocity, $U^* = 1/k$, which may be attained before the occurrence of flutter. Based on the physical description above, it is not obvious that there should be a single "critical" reduced velocity.

This is an idea which traces its roots to wing aeroelasticity (Bisplinghoff, Ashley, and Halfman, 1955, and Fung, 1955). It is intuitive that at zero relative velocity the aerodynamic damping is positive (e.g. the damping on a vibrating tuning fork is essentially fluid damping). The critical speed is, then, the speed at which this aerodynamic damping changes so that the system is destabilizing overall. This stable maximum speed is, in fact, termed the *flutter speed.*

This view, unfortunately, does not capture all the realities of turbomachinery aeroelasticity. In fact, much of flutter occurs at part-speed, not at a maximum speed. This point is shown strikingly in the experiments of Stargardter (1979) on the TS22 fan rig as shown in Figure 3-3. The data are plotted on the flutter map (Snyder, 1988) of flow incidence, i, versus reduced velocity, U^*. It appears that this is a case in which there is not a single, critical reduced velocity. In places, increasing the reduced frequency (i.e.

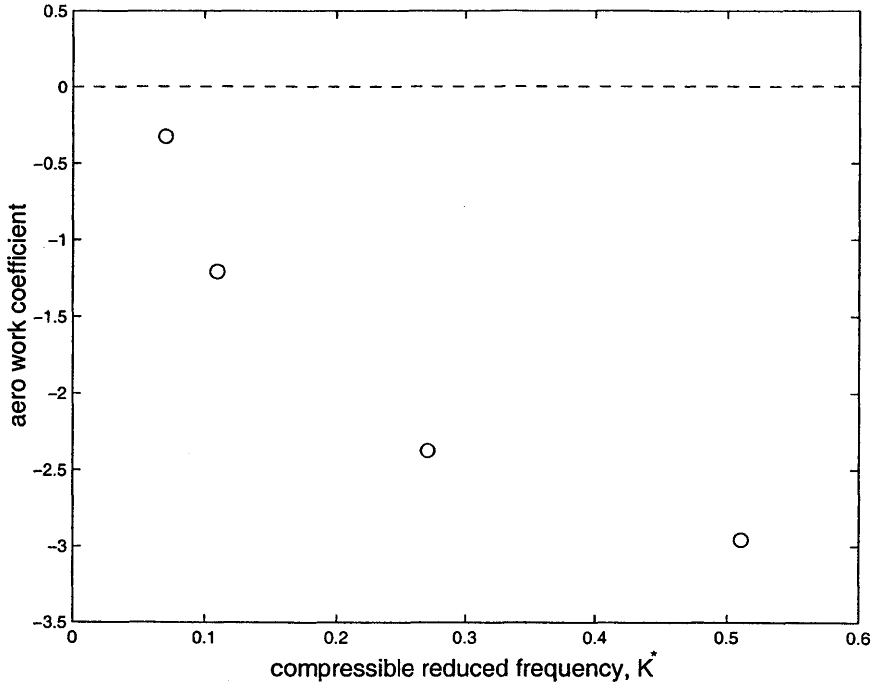

Figure 3-4: Effect of reduced frequency on aerodynamic damping in Fifth Standard Configuration, experimental results (Bölcs and Fransson (1986)). The interblade phase angle is held constant at 180°. The damping decreases as K^* decreases.

decreasing reduced velocity) is actually destabilizing.

In this case, the explanation lies in the fact that the Mach number changes significantly over the plot in Figure 3-3. The experiment was run, as is typical, at ambient conditions for constant geometry. Among the three time scales in Figure 3-2, the acoustic time scale is fixed (by the ambient condition), and the vibration time scale was also unchanged over the experiments. Thus, there is a linear dependency between the Mach number, M and the classical reduced velocity, k. Only if one holds the Mach number fixed, as in the incompressible computational study shown in Figure 3-1, can a "critical" reduced velocity may be defined.

Experimental data for a high subsonic compressor is available for the 5th standard configuration (Bölcs and Fransson, 1986) which addresses this point. Here, a cascade was oscillated at various frequencies at a constant interblade phase of 180° with the flow held at a constant inlet Mach number of 0.5, and the unsteady blade pressures were measured. Some results of these experiments are depicted in Figure 3-4. The aerodynamic work, is plotted as a function of compressible reduced frequency, K^*. The aerodynamic work is a non-dimensional form of the energy transfer from the fluid to the blade, which is negative for

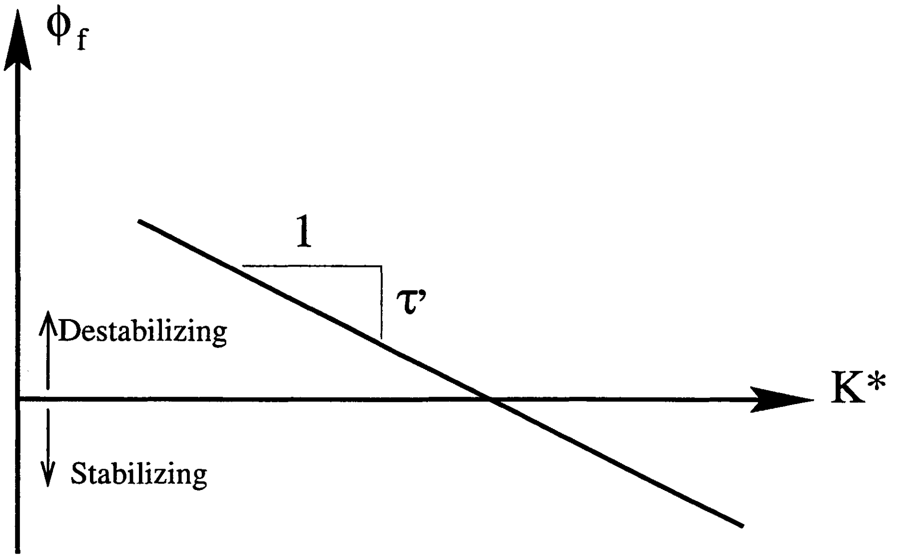

Figure 3-5: Schematic relationship between K^* and unsteady fluid phase lag, ϕ_f.

stabilizing motions and positive for destabilizing motions. The experiments show that for a constant Mach number, and constant inlet flow angle, increasing compressible reduced frequency is stabilizing. In these experiments, the parameter changed is the oscillating frequency; that is, the vibration time. Therefore, for a constant Mach number (as in these experiments), the measured trends are valid both for the classical reduced frequency and for the compressible reduced frequency.

We can interpret this stabilizing effect of reducing the vibration time (i.e. increasing frequency) by considering the time lag between the blade vibration and the fluid reactions. The lag allows an exchange of energy to take place between the blade and the fluid. The direction of energy transfer is determined by the phase shift (caused by the time lag) between the oscillating fluid force and blade motion. The governing mechanism which produces the lag in turbomachinery flutter has not been definitively established, and remains an active research question. However, since the lag ultimately arises from the unsteady fluid dynamics, we can expect that the time lag scales with the relevant fluid time scales. The phase shift, however, is determined by the relation between the lag time and the period of oscillation.

$$\phi_f = \phi_{f0} - \frac{\text{lag time}}{\text{Period}} = \phi_{f0} - \tau' \frac{\omega_0 c}{\sqrt{\gamma R T_0}} = \phi_{f0} - \tau' K^*$$

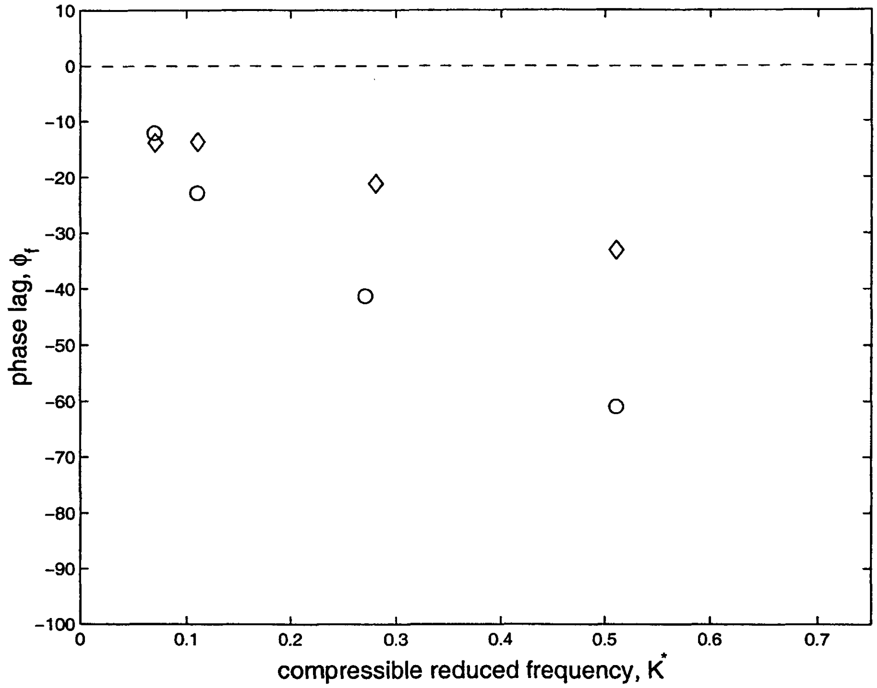

Figure 3-6: Effect of reduced frequency on phase between unsteady fluid forces and torsional oscillations in Fifth Standard Configuration, experimental results (Bölcs and Fransson (1986)). The interblade phase angle is held constant at 180°. Data are plotted for two incidence angles, 4°, as ○ symbols, and 6°, as ◊ symbols.

where ϕ_{f0} is an initial phase shift from steady effects and τ' is a non-dimensional fluid lag scaled by the pressure disturbance time scale. Since the fluid takes a finite time to react, τ' is a positive number. The relationship between ϕ and K^* is depicted in Figure 3-5. If the value of τ' is roughly constant for a given Mach number and flow angle, then the trends with reduced frequency are roughly linear for a range of K^*, as shown. Since the Mach number, M, is considered constant, the relationship between acoustic time and inertial time is fixed. Although K^* is used here (which we find convenient), a similar relationship holds with k.

Although this phase argument demonstrates that changes in stability can occur due to changes in K^*, it is not obvious that the trend should have the direction shown in Figure 3-5 in which increasing K^* stabilizes the system. This trend is consistent with the empirical trend that increasing natural frequency stabilizes blades with respect to flutter, as utilized in design practice (Snyder and Burns, 1988). Furthermore, the stabilizing trend of increasing natural frequency is also found in the results of several idealized analyses including the following: incompressible, potential flow over thin wings (Kemp and Sears, 1954), incompressible, potential flow over flat plate cascades (Whitehead 1960, 1962), inviscid cascades with strong shocks (Goldstein et.al., 1977), and fully stalled incompressible flow (Yashima and Tanaka, 1977, and Chi, 1980).

The experimental data from the 5th standard configuration also corroborates this interpretation. In Figure 3-6, the phase, ϕ_f, is plotted as a function of K^*. Two incidence angles are plotted, 4°, as o symbols, and 6°, as ◊ symbols. Clearly, the phase ϕ_f increases as K^* is decreased. Both flow angles elicit similar trends, but the effect of increasing incidence is destabilizing in general. Further results (Bölcs and Fransson, 1986) showed that with other parameters held constant, aerodynamic work increased smoothly as incidence was increased, eventually to a destabilizing condition.

3.2.3 Remarks

We have, thusfar, shown that the corrected performance point, $(\dot{m}_c, N_c)$, coupled with two new parameters, K^* and g/ρ^*, is a valid approach towards spanning the parameter space for flutter stability, and that this set uniquely satisfies some conditions (discussed in Appendix B). Further, trends have been developed which suggest that increasing K^* and increasing g/ρ^*, for a constant corrected performance point, have a stabilizing effect upon flutter stability. Here, we discuss the motivation for parsing the 4D parameter space using the suggested parameters, and evaluate the scope of validity of the trends with K^* and g/ρ^*.

The three conditions, mentioned earlier, are that two parameters span the corrected performance map, that the other two parameters span the flight envelope (inlet temperature and density) for a constant structure, and that the fluid force coefficient is dependent upon only three of the four parameters.

One way to view these conditions is as a decoupling of the effects of corrected performance point upon flutter stability from the other effects upon flutter stability. Before addressing the appropriate way to do this decoupling, it may be helpful to discuss the the performance quantities themselves, briefly.

Some important properties, such as the pressure ratio, the efficiency, and the occurrence of rotating stall, are a function of the corrected mass flow, $\dot{m}_c$, and the corrected speed, N_c. Physically, $\dot{m}_c$ and N_c turn out to be one equivalent representation of the flow Mach number, M, and flow angle, α. From an operability standpoint, however, $\dot{m}_c$ and N_c are a preferred form, since they can be easily related to changes in the rotor speed or operating line. This is evident in the terminology of the mass flow and rotor speed being "corrected" for the other variables (i.e. the flight condition). Other than these corrections, these other variables do not influence the performance quantities such as the pressure ratio.

In the case of aeroelasticity, however, the flight condition variables (i.e. the inlet temperature and density) have an influence which can not be accounted by simply using the corrected mass flow and corrected speed. Thus, two more parameters, besides $\dot{m}_c$ and N_c, are needed, as demonstrated in Chapter 2. It is desireable to "decouple" the effects of these other two parameters from the effects of $\dot{m}_c$ and N_c. Such a decoupling is not mathematically precise, but requires some interpretation. One way to accomplish this is to have the two other parameters span the space for which $\dot{m}_c$ and N_c are "corrected." The condition that these other two parameters span the flight condition for a constant structure does this. In Appendix B it is shown that the four parameters, $(\dot{m}_c, N_c, K^*, g/\rho^*)$, uniquely satisfy the conditions. Thus, the introduction of the parameters K^* and g/ρ^* can be thought of as an *aeroelastic extension* of the performance map of corrected mass flow, $\dot{m}_c$, and corrected speed, N_c, to include all the effects relevant to aeroelastic behavior. This point is developed in the next section.

We now turn to the trends of flutter stability with reduced damping, g/ρ^*, and compressible reduced frequency, K^*. The trend that increasing g/ρ^* stabilizes flutter is based upon the analytical derivation. An inspection of the stability criterion (2.13) shows that an increase in reduced damping, g/ρ^*, will always benefit flutter stability. By similarity, if the other parameters are kept constant, a change in reduced damping has the same sense as a change in the mechanical damping.

The trend that increases in K^* stabilize the rotor is a property of the unsteady fluid forces and the evidence for it is ultimately empirical. The physical argument presented supports the idea that increasing K^* will reduce the fluid force phase lag, and can change flutter stability. That this change with increasing K^* is stabilizing supposes that the quasi-steady behavior is destabilizing, and that the relevant value of K^* near the stability boundary is at the first zero-crossing of phase lag. The supposition that the quasi-steady behavior is destabilizing is supported in many special cases analytically, as previously documented.

By similarity, the trend that increasing compressible reduced frequency stabilizes flutter, at a constant corrected operating point, is equivalent to the trend that increasing blade modal frequency stabilizes flutter, which is a widely adopted design principle (Snyder and Burns, 1988). Further, similarity dictates that the

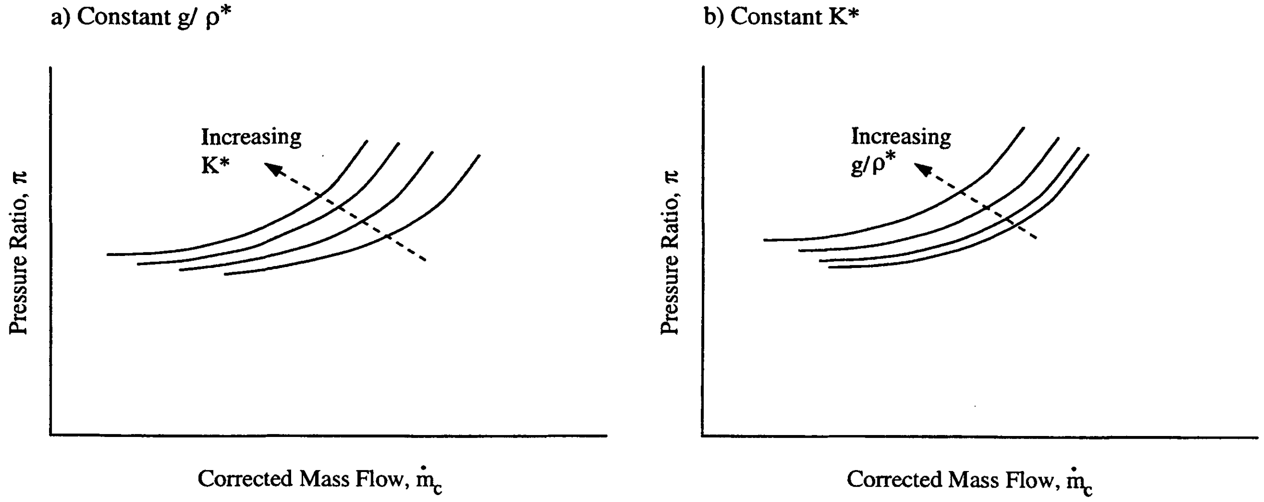

Figure 3-7: A family of boundaries, each for a particular g/ρ^* and K^*. Increasing either g/ρ^* or K^* has a stabilizing influence. Trends are shown for constant g/ρ^*, in (a), and for constant K^*, in (b).

same trend with K^* is also equivalent to the previously documented trend that increasing inlet temperature destabilizes flutter (Jeffers, 1988). The use of the K^* parameter, in fact, elucidates the direct relationship between the effects of inlet temperature and the effects of natural frequency. This directly addresses the issue raised by Jeffers (1988), as quoted in Chapter 1. We adopt this stabilizing trend of K^* as a general principle, relevant to aeroengines.

3.3 Fully specified flutter boundaries

In this section, the mass-damping, g/ρ^*, and the compressible reduced frequency, K^*, are used to extend the performance map flutter boundaries to include all of the operating parameters for a given machine, including flight condition. As discussed earlier, the set, $(M, \alpha, K^*, g/\rho^*)$, possesses some unique properties for operability assessment.

In fact, boundaries with a constant g/ρ^* and K^* have roughly the same shape as the "usual" measured boundaries boundary, as shown in Figure 2-1, assuming that the measurements are taken for constant inlet conditions (e.g. sea level standard). Furthermore, to first approximation[3], performance correlations in terms of corrected mass flow, $\dot{m}_c$, and corrected speed, N_c, are unaffected by the values of g/ρ^* and K^*.

---

[3] Assuming that any resultant changes in steady-state blade deflection have negligible effect upon steady-state performance

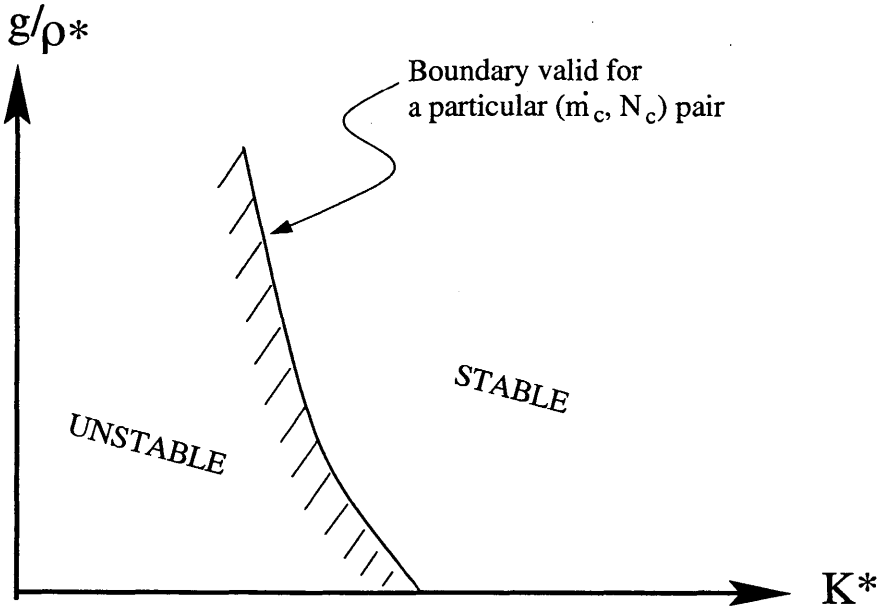

Figure 3-8: Map of compressible reduced frequency, K^*, versus mass-damping, g/ρ^*. Stability boundary corresponding to a particular point on the performance map is shown.

As described in the previous section, and as is widely recognized, increasing the mechanical damping and increasing the vibrational frequency have stabilizing effects. It follows that increasing g/ρ^* and K^* are both stabilizing. This means that isolines of g/ρ^* and K^* on the performance map shift in a stabilizing direction (away from the typical region of operation) with increasing g/ρ^* and K^*.

Therefore, a complete method for representing flutter boundaries is to use a *family* of curves on the performance map, each for a specific value of g/ρ^* and K^*, as schematically shown in Figure 3-7a and 3-7b. This family of curves extends the current formulation to one which can account for different flight conditions. For constant K^* (shown in Figure 3-7b), there is a limiting boundary as g/ρ^* tends to zero (i.e. $g/\rho^* \ll 1$).

It is also useful to look at a different view of the flutter boundary, restricted to a specific location on the performance map, but for varying K^* and g/ρ^*, as in Figure 3-8. Since increasing K^* and g/ρ^* are generally stabilizing, the stable region on Figure 3-8 is above and to the right of the boundary.

We can obtain a more complete look at the full flutter boundary using these two views simultaneously as in Figure 3-9. One of the graphs, in Figure 3-9a shows the performance map, while the other, in Figure 3-9b, shows a graph of mass-damping g/ρ^* versus compressible reduced frequency K^*. An × plotted

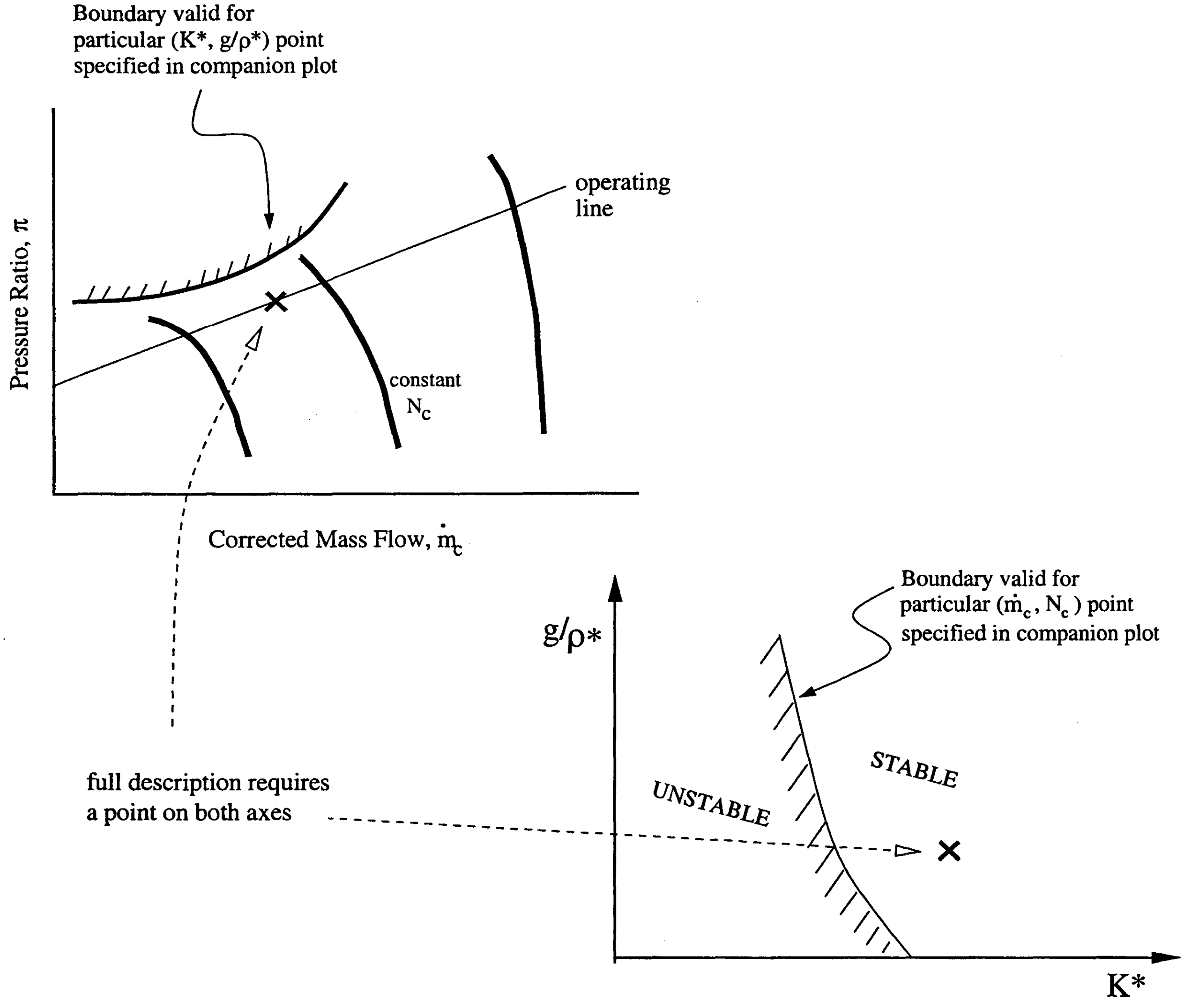

Figure 3-9: Dual view of performance map and $(K^*, g/\rho^*)$ map. Two simultaneous views give a reasonable picture of a point (denoted by the $\times$) in relation to the flutter boundary in the 4 dimensional parameter space.

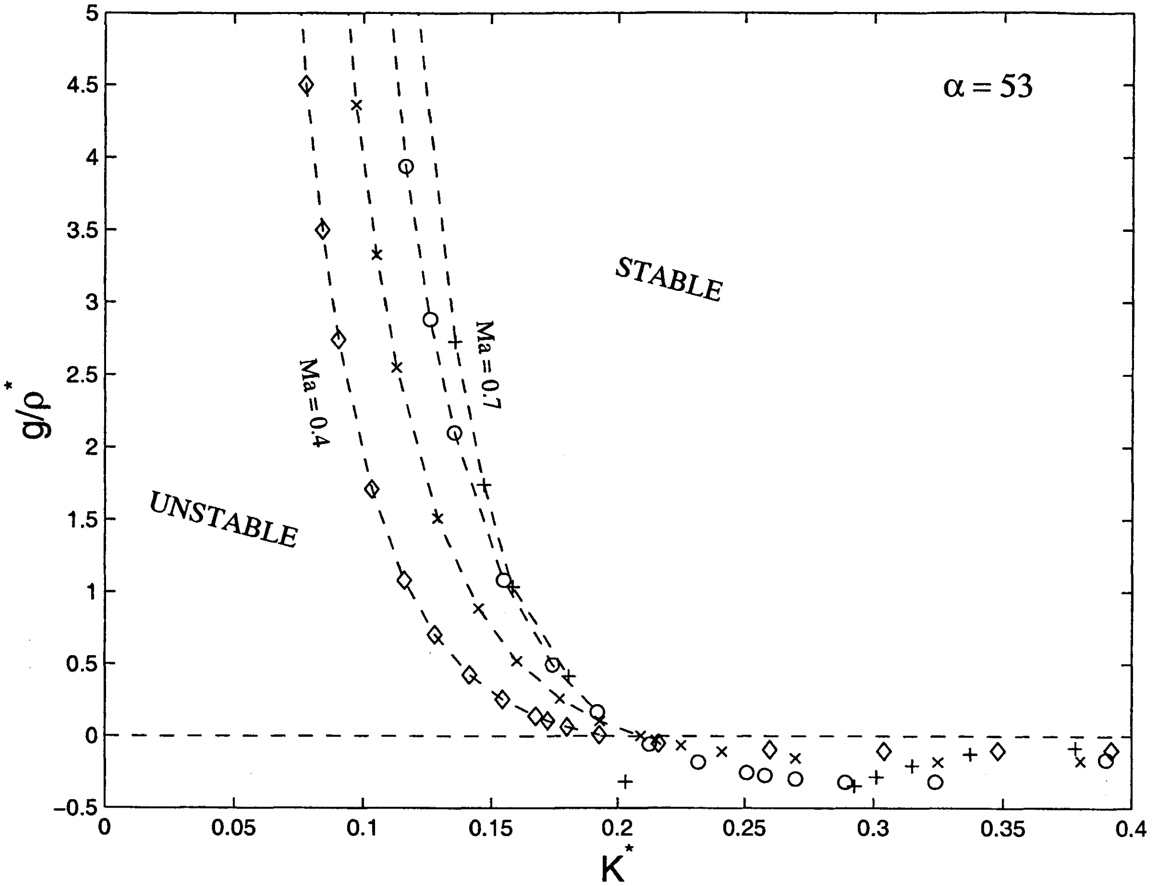

Figure 3-10: Boundaries from computational model on $(K^*, g/\rho^*)$ map. The effect of increasing Mach number at constant $(K^*, g/\rho^*)$ is destabilizing.

simultaneously in each graph specifies all four parameters. The flutter boundary drawn on the performance map, Figure 3-9a, corresponds to the $(K^*, g/\rho^*)$ value at the × on Figure 3-9b. Conversely, the boundary on the $(K^*, g/\rho^*)$ axes corresponds to the × on the performance map. Movement of the × in one set of axes causes the flutter boundary to move in the other set of axes. Thus, by using two axes simultaneously, we can obtain a reasonable picture of a point in the 4-D parameter space, and its relation to the flutter boundary.

Although stall flutter is generally associated with highly loaded operating lines, it is not always possible to ascribe generic trends to the movement of the boundary on the $(K^*, g/\rho^*)$ map with changes in the performance point. Figure 3-10 shows the results of subsonic, potential computations of a cascade in the 10th Standard Configuration undergoing a torsional vibration. The critical g/ρ^* is plotted as a function of K^* for various Mach numbers and for an inlet flow angle of 53°. This produces a boundary curve for each Mach number. The horizontal line at zero damping represents an absolute minimum for the reduced damping, g/ρ^*, which must always be positive.

The general shape of the stability boundaries is consistent with the idea that K^* and g/ρ^* are both stabilizing, since the boundary is monotonic (negatively sloped). In this case, increasing Mach number is destabilizing for constant flow angle, $\alpha = 53°$.

From the stabilizing effect of increasing K^* and its definition, equation (3.1), one may conclude that for constant Mach number, M, flow angle α, and reduced damping g/ρ^*, the destabilizing effect of temperature is to be expected by similarity. This provides an answer to the question of the origin of the temperature effect posed by Jeffers (1988). (i.e. it is a consequence of the stabilizing effect of K^*).

The application of these complete boundaries to assessing real designs is described in the next section. However, we first discuss a special case of the incompressible limit. It turns out that the traditional "flutter map" (plot of reduced velocity versus incidence), which is not sufficient for the general, high-speed case, has a firmer basis for low-speed machines.

3.3.1 Special Case: Incompressible limit and the "Flutter Map"

In the limit as Mach number becomes very small, the fluid dynamics problem tends to the incompressible limit. In this case, the temperature may not be a relevant parameter. The parameters used on the performance map (corrected speed, corrected weight flow, and pressure ratio) can be reduced to different variables, with which the effect of rotor speed is eliminated. These are the flow coefficient, C_x/U, and the pressure coefficient, ψ, defined as

$$\psi = \frac{\Delta p}{\frac{1}{2}\rho U^2}$$

where C_x is the axial velocity, Δp is the pressure rise, and $\frac{1}{2}\rho U^2$ is the dynamic pressure (based on relative velocity, U). This expression of the performance map is useful only to "low-speed" compressors (i.e. low Mach number).

In this case, the triangle of timescales in Figure 3-2 changes since the vertex associated with the acoustic timescale (i.e. pressure disturbance time) is no longer relevant anymore. Likewise, the Mach number, M, and the compressible reduced frequency, K^*, which relate inertial and vibrational scales to the acoustic scale are redundant in this case as well, and can be combined into a single variable, the classical reduced frequency, k.

The description of flutter stability can be dramatically simplified in this case. Two possible, equivalent, descriptions are:

$$\left(k, \frac{C_x}{U}, \frac{g}{\rho^*}\right) \leftrightarrow \left(U^*, i, \frac{g}{\rho^*}\right)$$

where $U^* = 1/k$ is the reduced velocity, and i is the incidence angle. The pressure coefficient, ψ, is a function solely of C_x/U, and may be omitted. These two descriptions are closely related because incidence can be directly obtained from the flow coefficient. The flow coefficient, C_x/U, is essentially a restatement of the flow angle, since

$$\alpha = \cos(C_x/U),$$

and the incidence, i, is the upsteam flow angle minus the blade angle.

The first description, $(k, C_x/U, g/\rho^*)$, relates flutter stability directly to the performance map flow coefficient, C_x/U, and pressure coefficient, Ψ. In particular, the critical flow coefficient can be found for various values of reduced frequency, k, and mass damping, g/ρ^*. Since the flow coefficient does not depend upon the absolute velocity magnitude (but only its magnitude relative to the axial velocity), k is independent of C_x/U for constant inlet state, unlike the corrected mass flow, $\dot{m}_c$, the analogue for high-speed machines.

The second description, $(U^*, i, g/\rho^*)$, corresponds to the "flutter map" which has been in common usage for a long time (see Fleeter, 1972). Typically, the effects of damping, g/ρ^*, are ignored, and the reduced velocity, $U^* = 1/k$, is plotted against the incidence, i, to form the classical "flutter map," as shown in Figure 3-11. That the classical flutter map not is always appropriate also has been recognized for a long time (Jeffers and Meece, 1975, Stargardter, 1979). However, its convenience (successful designs have

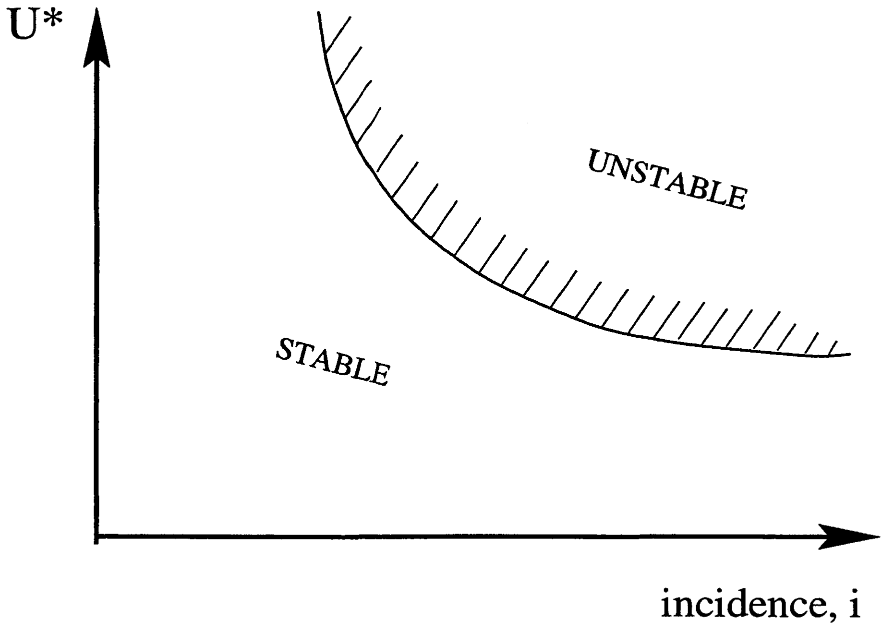

Figure 3-11: Classical flutter map of reduced velocity, U^*, versus incidence, i, should work for incompressible (low-speed) compressors, neglecting damping.

been made using correlations over a limited class of rotors) and lack of better alternatives has kept U^* vs. i correlations in use, with provisos to use them in accordance with "engineering judgment" (El-Aini, Bankhead, and Meece, 1986).

By showing the relationship of the flutter map to the general 4D parameter dependence of flutter, the strengths and weaknesses of the flutter map representation can be seen more clearly. The flutter map should be capable of capturing a stall flutter effect which is *incompressible* in origin. The work of Stargardter (1979), however, shows that compressible effects may limit the usefulness of the classical flutter map of U^* vs. i.

3.4 Stability of a design

A technique for drawing flutter boundaries with a completely specified parameter dependence (i.e. with all 4 required parameters) is an important tool in understanding the flutter properties of a given design. In this section, we show how this tool can be used to describe the flutter stability of a design on the basis of data from experiments upon real engines and from idealized computations.

The thermodynamic state at the rotor inlet can be expressed in terms of temperature and density. It is dependent upon flight condition in terms of weather, altitude, and flight speed. The weather and altitude

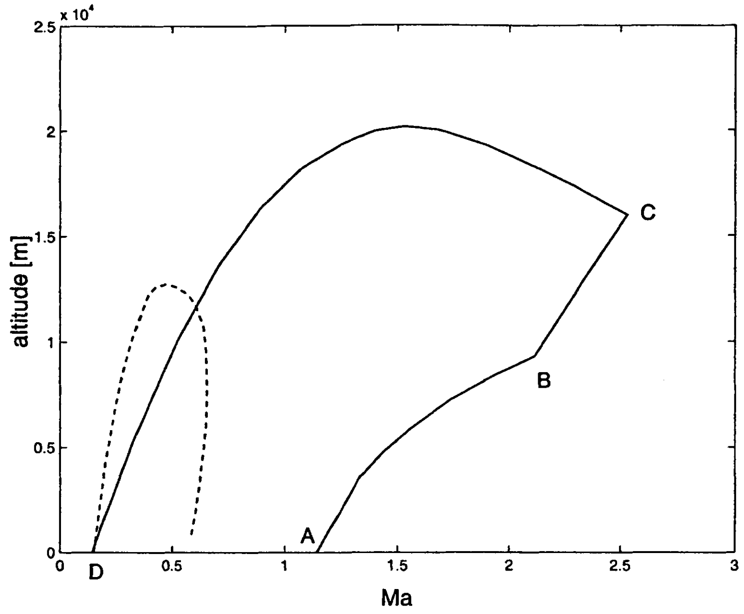

Figure 3-12: Typical flight envelopes for subsonic (dashed) and supersonic (solid) aircraft are shown in terms of the range of attainable Mach numbers for a given altitude. (Adapted from McCormick, 1995) In assessing the aeroelastic performance of a design, the operating environment set by the flight condition is relevant, as is the corrected performance.

determine the ambient density and temperature. Assuming standard weather conditions (i.e. standard atmosphere), the typical range of flight conditions depends upon the type of aircraft. Figure 3-12 shows flight envelopes of Mach number versus altitude for typical subsonic and supersonic aircraft (adapted from McCormick, 1995).

For subsonic designs, the top speed (i.e. Mach number) is typically limited by maximum power constraints, while the minimum speed is set by stall and buffeting of the wings and other flight surfaces. The supersonic aircraft is more complex. The maximum Mach number at lower altitudes (up to 10km) is set by a maximum dynamic pressure condition, while a minimum speed must be maintained to avoid stall and buffet. Although there is a small region of low speed flight attainable only by the subsonic airplane, in general, the supersonic aircraft operates throughout a significantly broader flight regime. The maximum altitude for the supersonic aircraft (flight ceiling) is set by an available power constraint, while the maximum mach number is limited, not by maximum power, but by maximum temperature. The warming of flight surfaces due to aerodynamic heating sets an upper limit to the Mach number of a typical supersonic airplane. (see McCormick, 1995, for further details on flight mechanics).

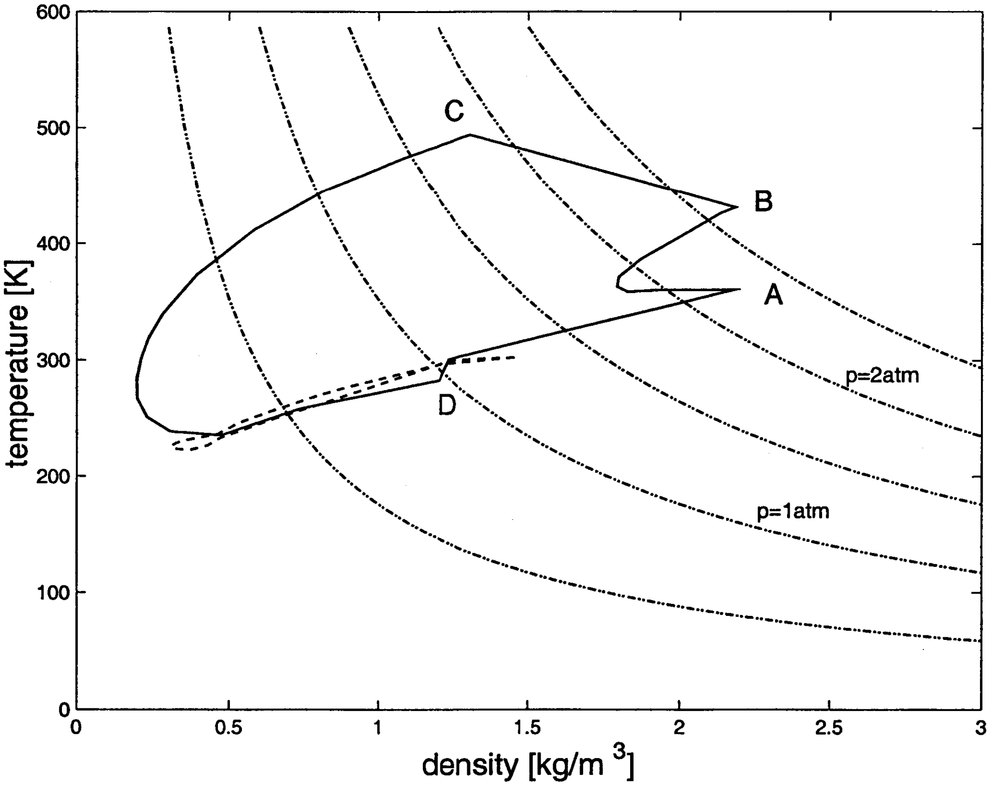

Figure 3-13: Envelope of inlet states for a front stage fan. Dotted lines indicate constant pressure. Two typical cases shown: a subsonic aircraft (dashed), and a supersonic aircraft (solid). The subsonic airplane is restricted to a thin sliver on the state diagram.

Depending upon the flight Mach number, the total temperature and total density may be significantly higher than ambient conditions. Engine inlets are designed to "recover" this temperature and density in a ram compression process, and are typically highly efficient. A fixed geometry inlet can provide a good stagnation pressure recovery (about 95% at design) for flight Mach numbers up to about 1.5 (Kerrebrock, 1992). Above this, shock losses rapidly become important, and a variable geometry is needed to maintain reasonably high (above 85% up to Mach 2.5) stagnation pressure recovery. For simplicity in what follows, we assume that the engine inlets have ideal (isentropic) pressure recovery.

The range of conditions for a front-stage fan corresponding to the two aforementioned cases is shown in Figure 3-13. Here, the flight envelopes for the subsonic (dashed line) and supersonic (solid line) aircraft are viewed, not in terms of Mach number and altitude as before, but in terms of the thermodynamic state of the air at the fan inlet. For latter stages, the relevant envelope in (T, ρ) shifts, approximately up a curve of constant entropy. The subsonic envelope is restricted to a narrow path, but the supersonic aircraft covers a sizeable region. One would expect flight condition effects to be a greater issue in the case of the supersonic aircraft, since it encompasses a larger flight envelope.

We consider, for simplicity, the case in which the structural parameters do not vary significantly (i.e. the modal mass, modal frequency, and modal damping are constant over the operating space). In this case, there is a direct correspondence between the state diagram of (T, ρ), and the graph of non-dimensional aeroelastic parameters, $(K^*, g/\rho^*)$. Thus, the envelope of relevant inlet conditions as depicted in Figure 3-13, can be directly mapped onto $(K^*, g/\rho^*)$ coordinates. This is done in Figure 3-14.

Consider the region in Figure 3-14 corresponding to the flight envelope in the context of the schematic flutter boundary of Figure 3-8. The dashed region, corresponding to the typical subsonic airplane, begins near $(1, 1)$, the sea level static condition. From there, the region moves up in both K^* and g/ρ^* along a thin path. However, the general trend is that increases in K^* and g/ρ^* are stabilizing at a given performance point, $(\dot{m}_c, N_c)$, as depicted in Figure 3-8. It follows that for the typical subsonic aircraft represented in Figure 3-12, the most unstable flight condition in terms of stall flutter occurs at low altitudes, near sea level static conditions. In fact, the lowest combination of $(K^*, g/\rho^*)$ is less than 5% away from the sea level static condition. (Such differences are too small to see on Figure 3-14.)

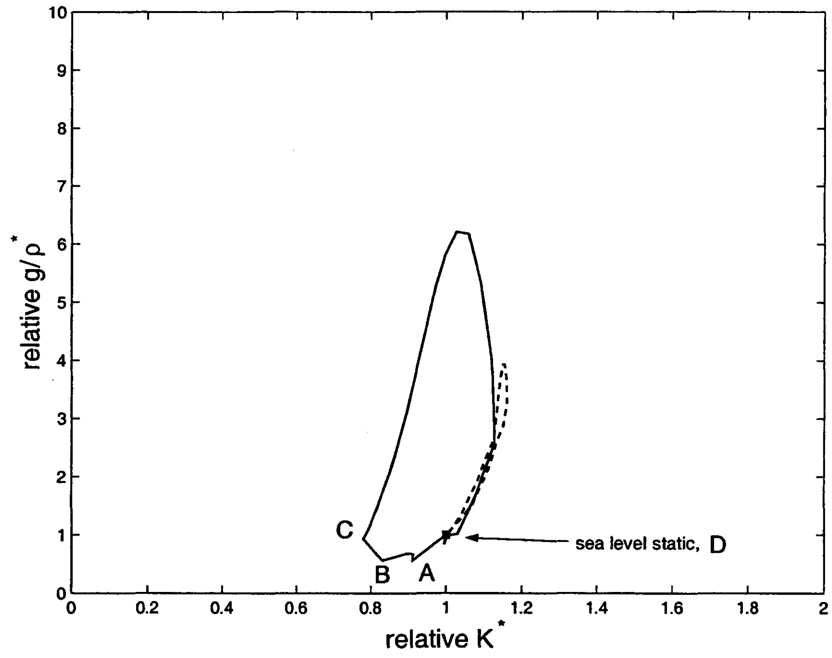

Figure 3-14: Typical flight envelopes from Figure 3-12 plotted on $(K^*, g/\rho^*)$ coordinates, assuming constant modal properties (mass, frequency, damping) and an ideal inlet. The points are plotted in relative coordinates in which the condition of sea-level static (SLS) conditions is at the sea level static point. Two cases are plotted: the subsonic (dashed) aircraft, and the supersonic (solid) aircraft.

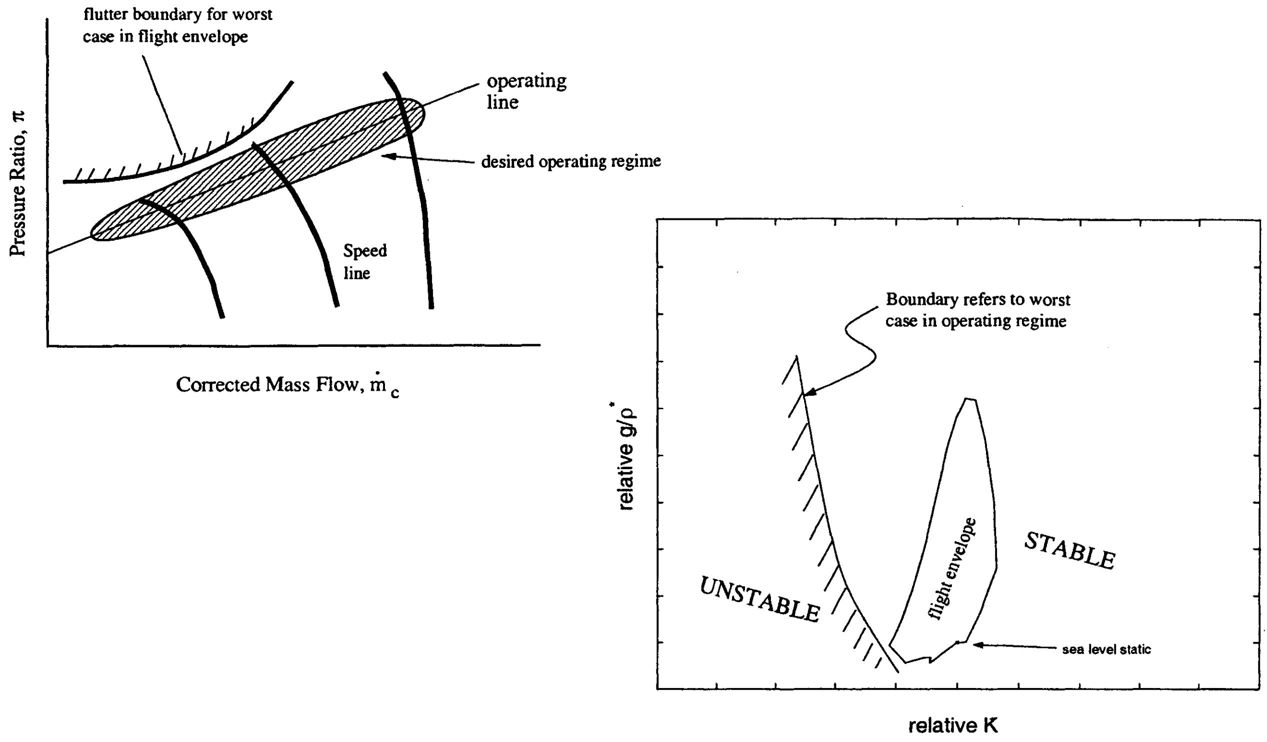

Figure 3-15: Regions of desired operation and flutter boundaries on performance map, and $(K^*, g/\rho^*)$ map

However, the plot in Figure 3-14 shows strikingly, that the sea level static condition is not the least stable case for supersonic aircraft (solid line). There are clearly flight conditions with the relative K^* and g/ρ^* less than the point $(1, 1)$. Even neglecting g/ρ^* effects, it would appear that an increase of at least 35% is needed in the modal frequency, over that required to maintain stability for the sea level static condition. As we shall see, for an engine discussed here (which, incidentally, has frictionally damped blades via the shroud and root attachment), the sensitivity to K^* is considerably more than the sensitivity to g/ρ^*.

Furthermore, we can specify on the performance map of $(\dot{m}_c, \pi)$, the region of desired operation (for example, as a particular operating line and a "buffer" region). This is schematically shown in the simultaneous plots of Figure 3-15. In each plot, there is a region shown which encompasses the range of conditions encountered during operation. On the performance map, this is a region surrounding the desired operating line. On the $(K^*, g/\rho^*)$ map, the region corresponds to the flight envelope. There is also a worst-case flutter boundary on each map. The boundary on the performance map is the worst case (least stable) of all those boundaries associated with points in the flight envelope on the $(K^*, g/\rho^*)$ map. Conversely, the boundary on the $(K^*, g/\rho^*)$ map corresponds to the worst case of all the points in the desired operating region of the performance map.

A sufficient condition for stability can be simply expressed. Clearly, if the worst-case boundary does not encroach upon the operating envelope then the design is stable. Each graph, thus, generates a separate, but equivalent, condition for design stability. In the schematic example of Figure 3-15, the design is stable.

Obtaining stability information

Now that we have discussed how the stability information should be represented, it remains to describe how to obtain the stability information.

In principle, the stability information could come from a computational model, as in the case of the previously presented trends from an idealized, 2D, subsonic, potential model. In practice, computation time and model fidelity are barriers. Aeroelastic codes have the potential to determine the aerodynamic damping, crucial to stability, but it is not possible to accomplish this in a reliable, and numerically accurate way. An important issue involves verifying the numerical accuracy aeroelastic codes, since the codes supply detailed information which is difficult to independently verify. Building sufficient and efficient aeroelastic codes to simulate stall flutter in turbomachinery is presently an active and important research topic (see reviews of Verdon, 1993, Marshall and Imregrun, 1996).

Actual data from engine testing are best, since measurements are taken in the actual, relevant enviroment. Unfortunately, the parameter space is vast (as we have shown, 4 dimensional for a fixed geometry) and it is difficult and expensive to obtain and analyze such data. Furthermore, it is not currently possible to reliably measure the aerodynamic damping. The best data currently available from fully scaled testing consists of a listing of steady-state measurements of test points, with occurence of flutter events noted. Systematic tests which encompass the effect of inlet state, such as those described in Chapters 5 and 6, are rare indeed.

3.4.1 Example: Application to early multimission engine

Experimental data exist for an early multimission aircraft engine. More extensive data analysis of another full-scale engine rig, which makes quantification of the sensitivities possible is presented in Chapter 5. The

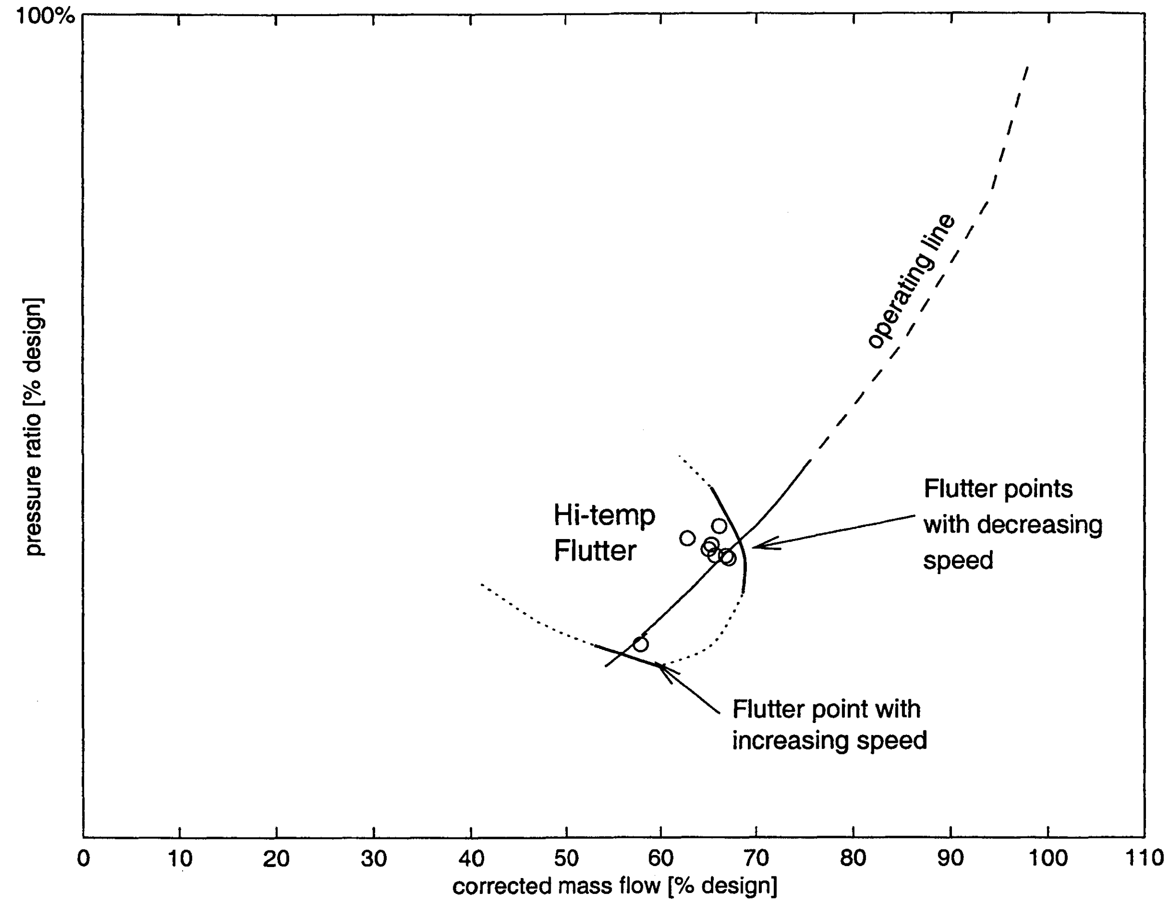

Figure 3-16: Performance map of early multimission engine. Flutter problem occurred at part-speed

current example is used to demonstrate how the new way of looking at flutter boundaries proposed in this chapter applies to a real problem.

The vibrational mode of the rotor in question was an above-shroud torsion mode. The flutter occurred exclusively at part corrected speed and raised inlet temperature conditions. This operating point is associated with high flight Mach number, on the upper right of the envelope in Figure 3-12. Subsequent full-scale engine testing showed that merely raising the inlet pressure at ambient temperature was not sufficient to elcit the instability. Inlet pressures from 0.5 atm to 1.5 atm were tested and shown to be stable at ambient temperature. However, at raised temperature in which flutter was observed, the extent of the flutter region was sensitive to the inlet pressure.

Several different trial configurations were tested before a satisfactory design was achieved, and the range of attainable K^* values was adjusted not only by changing temperature, but through structural modifications to the blade which changed the frequency, as well.

Furthermore, modifications to the inlet flow were tested in the form of various circumferentially uniform, radial distortion screens. As described in Chapter 2, the specification of a single, representative Mach number, M, and flow angle, α, assumes a specific swirl distribution along the blade span. Typically, such a swirl distribution is set by the upstream guide vanes and the inlet geometry, and perhaps scheduled with (i.e. a function of) operating point. Substantial radial distortions at the inlet modify the swirl distribution, which can simulate the effect of different inlet geometries. Unlike circumferential distortions. such radial distortions do not represent potential transient disturbances. Therefore, to consistently analyze a fan design, data with different inlet radial distortion screens should be distinguished.

The flutter points for one of the test configurations are shown in Figure 3-16. This particular run of tests is unusual in that both intersections of the flutter boundary with the fan operating line, with increasing speed and decreasing speed, were identified. The points at the upper intersection (decreasing speed) are more representative of the high Mach number flight condition, and therefore were focused upon. The cluster of points near this condition are taken with various different inlet pressures, and temperatures.

For the present purposes, we consider the upper intersection of the stall flutter boundary with the operating line. We consider the associated cluster of points to be at a single, effective operating condition. In this case, there is a single flutter boundary on the $(K^*, g/\rho^*)$ map. Thus, the $(K^*, g/\rho^*)$ map is a reasonable way to look at the data, as shown in Figure 3-17. The flutter points are shown as $\times$'s, along with the stable sea level static test on the rig, shown as a $\Diamond$, and the stable points for the successful redesign at raised temperature and pressure, shown as a $\circ$. Since the precise value of the damping is not known, the y-axis is, instead, the relative value g/ρ^* compared to atmospheric conditions. From this plot, one can separate the occurrences of flutter from the stable occurences by the shown dotted line.

It is clear that stability of the rig test, which was initially puzzling, is consistent with the raised temperature data using the current technique of representing the flutter boundary. Notably, the classical flutter map of (U^*, i) failed to capture this appropriately. In terms of the present formulation, the data can be interpreted as follows: the original rig tests were conducted at a value of K^* which was on the stable side of the part-speed flutter boundary on the $(K^*, g/\rho^*)$ map. In flight, however, the raised inlet temperature

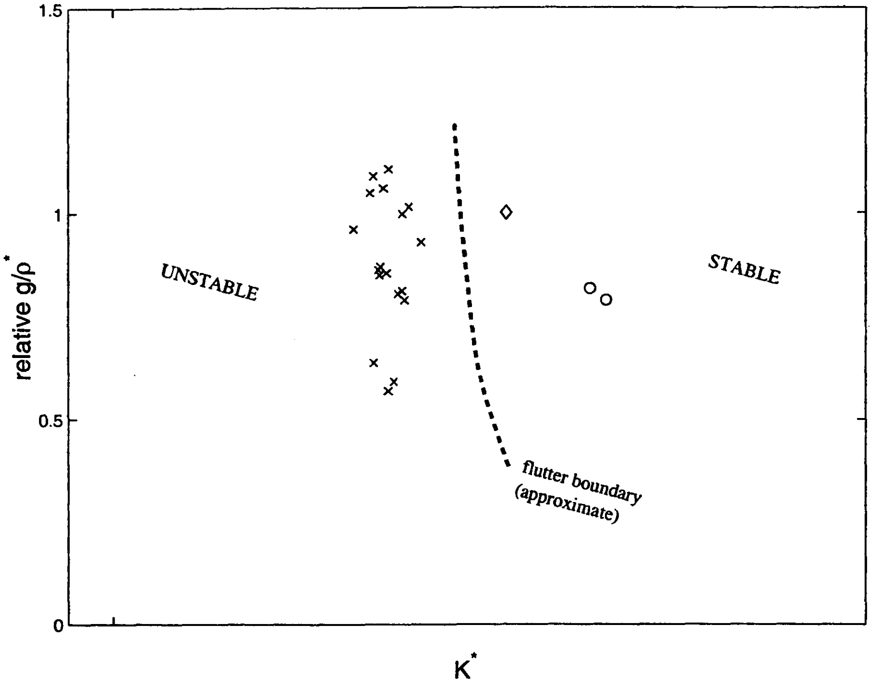

Figure 3-17: Fan data on $(K^*, g/\rho^*)$ map for early multimission aircraft engine. A × symbol represents a flutter point, while open symbols (◇, ∘) are stable points. The ◇ symbol shows the conditions for the stable rig test at sea level static conditions.

at ram conditions moved the value of K^* to the left, entering the unstable region of the stability boundary. The last redesign, which increased the natural frequency, moved the corresponding K^* value to the right far enough so that it was stable, even at raised temperature.

We can go a step further, using the flight envelope information. Although the flight envelope for the relevant aircraft was not available, we can use the generic supersonic aircraft of Figure 3-14. This flight envelope is plotted on the $(K^*, g/\rho^*)$ map in Figure 3-18 for two cases. The dashed envelope is computed using the modal frequency associated with the original design, while the dotted envelope uses the modal frequency associated with the eventual (successful) modification.

Note that the ◇ denoting the stable rig test at sea level static is in the correct relative location on the dashed envelope associated with sea level static (see Figure 3-14); also the ∘'s are on the relative location of the dotted envelope associated with high Mach number flight. In general, it can be said that changes in temperature move a given point within the envelope on $(K^*, g/\rho^*)$ coordinates, while changes in modal frequency shift the location of the envelope on $(K^*, g/\rho^*)$ coordinates, moving the given point along with

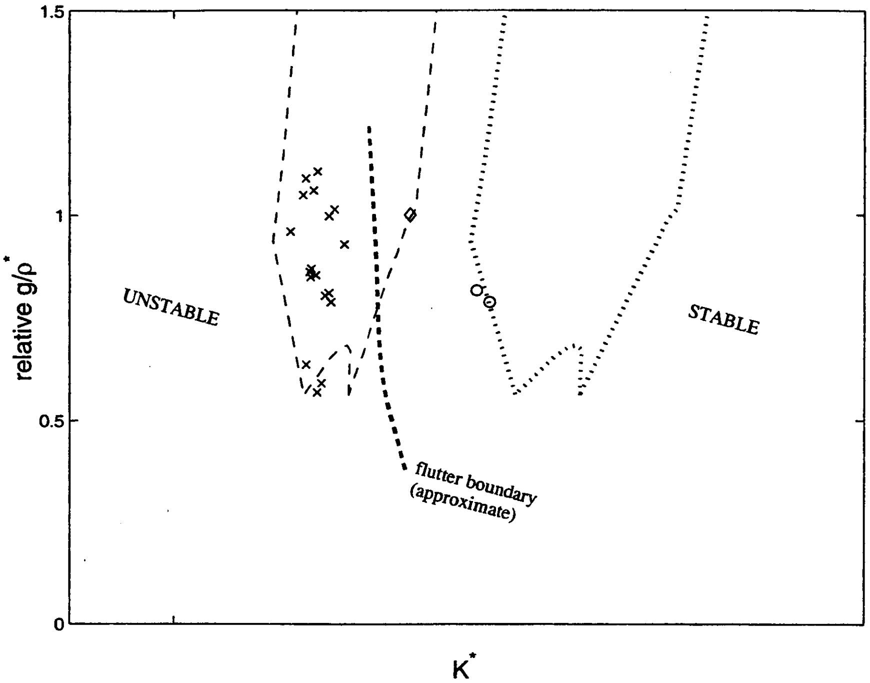

Figure 3-18: Fan data on $(K^*, g/\rho^*)$ map, for early multimission aircraft, with flight envelope for "generic" supersonic aircraft. The dashed envelope is anchored to the $\Diamond$, which is the original design at SLS. Note that although the original design was stable at SLS, it was unstable at other flight conditions. The dotted envelope is anchored to the $\circ$ which comes from the successful redesign.

it, but in the same relative location.

The general solution to this problem can be described in terms of the design stability concept embodied in Figure 3-15. The approximate boundary on Figure 3-18 represents the "worst case" boundary of Figure 3-15. The considerable stiffening associated with the successful redesign shifted the envelope on $(K^*, g/\rho^*)$ coordinates to the stable region.

3.5 Summary

A methodology has been introduced for the assessment of stall flutter instability in rotor blades, for a given flowpath and vibrational mode. It is framed in the full 4-D parameter space described in Chapter 2, in terms of the parameters, $(\dot{m}_c, N_c, K^*, g/\rho^*)$, based on the following criteria:

- The parameters should span the full 4D space
- Two of the parameters should span the corrected performance map

- The other two parameters should span the flight conditions (inlet temperature and density), for given structural properties.
- One of the parameters is independent of the unsteady aerodynamic coefficient

The reduced damping, g/ρ^*, combines the fluid inertia and the mechanical damping parameters. This combination is shown to collapse the results of Försching (1994) which treats them separately. Furthermore, the absence of density effects in Jutras et. al. (1980) may be explained by the lack of frictional effects, which would tend to make g/ρ^* negligible. For a typical case of inserted blades, however, the reduced damping, g/ρ^* is order 1, and impacts flutter stability. The effect of increasing g/ρ^* upon flutter stability is stabilizing.

The compressible reduced frequency, K^*, relates acoustic time scales with vibrational time scales. An increase in K^* tends to decrease the phase offset (i.e. increase the phase lag) between the fluid forcing and the blade vibration. In theoretical special cases, and in measured experiments, the implication is that increasing K^* is stabilizing.

The simultaneous representation of the corrected performance map, $(\dot{m}_c, N_c)$, and a map of $(K^*, g/\rho^*)$, provides a complete representation of the flutter stability for a given machine. To assess the stability, information concerning the flight conditions which determines the relevant region on the $(K^*, g/\rho^*)$ map is necessary. This is demonstrated in the development experience of an early, multimission engine.

Chapter 4

Exploratory study of aeroelastic computational model

This chapter describes a parametric study of a 2D, linearized, compressible potential model of the vibration-induced forces in a cascade. Unlike the actual case of a transonic rotor, this idealization can be accurately and rapidly computed. Moreover, potential flow models form a familiar "baseline" case which have been extensively studied in the literature dating back to the early work of Sisto (1955), Shiori (1958), and the seminal computations of Whitehead (1960, 1962), to the more recent parametric studies of Smith and Kadambi (1993), and Panovsky and Kielb (1998). The present parametric study explores the parameters relevant to a fixed cascade geometry in a subsonic, inviscid flow spanning Mach number, flow angle, reduced frequency, and interblade phase angle. In particular, we focus on the vibration-induced fluid forces which govern flutter stability.

Trends were studied in the parameter space of Mach number, M, flow angle, α, and reduced frequency, k. The most unstable case of 20 interblade phase angles, σ, computed was considered as representative for each point. Several cascade geometries were tested, notably the 10th Standard Configuration.

The primary computational model used is that of Hall (1993), which can handle airfoils of arbitrary geometry and mean loading. The limits of the potential flow approach are that the effects of viscosity are ignored, and the flow must be fully subsonic, $M < 1$ everywhere.

Particular attention is given to the interpretation of the trends of the vibration-induced fluid forces in terms of the parameters introduced in Chapter 3, namely the compressible reduced frequency, K^*, and reduced damping, g/ρ^*. The "critical" reduced damping is proposed as a stability metric with direct interpretation in terms of design parameters.

Vibrations in pure bending and pure torsion (about the midchord) were analyzed with the model. Destabilizing forces in bending occurred only at extremely low reduced frequency (order $k = 0.05$), whereas destabilizing forces in torsion occurred at relatively higher reduced frequencies (order $k = 0.3$). This is in keeping with trends from previous studies.

For subresonant, compressible flows at moderate Mach numbers (0.4 to 0.8), the compressible reduced frequency, K^*, can well-approximate the combined effects of Mach number and reduced frequency on the phase between motions and vibration-induced fluid forces, ϕ. The generality and implications of this reduction are explored.

4.1 Description of Study

4.1.1 Parameter Space Description

One of the complexities of the flutter problem in turbomachinery is the large number of design and operational parameters relevant in the problem. For our current focus on flutter clearance, we consider only those parameters which may vary during the operation of a machine. More specifically, we restrict the study to variations for a fixed flowpath geometry. Several different cascade geometries were tested to establish that the trends identified are not unique to one particular case.

In this context, design parameters such as solidity and camber are considered constants. The parameter dependency of the flutter criterion is given by equation (2.13), or

$$g/\rho^* > \max_{\sigma_n} \frac{Im(l'_{\sigma_n}(M, \alpha, k))}{k^2}$$

where l'_σ is the vibration-induced fluid force non-dimensionalized by inlet dynamic head, ρU^2, and the chord, and ρ is the inlet density and U^2 is the inlet relative flow velocity. In Chapter 3, a new version of the reduced frequency (termed the compressible reduced frequency), $K^* = k \cdot M$, is used. It can be shown to arise from non-dimensionalizing the fluid forces by the inlet pressure, p_0, as developed in Chapter 2. In this formulation,

$$g/\rho^* > \max_{\sigma_n} \frac{Im(l_{\sigma_n}(M, \alpha, K^*))}{K^{*2}}.$$

where l_σ is similar[1] to l'_σ, but instead of the inlet dynamic head, it is non-dimensionalized by γp_0, where p_0 is the inlet pressure and γ is the ratio of specific heats. The former version (l'_σ) is more conventional, and will be used in the present exploratory study.

Through linearized unsteady subsonic potential computations, we aim to characterize the fluid forces, $\max_{\sigma_n} Im(l_{\sigma_n})$. This model is clearly an idealization, since the real flow is viscous and may have strong shocks. However, the trends in this idealized case can be viewed as the "baseline" for comparison with more realistic physical effects found in experimental measurement or more complicated models, since it is analytically simpler. It should be recognized that such a parametric characterization of the vibration-dependent fluid forces is relevant to both flutter stability and forced vibration, the dynamic response of a stable rotor.

There have been many previous parametric studies using linearized potential models. An early study was reported by Whitehead (1960) in which the vibration-induced force coefficients are tabulated for an incompressible flat plate cascade at zero incidence as a function of interblade phase, σ, reduced frequency, k, and stagger angle (which equals the flow angle, α, for zero incidence). More recently, researchers have presented sensitivities of the zero-damping flutter boundary with respect to various parameters (e.g. Smith and Kadambi, 1993, Försching, 1994, and Lorence and Hall, 1995). The current study is unique in that it explores trends in l_σ within the full 3D parameter space of (M, α, k) for a fixed geometry.

---

[1] n.b. this issue of non-dimensionalization affects only the representation of the forces, but not their computation. It should be clear that $l_\sigma/k^2 = l'_\sigma/K^*$.

Table 4.1: List of non-dimensional parameters. Restrictions are imposed by assumption, to stay within the limits of the dynamic model. Incidence, i, and upstream angle, α_1, are equivalent since the geometry is fixed. The compressible reduced frequency, K^*, is the product of k and M. In the definitions column, U is upstream relative flow velocity, T is temperature, c is chord, and ω_0 is the blade natural frequency.

Name	Symbol	Definition	Model Restrictions
Mach No.	M	$U/\sqrt{\gamma_0 RT}$	$M < 1$ everywhere
reduced freq.	k	$\omega_0 c/U$	$k > 0$
upstream angle (incidence)	α_1 i		range set by $M < 1$ criterion
compressible red. freq.	K^*	$\omega_0 c/\sqrt{\gamma RT}$	$K^* > 0$

4.1.2 Description of Dynamic Model

The flow model consists of a two-dimensional, compressible, linearized unsteady, potential flow code, written by Hall (1993). Since it is a linearized unsteady model, there are two parts: a non-linear steady flow solver, and a linear unsteady flow solver. Although the code can handle compressible flow, the entire flow field must be subsonic. The blades are assumed to be in a tuned 2D cascade. Twenty possible interblade phase angles (from 0° to 360° in increments of 18°) were computed; so, in this sense, the rotor was 20 bladed. Cases of pure bending vibration and pure torsion (about midchord) were considered.

The code was found to be fast and robust. On a DEC AlphaStation 4100, each run of the steady solver took about 2.6 seconds of CPU time, and each unsteady case, for a specific reduced frequency and interblade phase, took 1.9 seconds of CPU time. This makes it possible to compute the 13 000 or so unsteady flowfields that it takes to cover a region of parameter space (20 σ's $\times$ 8 α's $\times$ 20 k's $\times$ 4 M's $= 12\,800$).

4.1.3 Code Verification

The code was verified using flat plate cascades at zero incidence, by comparison to D.S. Whitehead's LINSUB code, as described in Whitehead (1987). LINSUB uses an extension of the method of Whitehead (1960) to handle compressible flows and matches the tabulated results of Whitehead (1960) in the limit of incompressible flow. Further comparisons of the case of finite turning with a Linearized Euler code and with cascade experiments is contained in Hall (1993).

Two distinct cases were computed for bending and for torsional vibrations, as described in Table 4.2.

Table 4.2: Parameters for flat plate cascades used in verification runs. For the comparisions with LINSUB, the incidence is zero, and therefore, α equals the stagger angle.

Cascade	Gap/Chord Ratio	Stagger Angle	Mach Number	Reduced Frequency
Cascade A	1	45°	0.1	0.25
Cascade B	1.2	60°	0.6	0.5

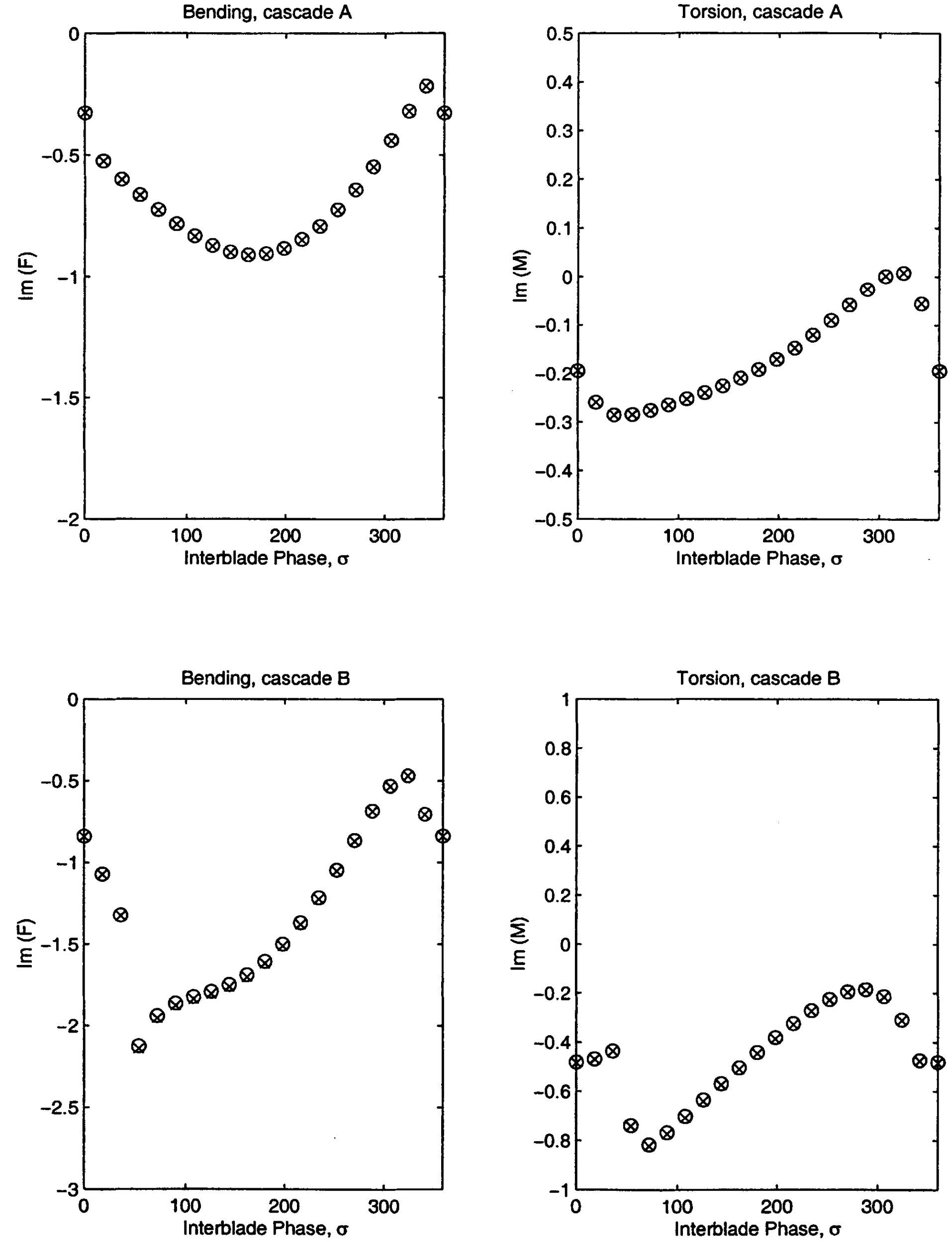

Figure 4-1: Comparison of Hall's linearized potential code, shown by o's, with LINSUB code, shown by ×'s. Cascade A refers to a flat-plate cascade, staggered at 45°, gap/chord=1, Mach 0.1, and reduced frequency of 0.25. Cascade B refers to a flat-plate cascade, staggered at 60°, gap/chord=1.2, Mach 0.6, and reduced frequency of 0.5. The values computed by the two codes are almost identical.

Table 4.3: Geometric summaries for various cascades computed in this study.

Name	Blade Type	Gap/Chord Ratio	Stagger Angle
Cascade A	flat plate	1	45°
Cascade B	flat plate	1.2	60°
1st Stand. Config	NACA 65 Series	0.75	55°
10th Stand. Config	Cambered NACA 0006	1	45°
Fan-C (Sect. J)	GE E^3 design	0.715	65°

These cases are labeled "Cascade A" and "Cascade B." The comparisons between LINSUB and the current code in these two cases are depicted in Figure 4-1. The two methods produced nearly identical results. The y-axis in each case is the out-of-phase part of the fluid forces, $Im(l_\sigma)$, which govern stability. In the case of bending, this is the imaginary part of the unsteady lift coefficient, $Im(F)$. In the case of torsion about the mid-chord, it is the imaginary part of the unsteady moment coefficient, $Im(M)$. The superb agreement between these quantities between the two codes is thus demonstrated for varying Mach number, reduced frequency, and different cascade geometries (in terms of stagger and gap/chord), indicated that the present implementation were an accurate numerical solution to the compressible potential problem.

Further detailed discussion and verification of the specific technique of computation may be found in Hall (1993). Notable features include using the Finite Element Method (FEM) to solve the variational form of the compressible potential problem, solving the unsteady problem on a deforming grid to provide numerical robustness for arbitrary vibrations, and a downstream condition which accounts for a harmonically oscillating wake without assumptions regarding the wake velocity.

4.1.4 Cascade Geometry

The cascade primarily studied was that of the 10th Standard Configuration, as defined in Fransson and Verdon (1993), and depicted in Figure 4-2. Other geometries such as the 1st Standard Configuration (Bölcs and Fransson, 1986), a section of the Fan-C rotor (Jutras, et. al. 1982), and flat plate cascades were investigated to investigate the generality of the trends with respect to changes in cascade geometry.

The geometric definitions of various cascades used is summarized in Table 4.3. The 10th Standard Configuration consists of a modified, cambered (camber of approximately 22°) NACA 0006 cascade. The

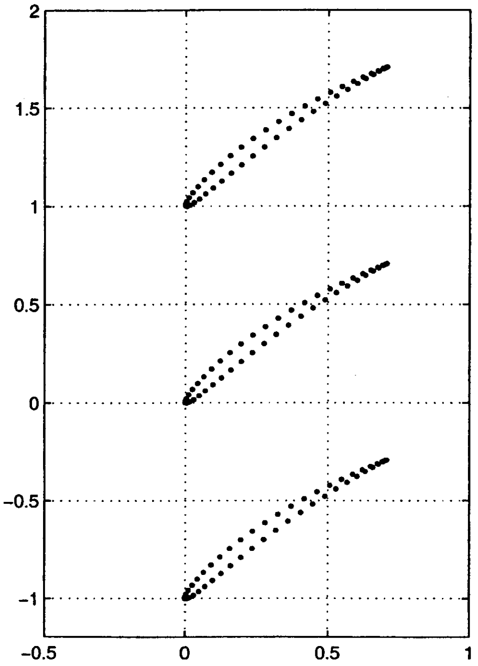

Figure 4-2: Geometry of Tenth Standard Configuration. The cascade used in the present computations consists of a cambered NACA 0006 aerofoil (modified at the trailing edge), staggered at 45°, with a gap/chord of 1. Points depicted here are the same as those used to define the aerofoils in computations.

upstream flow angle, α, specified in the Tenth Standard configuration is 55°, and the flow angle of the test were taken near this value. The cascade is depicted in Figure 4-2.

Other cascades tested included the 1st Standard Configuration, for which there is data at low Mach number, and the Fan-C Rotor configuration, for which there is steady-state data at ambient conditions. These cascades are depicted in Figure 4-3.

4.1.5 Range of Parameters

The attainable parameter space was limited, as was mentioned previously, by the condition that the flow be everywhere subsonic. When there are locally supersonic regions, the steady code diverges. The Prandtl-Glauert tranformation, $x' = x/\sqrt{1-(M)^2}$, to handle the compressibility effects becomes singular at $M = 1$. For a given geometry, the maximum local Mach number is a function of inlet relative Mach number, M, and of the inlet flow angle, α. The range of reduced frequency, k, tested ranged from about 0.1 to 1.2. Values outside this range, however, were computed in specific cases to investigate limiting behavior.

To assess the region of available Mach numbers and flow angles, runs with the steady potential flow

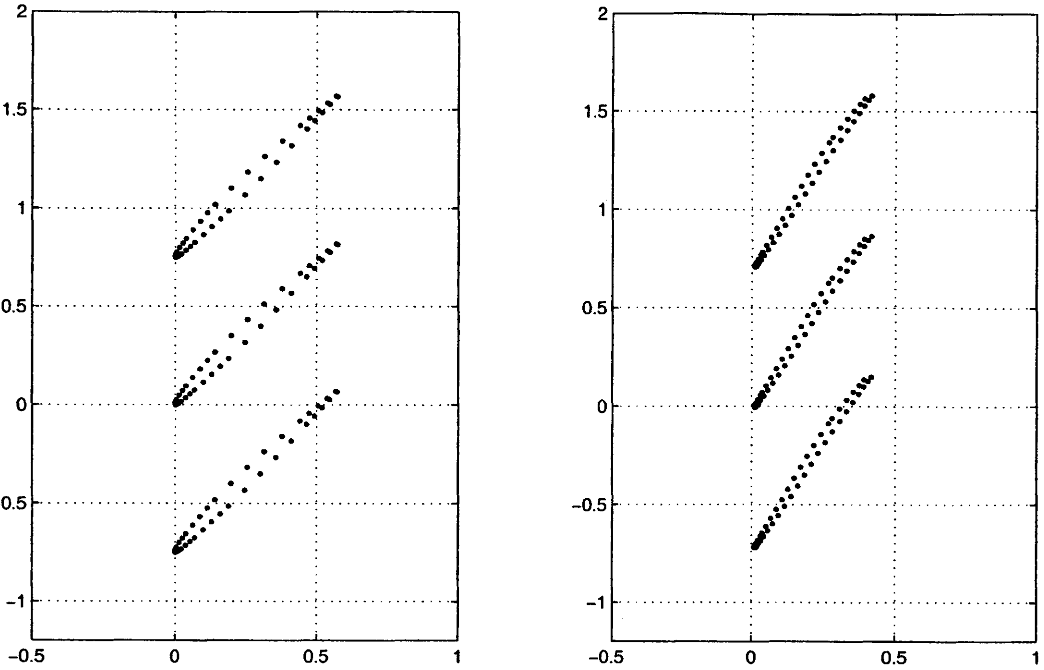

(a) (b)

Figure 4-3: Geometry of First and Fifth Standard Configuration, (a) and (b) respectively. Points depicted here are the same as those used to define the aerofoils in computations.

computations alone were surveyed relatively densely to define appropriate regions for the combined linearized unsteady runs. Figure 4-4 shows such a survey for the 10th Standard Configuration. As Mach number increases, the range of flow angles for which the code is valid decreases. The other cascade geometries had similar domains of validity, each centered near the zero-incidence inlet flow angle.

Two specific surveys of (M, α, k, and σ) within the range of validity of the code were focused upon in this study. These are depicted in Figure 4-5. In square region, region A, the critical stability parameter, $\max_\sigma Im(l_\sigma)$, typically corresponded to evanescent disturbances (in the range of k's tested). The triangular region, region B, contained points in which the least stable inter-blade phase was near the onset of acoustic waves, corresponding to a so-called "weak instability," or an acoustic resonance. Surveys in other regions were conducted to investigate specific questions, such as the trends at very low Mach number.

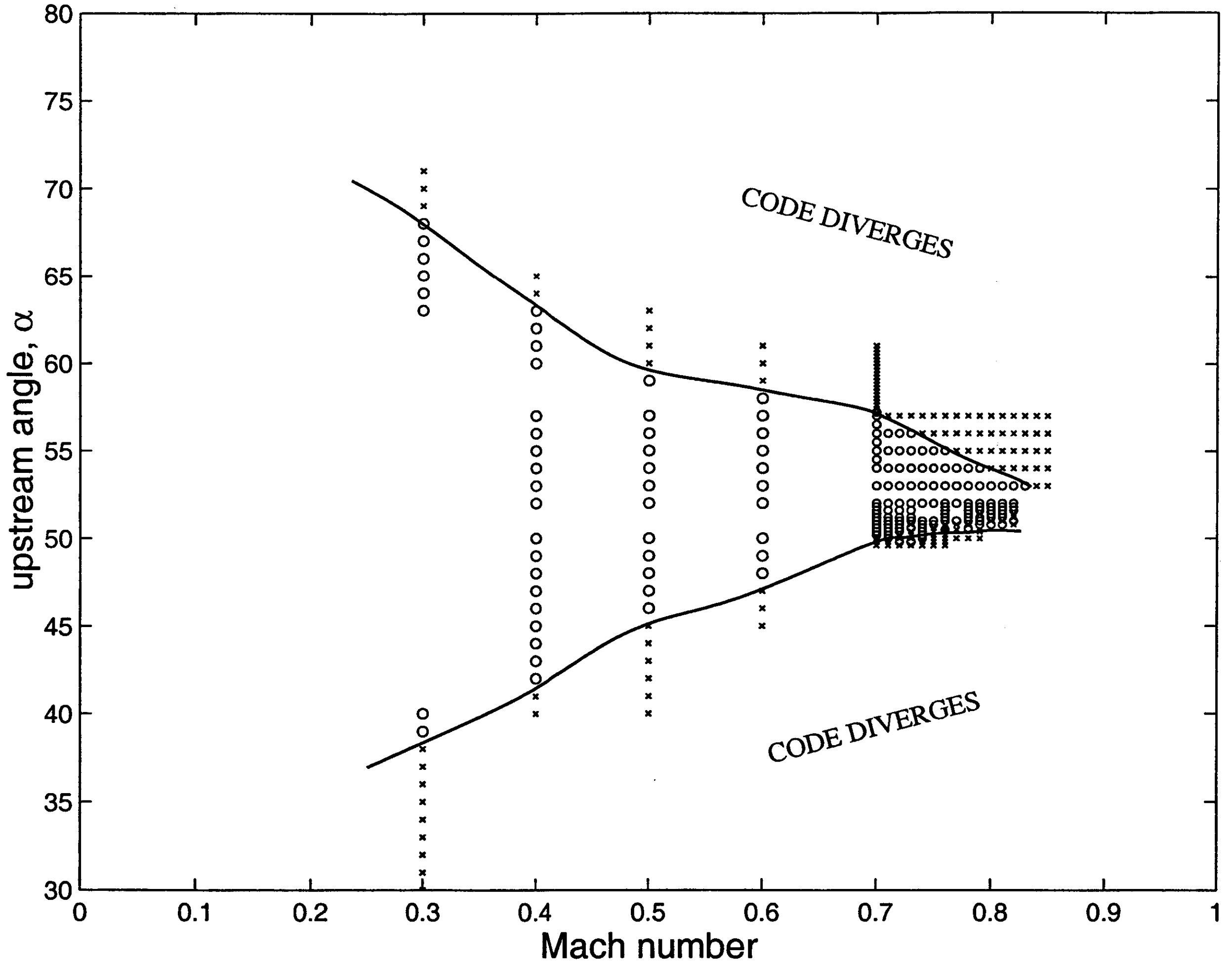

Figure 4-4: Region of steady code convergence 10th Standard Configuration. Open symbols, o, correspond to convergent steady runs, and ×'s correspond to places where the steady potential solver diverged.

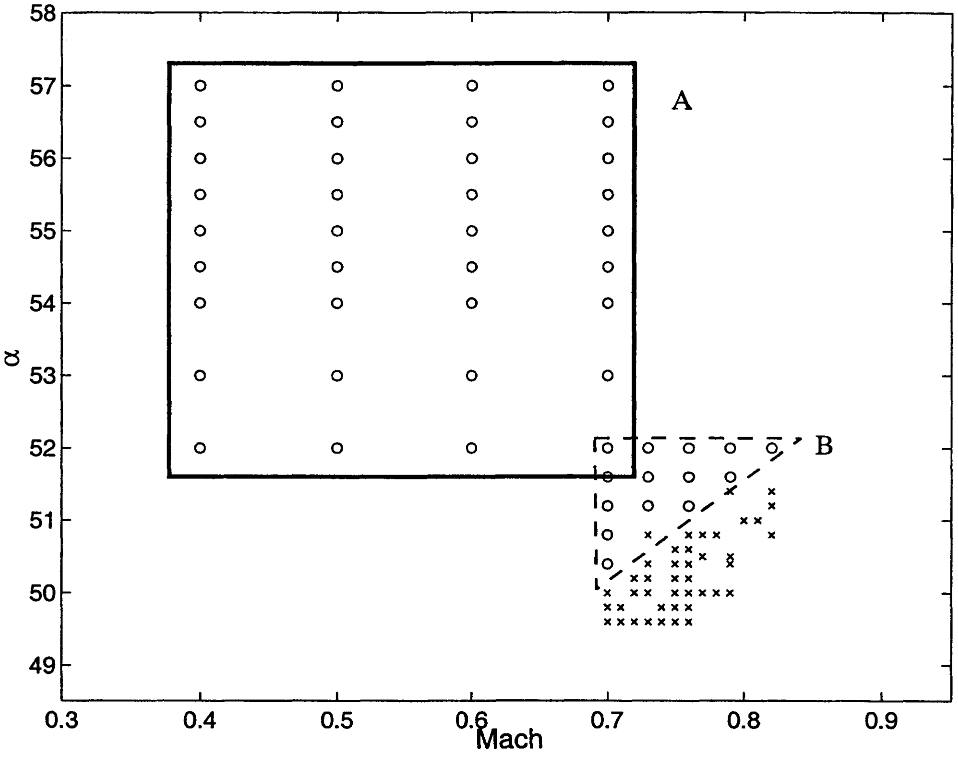

Figure 4-5: Schematic of regions of study in parameter space for 10th Standard Config. Two adjacent regions were studied in detail, labeled A and B, respectively. The o's denote points tested in the parameter space and the small ×'s denote areas outside the model's validity (code did not converge). The range of reduced frequency, k, tested was 0.1 to 1.2.

Table 4.4: Definition of unsteady force coefficent, various studies. The pressure is scaled in a variety of ways. Here, ρ is the air density, U is the blade relative velocity, c is the chord, and ω is the vibrational frequency.

Study Name	Type	Pressure Scale
Hall and Clark [1993]	Subsonic/ Transsonic CFD	ρU^2
Crawley [1988]	Theory, review	$\frac{\pi}{4}\rho c^2\omega^2$
Hall [1993]	Pot. Flow (CFD)	ρU^2
Hall and Silkowski [1997]	Multi-row, (CFD)	$\rho c\omega U$
Whitehead [1960],[1962]	Vortex (Potential) Model	$\pi\rho c\omega U$ $\pi\rho^*(U^*)^2$
Buffum and Fleeter [1990]	Experiment	$\frac{1}{2}\rho U^2$
Kielb and Ramsey [1989]	Supersonic (Lane) Theory	$\frac{\pi}{4}\rho c^2\omega^2$
Försching [1993]	Review	$\frac{1}{2}\rho U^2$
Srinivasan and Fabunmi [1984]	Theory	$\frac{\pi}{4}\rho U^2$ $\frac{\pi}{4}\rho^*(U^*)$
Smith and Kadambi [1993]	CFD (Euler)	ρU^2
Yashima and Tanaka [1977]	Expt./ Theory	ρU^2
Bendikson [1986]	Supersonic Theory	ρU^2 $\rho^*(U^*)$
Bölcs and Fransson [1986]	Comparison Report	$p_x - p_{-\infty}$

4.2 Metric for Stability Assessment

Before describing the results of the computations, it is important to define the metric for stability in this context. We show that the metric of critical reduced damping, $(g/\rho^*)_{\mathrm{cr}}$ has some unique[2] and advantageous properties for assessing forced vibration and stability of a particular unsteady aerodynamic model.

For a tuned rotor, the aerodynamic stability may be assessed using the non-dimensional work-per-cycle, or equivalently, $Im(l_\sigma)$ (Fung, 1955). However, there is no consensus regarding the appropriate technique of non-dimensionalization. Table 4.4 lists various studies of turbomachine flutter and the pressure scale

---

[2] More precisely, the class of smooth, monotone functions of $(g/\rho^*)_{\mathrm{cr}}$ have these properties.

used to non-dimensionalize l_σ in each case, which shows the differences in formulations. In the discussion of Chapters 2 and 3, the choice of parameters based upon operability assessment suggests a scaling based upon the inlet pressure, as in equation (2.3).

Although the metric of $Im(l_\sigma)$ is certainly valid but it is not uniquely defined in the literature. Furthermore, the answer to the basic question "What is a large value of $|Im(l_\sigma)|$" is not obvious. These issues are addressed by using the critical reduced damping, $(g/\rho^*)_{\text{cr}}$ as a stability metric. Since the value of reduced damping, g/ρ^*, itself does not influence the aerodynamic work-per-cycle, it forms a plausible basis for comparison. At sea level static, a typical bladed rotor with inserted blades has a value of g/ρ^* of order 1. This order of magnitude approximation can be used to assess the magnitude of the vibration-induced fluid forces at a given point. At different flight conditions, density variations affect the reduced damping, g/ρ^*.

Using the unsteady fluid model, the critical value of g/ρ^* can be computed for each point, according to equation 2.13

$$(g/\rho^*)_{\text{cr}} = \frac{\max_\sigma Im(l'_\sigma)}{k^2} \tag{4.1}$$

Thus, the stability condition becomes

$$g/\rho^* > (g/\rho^*)_{\text{cr}} \tag{4.2}$$

for stability. For values of g/ρ^* above the critical, the cascade is stable. Note that the expression (4.1) is relevant to the specific case of non-dimensionalizing l'_σ with the inlet pressure, ρU^2. For other cases, equation (4.1) contains a different factor instead of k^2.

Note that using $(g/\rho^*)_{\text{cr}}$ is completely general, since it is simply a rescaling of $Im(l'_\sigma)$. However, this rescaling makes it comparable to the reduced damping, which is *independent* of the unsteady flow problem, and is set solely by the mechanical damping and the flight condition.

4.3 Results for torsional and bending stability

4.3.1 Bending vibrations

We now turn to the results of the computations of the flow model for bending vibrations. In the range of k from 0.1 to 1.2, the flow model predicts a stable cascade throughout regions A and B defined in Figure 4-5. However, a bending instability was observed at very low k, for finite turning. The critical reduced damping is plotted as a function of interblade phase, σ for a typical case in Figure 4-6. The least stable case occurs at an interblade phase of $\sigma = 0°$ (i.e. all the blades move in unison). The critical reduced damping is sharply peaked at zero, and falls off away from zero with the most stable case being at $\sigma = 180°$.

One way to interpret these results is to consider the influence of the individual blades upon one another. It can be shown (Crawley, 1988) that the rotor description in interblade phase coordinates is related to the individual blade description. The transformation formula is the same as that of a Digital Fourier Transform (DFT). Thus, the influence of the blade upon itself is reflected in the mean value (zeroth harmonic with respect to interblade phase), the influence of the nearest neighbors depends upon the first harmonic, and so on. The influence of "local effects" upon a reference blade by its own vibrations and the vibrations of its nearest neighbors is reconstructed as the solid line in Figure 4-6. Near an interblade phase angle of $\sigma = 0$, the "local" effects do not well describe the critical reduced damping which is where the region of minimum damping is.

Figure 4-7 summarizes the parameter study of bending vibrations in regions A and B. The most unstable interblade phase is selected for each (M, α, k) point. This is presented in two ways in Figure 4-7a as the non-dimensional work-per-cycle, and in Figure 4-7b in terms of the critical reduced frequency. For each reduced frequency, k, value, there is a spread of points, indicating variations due to Mach number and incidence. For comparison purposes, data for (essentially) incompressible flow, $M = 0.01$, and a constant flow angle, $\alpha = 55°$, are plotted as large circles, which lie in the middle of the spread of points for a given reduced frequency, k.

Interestingly, the trend for the work-per-cycle appears to be a reduction in stability as the reduced frequency, k, is reduced, whereas the critical reduced damping becomes more negative as k is reduced. This

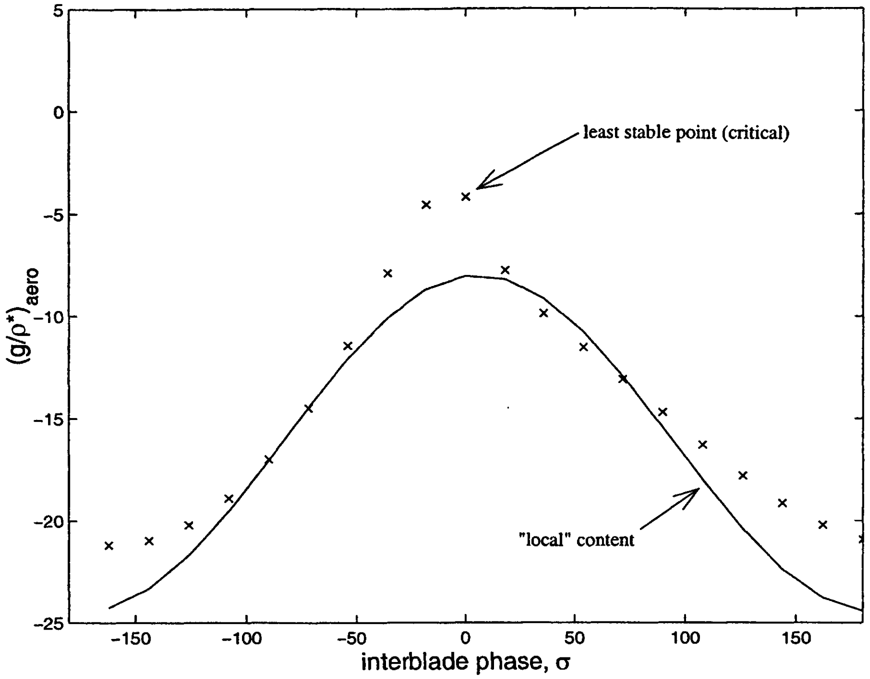

Figure 4-6: Typical case of bending vibrations of 10th Standard Configuration. The y-axis is $(g/\rho^*)_{\text{aero}} = Im(F/k^2)$, which is the reduced damping at neutral stability for a particular interblade phase. The solid line denotes the reconstruction of effects of blade self-damping and neighboring blade influence, given by the content of the zeroth and first harmonics with interblade phase, σ.

apparent discrepancy occurs because the magnitude of the fluid forces increases as k is reduced (like $1/k^2$). Therefore, although the non-dimensional work-per-cycle appears to tend towards zero as k is reduced, the net effect is to *increase* the stabilizing fluid forces. The critical reduced damping, $(g/\rho^*)_{\text{cr}}$, can be used, for example, to determine how disturbances would decay (or amplify) with no mechanical damping, according to the model. For example, other things being equal, at $k = 0.2$ a bending disturbance will likely decay significantly faster than at $k = 0.6$, although this is not readily obvious from the work-per-cycle plot Figure 4-7a.

Although the trends from region A and B appear to indicate that the bending mode is completely stable, we will see that reducing the reduced frequency, k, can cause an instability if there is blade loading.

Loading Effects in Bending

The results from regions A and B suggest that the model does not predict a bending instability, which is consistent with some results in the literature (e.g. Smith and Kadambi, 1993). However, it turns out

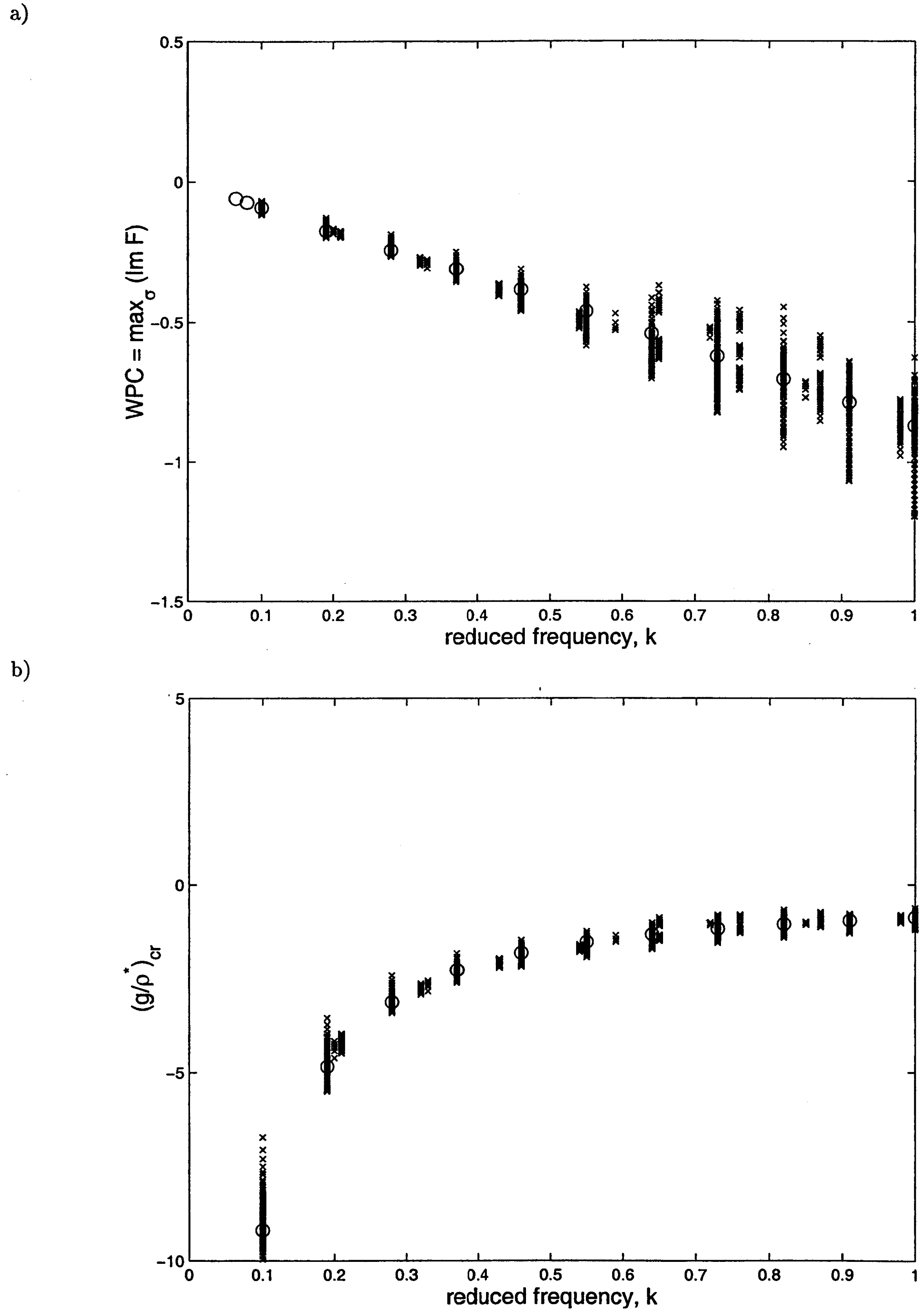

Figure 4-7: Overall trend with k in bending vibration parameter study. For each (M,α,k) point in 'Region A', the stability is presented two ways: in figure (a) in terms of the Work-per-cycle for the worst interblade phase, σ, and in (b) in terms of the critical reduced damping. The large circles are data for a Mach number of 0.01 and a flow angle, α, of 55°.

that for very low k, which corresponds to the case of quasi-steady flow, the current model predicts an instability if there is blade loading. A quasi-steady flutter mechanism for such an instability in bending has been proposed for cascades with finite turning (Ginzburg, 1974, see also Kerrebrock, 1992). Furthermore, previous computational models of incompressible flat plate cascades with turning have predicted instability in the bending mode for cases of large turning (Shiori, 1958, Whitehead, 1962).

To further look at these affects of blade loading, the code was run for 'Cascade A' (see Table 4.3), a flat plate cascade, in the incompressible limit which corresponds to similar computations in previous studies by Whitehead (1962) and Shiori (1958). The code was run for Cascade A at an inlet flow angle of $-10°$ and a reduced frequency of $k = 0.1$. The critical damping under these conditions is plotted for the current study, from Whitehead (1962), and from Shiori (1958) in Figure 4-8. The trends in unsteady forces with interblade phase angle are similar, although the values differ. It should be recognized that the current model handles the flow (especially the wake) in a physically more realistic manner than the model of Whitehead (1962) or Shiori (1958). Shiori's analytical method used a single bound vortex for each blade to simulate loading superimposed with an asymptotic solution for the problem for the case of $\sigma =?$. In Whitehead's computation, the vorticity wake generated during vibration was assumed to travel in a straight line following the aerofoils at the mean flow velocity. Hall's code, on the other hand, includes a harmonically oscillating wake, and does not make any assumptions regarding its velocity. This may account for the discrepancy. It is significant to note that the case of large negative incidence, with the inlet flow angle of $\alpha = -10°$, has a positive critical reduced damping for $\sigma = 270°$.

To investigate this bending instability further, bending runs on the 10th Standard Configuration were conducted in the limit of incompressible flow ($M = 0.01$), for a larger range of flow angles, and lower reduced damping, k. With significant loading, lowering the reduced velocity k consistently led to an instability. Typical cases are depicted in Figures 4-9a, which shows a high incidence ($\alpha = 65°$) case at $k = 0.035$, and Figure 4-9b, which shows a large negative incidence ($\alpha = 40°$) at $k = 0.065$. The behavior with interblade phase is very different from the typical case of Figure 4-6. The "local" effects in each case, represented by the solid curve, captures the overall behavior well. The zeroth harmonic (mean value), which corresponds to the blade's self-influence, is stable, but the first harmonic, which corresponds to the influence of the

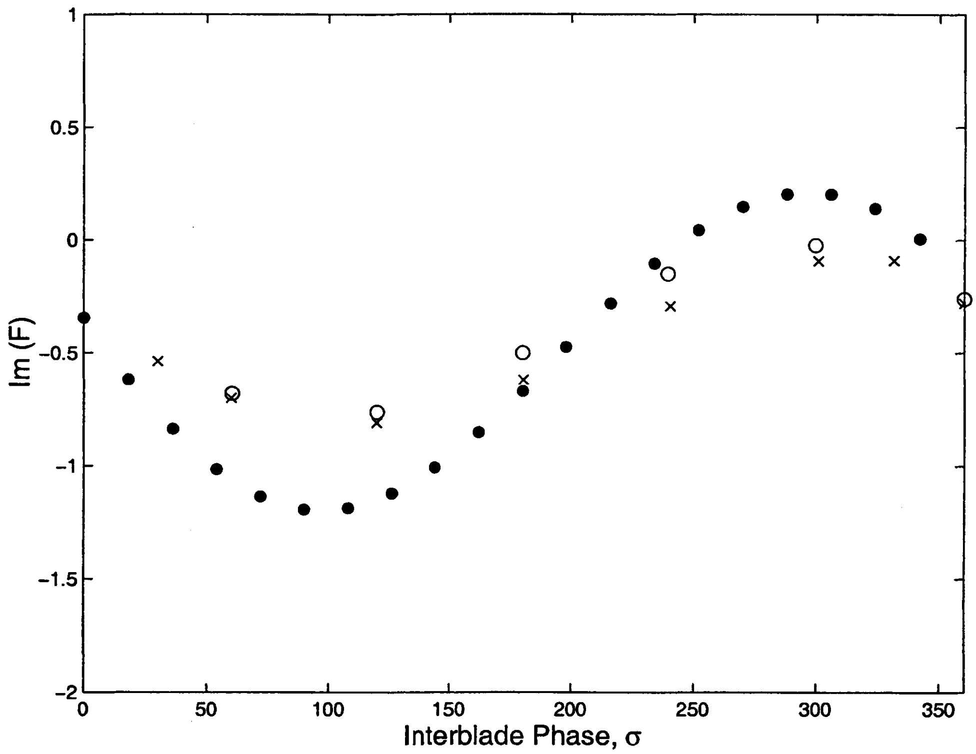

Figure 4-8: Bending instability of a flat plate cascade at negative incidence. The fluid forces from Hall's code, shown by •'s, are compared with the computations of Whitehead (1962), shown by o's, and the model of Shiori (1958), shown by ×'s for bending vibrations at finite incidence. A flat plate cascade with 45° stagger and gap/chord ratio of 1 was computed with an upstream flow angle of $\alpha_1 = -10°$. The imaginary parts of the unsteady lift, which governs stability, is plotted.

neighboring blades, is large enough to generate an instability.

In the high incidence case, an instability emerges for low k near $\sigma = 72°$, while in the large negative incidence case, the instability occurs near $\sigma = 270°$. This is consistent with the quasi-steady mechanism proposed by Ginzberg (1974). According to this mechanism (also described in Kerrebrock, 1992), the neighboring vibrating blades generate a variation in the streamtube width which can generate destabilizing forces. For cases, such as compressors, in which the loading is positive an instability would be expected for inter-blade phase of $\sigma = 90°$. However, if the loading is negative (i.e. for turbines), which occurs in our case of large negative incidence, the interblade phase for instability is expected at $\sigma = 270°$.

The trend of $(g/\rho^*)_{\mathrm{cr}}$ of the least stable interblade phase with k is shown in Figure 4-10. Decreasing k is stabilizing up to a point, but dramatically becomes destabilizing for very low k. It should be mentioned that the values of k considered here are much lower than encountered in aeroengine applications. For example, the instability in the case of high incidence occurs near $k = 0.04$, or a reduced velocity, $U^* = 25$. The typical reduced velocity at flutter in real machines is order 1. Thus, for this bending flutter mechanism to be relevant in aeroengines, other effects not captured in the inviscid model (e.g. viscous lags), must be present.

4.3.2 Torsional vibrations

Typical trends in subresonant regime

Unlike the case of bending vibrations, the current compressible potential flow model predicts that a stability boundary lies for torsional vibrations in the range of k from 0.1 to 1.2. Typically, for zero reduced damping, the boundary lies near $k = 0.25$. While this is still somewhat low compared to the situation in applications, it is about an order of magnitude larger than the reduced velocity, k, for the bending instability. Also, while the Mach number sensitivity is relatively weak in bending, the case of torsional vibrations has a substantial sensitivity to Mach number.

The critical reduced damping for torsional vibrations is plotted as a function of interblade phase, σ, for two typical cases in Figure 4-11a and Figure 4-11b. The first case, in Figure 4-11a, shows a roughly sinusoidal variation with interblade phase, which corresponds well with the influence of a reference blade

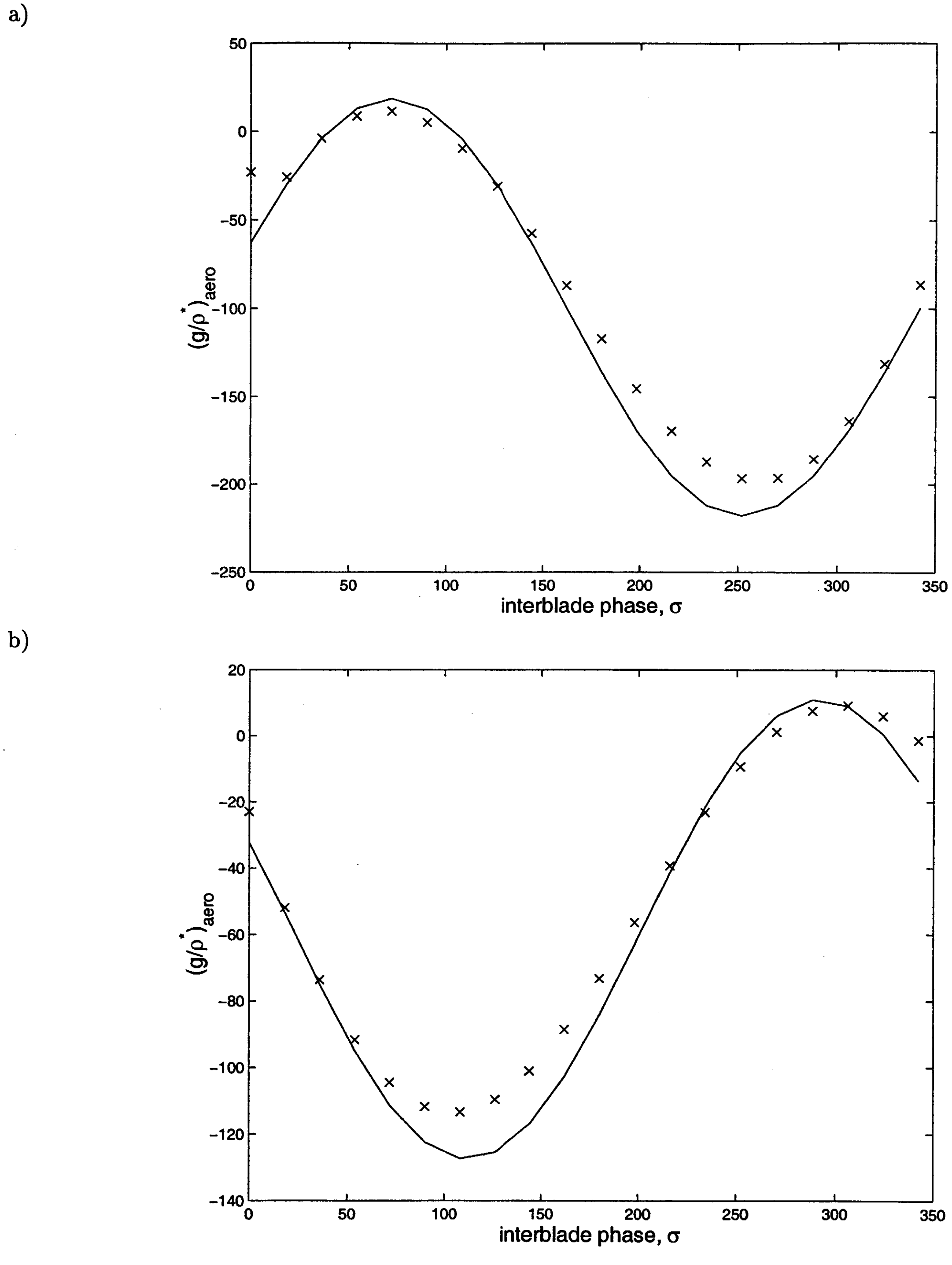

Figure 4-9: Instability in Bending. Trends with interblade phase, σ, for high incidence, $\alpha = 65°$, at $k = 0.035$ depicted in figure (a), and large negative incidence, $\alpha = 10°$, at $k = 0.065$ depicted in figure (b). In both cases the symbols represent actual values, and the curves represent the "local" content.

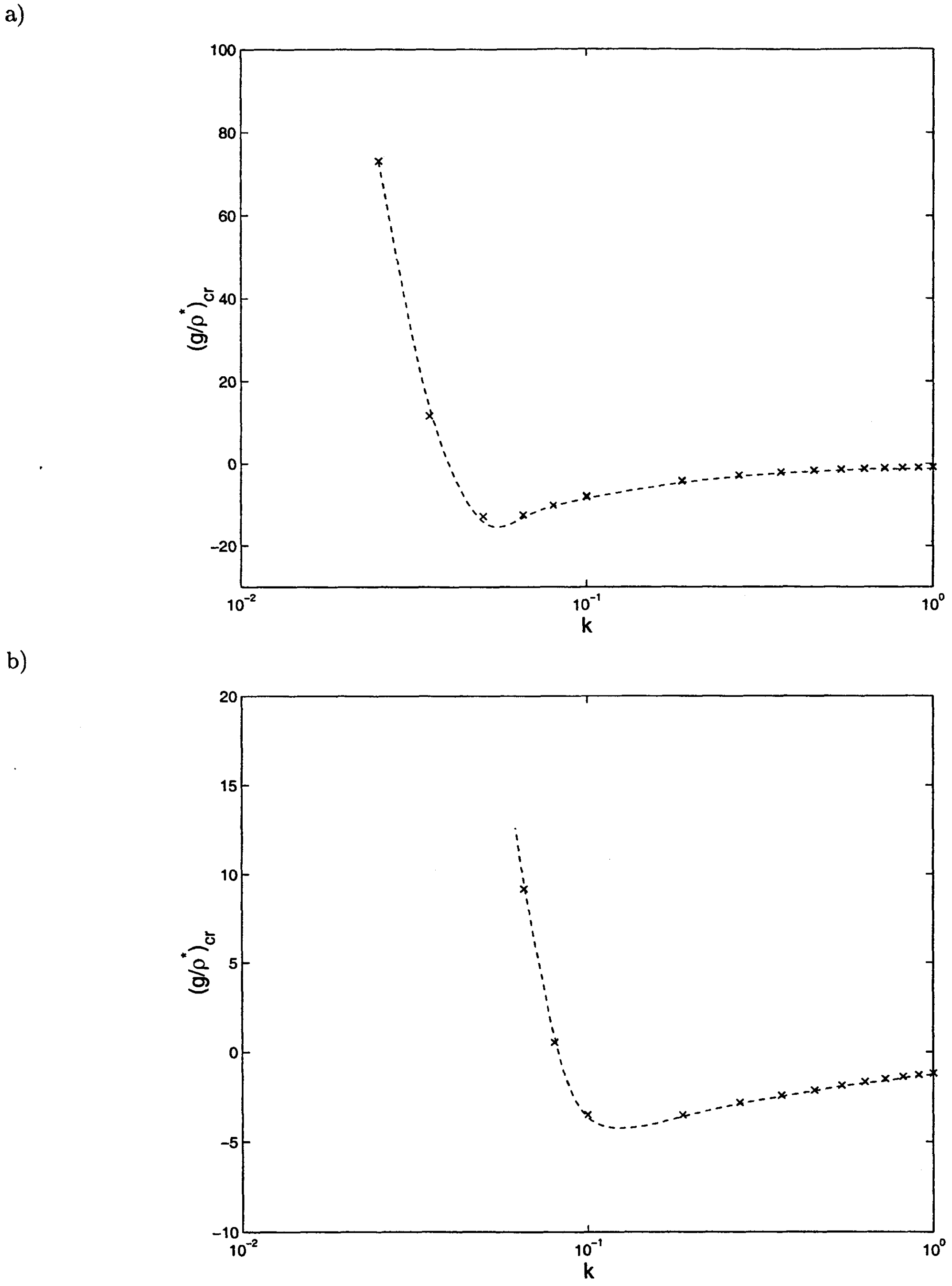

Figure 4-10: Instability in Bending. Trends with reduced frequency, k, for high incidence, $\alpha = 65°$, depicted in figure (a), and large negative incidence, $\alpha = 10°$, depicted in figure (b).

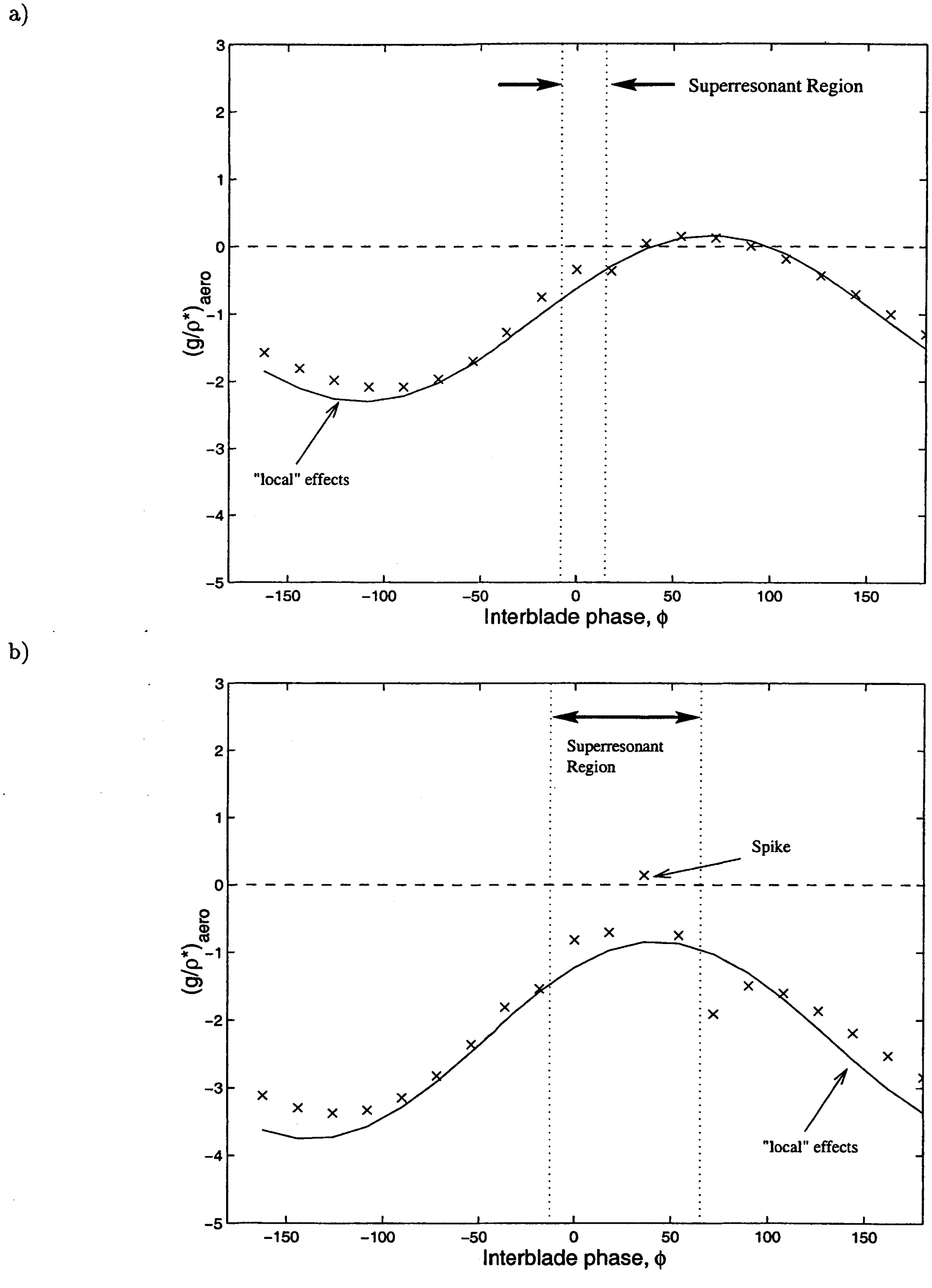

Figure 4-11: Trend of critical reduced damping versus interblade phase, σ, in torsion. In Figure (a), a typical torsional vibration case in region A is shown, which roughly corresponds to the "local" effects of the influence of the reference blade and its immediate neighbors (solid curve). In region B, however, as shown in figure (b), there is significant deviation from the "local" effects. This spike occurs for interblade phase angles, σ, corresponding to the superresonant region.

and its neighbors, shown by the solid curve. The second case, in Figure 4-11b, is taken at a higher k and also has a clearly discernable first harmonic component. However, near zero interblade phase, σ, there is a large deviation from the solid curve, which again represents the influence of a reference blade and its neighbors. As indicated in the figure, this spike is coincident with the superresonant region (i.e. with propagating acoustic modes).

4.3.3 Separation of subresonant and superresonant regions

Since the axial flow is subsonic, circumferential acoustic modes are "cut-off" in the duct, meaning that energy in these modes does not propagate axially. Spikes which deviate from the "local" trends consistently occur in the range of interblade phase angles in the superresonant region, corresponding to propagating acoustic waves, indicate that the spikes are associated with such waves. A definitive interpretation of the mechanism for acoustic wave instabilities is a relatively involved issue, and beyond the scope of our exploratory study. Acoustic wave resonances have been studied in the recent experimental work of Camp (1999) on a low speed compressor. Roughly speaking, conditions are set up in which acoustic modes can travel circumferentially, but not axially. This allows for the possibility of build-up of acoustic energy in the cut-off region. Rather than focusing here upon possible mechanisms for destabilizing effects, we simply describe the conditions which lead to the occurrence of propagating circumferential acoustic waves (i.e. the superresonant region).

The condition for propagating circumferential acoustic waves (i.e. the superresonant region) is analytically derived in the case of a 2D duct with flowing fluid based on the linearized compressible potential equations. In our case, the frequency of the acoustic mode is determined by the reduced frequency, k, and the wavelength, λ, is dependent upon the interblade phase, σ. The corresponding condition for the propagating circumferential acoustic waves (i.e. the superresonant region) is as follows (Whitehead, 1987)

$$\sigma_{\text{lo}} < \sigma < \sigma_{\text{hi}} \tag{4.3}$$

where

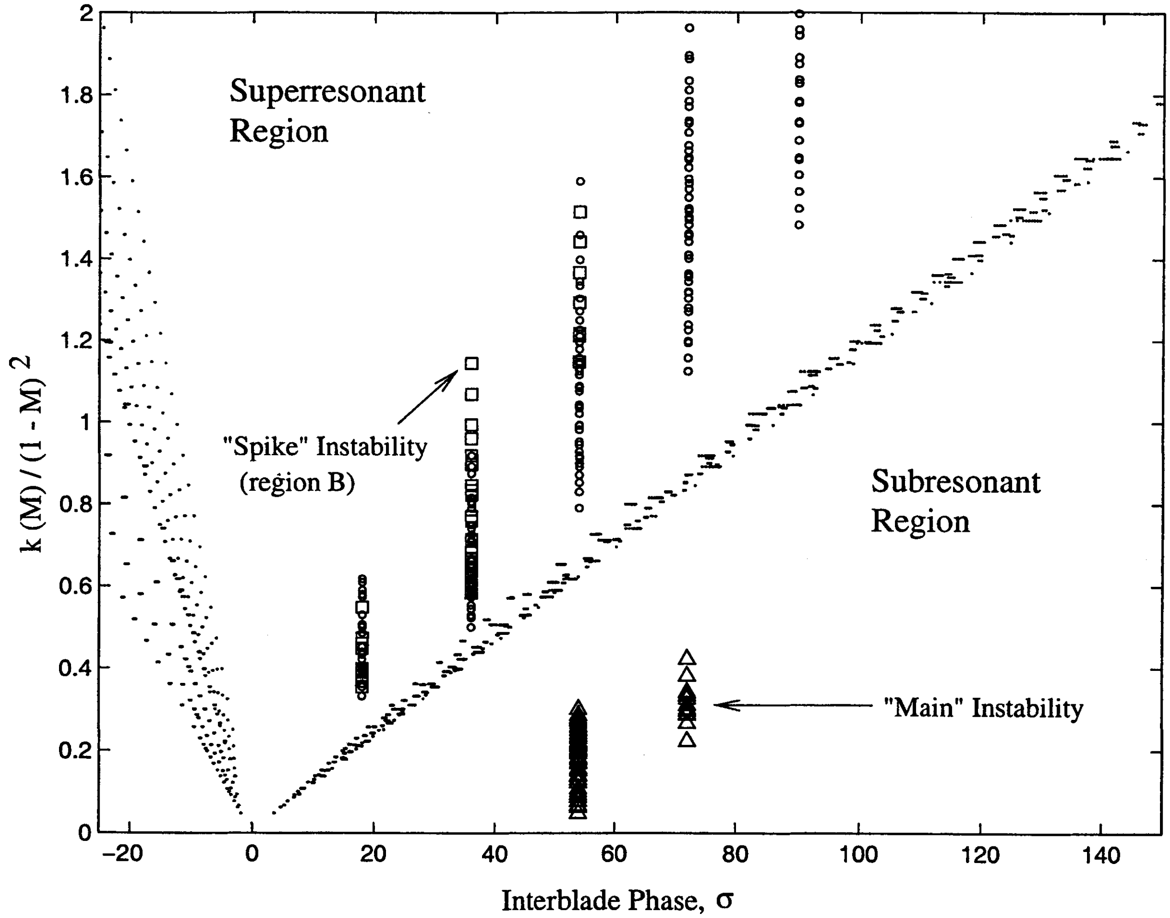

Figure 4-12: Least stable interblade phase, σ, versus $K^*/(1-M^2)$. The superresonant region of propagating acoustic waves (between $\sigma_{\rm lo}$ and $\sigma_{\rm hi}$) is depicted, relevant for the torsional vibration study. There are two identifiable groups of points: the superresonant points (□ and ○) and the subresonant ones (△). Within the superresonant region, the majority (○) have stable fluid forces, while some (□) have destabilizing fluid forces, which predominantly occur in region B (of Figure 4-5).

$$\sigma_{\mathrm{lo,hi}} = \frac{M \cdot k}{1 - M^2} (s/c) \left(M \sin\alpha \pm \left(1 - M^2 \cos^2\alpha\right)^{\frac{1}{2}} \right). \tag{4.4}$$

where s/c is the spacing-to-chord ratio.

It turns out that the range of interblade phase for superresonant behavior, especially σ_{hi} is relatively insensitive to flow angle in regions A and B. Therefore, the superresonant range is approximately a function of the first factor of equation (4.4), $K^*/(1 - M^2)$. Figure 4-12 is a plot of least stable interblade phase, σ, versus the aforementioned factor of $K^*/(1 - M^2)$ for all of the points in regions A and B (spanning Mach number, M, flow angle, α, and reduced frequency, k). The dotted lines represent the values of σ_{hi} and σ_{lo}, which shows that the variations in flow angle did not significantly affect σ_{hi}. There is some scatter in the lines specifying σ_{lo} due to flow angle effects. However, none of the cases in regions A and B had the least stable interblade phase near σ_{lo}, so this scatter does not affect the analysis of the least stable points.

The points on Figure 4-12 in the upper region are cases in which the least stable interblade phase occurred under conditions conducive to superresonant behavior, while the points below the σ_{hi} line occurred under subresonant conditions. Thus, by determining whether a particular case is in one group or the other provides a means of separating the conditions associated with the behavior in Figure 4-11a from those conditions which are associated with Figure 4-11b.

In region A, the effects of propagating acoustic waves (in the superresonant region) do not play an essential role for determining stability, since the points associated with destabilizing forces are almost exclusively in the subresonant regime (the triangles of Figure 4-12). Although there were some situations in region A in which the least stable interblade phase was in the superresonant region, these typically were stable (small circles of Figure 4-12).

4.3.4 Torsional stability in region A

The boundary according to equation (4.2) in region A for $g/\rho^* = 0$ is shown in Figure 4-13. The unstable portion of parameter space is "under" the surface in the orientation of plot. In every case in region A (and, in fact, generally), a sufficient reduction of k leads to an instability.

This boundary, however, is only valid for zero reduced damping, $g/\rho^* = 0$. We can gain more information

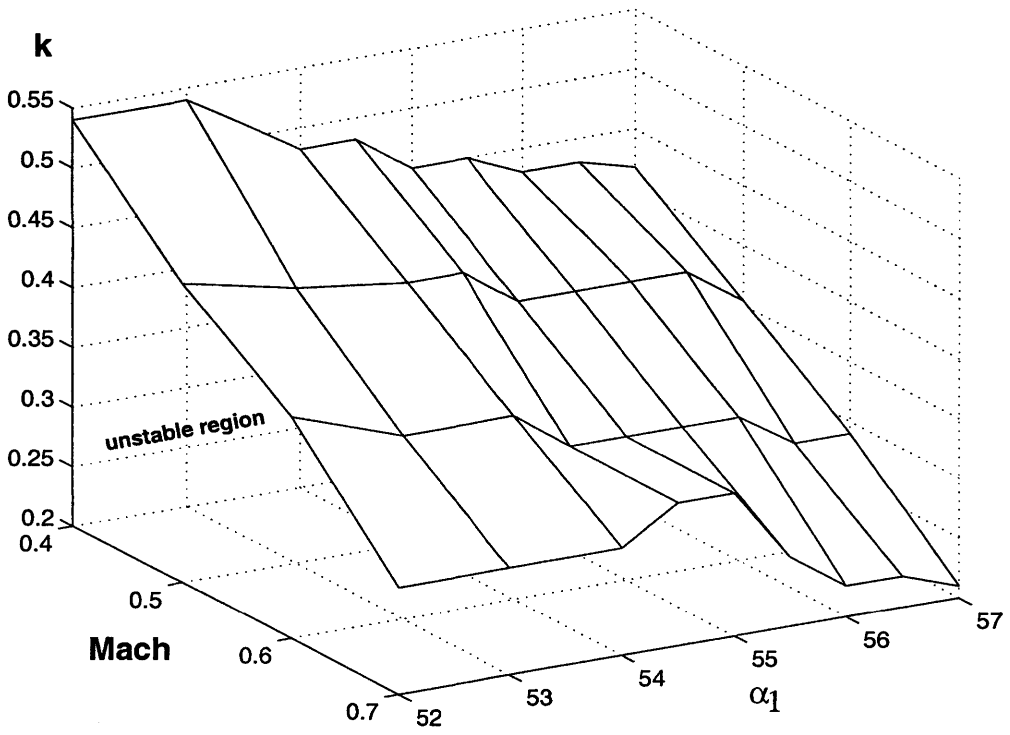

Figure 4-13: Depiction of stability boundary in region A.

by looking at the critical reduced damping for specific cases. The stability is most sensitive to the reduced frequency, k. Therefore, we consider trends in critical reduced damping, $(g/\rho^*)_{\text{cr}}$, with reduced frequency, k, as shown in Figure 4-14 for $M = 0.6$ and two separate inlet flow angles. From Figure 4-13, it can be inferred that for any values of Mach number, M, and flow angle, α, we pick there is always a transition to instability as k is reduced, for the case of $g/\rho^* = 0$. Thus, as expected, a zero-crossing in the trend of $(g/\rho^*)_{\text{cr}}$ with k always occurs at some point for decreasing k.

The stability for a given case, such as the circles associated with $M = 0.6$ and $\alpha = 53°$, can be interpreted according to equation (4.2). If the value of the reduced damping is greater than the critical damping, then the cascade is stable. Thus, the cascade is stable on the upper right part of the graph for the condition given. For example, for $g/\rho^* = 2$, the point of stability occurs for k at approximately 0.23. For values of k above this (keeping M and α constant), the system is stable.

The effect of changing the inlet flow angle, α, is also reflected in Figure 4-14. As the inlet flow angle is changed from $\alpha = 53°$ to $\alpha = 57°$, the critical reduced damping becomes lower. Thus, a lower value

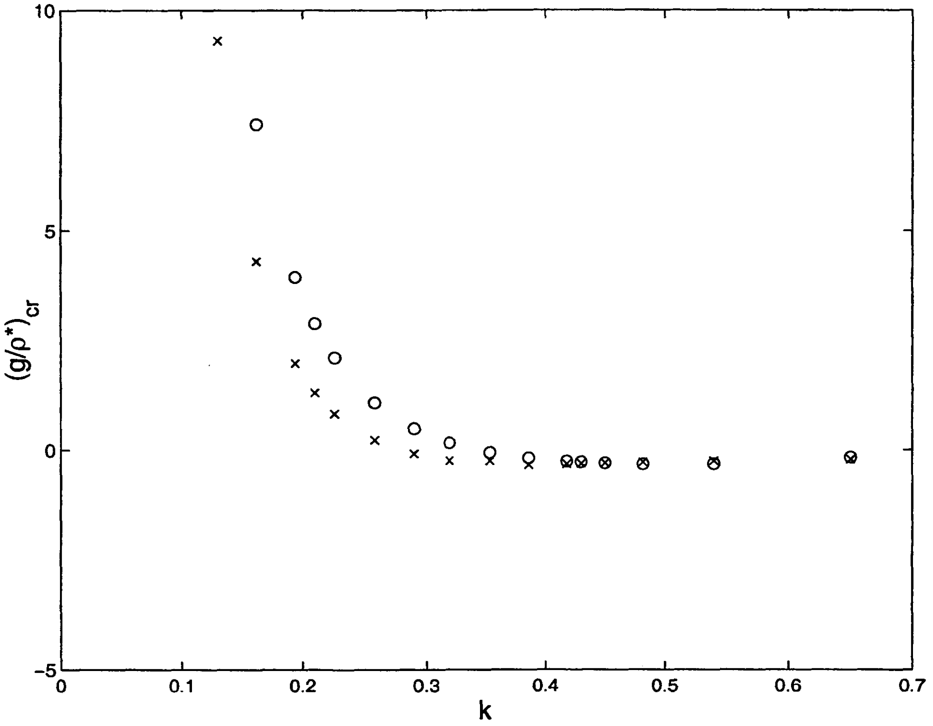

Figure 4-14: Trends of flutter stability $(g/\rho^*)_{\mathrm{cr}}$with reduced frequency, k, at $M = 0.6$, for two cases of inlet flow angle. The cascade geometry is the 10th Standard Configuration, in torsion. The symbol × represents the case of $\alpha = 57°$, while the symbol $\circ$ represents the case of $\alpha = 53°$. For the current compressible potential flow model, the effect of increasing α is to decrease the critical reduced damping , a stabilizing effect, at a constant Mach number and reduced frequency.

of reduced damping is necessary to ensure stability at a given k. For a fixed g/ρ^* value, the minimum allowable k is lower for the higher value of α. Other results using an inviscid model, such as those of Smith and Kadambi (1994), also exhibit this same trend.

In real machines, however, observations show that increasing the flow angle often leads to a (stall flutter) instability. Thus, inviscid models can not capture some important trends found in real machines.

This view of the flutter stability using k and g/ρ^* is similar to the $(K^*, g/\rho^*)$ map was was shown to be helpful in Chapter 3 for constructing a complete methodology for operability assessment with respect to flutter. Since the Mach number is held constant at 0.6, variations in k are equivalent to variations in K^*. Therefore, this similarity is to be expected.

If the Mach number is varied, as in Figure 4-15, then the behavior with respect to K^* looks different from the behavior with respect to k. This shows through in the difference between Figure 4-15a and 4-15b. In figure 4-15a, the x-axis is the classical reduced frequency, k, while the x-axis in Figure 4-15b is the compressible reduced frequency, K^*. In each plot, the trends of torsional stability, $(g/\rho^*)_{\text{cr}}$, with reduced frequency, k are depicted, for a flow angle of $\alpha = 55°$ and for two different Mach numbers, 0.4 and 0.7 respectively.

In the case that the stability data are plotted with respect to k, as in Figure 4-15a, the effect of increasing Mach number (at a constant k and α) is to lower the critical reduced velocity. Such a change in Mach number at constant k and α is stabilizing, and it moves the critical reduced damping boundary down and to the left. However, if the data are plotted with respect to K^*, the same increase in Mach number has the effect of moving the critical reduced damping boundary to the right, which is destabilizing. Although this may at first appear to be contradictory, it simply indicates that comparisons at constant K^* are very different from comparisons at constant k. From the standpoint of operability of a machine with constant structural parameters, the comparison at constant K^* is one in which the inlet temperature is kept constant, while a comparison at constant k is one in which the inlet relative velocity is kept constant.

a)

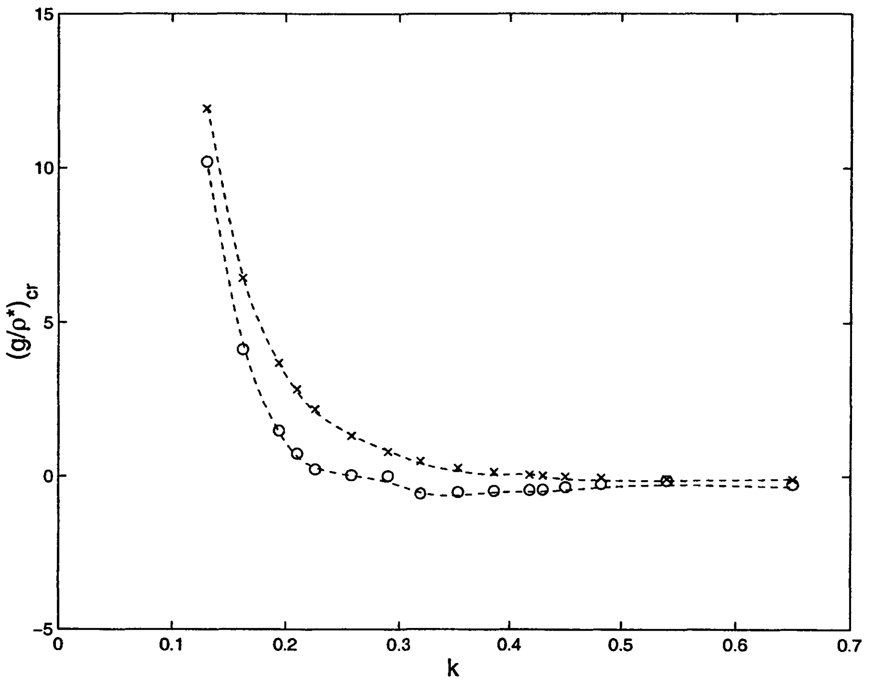

b)

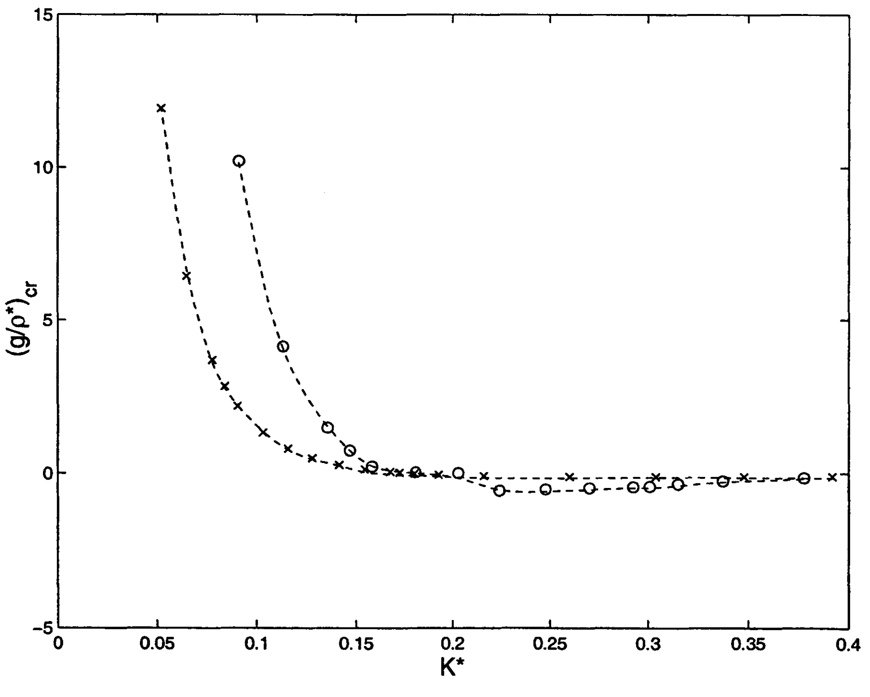

Figure 4-15: Instability in Torsion. Trends of flutter stability $(g/\rho^*)_{cr}$with reduced frequency, k, at $\alpha = 55°$, for two cases of Mach number. The symbol × represents the case of $M = 0.4$, while the symbol o represents the case of $M = 0.7$. At a constant flow angle and reduced frequency, the effect of increasing Mach number is to decrease the critical reduced damping for torsion.

4.3.5 Torsional stability in region B

So far, we have focused upon the "main" boundary of region A, depicted in Figure 4-13 for zero mechanical damping. These trends are due to the typical cases in which the critical stability point is in the subresonant region, as in Figure 4-11a. We now address the effects of the "spikes" of Figure 4-11b, which are an exception to the general behavior. Since these spikes are in the superresonant region, one should note that in the current flow domain, the upstream and downstream boundaries are non-reflective. This corresponds to the case of a rotor in an infinite duct. In reality, of course, a given rotor will not lie in an infinite duct and may have other components in close proximity. The values of the vibration-induced forces have been shown to be sensitive to the details of the upstream and downstream boundary (Hall and Silkowski, 1997), but we limit the current exploratory study to the infinite duct case.

The spikes have been observed in previous linearized inviscid flow studies (e.g. Bendiksen and Friedmann, 1981), and are considered a "weak" instability since their destabilizing effects can be eliminated with sufficient damping. Figure 4-16 shows the points in parameter space simulated from both region A and region B. A ∘ denotes a stable point, and an × denotes an unstable point. Solid lines mark the boundary between stable and unstable regions. The boundary shown in Figure 4-13 can be identified with the lines in Figure 4-16a, but the latter view is upside-down from the former. Inspection of Figure 4-16a indicates that several disconnected "lobes" of instability are present, in the low flow angle (negative incidence), and high Mach number are corresponding to region B (of Figure 4-5). These lobes come from the superresonant region. A small amount of reduced damping, $g/\rho^* = 0.5$, generates a new stability boundary, as shown in Figure 4-16b, in which the lobes diappear. The "main" stability boundary is also modified, however. At low mach numbers, such as $M = 0.4$, the boundary moves significantly, while the effect of increasing reduced damping, g/ρ^*, is much less effective at higher Mach numbers such as $M = 0.7$. This is consistent with the trends with Mach number that one might observe in Figure 4-15a.

A slice of unstable region near the lobes is in greater detail by considering the critical reduced damping, or as a function of reduced frequency in the region of parameter space where the lobes occur. Figure 4-17 shows the trend of $(g/\rho^*)_{\text{cr}}$ with k for the conditions $(M, \alpha) = (0.73, 52°)$. The main trend from region A, as shown in Figure 4-15, still exists, but some bumps occur at higher k addition to the main trend. These

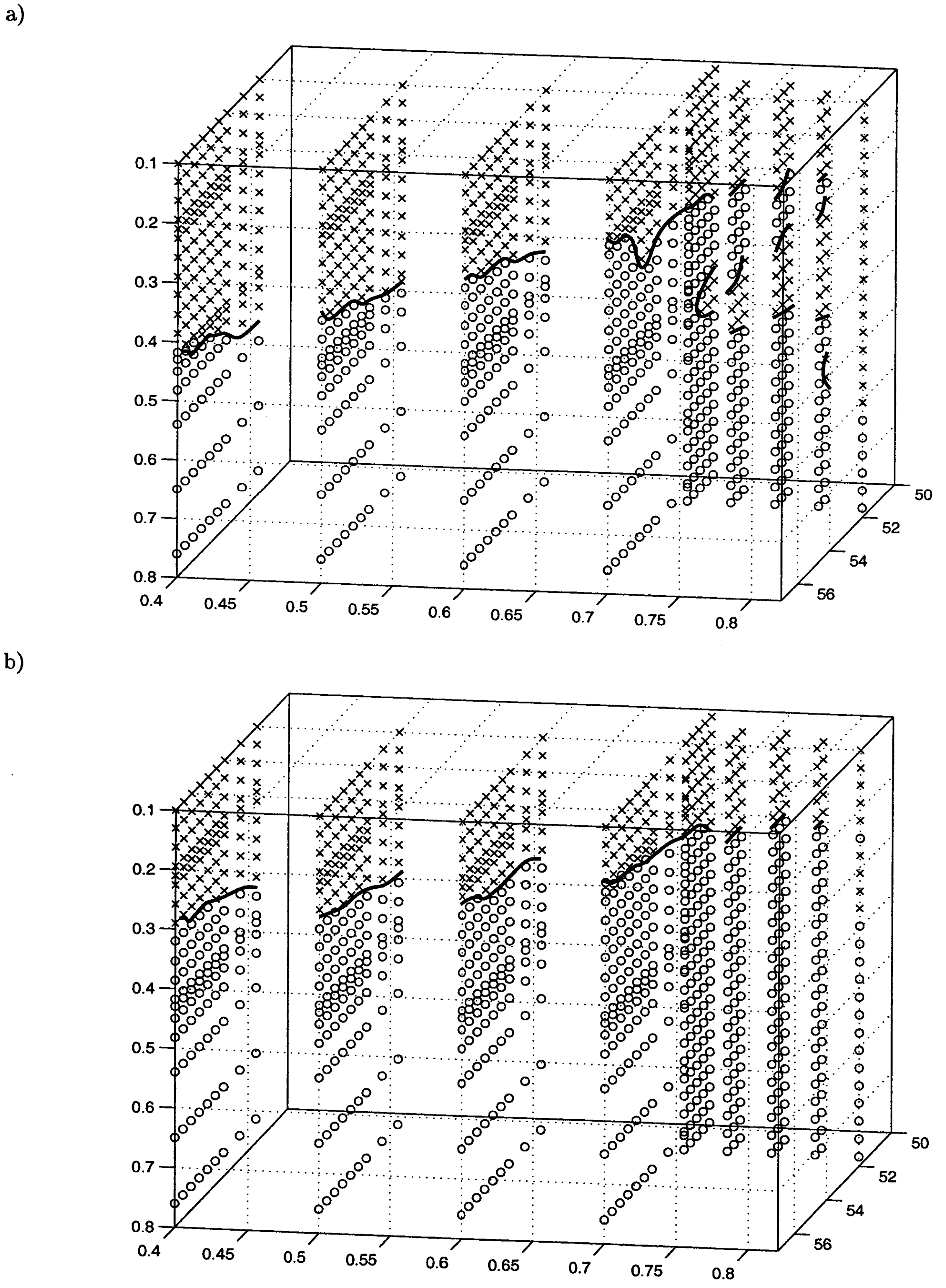

Figure 4-16: Torsional stability, 10th Standard Configuration. Two cases are shown: $g/\rho^* = 0$ in (a), and $g/\rho^* = 0.5$ in (b). Symbols denote stable (•) points and unstable (∘) points. There are lobes of "weak" instability in the zero damping case (a) which are mitigated by a finite damping (b).

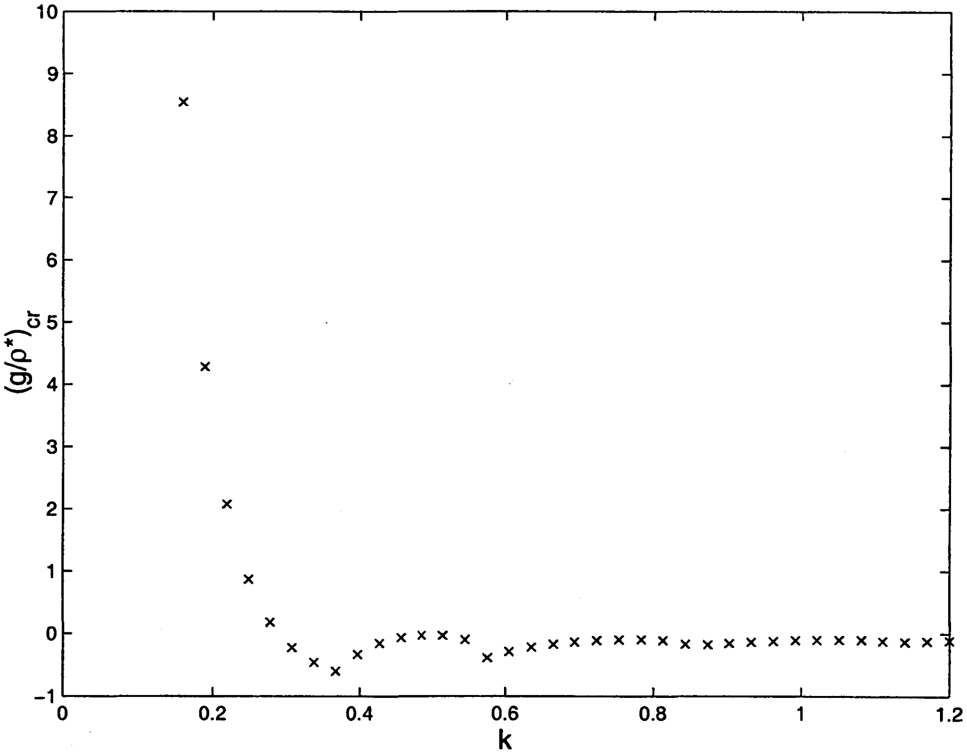

Figure 4-17: Trends of critical reduced damping, $(g/\rho^*)_{\mathrm{cr}}$, with reduced frequency, k, in the superresonant region. The Mach number and flow angle are fixed at $M = 0.73$, and $\alpha = 52°$, respectively. A small amount of reduced damping, g/ρ^*, can mitigate the effect of the spikes.

bumps correspond to the lobes of instability, as seen in Figure 4-16a. The plot in Figure 4-17 shows that just a small amount of reduced damping, relative to the O(1) typical value, may be sufficient to mitigate the bumps.

The details of the bumps/lobes of Figure 4-17 can be seen more clearly in terms of the work-per-cycle, which is shown in Figure 4-18. The critical reduced damping scaling tends to hide some of the details at high k, since the *magnitude* of the fluid forces diminishes here. The work-per-cycle is helpful in seeing this structure. One can see in Figure 4-18 several distinct bumps. Each bump corresponds to a different interblade phase, σ, for the spike of Figure 4-11b. As the range of interblade phases corresponding to the superresonant case increases (i.e. as σ_{hi} of equation 4.4 increases), the interblade phase, σ, associated with the spike of Figure 4-11b increases as well.

These bumps contradict the main trend that increasing frequency improves stability. This is an exception to the general rule of Chapter 3 that increasing K^* improves stability (n.b. in this case of constant M, trends with k are equivalent to trends with K^*). However, the dominant trend, even in the region of the lobe, is that of stabilizing K^* rather than of the exception (i.e. the lobes). Furthermore, this exception is the result of acoustic wave resonance, which has not been observed as self-excited phenomenon. Rather, such acoustic resonances are usually fed by upstream disturbances, and are increasingly considered as distinct from flutter (Camp, 1999).

4.4 Reduction of mach number trend

4.4.1 General trends of phase with Mach number

Although only the out-of-phase portion of the fluid forces affects flutter stability, it is useful to look at other information which characterizes the unsteady flow problem. Trends in these other parameters may reveal insights into the unsteady forcing mechanism. In particular, the phase of the vibration-induced forces (relative to the blade motion) is related to the time lag in the unsteady flow, as mentioned in Chapter 3. Thus, by studying the phase, we can learn more about the unsteady fluid lags, in the approximation of 2D compressible potential flow.

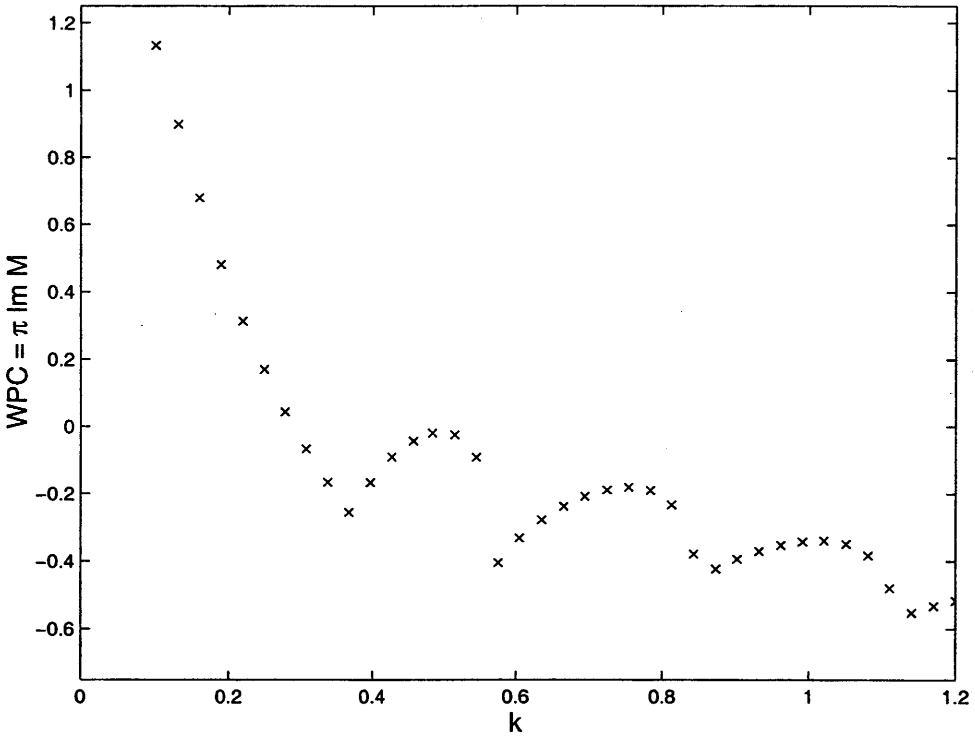

Figure 4-18: Trends of work-per-cycle, $\pi Im(M)$, with reduced frequency, k, in superresonant cases. The Mach number and flow angle are fixed at $M = 0.73$, and $\alpha = 52°$, respectively, which cuts through several "lobes" of instability.

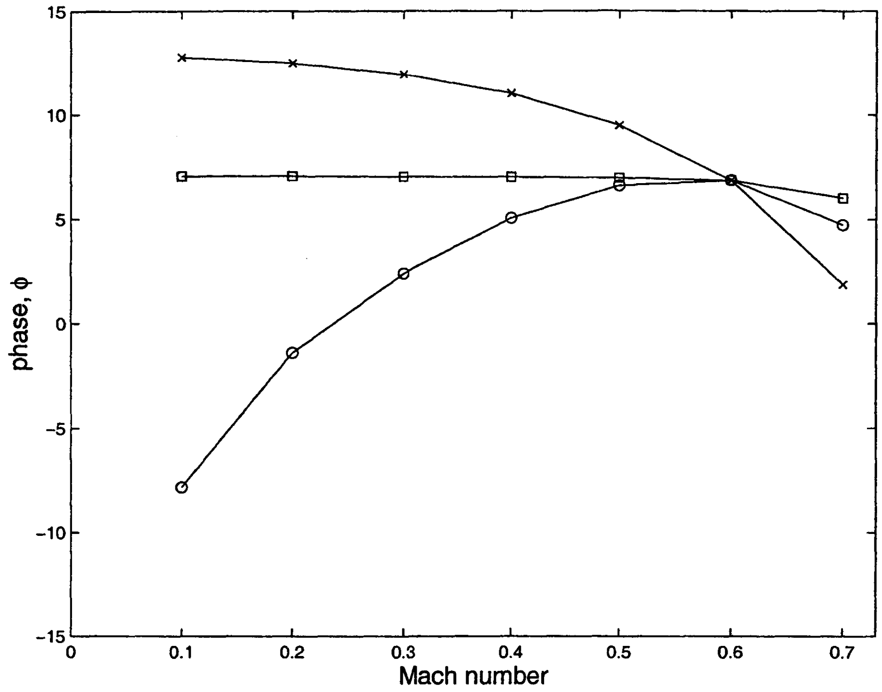

Figure 4-19: Fluid force phase, ϕ, as a function of Mach number for the 10th Standard Configuration. Trends are shown for constant inlet flow angle, $\alpha = 55°$, for three cases: constant $k = 0.2$ (×'s), constant $K^* = 0.12$ (○), and constant $k/(1-M^2) = 0.3125$ (□). There is little variation in the case of constant $k/(1-M^2)$.

In the context of this exploratory study, we identify gross trends and comment on their implications. We focus on the torsional mode, in which there exist destabilizing fluid forces within regions A and B of Figure 4-5. In general, a negative phase, $-1800° < \phi < 0°$, indicates that the fluid forces have a stabilizing influence, while a positive phase, $0° < \phi < 1800°$, indicates that the fluid forces have a destabilizing influence. The ultimate system stability, for finite mechanical damping, depends on the magnitude of forces as well, since a flutter instability requires that the destabilizing fluid forces overcome the mechanical damping.

The unsteady flow problem involves three physically distinct time scales: the vibration time, $1/\omega_0$, the acoustic time, $c/\sqrt{\gamma R T_0}$, and the flow-trhough time, c/U. Their relationship can be described using the non-dimensional parameters of the Mach number, M, the classical reduced frequency, k, and the compressible reduced frequency, K^*, which is schematically represented in Figure 3-2. By similarity, only two non-dimensional parameters are necessary to capture the time scale behavior.

Figure 4-19 shows some trends in fluid force phase, ϕ, as a function of Mach number, M in the 10th Standard Configuration for a constant inlet flow angle of $\alpha = 55°$. Three curves are shown, each keeping some combination of the three relevant timescales constant: the × symbols keep the classical reduced frequency constant at $k = 0.2$, the ∘ symbols keep the compressible reduced frequency constant at $K^* = 0.12$, and the □ symbols keep a combination of the three relevant timescales, $k/(1-M^2)$ constant at 0.3125.

The trend of Mach number with classical reduced frequency, k, is roughly constant for low Mach number, but sees significant Mach number effects at higher Mach numbers. At low Mach numbers, we do not expect the acoustic effects to play a significant role. Eliminating the acoustic time, leaves k as a single non-dimensional parameter to describe the unsteady behavior. Thus, the limiting behavior for k at low Mach number is to be expected.

With the compressible reduced frequency, K^*, constant there is a maximum in the phase, ϕ, near $M = 0.6$ where the phase appears to be relatively insensitive to Mach number effects. However, at low Mach numbers (below 0.4), there is a strong effect.

Keeping the quantity $k/(1-M^2)$ constant leads to a roughly constant value of fluid force phase, ϕ, for the whole range of Mach numbers tested (at higher Mach numbers the potential code diverges). This is significant since it suggests that, for cascade potential flow, the vibration-induced fluid force phase is *solely* a function of $k/(1-M^2)$, independent of the Mach number.

Ultimately, the trends we are studying come from solutions to the linearized unsteady potential equations. If the mean flow has a Mach number, M, and is in the x-direction, then the pressure perturbation is described by (Lane and Friedman, 1958, Whitehead, 1970) the following equation:

$$(1-M^2)\frac{\partial^2\Psi}{\partial x^2} + \frac{\partial^2\Psi}{\partial y^2} + \frac{k^2 \cdot M^2}{1-M^2}\Psi = 0 \tag{4.5}$$

where Ψ is the harmonic perturbation amplitude, described by

$$\Psi = p\exp\Big(iK^*(tc/\sqrt{\gamma R T_0}) + iK^*(x/c)\Big) \tag{4.6}$$

Of course, boundary conditions are needed to complete these field equations, but we have already imposed a spatio-temporal periodicity associated with the vibration. An analytical, explicit solution for the fluid phase, ϕ, is not known, even in restricted cases (which is the reason why the computational code is necessary). There are several non-dimensional coefficients suggested by the above equations, such as K^*, k, and the coefficient to Ψ in equation (??), or $(K^*)^2/\sqrt{1-M^2}$. It turns out that keeping these quantities constant does not minimize the variation of the fluid force phase, ϕ, as much as $k/(1-M^2)$. Evidently, the quantity $k/(1-M^2)$, captures a mixture of timescales which is relevant to the flutter mechanism in this case. Since the flutter mechanism still not completely understood on a physical basis, this trend may provide an important clue towards establishing the physical basis to flutter in this idealized case.

We investigate the range of conditions under which the phase is described by $k/(1-M^2)$ by running the model in a series of test cases. The issue of finding an analytical connection between fluid force phase, ϕ, and the quantity $k/(1-M^2)$ is left to future studies. The trend in Figure 4-19, there is shown for a single value of $k/(1-M^2)$, for a specific cascade geometry (10th Standard Configuration), for a single value of inlet flow angle, α, and for conditions of decaying acoustic waves (i.e. for subresonant behavior). We explore each of these issues in the remainder of this section.

4.4.2 Effects of varying frequency on trends of fluid force phase

Figure 4-20 shows the fluid force phase, ϕ, for several Mach numbers, M (0.4 to 0.7), for a range of values of reduced frequency, k, and for a constant inlet flow angle at $\alpha = 56°$. The fluid force phase data are plotted in two ways: (a) as a function of $k/(1-M^2)$, and (b) as a function of reduced frequency, k. The quantity, $k/(1-M^2)$, appears to collapse the Mach number dependence. As the fluid force phase leaves a band from about 0° to 10°, the scatter for the different values of Mach number increases. At $k/(1-M^2) = 0.2$, there is about a 3° difference between $M = 0.4$ and $M = 0.7$. This is larger than the difference of less than 1° at a value of $k/(1-M^2) = 0.3125$ shown in Figure 4-19. There is a similar growth in scatter for low values of ϕ. This indicates that the "collapse" is not exact, but simply an approximation which minimizes the Mach number dependence.

By contrast, the trends in the same data with respect to reduced frequency, k, as shown in Figure 4-20b, have a discernable Mach number dependence. At a constant k, increasing the Mach number reduces the fluid force phase, ϕ. This behavior with Mach number is consistent with the previously discussed trends of Figure 4-15.

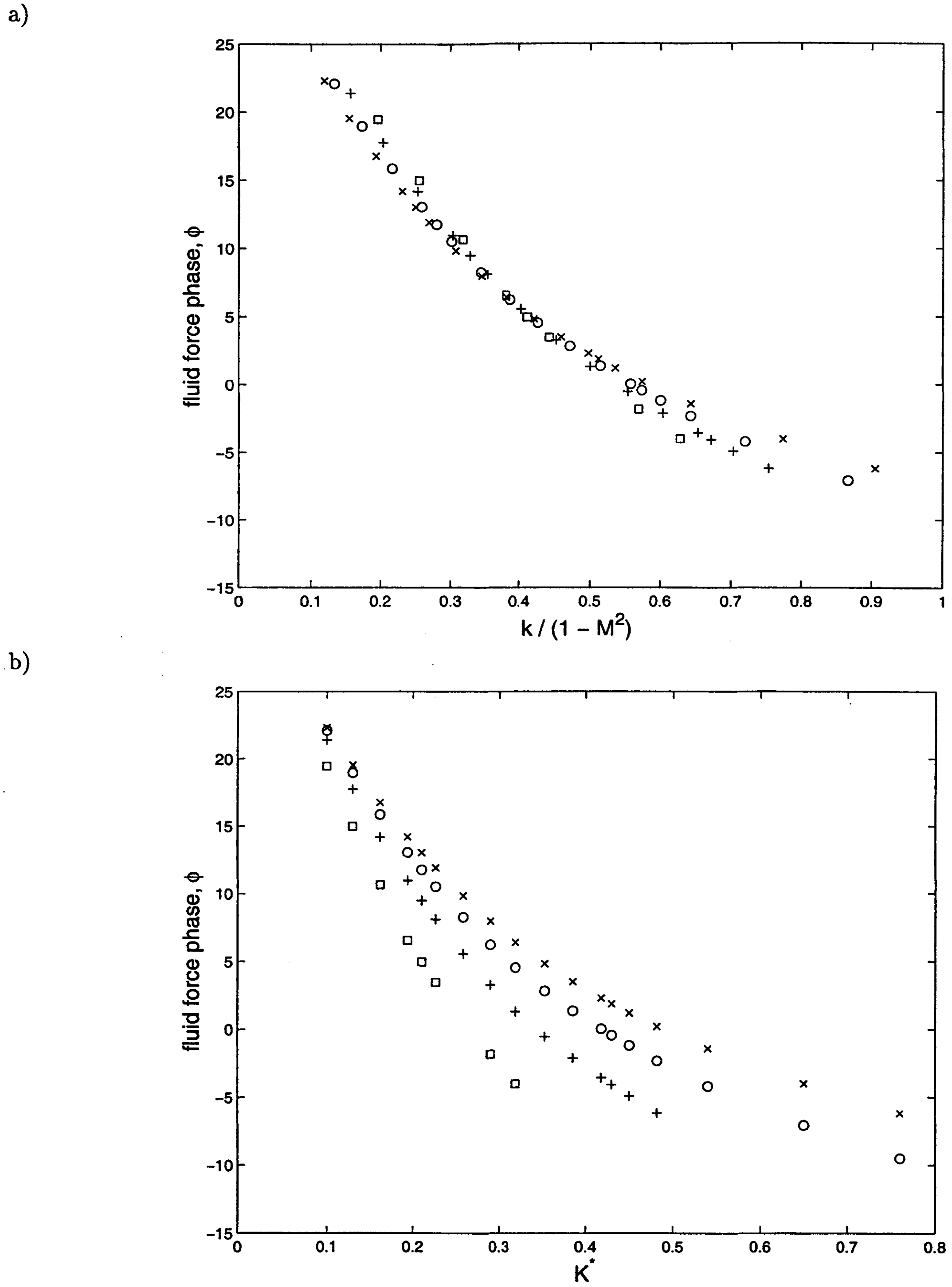

Figure 4-20: The fluid force phase, ϕ, is plotted for constant inlet flow angle, $\alpha = 56°$, in figure (a) as a function of $k/(1 - M^2)$ for various Mach numbers, $\times$ for $M = 0.4$, $\circ$ for $M = 0.5$, $+$ for $M = 0.6$, and $\square$ for $M = 0.7$. The parameter $k/(1 - M^2)$ effectively collapses the effect of Mach number in region 'A' of Figure 4-5. For reference, the phase is plotted with reduced frequency, k, in figure (b).

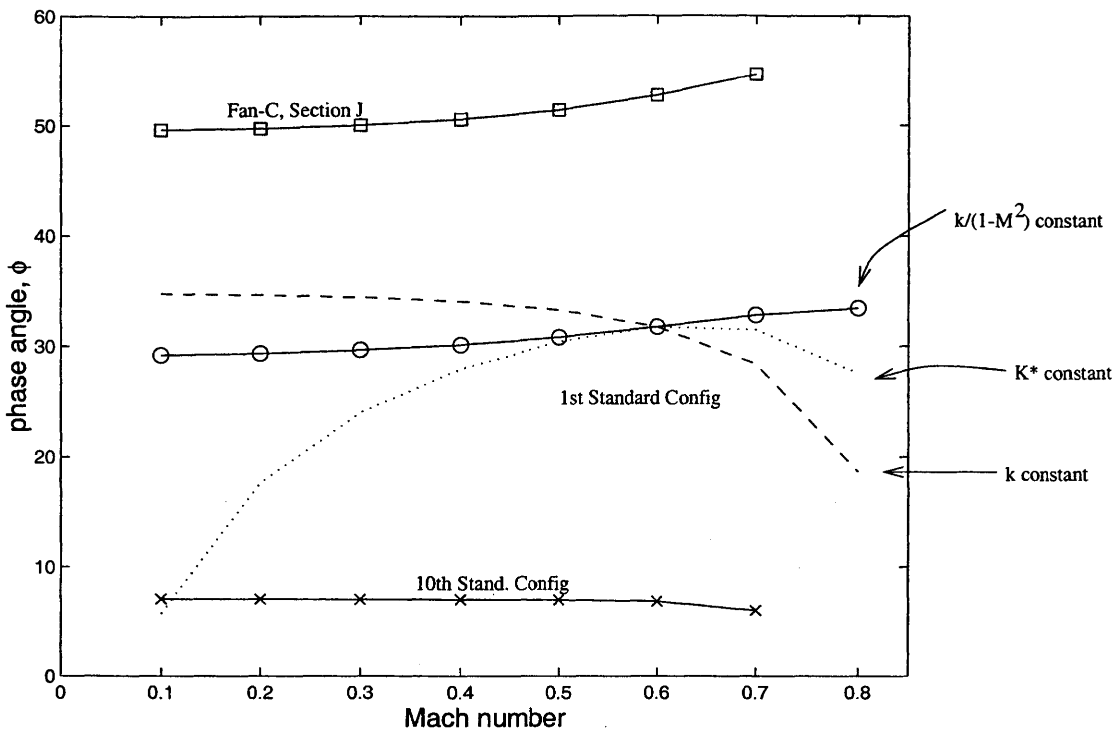

Figure 4-21: The phase of the fluid forces is plotted versus Mach number for constant $\alpha = 55$ and constant $k/(1-M^2)$ for several geometries (solid lines). For reference, the constant k and the constant K^* cases are shown for the 1st standard configuration as dashed and dotted lines, respectively.

4.4.3 Effect of varying geometry on trends of fluid force phase

We now turn to the question of sensitivity of the collapse with respect to changes in the cascade geometry. Figure 4-21 shows as solid lines the trend with Mach number for a constant $k/(1-M^2) = 0.3125$, and a constant inlet flow angle (at a small positive incidence) for three different geometries: the 1st Standard Configuration (Bölcs and Fransson, 1986), the 10th Standard Configuration (Fransson and Verdon, 1993), and a radial section of the Fan-C rotor (Jutras et. al., 1982). For reference, trends with constant k and K^* are shown for the 1st Standard Configuration as dashed and dotted lines, respectively.

It is clear that the stability characteristics of the three geometries are different, since the Fan-C section categorically has a much higher phase, ϕ, than does the 1st Standard Configuration, and (in turn) the 1st Standard Configuration has a significantly higher phase, ϕ, than the 10th Standard Configuration. Keeping the quantity, $k/(1-M^2)$, constant appears to diminish the Mach number effects on fluid force phase, ϕ, in all of the geometries. The 1st Standard Configuration and the Fan-C section have greater spread in terms of absolute value of phase over the Mach number range. However, the relative scatter over the range of

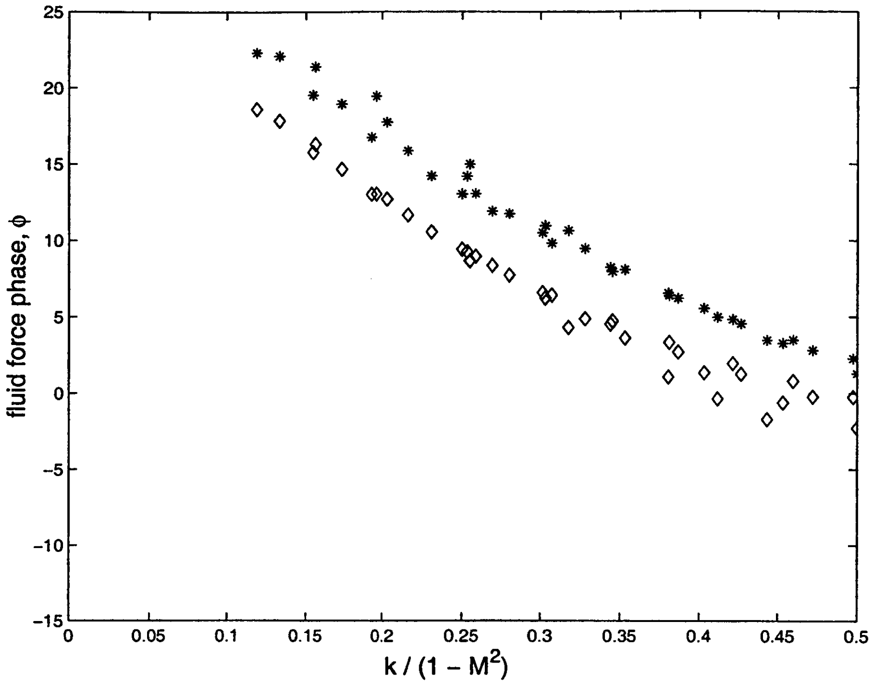

Figure 4-22: Effect of inlet flow angle on fluid force phase. A range of Mach numbers (the range tested in region 'A' of Figure 4-5) is shown for two inlet flow angles: $*$ for $\alpha = 53°$ and $\Diamond$ for $\alpha = 57°$. For the current potential flow model, the effect of increasing the inlet angle is to reduce the fluid force phase.

Mach numbers is about the same, around 10%.

4.4.4 Effect of varying inlet flow angle on trends of fluid force phase

Changing the inlet flow angle, α, affects the fluid force phase, ϕ, as might be expected from the fact that α influences stability (see Figure 4-14). However, the collapse of phase, ϕ, with $k/(1 - M^2)$ does not depend on the value of inlet flow angle, α, kept constant, as long as one remains in the subresonant regime.

This is shown in Figure 4-22. Two inlet flow angles are shown: $\alpha = 53°$, as $*$'s, and $\alpha = 57°$, as $\Diamond$ symbols. For each flow angle, a range of Mach numbers (within region A), are plotted. The collapse of Mach number effects on the fluid force phase, ϕ, occurs for both inlet flow angles, but increasing α from 53°to 57°shifts the trend (for all the Mach numbers) down. This is a stabilizing shift which is consistent with the trends previously identified in the critical reduced damping.

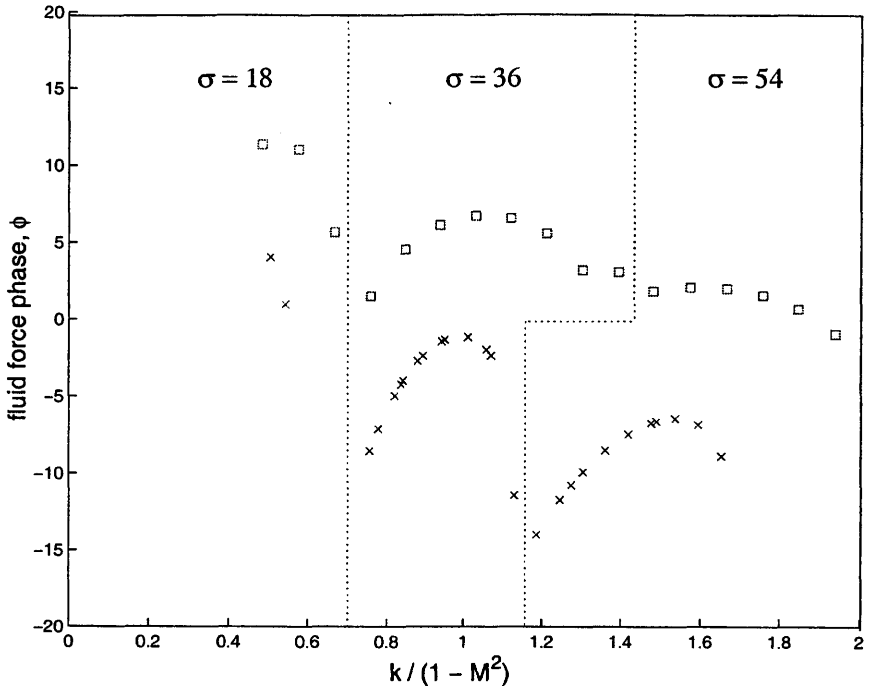

Figure 4-23: Fluid force phase, ϕ, in the region B as a function of $k/(1-M^2)$, for superresonant points. The flow angle is kept fixed at $\alpha = 51.8°$, and two Mach numbers are shown: × for $M = 0.7$ and □ for $M = 0.84$. In contrast to the points near the main stability boundary of region A, the factor of $k/(1-M^2)$ does not collapse the Mach number dependence. Each bump corresponds to a different (worst-case) interblade phase, σ, as designated.

4.4.5 Break down of Mach number "collapse" in superresonant regime

The "collapse" of Mach number effects with the single parameter, $k/(1-M^2)$, breaks down when the condition of superresonant behavior occurs for the least stable interblade phase angle. That is, even for a constant $k/(1-M^2)$, changing the Mach number, M affects the value of ϕ. This is depicted in Figure 4-23 in which the flow angle is kept constant at $\alpha = 51.8°$. Each bump in the trend corresponds to the acoustic resonance of a different interblade phase angle, σ. Since 20 interblade phase angles, σ, were considered for each point in parameter space, these bumps correspond to 18°increments in interblade phase, σ, as shown in the figure. In this instance, increasing the Mach number from 0.7 to 0.84 at a constant $k/(1-M^2)$ increases the fluid force phase, ϕ, significantly. At $k/(1-M^2) = 1$ the gap is about 8°, while at $k/(1-M^2) = 1.2$, the gap is almost 20 degrees. Evidently, there is not just a shift in value of ϕ, but a difference in trend in the superresonant regime.

4.5 Summary

A computational study of the vibration-induced fluid forces upon a 2-D cascade was conducted using a subsonic, linearized-unsteady, potential flow code (Hall, 1993). Mach numbers up to 0.7 were considered. The primary cascade studied was in the 10th Standard Configuration, but other geometries were also investigated.

It is suggested that $(g/\rho^*)_{\text{cr}}$ is a useful metric for stability to replace the "work-per-cycle." The critical reduced damping can be computed using only information from the unsteady flow problem (not the modal mass, or damping, for example), but is directly comparable to the actual reduced damping.

The results of the exploratory parametric study exhibited an instability in both bending and in torsional modes. In both cases, the predominant instability mechanism was *local*; that is, it was associated with the influence of the vibrating blade upon itself and its nearest neighbors. In these cases, the effect of increasing the compressible reduced frequency was stabilizing.

The bending instability occured for very low reduced frequency ($k \approx 0.03$), and high loading. This is consistent with classical studies of bending using a flat-plate potential model (Whitehead, 1962, Shiori, 1958).

In torsion, however, the instability occurred at a significantly higher reduced frequency ($k \approx 0.2$), and was explored across the full range of parameters. These results indicated that the torsional instability had independent effects of reduced frequency, k, Mach number, M, and of flow angle, α.

In the case of torsion, there was also a destabilizing non-local effect, associated with an acoustic resonance. The physical viability of acoustic resonance is controversial in the literature, but it has been previously shown to be a solution to the idealized model equations. This acoustic resonance led to small "lobes" of instability for low α and high M, which violated the trend that increasing frequency is stabilizing. The case of finite damping, $g/\rho^* = 0.5$, does not have these lobes, but has the local instability mechanism.

In the case of decaying acoustic waves (i.e. no acoustic resonance), it was found that, for a given flow angle, the quantity $k/(1 - M^2)$ described the fluid force phase, with relatively small independent effects of Mach number, M. These trends were checked for varying Mach number, and reduced frequency. Modifying the cascade geometry, or the inlet flow angle retains the same trends.

Chapter 5

Technique for Analysis of Full-Scale Engine Data

5.1 Overview

The most reliable way to learn about the stability characteristics of a machine is to experimentally test it. In this chapter, we focus upon data analysis of full-scale test data using the non-dimensional variables and the methodology described in previous chapters.

Flutter data for full-scale test data are relatively scarce, especially those data in the public-domain. Previous efforts, discussed in the introduction, have been able to characterize the problem and identify the major trends, but have not been able to quantify these trends and have left some important questions unanswered. This is partially because it is very expensive to conduct a full-scale test, and flutter testing which spans various points on the flight envelope is rare.

Here, we consider data taken from full-scale testing at the Volvo Corporation of a fan which exhibited flutter in the 2nd bending mode. This data spans the performance map as well as flight conditions, giving more information onto the full 4-dimensional parameter space than available from the aforementioned studies. Using the non-dimensional parameters discussed previously, along with novel data analysis techniques, it possible to characterize the flutter stability in the full four-dimensional space, and quantify these trends.

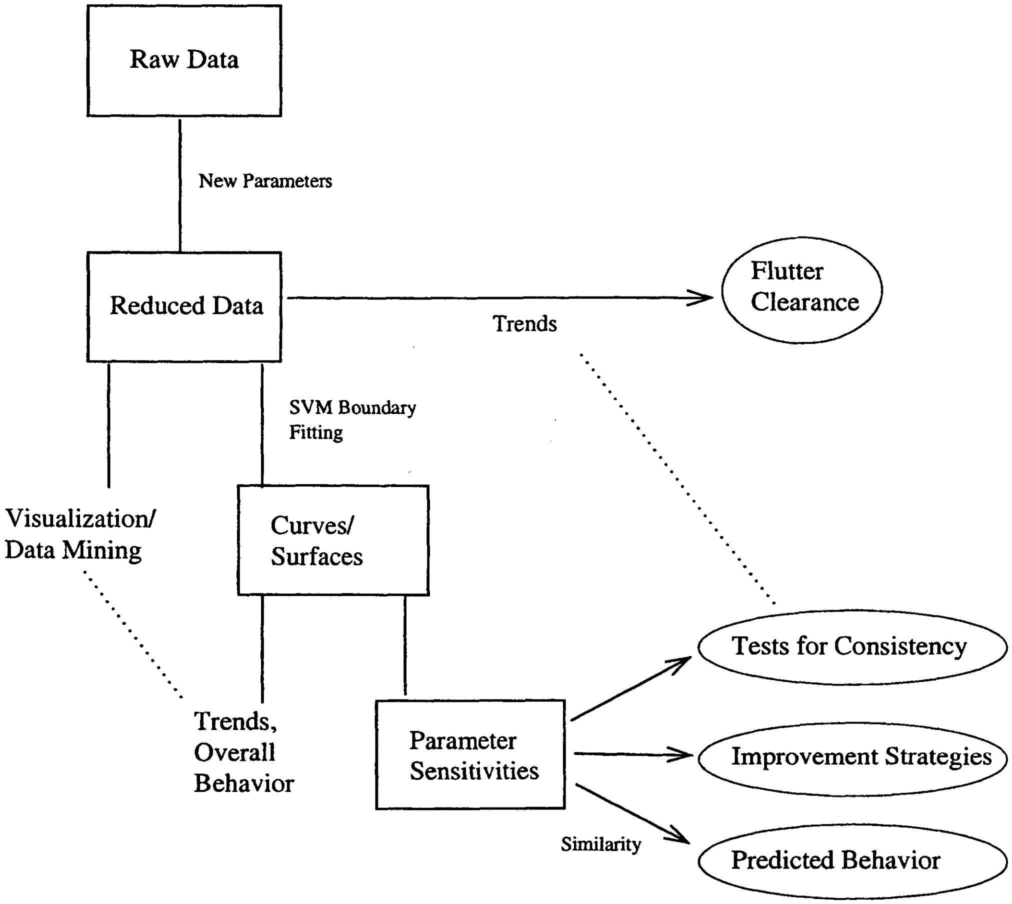

Figure 5-1: Schematic of the data analysis process. This schematic addresses the reduction of measured steady-state operating conditions for a specific machine to characterize the flutter stability. For engine development, the goal is flutter clearance. However, by careful analysis, the data can be used to obtain the sensitivity of stall flutter to parameters.

5.1.1 Analysis Process

Figure 5-1 shows the overall data analysis process for a given machine and modeshape. The process begins with *raw data*, which are usually steady state measurements of the inlet conditions and the compressor performance, and an indication of whether or not the mode in question is in flutter. These raw data are reduced into a non-dimensional set of *reduced data.*

With the reduced data, perhaps with the aid of *trends* and sensitivities, one may be able to find the range of parameters for *flutter clearance* for a particular design. This is typically the goal of flutter testing during engine development.

However, one may also further explore the data, by *visualization*, or by abstracting the data into *curves and surfaces.* To address the problem of finding boundary curves from this sort of data, a novel reduction procedure using Support Vector Machines was used, as described later in this chapter and in Appendix C.

With the curves, the trends may be quantified to obtain the *parameter sensitivity* of the flutter boundary. These sensitivities can then be used for several purposes, including demonstrating consistency of the trends used in the flutter clearance process.

5.1.2 Range of Sampled Data

The measured data on the Volvo rig are spread across the performance map, as shown in Figure 5-2. The stable points, shown as $\times$, and the unstable points, shown as $\circ$, are intermingled in a cloud which occupies most of the lines (dashed) of constant corrected speed. The overlap between stable and unstable points is caused by variations in K^* and g/ρ^*. One must, therefore, remove the effects of K^* and g/ρ^* to separate the performance map into regions of stable and unstable operation.

In principle, this is simple: restrict attention to a narrow range of K^* and g/ρ^*, and then determine the flutter boundary with this restricted set of data. In practice, however, there are not usually enough data points in such a "narrow" range to determine a flutter boundary.

To address this problem, we must choose the subset of points more carefully. In particular, we account for the effect of centrifugal stiffening, and we use the result, motivated in previous chapters, that increases in K^* and g/ρ^* are generally stabilizing. This leads to a rule for selecting subsets of data with distinct

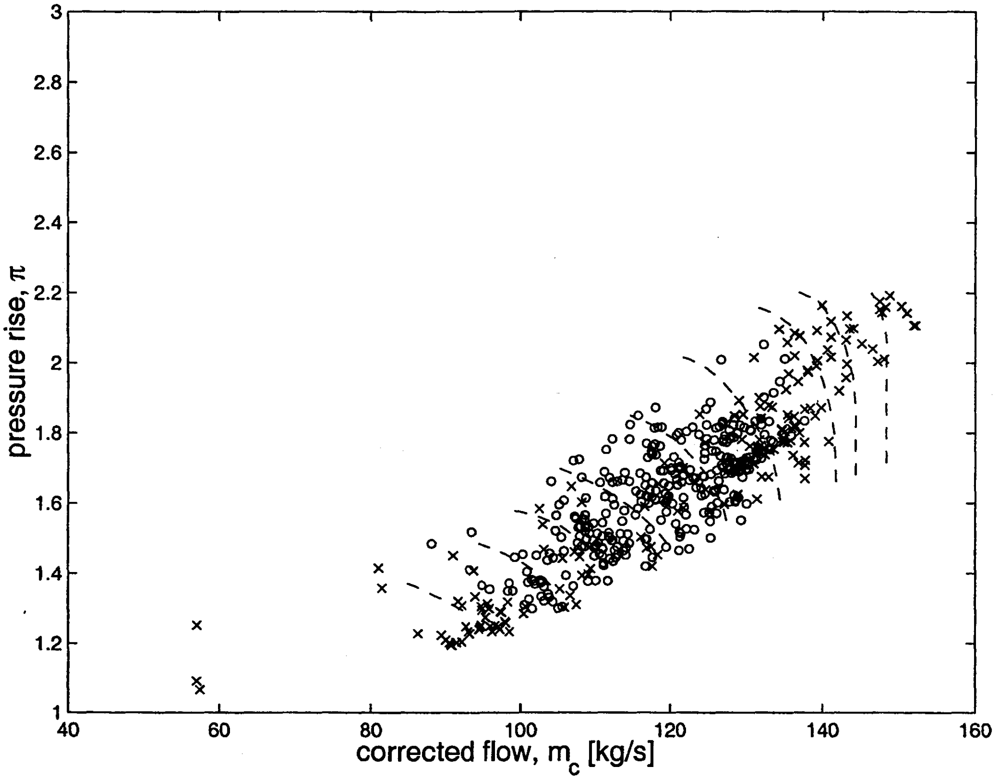

Figure 5-2: Measured data on the Performance Map. The stable points (×) and the unstable points (o) overlap due to variations in simulated flight condition.

Name	Symbol
inlet temperature	T_{in}
inlet pressure	p_{in}
inlet density	ρ_{in}
rotor speed	N
mass flow rate	$\dot{m}$
exit pressure	p_{out}
vibrational frequency	ω_0
stress level	σ_b

Table 5.1: Raw variables measured in engine tests.

stable and unstable regions on the performance map, while retaining enough data in the subset to estimate the boundary between regions.

The problem of estimating the flutter boundary, even with sufficient data of this form, is challenging. Standard regression techniques, such as a least-squares fit, are geared towards finding a curve which passes through a set of points. In this case, we need the curve which *separates* the stable points from the unstable points, rather than one which passes through the points. A new, generic method for this type of problem was developed. This method is based upon the theory of Support Vector Machines (Vapnik, 1995).

In the remainder of this chapter, the aforementioned steps are described more specifically. First, the reduction of the raw data is described. Second, the effects of centrifugal stiffening are assessed. Third, the rule is developed for extracting distinct stable and unstable regions on the performance map, followed by a discussion of how to interpret the boundary between regions. Finally, the aforementioned boundary fitting technique is discussed.

5.2 Reduction of Raw Data

The raw data available from the steady state experimental measurements are listed in Table 5.1. These include inlet temperature and pressure, rotor speed, mass flow rate, exit pressure, frequency of vibration and stress level.

Unfortunately, the mechanical damping is not among the measurements available. We, therefore, cannot determine the actual value for g/ρ^*. Instead, the mechanical damping of the machine is presumed constant during operation, and a *relative* value of g/ρ^* is used, referenced to the ambient condition.

Name	Symbol	Definition
Reduced damping, relative	$(g/\rho^*)_{\text{rel}}$	see eqn. (5.1)
Compressible reduced frequency	K^*	$\omega_0 c/\sqrt{\gamma RT}$
Centrifugal corrected K^*	K_0^*	see eqn. (5.6)
Corrected mass flow	$\dot{m}_c$	$\dot{m}(p/p_0)/\sqrt{T/T_0}$
Corrected speed	N_c	$N/\sqrt{T/T_0}$
Rotor Pressure Ratio	π	$p_{\text{out}}/p_{\text{in}}$
Tip relative Mach number	M	see eqn. (5.3)
Inlet flow angle	α	see eqn. (5.2)

Table 5.2: Similarity variables determined from measurements.

$$\left(\frac{g}{\rho^*}\right)_{\text{rel}} = \frac{g/\rho^*}{(g/\rho^*)_{\text{amb}}} = \frac{\rho^*_{\text{amb}}}{\rho^*} = \frac{\rho_{\text{amb}}}{\rho} \tag{5.1}$$

A value of 1 in $(g/\rho^*)_{\text{rel}}$, therefore, corresponds to the reduced damping under ambient conditions. Although four non-dimensional parameters are sufficient to represent the system, as shown in Chapter 2, various formulations of these four can be considered to focus upon one aspect or another. Table 5.2 lists some non-dimensional[1] system parameters which can be determined from the raw data.

If the duct area and the rotor radius are specified, then there is a direct relationship between the corrected quantities (corrected mass flow and corrected speed) and the inlet relative Mach number, M, and the inlet (relative) flow angle, α. Using the relation for 1-D compressible flow (Shapiro, 1953), a relationship can be made between the corrected mass flow and the axial Mach number, M_{ax}, as follows:

$$\dot{m}_c = \gamma M_{\text{ax}} \cdot \left(1 + \frac{\gamma - 1}{2} M_{\text{ax}}\right)^{-\frac{\gamma+1}{\gamma-1}} \left(\frac{A_d p_{\text{ref}}}{\sqrt{\gamma R T_{\text{ref}}}}\right)$$

where A_d is the duct area and "ref" indicates conditions at sea level standard atmosphere.

One can also relate the corrected speed to the tangential Mach number, M_{tan}.

$$M_{\text{tan}} = \frac{2\pi N_c r}{\sqrt{\gamma R T_{\text{ref}}}}$$

where, in this case, π represents the number, not the stage pressure ratio.

---

[1] Actually, corrected quantities such as corrected speed and corrected mass flow are a non-dimensional variable multiplied by a dimensional constant based on the definition of standard atmosphere

The blade relative Mach number and flow angle, then, are clearly defined in terms of the axial and tangential Mach number.

$$\tan\alpha = \frac{M_{\mathrm{tan}}}{M_{\mathrm{ax}}} - \tan\theta_{\mathrm{IGV}} \qquad (5.2)$$

$$M = \frac{M_{\mathrm{ax}}}{\cos\alpha} \qquad (5.3)$$

where θ_{IGV} is the inlet guide vane (IGV) exit angle. In the case that the inlet flow is axial, $\theta_{\mathrm{IGV}} = 0$, as in the case in a front-stage fan with no inlet guide vanes, the formula for the relative Mach number simplifies to

$$\sqrt{M_{\mathrm{ax}}^2 + M_{\mathrm{tan}}^2}$$

Categorization of flutter points vs. stable points

There is an issue of categorizing the points as either *stable* points or *flutter* points. There are also points due to forced vibrations which are identified and eliminated from further consideration. This was done on the basis of the magnitude and frequency of the stress signals.

The magnitude of the stress signal was used to determine whether or not there were significant vibrations present. If the stress signals exceeded a cutoff of 1 MPa, they were considered significant. A histogram of the stress measurements is shown in Figure 5-3.

The frequency of the stress signal was used to determine whether a point of significant magnitude was a flutter point or whether it was a forced vibration. If the frequency was within 2% of the blade's rotating natural frequency, ω_0, (discussed in the next section), then it was considered a flutter point. Otherwise, it was considered a forced vibration and discarded from further consideration. Some points associated with an engine-order excitation were discarded by this criterion (see Figure 5-5).

The following table indicates the selection criteria:

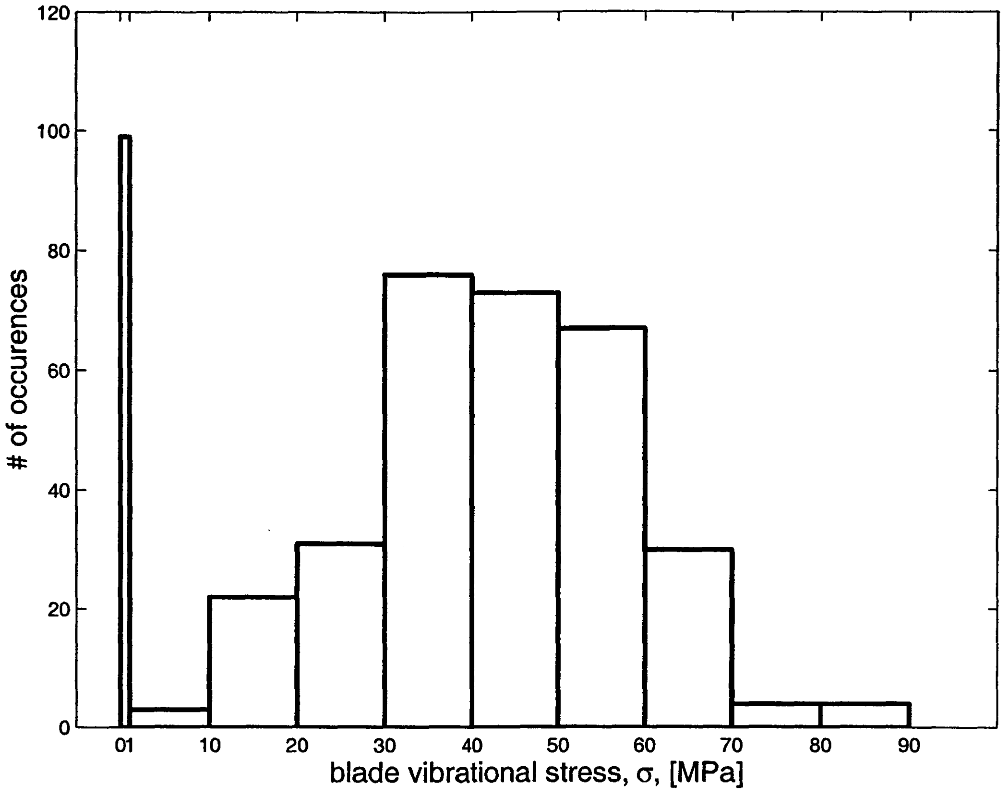

Figure 5-3: Histogram of Measured Stress Level. The stress (normalized by the maximum stress) is plotted on the x-axis. There is a peak at zero stress (corresponding to the "clear" points) and a broad peak at a finite stress level, corresponding to the measurements in flutter.

Stress > 1 MPa	Freq. within 2% of ω_0	Category
No	-	Stable
Yes	No	Discard
Yes	Yes	Flutter

5.3 Centrifugal Stiffening

When the rotor is spinning, the natural frequencies of the blades may increase for a given modeshape. This is called *centrifugal stiffening*, which occurs when the modeshape of vibration has a small radial component. As the blade mass moves radially, it changes in potential energy due to the action of the centrifugal forces. This is analogous to the case of a spring-loaded pendulum shown in Figure 5-4, in which a spring represents the elastic restoring forces, the gravitational acceleration is analogous to the centrifugal acceleration, and

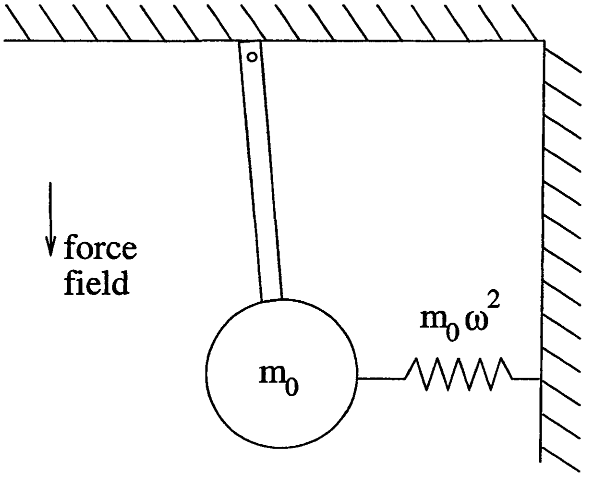

Figure 5-4: Idealized, suspended, mass-spring system. A gravitational, force field, g, can increase the natural frequency. Similarly, a centrifugal force field can stiffen a flexibly supported rotating mass.

the rigid-body pivoting of the pendulum is analogous to the modeshape of the blade. In the case of a spring-loaded pendulum, the effect of the gravitational acceleration increases the natural frequency, just as the centrifugal effects increase the natural frequency of a rotor blade.

The effects of centrifugal stiffening upon the blade frequency can be seen on the *Campbell diagram*, which is shown in Figure 5-5. Here, the rotor speed is plotted on the x-axis, and the frequency of vibration is plotted on the y-axis. The resonant points follow an upward sloping curve shown by the dashed line. The dotted lines correspond to the engine orders (i.e. the multiples of the rotor speed). Forced vibrations typically occur along these lines, and the corresponding points were eliminated from the analysis.

The dashed line is fit to a model which follows the spring-loaded pendulum analogy. This leads to the following form for the frequency:

$$\omega_0 = \left(\omega_{\text{rest}}^2 + sN_{\text{raw}}^2\right)^{\frac{1}{2}} \tag{5.4}$$

where ω_{rest} is the frequency (at rest) without rotational effects, N_{raw} is the (uncorrected) rotor speed, and s is an empirical coefficient, the *Southwell* coefficient, which is modeshape dependent. For the case of the present rotor, $s = 0.5$.

Since the frequency, ω_0, is speed-dependent, it is difficult to experimentally survey the performance map at a constant compressible reduced frequency, K^*, since the inlet temperature must be adjusted as a

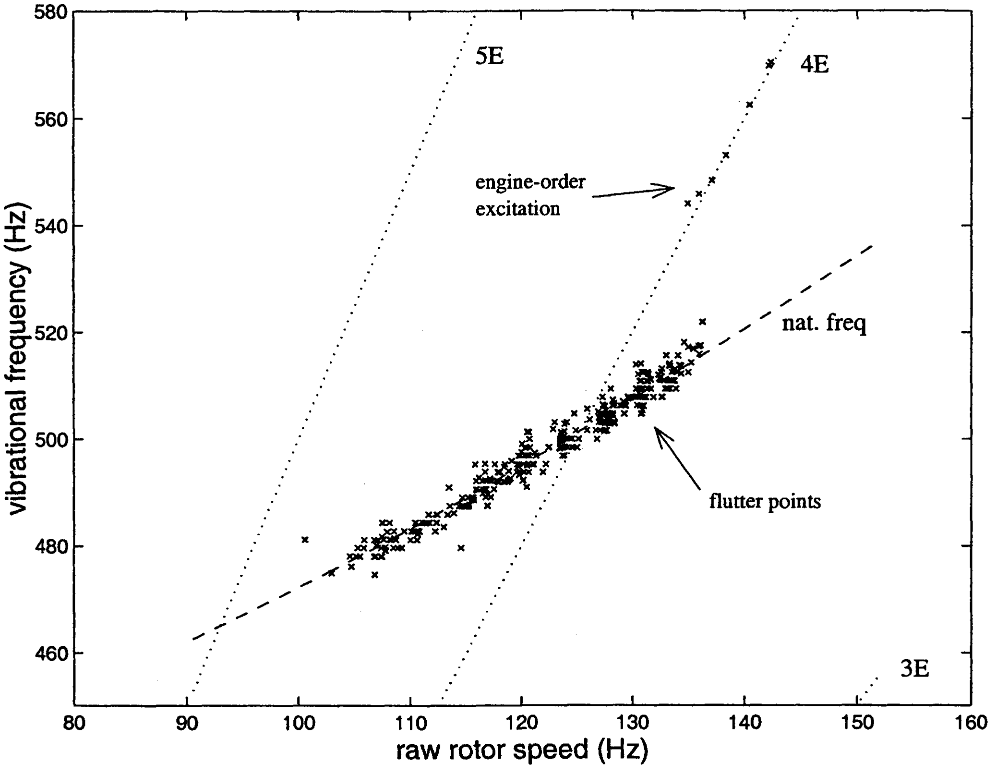

Figure 5-5: Campbell diagram of full-scale engine test data. The x-axis is the wheel speed, and the y-axis is the measured vibrational frequency. Dotted lines indicate engine orders (i.e. multiples of the wheel speed). The blade natural frequency, which is excited due to flutter, has a speed sensitivity due to centrifugal stiffening effects. The dashed line is a fit to the natural frequency, using a *Southwell* coefficient of 0.5.

function of rotor speed to maintain a constant K^*. In the present data, the surveys were taken at constant inlet temperature and pressure, rather than scheduling these quantities to maintain constant K^*.

Recall, however, that the construction of the K^* parameter was based upon separating the flight condition effects from the performance map *for constant structural quantities.* In the present case, the natural frequency is not constant, but changes with speed. We can, however, extend the separation of flight condition from performance to this case in which the frequency shifts according to (5.4). Substituting the frequency dependence from (5.4) into the definition of the compressible reduced frequency, we find

$$K^* = \left((K_0^*)^2 + \frac{sc^2}{\sqrt{\gamma R T_{\text{ref}}}} N_c^2 \right)^{\frac{1}{2}}. \tag{5.5}$$

where K_0^* is

$$K_0^* = \frac{\omega_{\text{rest}} c}{\sqrt{\gamma R T}}. \tag{5.6}$$

Therefore, the compressible reduced frequency, K^*, can be separated into a speed-independent part, K_0^*, and a part dependent upon the corrected speed, N_c. The coefficient of the N_c term in (5.5) is a constant depending upon modeshape (through the Southwell coefficient), and the chord.

Since ω_{rest} is constant for a given machine, and K_0^*, is the speed-independent portion of the compressible reduced frequency, replacing K^* with K_0^* leads to the desired separation of the performance map from the flight conditions in the case of centrifugal stiffening (see Appendix B). Furthermore, the manner in which the data are sampled (i.e. surveys at specified flight conditions), clusters the sampled data in small bands of K_0^* and $(g/\rho^*)_{\text{rel}}$. Figure 5-6 shows how data are clustered in small ranges of K_0^* and $(g/\rho^*)_{\text{rel}}$. A similar, small range using K^* instead of K_0^* would have considerably fewer points.

5.4 Rule for Selecting Data Subsets

Within each cluster on the $(K_0^*, (g/\rho^*)_{\text{rel}})$ map, the points are taken across a broad range on the performance map. This contrasts to the situation of the multimission engine discussed in Chapter 3 in which the data were sampled near a particular location on the performance map. Thus, the flutter boundaries can not yet

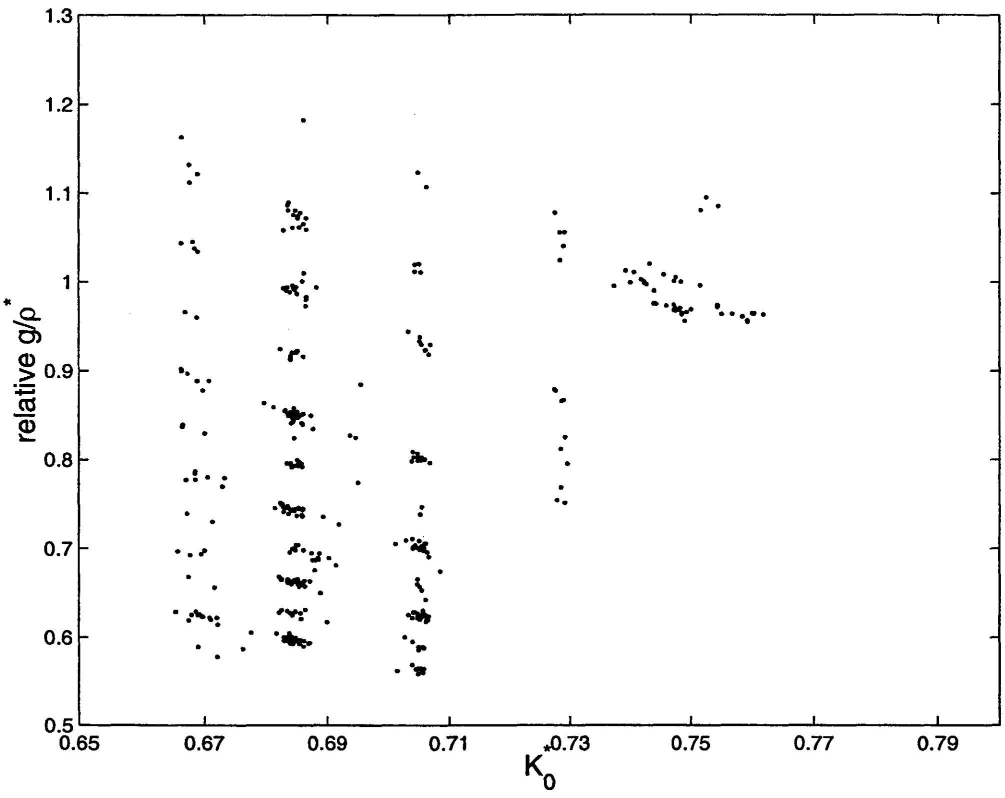

Figure 5-6: Data spread on (K_0^*, $(g/\rho^*)_{\mathrm{rel}}$) map. Clusters of data are available at specific intersections.

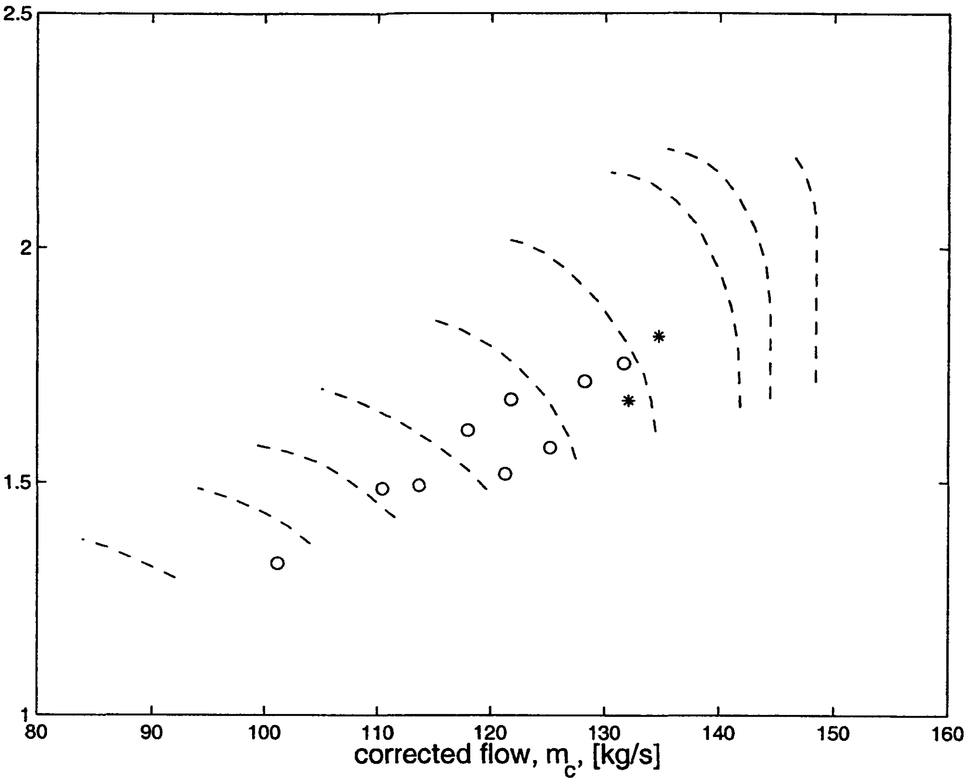

Figure 5-7: Flutter data for a specific (K_0^*,$(g/\rho^*)_{\text{rel}}$) cluster in which $0.68 < K_0^* < 0.69$ and $0.74 < g/\rho^* < 0.75$. A ∘ represents a flutter point, and a $*$ represents a clear point. Without further information, the data do not well define the flutter boundary.

be directly drawn on the (K_0^*, $(g/\rho^*)_{\text{rel}}$) map, without accounting for this variation in performance point.

To do this, we estimate the flutter boundary on the performance map, for each (K_0^*, $(g/\rho^*)_{\text{rel}}$) pair in question. Unfortunately, the clusters of Figure 5-6 do not always fully specify the flutter boundary. An example of this case is in Figure 5-7, which shows the data corresponding to a specific cluster, plotted on the performance map.

An experienced practitioner may be able to interpret such data, by using the right assumptions. For example, by knowing that the instability is stall flutter, one can ensure that the instability region encompasses the upper part of the speedlines. The assumption (e.g. that of stall flutter) could be justified by global trends, or perhaps by a computational analysis. Furthermore, the extent of the flutter region might be estimated using stable points from nearby clusters, leading to an "eyeball fit" of the flutter boundary. Such an ad hoc technique can be a positive step beyond the raw data, making it possible to assess the flutter boundary using "engineering judgement."

Unfortunately, this technique is not sufficient for our analysis, since we would like to quantify trends in the flutter boundary. Such a quantification requires an unbiased estimate of the boundary location. To accomplish this, we apply the following:

- Increasing reduced damping, g/ρ^*, has a stabilizing effect upon flutter stability
- Increasing compressible reduced frequency, K^*, has a stabilizing effect upon flutter stability

These two concepts were discussed in Chapter 3. In terms of applying these to selecting a subset, we can augment the data from a particular (K_0^*, $(g/\rho^*)_{\text{rel}}$) box (see Figure 5-8) with corners at (x_{min},y_{min}) and (x_{max},y_{max}), using the following rules:

1. Unstable points with a K_0^* greater than x_{max} and a $(g/\rho^*)_{\text{rel}}$ greater than y_{max} can be included.
2. Stable points with a K_0^* less than x_{min} and a $(g/\rho^*)_{\text{rel}}$ less than y_{min} can be included.

These conditions are schematically shown in Figure 5-8. The logic is as follows: if both K_0^* and $(g/\rho^*)_{\text{rel}}$ are greater than the values in the box, then according to the assumptions, the machine should be more stable in this region than in the box. Therefore, an unstable point in this region should be unstable in the box as well. Conversely, if both K_0^* and $(g/\rho^*)_{\text{rel}}$ are less than the values in the box, then the machine should be less stable than in the box. Thus, stable points in this region should also be stable in the box.

Applying these conditions leads to a technique of selecting enough data in a subset to estimate the flutter boundary. In Figure 5-9, the subset of data shown in Figure 5-7 is augmented sufficently to delineate the stable and unstable regions. The technique for fitting the boundary between regions, shown as a solid curve, with such data is non-standard, however, and the approach developed to estimate this curve is described in the next section.

5.5 Fitting the Stability Boundary using Sampled Data

The boundary curve in Figure 5-9 divides the performance map into stable and unstable regions. The procedure which governs the construction of this curve is derived in Appendix C. Here, only the main principles are described.

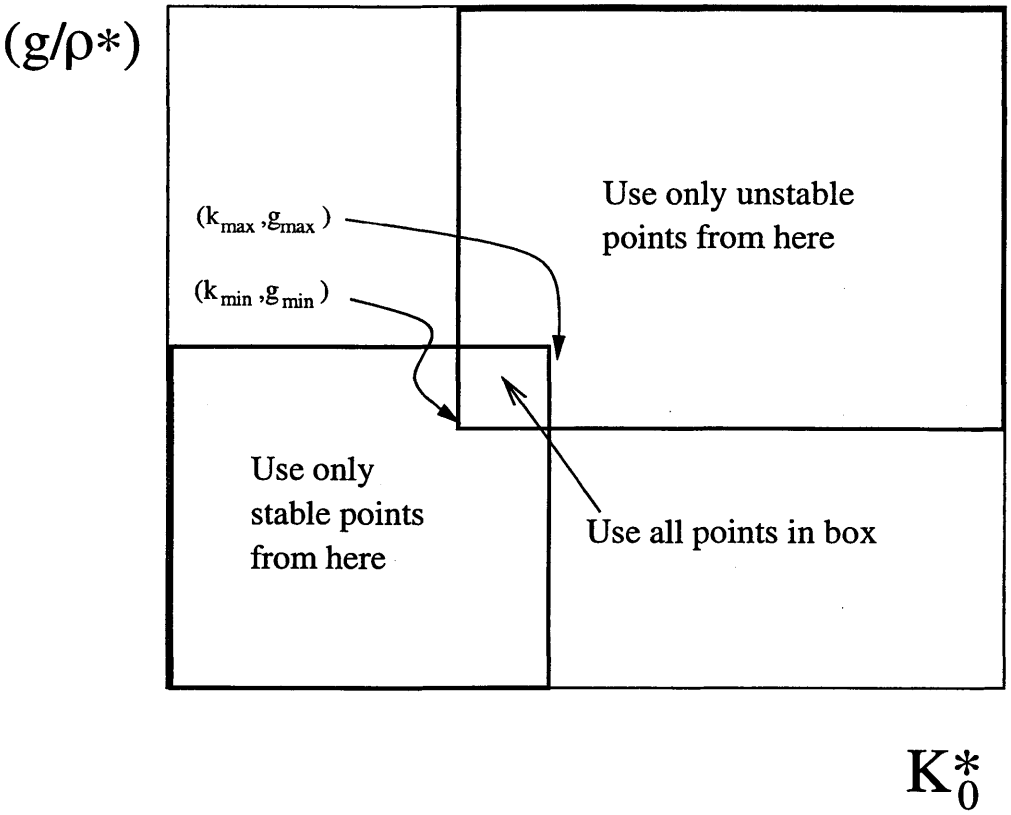

Figure 5-8: Schematic of rules for selecting data on K_0^*, (g/ρ^*) map. Based upon the trends with K_0^* and g/ρ^* previously specified, measured data of the designated type outside the box specified by $(k_{\min}, g_{\min})$ and $(k_{\max}, g_{\max})$ are assumed to be relevant within the box as well.

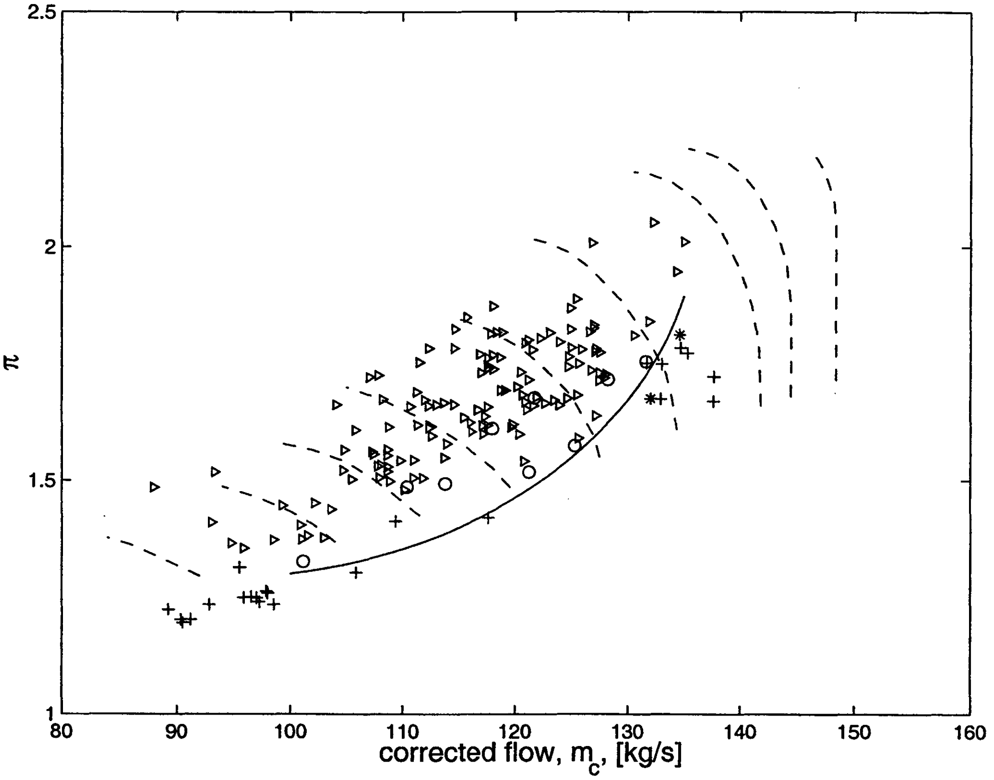

Figure 5-9: Use of "assumed data" in boundary fits. Here the stability boundary is fit to the data on the performance map for a specific $(K_0^*, g/\rho^*)$ pair ($0.68 < K_0^* < 0.69$ and $0.74 < g/\rho^* < 0.75$). A $\circ$ is a point in flutter, and a $*$ shows the clear point, inside the above specified ranges. The $+$ locations are stable measurements taken at a lower K_0^* and g/ρ^* than the range, and the $\triangleright$ points are taken from unstable measurements at a higher K_0^* and g/ρ^*. The $+$'s and the $\triangleright$'s are assumed to apply in the box of $(K_0^*, g/\rho^*)$ under consideration according to the principle depicted in Figure 5-8. A flutter boundary is estimated from the data using the technique described in the text.

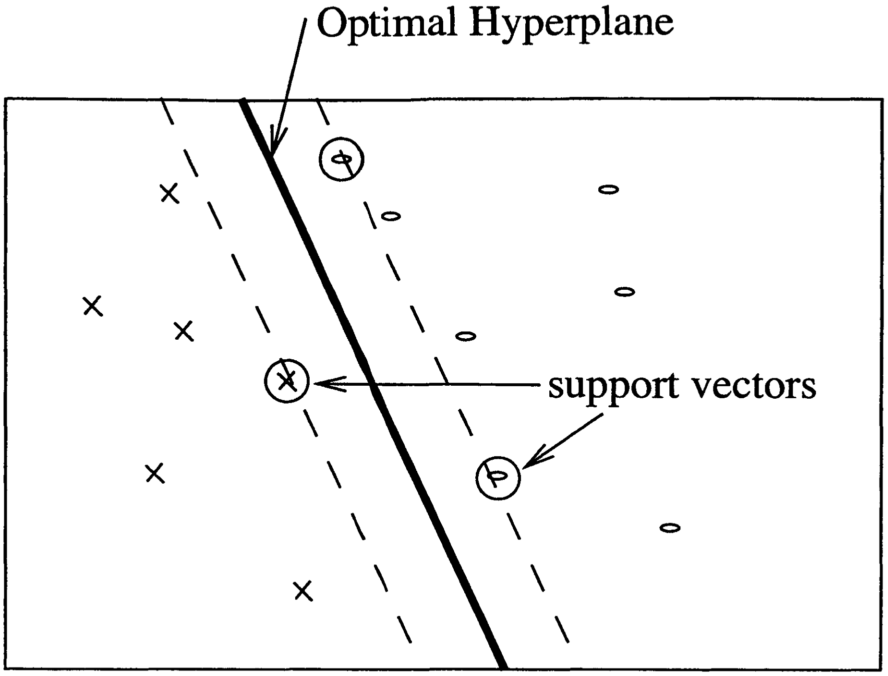

Figure 5-10: Diagram of the optimal separating hyperplane between two groups of data, represented by the ×s and ovals, respectively. The separating hyperplane, a line in this 2D case, maximizes its distance from *both* groups of points. In this sense, it is optimally "between" these groups. The dashed lines, parallel to the optimal line, are supported by data of each group. The points in each group which touch the dashed lines (between which the optimal curve is equidistant) are called "support vectors."

As mentioned earlier, the problem of drawing the boundary is more akin to classification than to regression (curve-fitting). By classification, we mean to separate the space, the performance map in this case, into regions. Our approach is based upon the use of Support Vector Machines (SVM) developed by Vapnik (1995). The SVM algorithm finds the "optimal" separating hyperplane between two groups of points, shown in Figure 5-10 as a solid line. Optimality is defined in terms of maximizing the normal distance from the hyperplane to the data. The dashed lines, which are "butted" against the data (mathematically speaking, ***supported***) on either side, have a maximal distance between them in the optimal case. The points which touch the dashed lines (i.e. support them), are called "support vectors" which gives rise the name "Support Vector Machine."

Unfortunately, not every group of data can be separated by a hyperplane. In these cases, we use the technique of Cortes and Vapnik (1995) in which points which fall on the wrong side of the boundary are penalized in the optimization. This is described more fully in Appendix C.

Using this principle of finding the optimal separating hyperplane makes it relatively straightforward

$$\begin{tikzcd}
\begin{matrix}\text{Reduced Data}\\ (\mathrm{M}, \alpha, \mathrm{K}^*)\end{matrix} \arrow[r] \arrow[d, "\psi"] & \begin{matrix}\text{Non-linear Boundary}\\ \text{Surface}\\ (\mathrm{M}, \alpha, \mathrm{K}^*)\end{matrix} \\
\begin{matrix}\text{Model}\\ \text{Space}\end{matrix} \arrow[r, "\text{SVM}"] & \begin{matrix}\text{Linear Boundary}\\ \text{in Model Space}\end{matrix} \arrow[u, "\psi^{-1}"']
\end{tikzcd}$$

Figure 5-11: Commutation diagram for non-linear extension to SVM fit. The optimal hyperplane procedure can be extended to perform non-linear boundary fits by putting the original data through an invertible map, Ψ, then finding a linear hyperplane, and finally then transforming through the inverse map, Ψ^{-1}. The non-linear boundary shape is Ψ^{-1} composed with the hyperplane.

to see how a linear boundary might be found. However, the flutter boundary (for example, the one in Figure 5-9) is not a line, but curved.

To generate non-linear boundaries, we send the data through a transformation, Ψ, into a new space, then find a linear boundary in this space, and finally put the boundary through the inverse transform, Ψ^{-1}. If Ψ is non-linear, then a curved boundary may be obtained. This procedure is summarized in the *commutation diagram* of Figure 5-11.

The selection of a particular Ψ determines the class of functions from which the boundary may be expressed. For the current purposes, a polynomial fit was used of the following form:

$$\alpha \cdot \Psi(x, y) = \alpha_1 x^3 + \alpha_2 x^2 + \alpha_3 x + \alpha_4 xy + \alpha_5 y^3 + \alpha_6 y^2 + \alpha_7 y + \alpha_8 \tag{5.7}$$

where α is a 8-dimensional vector. In this case, Ψ transforms the vector space from the 2-dimensional space of (x,y) to the 8-dimensional space of α. For boundaries on the performance map, the transformation Φ operates upon the corrected mass flow, $\dot{m}_c$ and the pressure rise, π, in which case the (x, y) of equation (5.7) are replaced by $\dot{m}_c$, and π. Variations on this form for Ψ, using different polynomial terms for example, did not measureably change the fitted boundaries.

Note that although the expression (5.7) is non-linear in x and y it is linear in α. The boundary is a hyperplane in the 8-dimensional space of α, which satisfies the equation, $\alpha \cdot \Psi = 0$. The SVM algorithm determines the α, which specifies a hyperplane in α-space but specifies a curve in (x, y) coordinates.

5.5.1 Error Estimates

The dashed lines on Figure 5-10 represent the range over which the optimal line can be moved and still separate the data. This range can be used to assess the error in how well the boundary, from a given function class, fits the data.

The error range for the data from Figure 5-9 is shown in Figure 5-12 as dashed curves surrounding the "optimal" boundary. In this case, there are data points within the range of uncertainty, unlike the schematic of Figure 5-10 in which no data lie between the dashed lines. If the data can not be perfectly separated with a curve from the function class specified by Ψ, then the dashed curves are pushed apart. The misclassified data are a result of a mismatch between the function class specified by Ψ and the data.

In general, the "assumed data" appear to be consistent with the assumptions. The assumed unstable data, $\triangleright$, tend to be at higher pressure ratios than the unstable data in the "box" of Figure 5-9, and the assumed stable data, $+$, occurs at lower pressure ratios. To assess the validity of the assumptions in the present case of the Volvo data, one can look at the cases of "misfit" data. That is, assumed points which wind up on the wrong side of the flutter boundary. The occurrence and the specifics of such cases show that the data is consistent with the assumption. In fact, such misfit points are rare, with only 5 such cases out of 1387 assumed points in all of the boundaries analyzed.

One misfit point is shown on Figure 5-12, a stable point near $\dot{m}_c = 110$, lying above the upper dashed line. Since the data are sparse in this region, it is concievable that the boundary curve could be drawn around this point. However, this requires a boundary with considerably higher order terms than the one specified by (5.7), since small modifications to (5.7) which keep it roughly the same order do not significantly affect the boundary. The data are sparse around this particular point, so the boundary shape is not definitive. In particular, there are no contrary (i.e. unstable) points between the misfit point and the fitted boundary. All five of the misfit cases have this same property, and could be higher-order effects rather than exceptions to the assumption. Without further information, it is not possible to confirm this, however.

The fitted boundary curve appears to be a reasonable approximation to the flutter boundary. This behavior holds generically for subsets of the data, corresponding to a specific (K_0^*, $(g/\rho^*)_{\text{rel}}$) box. For a detailed look at other subsets see the raw fits in Appendix D.

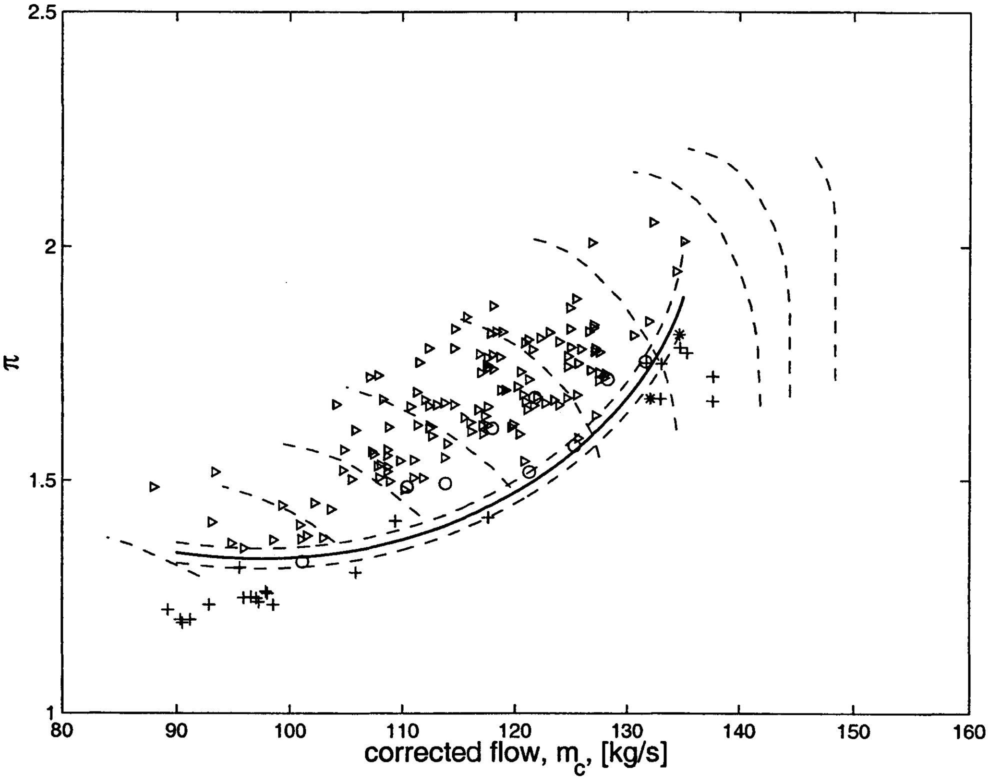

Figure 5-12: Range of uncertainty in boundary fits. The stability boundary of Figure 5-9 is shown with dashed curves indicating the uncertainty of the fit. A ∘ is a point in flutter, and a $*$ shows the clear point, inside the above specified ranges. The + locations are stable measurements taken at a lower K_0^* and g/ρ^*, and the ▹ points are taken from unstable measurements at a higher K_0^* and g/ρ^*.

5.6 Summary

A technique for analyzing raw data from scaled flutter tests is described in the context of the measured data from a Volvo test rig. It is presumed, as in the case of the Volvo rig, that only steady-state data is available, with the flutter measurements limited to a frequency measurement and the stress level. The stress level leads to a binary classification into stable and unstable points, depending upon whether the stress is below or above a given (low) threshhold.

Centrifugal stiffening, which causes a dependency of the blade frequency upon the rotor speed is discussed. The blade frequency is characterized in terms of a fundamental frequency and a Southwell coefficient, which is useful in assessing the appropriate frequency for stable points which did not exhibit vibrations. For this case of centrifugal stiffening, the K_0^* parameter, which is a generalization of K^*, is used.

Since the data spanned all four non-dimensional parameters, data sparcity was a major issue. To address this, a procedure was developed for selecting data relevant to a particular $(K_0^*, g/\rho^*)$ location based upon the trend that K_0^* and g/ρ^* are stabilizing.

Furthermore, a novel boundary-fitting procedure was introduced, based upon Support Vector Machines (see Appendix C), which allowed for automatic determination of the stability boundary *between* the stable and unstable sampled data.

This analysis procedure was able to reliably, and automatically generate flutter stability boundaries from the raw data.

Chapter 6

Results of Experimental Data Analysis

This chapter is focused upon describing the results of analyzing full-scale engine test data for aeroelastic stability of a shrouded fan in a second bending mode. As mentioned in the previous chapter, data which include variations in simulated flight condition were available from testing conducted at the Volvo Corp. In general, the behavior was found to be consistent with the trends outlined in the introduction and further discussed in Chapter 3.

Flutter boundaries were estimated on the performance map, corresponding to "analysis boxes" on the $(K_0^*, g/\rho^*)$ map, using the procedure described in the previous chapter. The corresponding analysis boxes are shown in Figure 6-1. These boxes in Figure 6-1, which are used in this chapter, all meet the criterion that the boundary points (i.e. the points near the boundary which determine its shape) have a median K_0^* and g/ρ^* which falls inside the box. If there are too few data in the box, then the appropriate $(K_0^*, g/\rho^*)$ location corresponding to the resulting boundary is ambiguous, since the boundary shape is primarily determined by data outside the initial analysis box. A comparison of the raw data to the fitted boundaries for each box used in the current analysis, including boundary uncertainty estimates are given in Appendix D. Here, we focus upon the parametric dependencies of the fitted boundaries.

The $(K_0^*, g/\rho^*)$ locations of the boxes in Figure 6-1 make it possible to investigate three types of trends:

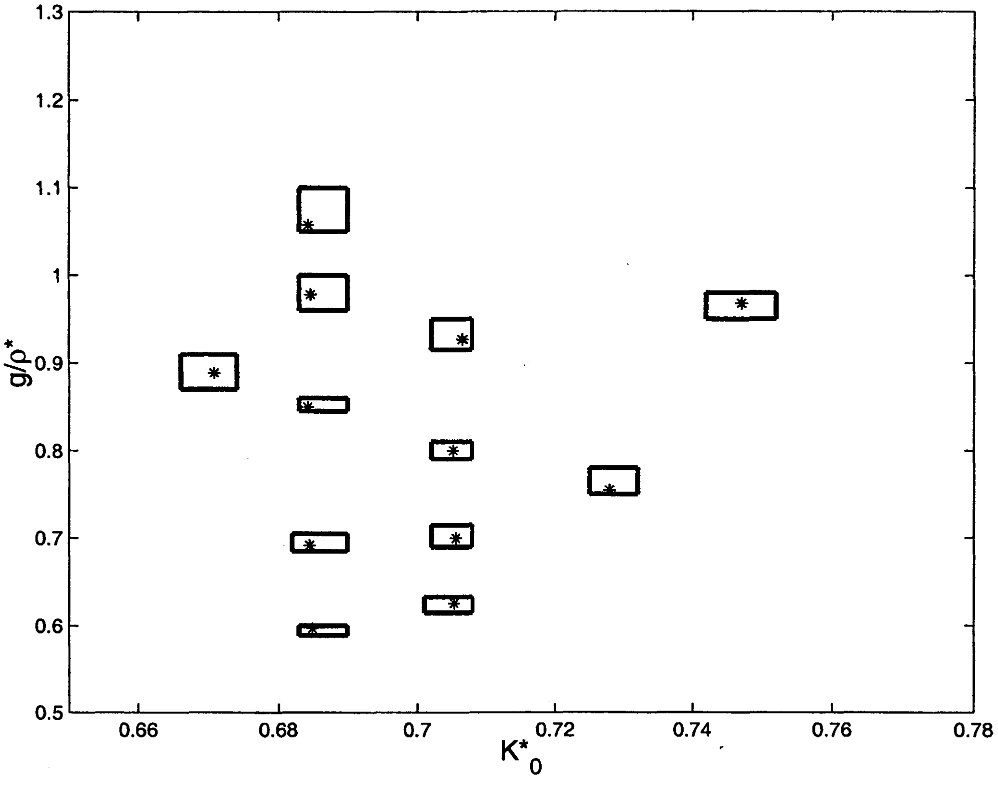

Figure 6-1: Boxes on the $(K_0^*, g/\rho^*)$ map for analysis of the full-scale engine data presented in this chapter. A flutter boundary for each of these locations was estimated using the procedure of Chapter 5. A comparison of the boundaries with the raw data are located in Appendix D. In each case, the median of the points adjacent to the boundary was located inside the box, as shown by the $*$s.

variations of K_0^* at constant g/ρ^*, variations of g/ρ^* at constant K_0^* (at two K_0^* locations), and variations, for the given configuration, at constant inlet pressure.

To quantify the trends, we consider the effects at a constant corrected speed, N_c. That is, we track the intersection of the flutter boundary and a speedline on the performance map. For any chosen corrected speed, this intersection occurs at a critical pressure ratio, π_{cr}, and a critical corrected mass flow, $(\dot{m}_c)_{\mathrm{cr}}$. Although the corrected mass flow and corrected speed, together, sufficiently specify the intersection, it is useful to track the critical pressure ratio as well, since this makes it easier to interpret requirements framed in terms of the pressure ratio.

The effects of changing the reduced damping, g/ρ^*, or the compressible reduced frequency, K_0^*, can be quantified in terms of the changes in the critical $\dot{m}_c$, or the critical π. We estimate *sensitivities*, or partial derivatives, of the critical $\dot{m}_c$ and critical π with respect to g/ρ^* and K_0^*.

Viewing the boundary on the $(K_0^*, g/\rho^*)$ map corresponding to a specific location on the performance map, is particularly insightful for flutter clearance purposes since this can be directly interpreted in terms of the flight conditions. We estimate these boundaries through an "inversion" procedure which uses the fitted boundaries on the performance map.

6.1 Trends in Flutter Stability

In previous chapters, the stabilizing trend of increasing the reduced damping, g/ρ^*, or of increasing the compressible reduced frequency, K_0^*, was discussed. In this section, we wish to look at the overall parametric trends in terms of the measured data, preceeding the more detailed investigation in following sections.

The general shape of the boundary is shown in the example of Figure 5-9, and is consistent with a subsonic/transonic stall flutter classification. That is, the flutter region occurs at part-speed, on the upper part of the speedlines. The current rotor has a relatively broader region of flutter, relative to the case of the historic, multimission engine of Figure 3-16. In each case, the region above the boundary (i.e. for higher pressure ratio) is the unstable region, and below the boundary is stble.

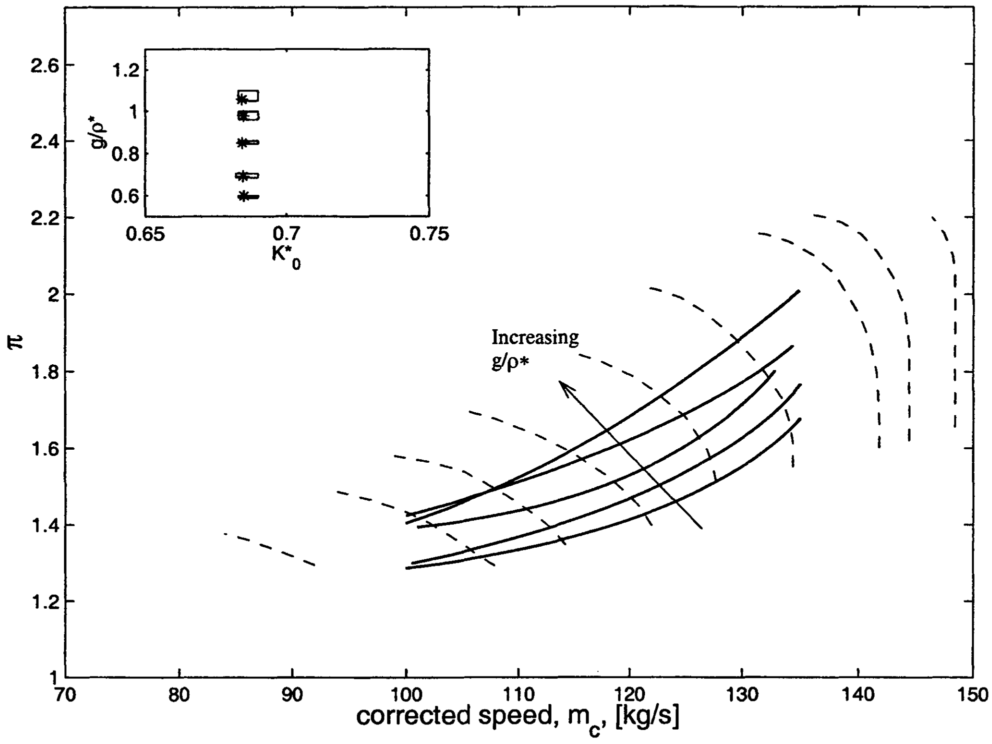

Figure 6-2: Shown here, on the performance map, are a family of boundaries with $K_0^* = 0.685$, and varying g/ρ^*. Each boundary corresponds to one of the analysis boxes of the inset plot; the $*$ indicates the median location of points adjacent to the boundary. The topmost boundary (highest π) corresponds to the topmost box (highest g/ρ^*), and so on. The trend for decreasing g/ρ^*, at constant K^* is for the flutter region to become larger and for the boundary to shift down to lower values of π.

6.1.1 Trends with varying reduced damping

To determine the qualitative effect of varying g/ρ^*, we compare the boundaries from a series of boxes in which the compressible reduced frequency, K_0^*, is held constant and the reduced damping, g/ρ^*, is varied. This is depicted in Figures 6-2 and 6-3, for two different cases of K_0^*, 0.685 and 0.705, respectively. For the sake of clarity, only the boundaries are shown; the uncertainty estimates are shown, along with the raw data, on the individual boundary plots in Appendix D. Each boundary separates the flutter region (above the boundary) from the non-flutter region (below the boundary).

The trend in the flutter boundary with increasing g/ρ^* is, as expected, to stabilize the flutter boundary, and to move the flutter region away from the region of operation. The crossing of boundaries in Figure 6-2 in the region between $\dot{m}_c = 100$ and $\dot{m}_c = 110$ falls within the uncertainty of those boundaries.

The movement corresponding to shifting the value of g/ρ^* from 0.6 to 1 is striking since it moves the

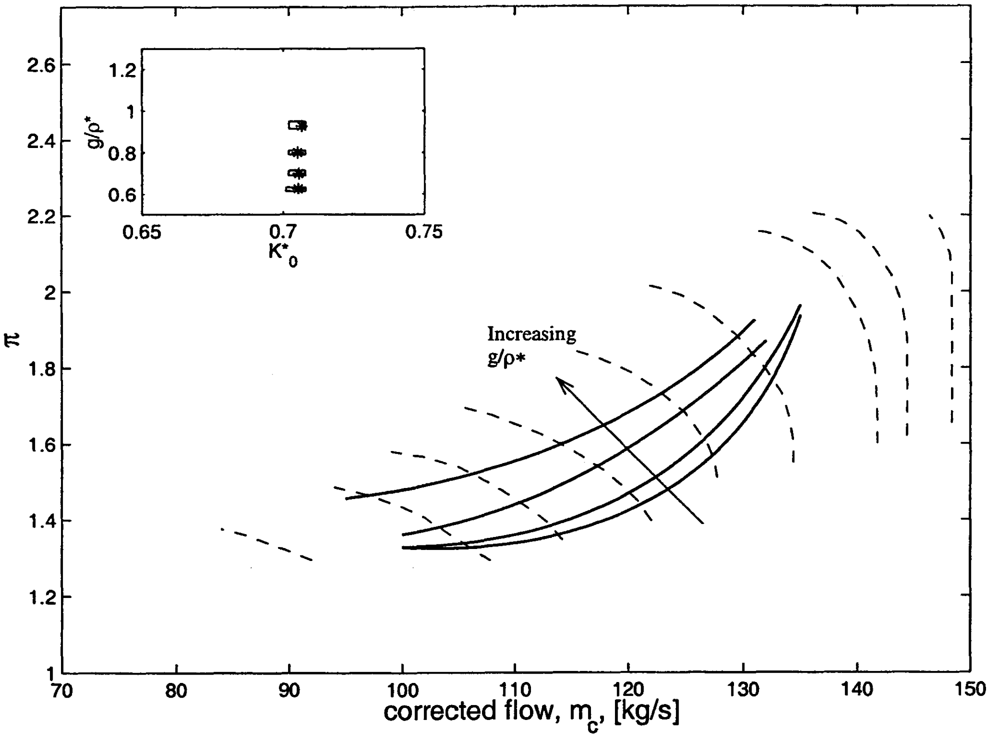

Figure 6-3: Shown here, on the performance map, are a family of boundaries with $K_0^* = 0.705$, and varying g/ρ^*. This has a similar trend to the case of $K_0^* = 0.685$ of Figure 6-2 in that decreasing g/ρ^* is destabilizing. However, these boundaries are, on the whole, more stable than those of Figure 6-2 due to the higher value of compressible reduced frequency, K_0^*.

boundary nearly halfway up the range tested on a particular speedline. For example, on Figure 6-2 at 83% corrected speed, a change in the reduced damping from $(g/\rho^*)_{\text{rel}} = 0.6$ to $(g/\rho^*)_{\text{rel}} = 1$ leads to an increase in the pressure ratio at the boundary of 15%.

The trends with g/ρ^* are similar for the two values of K_0^* of Figures 6-2 and 6-3. However, the case of $K_0^* = 0.70$ is generally more stable, particularly for higher corrected speeds (dashed lines are constant N_c). More subtle relationships can be assessed by looking at the intersection of the corrected speed lines with the flutter boundaries. This approach is taken up in later sections.

6.1.2 Trends of varying compressible reduced frequency

Some sense of the stabilizing effect of increasing K_0^* can be gained from comparing the boundaries in Figures 6-2 and 6-3. This is shown more explicitly, for the case of $g/\rho^* \approx 1$, in Figure 6-4, which spans a larger variation in K_0^* from 0.68 to 0.75. The overall trend of increasing the compressible reduced frequency, K_0^*, is towards a more stable boundary, as expected. The boundaries shown in Figure 6-4, are at a relatively high $g/\rho^* \approx 1$, and are more stable than those boundaries near $g/\rho^* = 0.6$ in Figures 6-2 and 6-3.

One point to note is that on Figure 6-4, the stabilizing effect of increasing K_0^* is prominent at lower corrected speeds. At lower values of g/ρ^*, near 0.6, comparing between Figures 6-2 and 6-3 shows little difference between the boundary curves at the two values of K_0^*. This indicates that the sensitivity of the flutter boundary to K_0^* can be dependent upon the value of g/ρ^* and N_c. This is investigated more fully in later sections, by focusing upon the intersections between the flutter boundary and the (dashed) corrected speed lines.

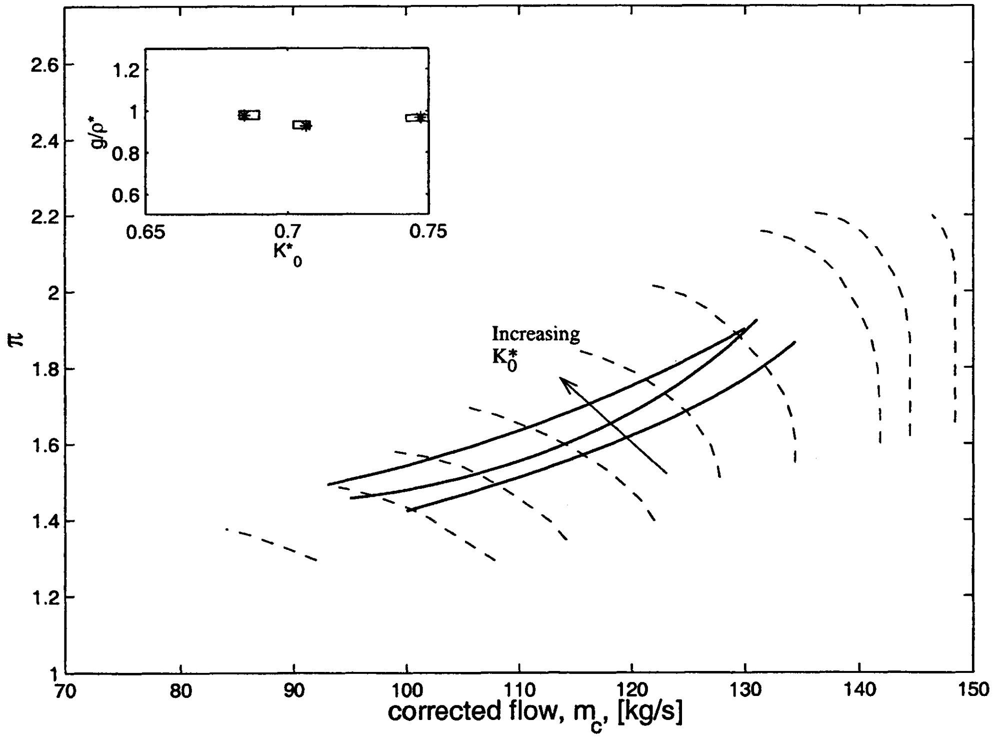

Figure 6-4: A family of flutter boundaries are plotted on the performance map, for $g/\rho^* \approx 1$, with each member having a different K_0^*, as shown in the inset figure. The uppermost boundary corresponds to a value of $K_0^* = 0.75$, the middle boundary corresponds to $K_0^* = 0.705$ and the lowest boundary corresponds to $K_0^* = 0.685$. The trend for decreasing K_0^*, is a reduction in stability, shifting the flutter boundary to lower pressure ratios, π.

6.2 Effect of Pressure

The analysis, up until now, has followed along the lines of considering the temperature and density as independent parameters, which contribute to the various non-dimensional groups discussed in Chapter 2. These non-dimensional groups can be expressed in terms of any selected primitive variables, and the temperature and density were selected for ease of derivation.

Using the ideal gas law to relate the pressure, temperature, and density, these similarity groups can be written explicitly in terms of the inlet pressure, if desired. For example, if one chooses temperature and pressure as primitive thermodynamic variables (leaving density as a dependent variable), then the compressible reduced frequency, K^*, remains unchanged, but the reduced damping becomes

$$g/\rho^* = \frac{g m_0 R T}{p c^3} \tag{6.1}$$

which comes from replacing ρ with RT/p in the definition of g/ρ^* for the case of 3-D blades. Thus, the effect of pressure (at constant temperature) can be interpreted in terms of its effects upon g/ρ^*.

However, it is widely understood that the effects of flight condition, at constant corrected quantities, can be understood in terms of the change in inlet pressure. The pressure ratio is correlated with the corrected quantities, from which the exit pressure may be found if one knows the inlet pressure. Thus, in terms of performance, the corrected quantities and the inlet pressure are sufficient to assess the performance.

One might think that, by analogy, the aeroelastic effects can also be summarized solely (or at least primarily) in terms of the inlet pressure. We study this possibility in the context of the measured data.

6.2.1 Static Deformations

An assumption used to derive the similarity parameters was that the flowpath geometry was nominally constant. This assumption may not hold if the changes in inlet pressure deform the blade angles and thereby influence flutter stability. This pressure effect was first proposed by Jeffers and Meece (1975) as a contributor to the pressure effects they observed, but has not been experimentally assessed in the literature. We show that such effects are negligible in the present case.

To investigate this possibility, we look for deviations in the performance correlations with inlet pressure. A given corrected speed, N_c, and corrected mass flow, $\dot{m}_c$, can be correlated with the pressure ratio, π, for a specific blade geometry. If the inlet pressure deforms the blades and significantly changes the blade angle, then the performance correlation (i.e. the pressure ratio) should change accordingly. Conversely, if the effect of the inlet pressure upon the performance correlation is negligible, then static deformations do not significantly alter the steady flow problem, and thus do not significantly affect flutter stability.

Figure 6-5 shows measured points, with varying inlet pressure, which correspond to the same corrected speeds as those used to measure the performance correlation (i.e. the dashed speedlines). The data appear to follow the speedlines fairly well, irrespective of pressure ratio. This is quantified more fully in Figure 6-6, in which the inlet pressure is plotted against the fractional deviations from the speedlines. There appears to be no obvious correlation between inlet pressure and deviations from the performance correlation. Furthermore, the fractional deviations are in the range of the measurement noise, and are considerably smaller than the effect of K_0^* and of g/ρ^* upon the flutter boundary. Therefore, in this case, the effect of static blade deformation cannot explain the effects of flight condition (i.e. K^* and g/ρ^*) upon flutter stability to any significant extent.

6.2.2 Effect of temperature at constant pressure

Increases in inlet pressure due to ram effects have corresponding increases in temperature and density, as shown in Figure 2-2. As mentioned earlier, for purposes of performance assessment, the inlet pressure alone summarizes the flight condition effects.

In the case of a typical low-speed aircraft, Figure 3-13 shows that the temperature and pressure effects are coupled. Clearly, if the thermodynamic state variables are coupled, then a single variable can be used to summarize the effects. This single variable can be either the temperature, the pressure, or the density; however, the pressure may be most convenient in this case.

For a high-speed aircraft (e.g. a supersonic fighter), however, the temperature and the pressure can independently vary, also shown in Figure 3-13. To assess whether the flight condition effects on flutter can be understood solely in terms of the pressure, we investigate whether, at a constant pressure, temperature

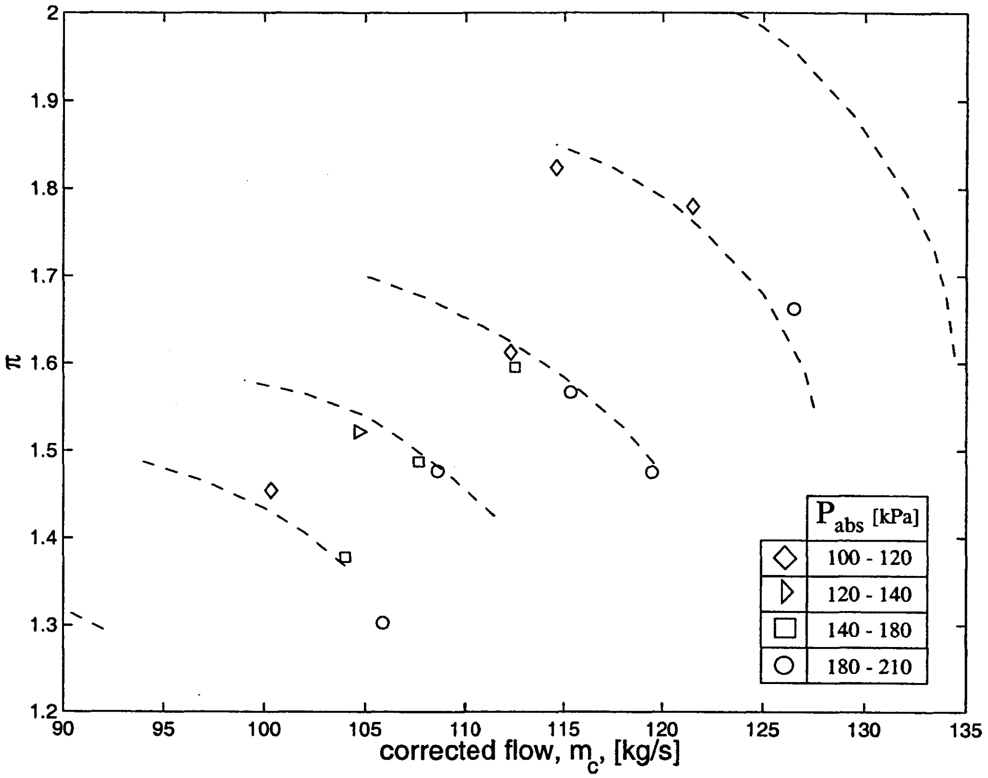

Figure 6-5: The performance correlation, taken at sea level static conditions, is shown here along with data at the same corrected speed and at varying pressures. There is no obvious correlation between the pressure level and deviations from the speedline, indicating that the effect of inlet pressure on the blade angle is not significant.

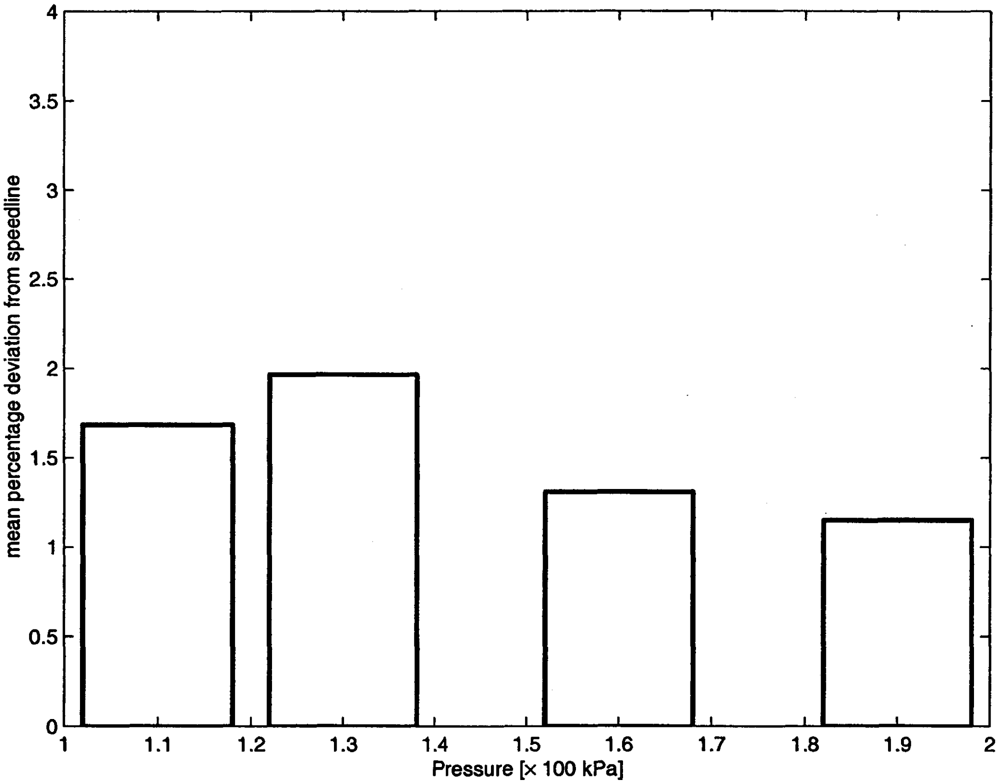

Figure 6-6: The fractional difference between the measured stage pressure ratio for a given inlet pressure and at sea level static, at the same corrected speed and corrected flow is shown. The data shows no significant deviations in the performance characteristics as a function of inlet pressure. Therefore, static deformations of the blades due to differences in inlet pressure do not significantly alter the flowpath geometry.

can have a significant effect on the flutter boundary, especially in the context of our measured data, which represents a typical case.

By inspection of the definitions of K^* (equation 3.1), and g/ρ^* (equation 6.1), we can see that the pressure only appears explicitly in g/ρ^*. Thus, for the case of zero damping, the value of $g/\rho^* = 0$, and changes in inlet pressure at constant temperature are irrelevant to flutter stability.

In general, since the temperature appears in both K^* and g/ρ^*, increasing the temperature at a constant pressure implies an increase in g/ρ^*, but a decrease in K^*. This trades off the stabilizing effect of increasing g/ρ^* with the destabilizing effect of decreasing K^*. Thus, for a typical case with finite damping, it is at least possible that the competing effects cancel out and that the inlet pressure alone governs flutter stability.

In the case of the multimission engine of Chapter 3, the flutter stability appeared to be relatively less sensitive to the g/ρ^* parameter than to the K^* parameter, indicating that the pressure may not summarize all the effects.

Using the measured data in the current analysis, we can address this question more precisely. We compare the flutter boundaries from two $(K^*, g/\rho^*)$ locations corresponding to approximately the same pressure, but with substantially different temperatures, as shown in Figure 6-7. There is a measureable decrease in stability for the case at higher temperature (i.e. lower K^*). Thus, the pressure alone cannot adequately explain all of the flight condition effects upon flutter stability, unlike the case of flight condition effects upon performance.

In general, changes in pressure at constant corrected operating point combine two distinct effects upon flutter stability: first, a change in the vibration-induced fluid force phase associated with the change in K^*, and second, a change in the relative magnitudes of the mechanical dissipation to vibration-induced fluid force magnitude embodied in g/ρ^*. Thus, a single parameter such as the pressure cannot simultaneously capture these two effects.

6.3 Effects of K_0^* and g/ρ^*

In this section, we quantify the previous statements made concerning the trends with respect to reduced damping, g/ρ^*. To accomplish this, the intersections between the estimated flutter boundary and the

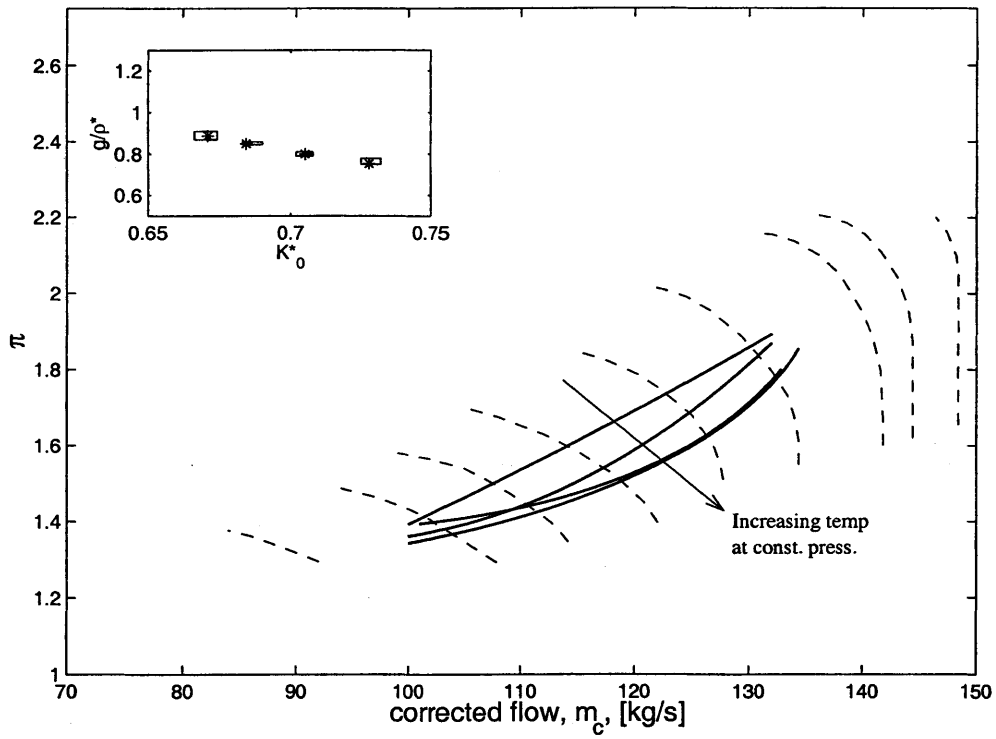

Figure 6-7: Effect of temperature at a constant pressure. A series of flutter boundaries are shown corresponding to points at the same pressure (within 2%). Increasing in temperature, at constant pressure, destabilizes the flutter boundary.

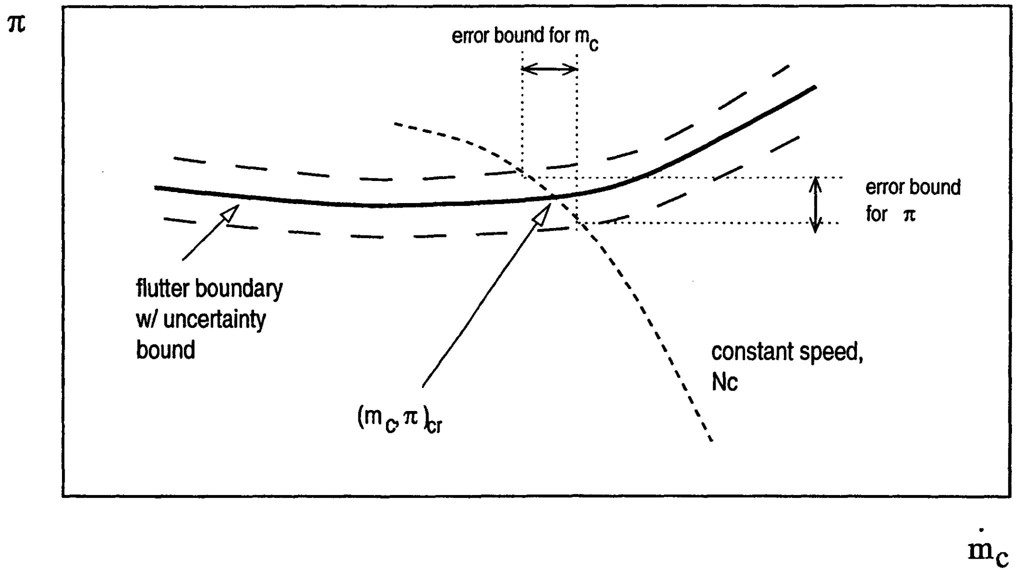

Figure 6-8: Points were selected at the intersection of a flutter boundary, corresponding to a specific $(K_0^*, g/\rho^*)$ pair, and a line of constant N_c. For this $(K_0^*, g/\rho^*, N_c)$ triplet, a critical corrected mass flow, $(\dot{m}_c)_{\text{cr}}$, and pressure rise, π_{cr}, are found. Uncertainty estimates upon the critical parameters can be made using the uncertainty bounds on the flutter boundary.

measured speedlines were found. These are the intersections between the solid curves and the dashed curves in Figures 6-2, 6-3, and 6-4.

6.3.1 Speedline/Flutter Boundary Intersections

Each intersection is associated with a $(K_0^*, g/\rho^*)$ pair corresponding to the boundary, and a value of N_c corresponding to the speed line. Furthermore, at each intersection, a critical value is determined for corrected mass flow, $(\dot{m}_c)_{\text{cr}}$, and pressure ratio, π_{cr}. Thus, for the $(K_0^*, g/\rho^*, N_c)$ combination associated with a particular intersection, flutter occurs for corrected mass flow *less than* the critical value, $(\dot{m}_c)_{\text{cr}}$, and pressure ratios *larger than* the critical value, π_{cr}. To obtain uncertainty bounds for these critical values, $(\dot{m}_c)_{\text{cr}}$, and π_{cr}, at the intersections, the uncertainty estimate for the flutter boundary was used (see Appendix D for uncertainty estimates of any particular boundary). This process is schematically shown in Figure 6-8.

6.3.2 Trends with respect to changes in reduced damping

The critical mass flow, $(\dot{m}_c)_{\text{cr}}$, and critical pressure ratio, π_{cr}, are shown as a function of reduced damping, g/ρ^*, in Figure 6-9 for five cases of corrected speed. For each corrected speed, increasing reduced damping

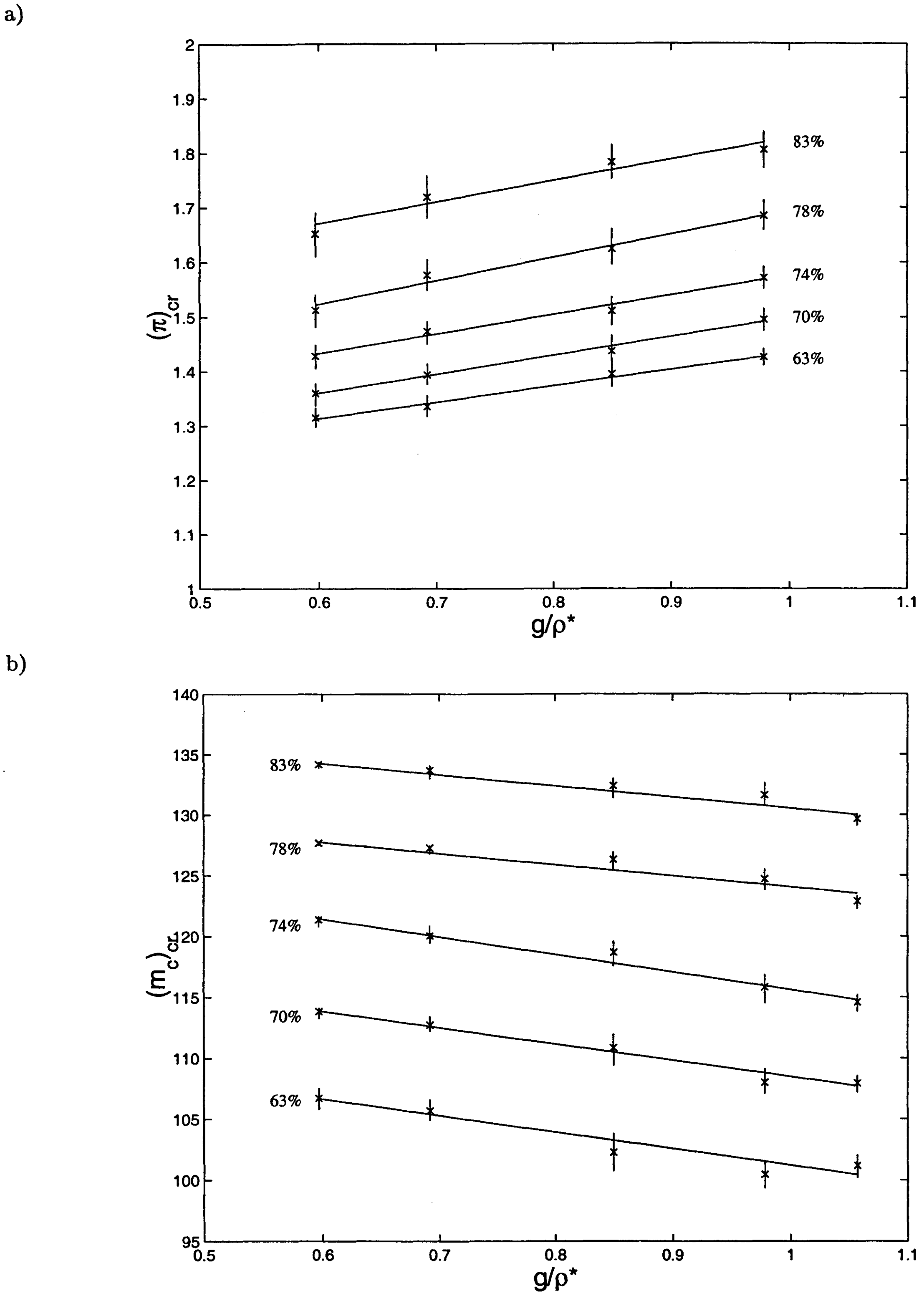

Figure 6-9: Critical mass flow and pressure ratio at flutter for $K_0^* = 0.685$, and varying g/ρ^*. Figure (a) is the critical pressure ratio, and figure (b) is the critical mass flow. In each case, there are five corrected speeds, N_c = 63%, 70% 74%, 78%, and 83% design, as a function of reduced damping, g/ρ^*.

Table 6.1: Flutter boundary sensitivity estimates. Sensitivities of critical pressure ratio and critical mass flow with respect to changes in reduced damping, g/ρ^*, and compressible reduced frequency, K_0^*, are listed.

	$K_0^* = 0.685$		$K_0^* = 0.705$		$g/\rho^* = 0.98$	
% N_c	$\partial\pi_{\text{cr}}/\partial(g/\rho^*)$	$\partial(\dot{m}_c)_{\text{cr}}/\partial(g/\rho^*)$	$\partial\pi_{\text{cr}}/\partial(g/\rho^*)$	$\partial(\dot{m}_c)_{\text{cr}}/\partial(g/\rho^*)$	$\partial\pi_{\text{cr}}/\partial K_0^*$	$\partial(\dot{m}_c)_{\text{cr}}/\partial K_0^*$
63	0.25	-14	0.4	-20	1.0	-136
70	0.3	-13	0.5	-20	1.1	-88
74	0.35	-15	0.55	-22	1.2	-79
78	0.45	-9	0.6	-14	1.4	-52
83	0.45	-9	0.4	-10	1.1	-32

increases the critical pressure ratio, and decreases the critical mass flow. These stabilizing effects are the same as those shown in Figure 6-2. A linear fit to the data, is displayed for each corrected speed. The slope of this linear fit is the sensitivity of the flutter boundary to reduced damping, for each corrected speed, for the case $K_0^* = 0.685$. These sensitivities can be expressed as the following partial derivatives

$$\frac{\partial(\dot{m}_c)_{\text{cr}}}{\partial g/\rho^*}, \text{and}, \frac{\partial\pi_{\text{cr}}}{\partial g/\rho^*}.$$

where it is understood that these partial derivatives are taken at constant N_c and constant K_0^*. In Figure 6-9, it appears that the sensitivities with respect to $(\dot{m}_c)_{\text{cr}}$ are approximately constant for different corrected speeds, while the sensitivity with respect to π_{cr} increases as N_c is increased. An inspection of Figure 6-2 shows that, at the intersection locations, the slope of the speedlines is greater at higher N_c, which explains this. In fact, the speedline slope can be found by taking the ratio of the sensitivities. That is,

$$\frac{(\partial\pi_{\text{cr}})/(\partial g/\rho^*)}{(\partial(\dot{m}_c)_{\text{cr}})/(\partial g/\rho^*)} = \left.\frac{\partial\pi}{\partial\dot{m}_c}\right|_{N_c}.$$

Alternately, this shows that one may deduce one of the sensitivities (e.g. that of π_{cr}) from the other and the speedline slope $(\partial\pi/\partial\dot{m}_c)$.

6.3.3 Comparison of g/ρ^* effects at $K_0^* = 0.685$ and $K^* = 0.705$

Similarly to the analysis of Figure 6-9 for $K_0^* = 0.685$, an analysis of the case of $K_0^* = 0.705$, corresponding to the boundaries in Figure 6-3 can be conducted. It is useful to compare the results of these two analyses to get some indication of the effects of K_0^* upon the flutter boundary location and sensitivity with respect to g/ρ^*. A separate sensitivity analysis with respect to K_0^* is conducted in the next section. A listing of the sensitivities estimated for the various cases is shown in Figure 6.1.

A comparison of the critical pressure ratio, π_{cr}, between the two cases is shown in Figure 6-10 for four different corrected speeds, ranging from 70% to 84% design speed. The critical mass flow, $(\dot{m}_c)_{\mathrm{cr}}$, for the same cases are shown in Figure 6-11.

Just as in the case of $K_0^* = 0.685$, the trends with reduced damping are monotonic for K_0^* as well. Increasing g/ρ^* has a tendency to stabilize the machine by increasing the critical pressure ratio, π_{cr} and decreasing the critical mass flow, $(\dot{m}_c)_{\mathrm{cr}}$. Furthermore, the change in K_0^* from 0.685 to 0.705 improves the stability of the machine, since it typically leads to higher values of critical pressure ratio, π_{cr}, and lower values of critical mass flow, $(\dot{m}_c)_{\mathrm{cr}}$.

Depending upon the rotor speed, the *sensitivity* to reduced damping may differ. These sensitivities can be estimated by the slopes of the fitted trend lines in each comparison plot. For the lower speeds shown in plots (a), (b) and (c) of Figures 6-10 and 6-11, the critical values (π_{cr} and $(\dot{m}_c)_{\mathrm{cr}}$) for $K_0^* = 0.705$ are more sensitive to the effects of g/ρ^* than for $K_0^* = 0.685$. This increased sensitivity appears to decrease as corrected speed increases so that at 83% speed, the slope of the π_{cr} trend, shown in Figure 6-10d, is approximately the same for the two K_0^* values, and the slope of the $(\dot{m}_c)_{\mathrm{cr}}$ trend appears to be slightly less for the case of $K_0^* = 0.705$ than for $K_0^* = 0.685$. This indicates that the sensitivities with respect to g/ρ^* near $K_0^* = 0.7$, as listed in Table 6.1, change for different values of K_0^*, near $K_0^* = 0.75$. Estimates near $K_0^* = 0.75$ can be roughly estimated, as done in the next section.

Thus, it appears that the sensitivity to g/ρ^* is dependent upon both corrected speed, N_c, and the value of K_0^*. There are two effects which are relevant as corrected speed increases, and which may be responsible for the difference in sensitivity. First, there is a transition, at the fan tip, from subsonic relative flow to supersonic relative flow, which occurs near $N_c = 74\%$. As the corrected speed increases, the region of the blade with supersonic relative flow will increase as well. Second, for a constant K_0^*, as the corrected speed increases, there is a smooth increase in the value of K^* due to the centrifugal stiffening effects, as described in equation (5.5). Therefore, even independent its role in determining the mean flow, one would expect the

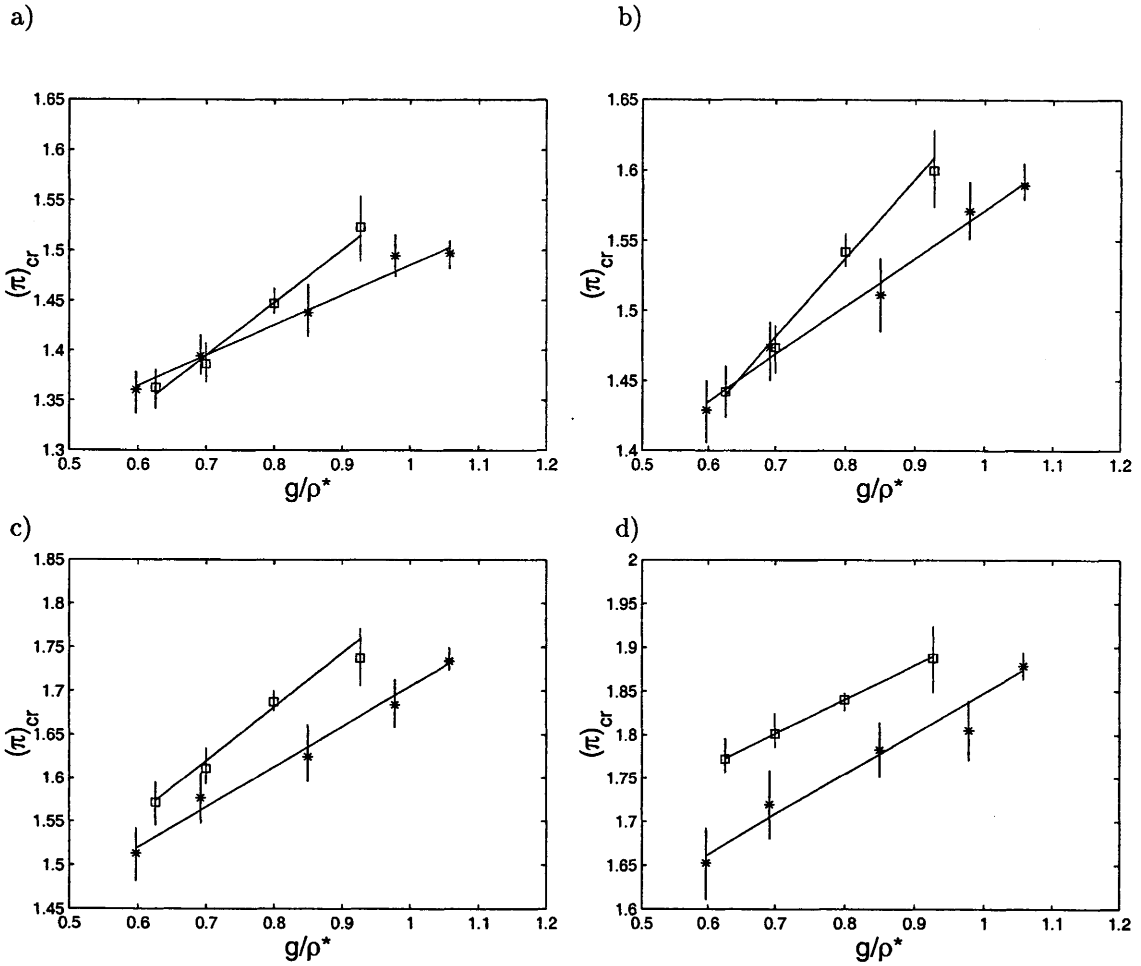

Figure 6-10: Critical π comparison between $K_0^* = 0.685$ (shown by $*$'s) and $K_0^* = 0.705$ (shown by □'s), at several corrected speeds. Figures (a), (b), (c), and (d), correspond to N_c = 70%, 74%, 78%, and 83% design, respectively.

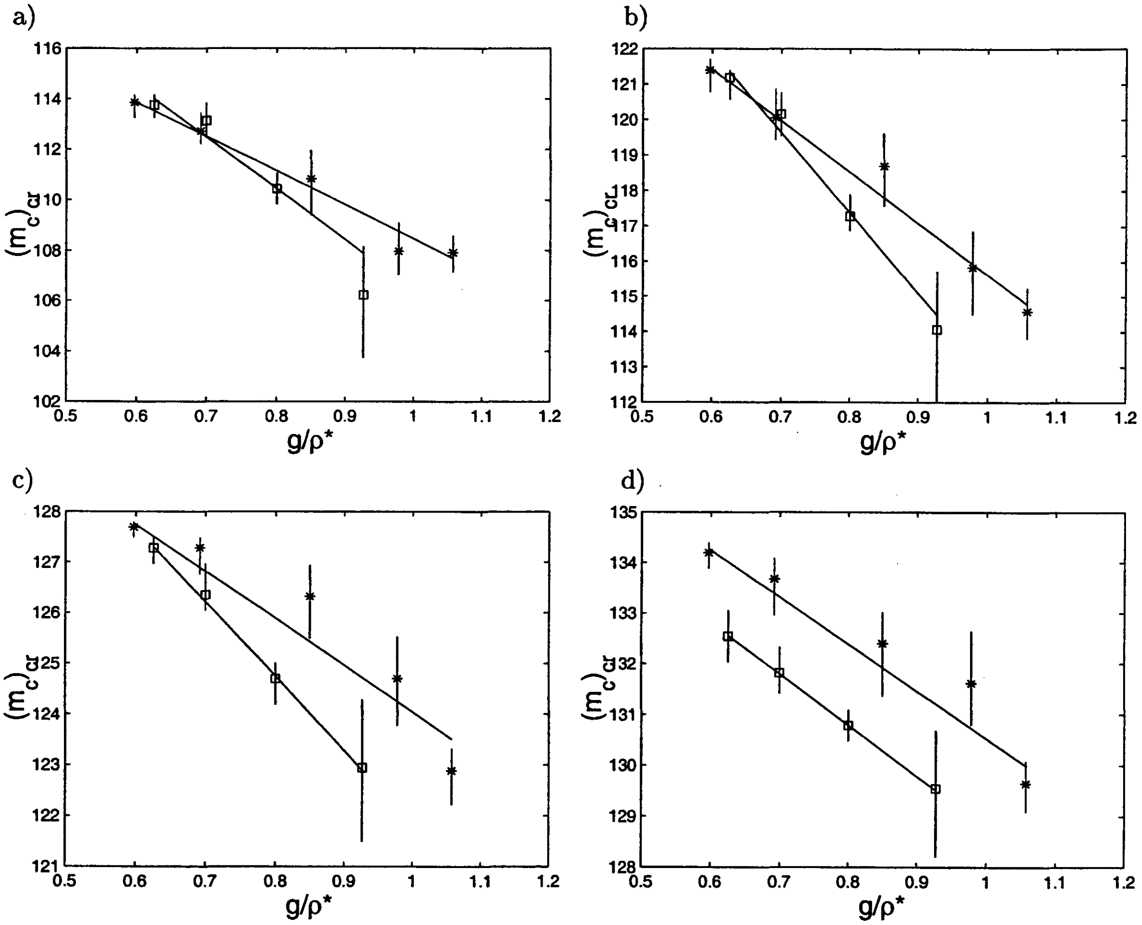

Figure 6-11: Critical $\dot{m}_c$ comparison between $K_0^* = 0.685$ (shown by $*$'s) and $K_0^* = 0.705$ (shown by $\square$'s), at several corrected speeds. Figures (a), (b), (c), and (d), correspond to N_c = 70%, 74%, 78%, and 83% design, respectively.

value of corrected speed to have an effect.

6.3.4 Trends with respect to changes in K_0^*

The effect of K_0^* is evident in the comparison plots of Figures 6-10 and 6-11. For the case of $g/\rho^* = 0.98$, the trends with K_0^* in critical pressure ratio, π_{cr}, and critical mass flow, $(\dot{m}_c)_{\text{cr}}$, are shown in Figure 6-12. This further confirms the montonicity of trends with the K_0^* parameter at a constant corrected speed. As K_0^* is increased, π_{cr} increases and $(\dot{m}_c)_{\text{cr}}$ decreases.

Judging from Figures 6-10 and 6-11, the level of reduced damping, g/ρ^*, as well as the corrected speed, N_c, significantly influence the sensitivity of the K_0^* parameter. At $g/\rho^* = 0.6$, there is very little difference in the values of π_{cr} for 70% and 74% corrected speed. At 84% corrected speed, however, there is a substantial difference. Near $g/\rho^* = 1$, there are substantial effects of K_0^* at all speeds.

We can look at this case more fully in Figure 6-12. This includes the data for a higher K_0^* value as well, near $K_0^* = 0.75$. The K_0^* trends from the comparisons in Figures 6-10 and 6-11 are consistent the data at the $K_0^* = 0.75$, within the error of the estimates for π_{cr} and $(\dot{m}_c)_{\text{cr}}$.

Changes in K_0^* affect the sensitivity with respect to reduced damping, g/ρ^*. The dependence upon g/ρ^* is characterized fairly well near K_0^* near 0.7, using several points for each sensitivity estimate. Although the data to estimate this in the same way near $K_0^* = 0.75$ is not available, we can generate upper and lower bounds near (K_0^*, g/ρ^*)=(0.75,1). This sensitivity is of particular interest, since it is the sensitivity at the "most stable" extent of the measured regime.

An obvious lower bound is zero, which comes from the assertion that mechanical damping can not ***destabilize*** the machine. Other estimates can be estimated by using two (K_0^*,g/ρ^*) points: the measured locations at (0.75,1) and the location at (0.73,0.75). See Figure 6-1. Applying the trend that increasing K_0^* is stabilizing, an upper bound for the sensitivity comes from ignoring the K_0^* difference. Labeling the point at (0.75,1) point A, and the point at (0.73,0.75) point B, we have

$$0 < \left(\frac{\partial \pi_{\text{cr}}}{\partial g/\rho^*}\right)_A < \frac{\pi_{\text{cr}}|_A - \pi_{\text{cr}}|_B}{(g/\rho^*)_A - (g/\rho^*)_B}. \tag{6.2}$$

An estimate which lies between these bounds, and which is expected to be more accurate, is to use the

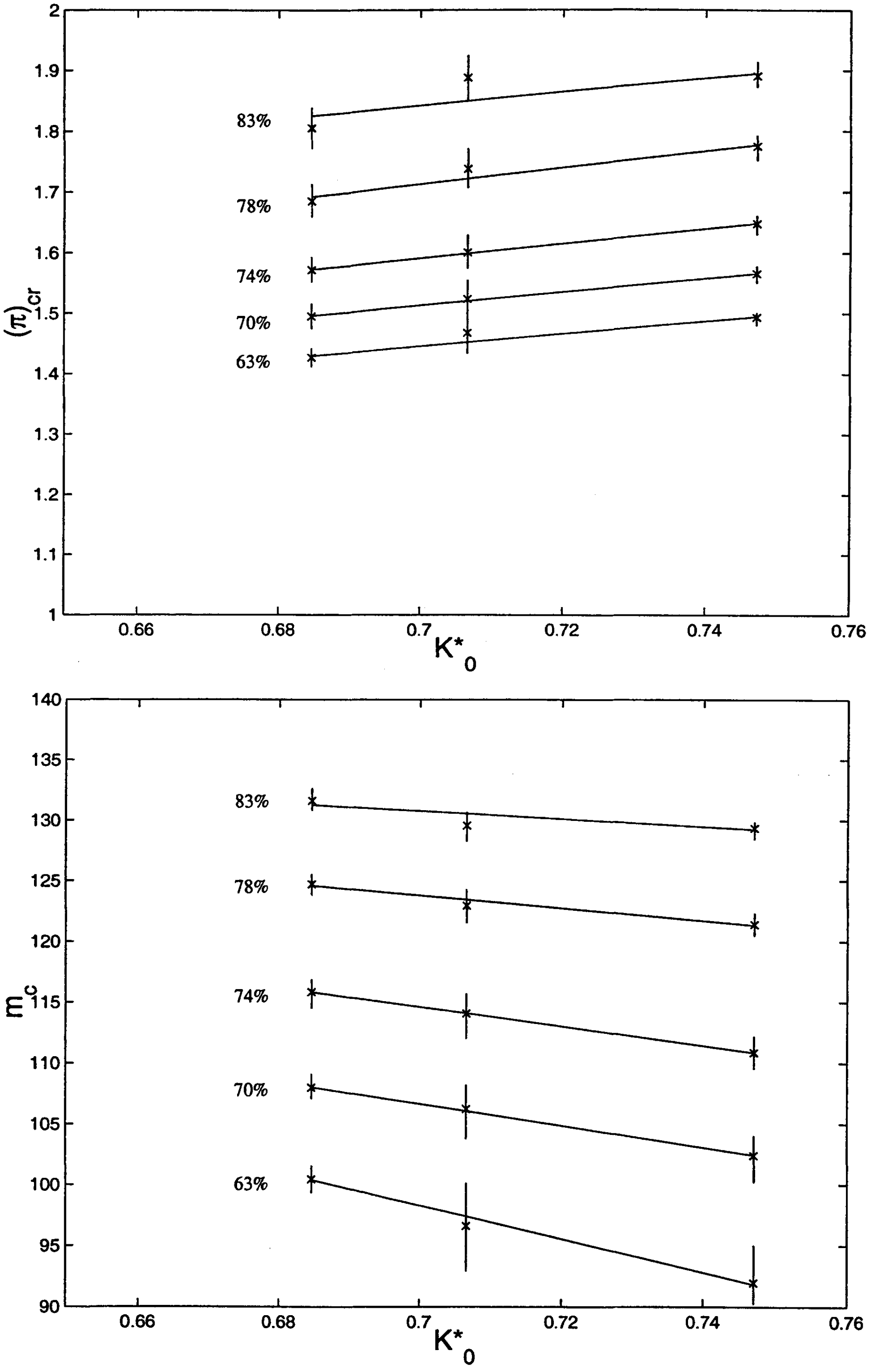

Figure 6-12: Critical mass flow and pressure ratio at flutter for $(g/\rho^*)_{\mathrm{rel}} = 1$, and varying K_0^*. Figure (a) is the critical pressure ratio, and figure (b) is the critical mass flow. In each case, there are five corrected speeds, N_c = 63%, 70% 74%, 78%, and 83% design, as a function of reduced damping, g/ρ^*.

Table 6.2: Estimate and upper bound of flutter boundary sensitivity using point data. The sensitivity with respect to reduced damping, $\partial\pi_{\text{cr}}/\partial(g/\rho^*)$, at $K_0^* = 0.75$ and $g/\rho^* = 1$ is assessed using a 2-point estimate. An approximation and an upper bound to the sensitivity are listed. The lower bound is zero.

% N_c	$\partial\pi_{\text{cr}}/\partial(g/\rho^*)$ estimate	$\partial\pi_{\text{cr}}/\partial(g/\rho^*)$ upper bound
63	0.29	0.37
70	0.19	0.28
74	0.12	0.21
78	0.07	0.16
83	0.03	0.12

previously assessed K_0^* sensitivity to eliminate the K_0^* effects. This can be expressed

$$\left(\frac{\partial\pi_{\text{cr}}}{\partial g/\rho^*}\right)_A \approx \frac{(\Delta\pi_{\text{cr}})_{A-B} - \left(\frac{\partial\pi_{\text{cr}}}{\partial K_0^*}\right)_A \cdot (\Delta K_0^*)_{A-B}}{(\Delta g/\rho^*)_{A-B}} \tag{6.3}$$

where Δ is used to indicate the difference between the subscripted points. Equations (6.2) and (6.3) can be used generally for local sensitivity estimates in regions of sparse data.

For the case of interest, point A at $K_0^* = 0.75$ and $g/\rho^* = 1$, these estimates for the g/ρ^* sensitivity are listed in Table 6.2.

6.4 Flutter boundary on frequency-damping map

Projecting the flutter boundary onto the performance map for specific values of reduced damping and compressible reduced frequency, although it is particularly familiar, is only one way to represent the flutter boundary. We now look at the boundary on the map of compressible reduced frequency, K_0^*, versus reduced damping, g/ρ^*. This is useful since this map is understandable in terms of the flight envelope of the aircraft powered by the engine, as depicted in Figure 3-14. In particular, one can assess the flight regime of flutter stability corresponding to a chosen operating point.

Furthermore, such a view can help sort out the effects of K_0^* and g/ρ^*. From the previous analysis, it is clear that these parameters have a coupled effect on flutter stability. It has also been demonstrated that the coupling can not be explained only as a pressure effect. Looking at the information on the K_0^* versus $(g/\rho^*)_{\text{rel}}$ map can help us gain insight into the coupled effects.

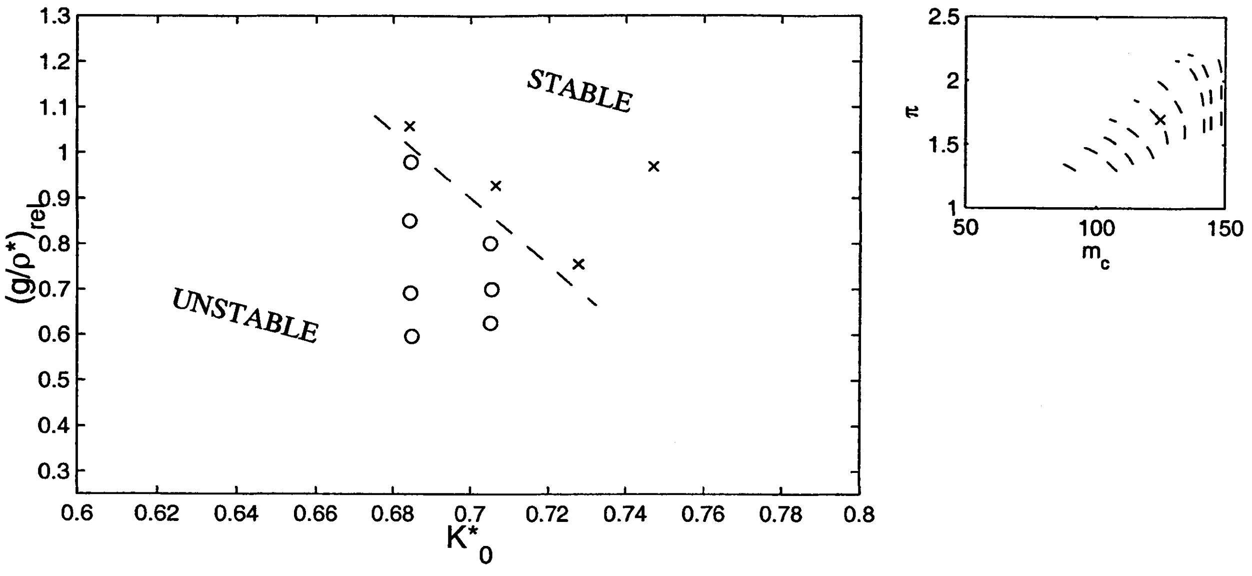

Figure 6-13: A flutter boundary on $(K_0^*, g/\rho^*)$ map is shown for a specific point on the performance map, corresponding to the × on the small set of axes. The stable points on the $(K_0^*, g/\rho^*)$ map are shown as × symbols and the unstable points are shown as o symbols. A $(K_0^*, g/\rho^*)$ point is considered stable if its corresponding boundary points is lies above the performance point under consideration. A dashed line indicates an estimated flutter boundary on the $(K_0^*, g/\rho^*)$ map for the point in question.

Figure 6-13 shows a boundary estimate, corresponding to a given point on the performance map, depicted on the inset plot. This boundary was found using the previous boundary fits on the performance map, which are shown individually in Appendix D. Whether the given point on the performance map falls within the flutter region of each boundary on the performance map determines the stability of the corresponding point on the $(K_0^*, g/\rho^*)$ map. Since there are only 12 $(K_0^*, g/\rho^*)$ points considered, the boundary on these coordinates can only be roughly estimated as the dividing line between these 12 points. If one had more points, then a better fit using the SVM boundary fitting technique described in Appendix C can be done.

One benefit of this approach is that, although the resolution on the $(K_0^*, g/\rho^*)$ map is limited, one can form a boundary for any chosen pair of corrected speed, N_c, and critical mass flow, $(\dot{m}_c)_{\text{cr}}$. Equivalently, one may specify the corrected speed and the critical pressure ratio, π_{cr}. Figures 6-14 through 6-18 show $(K_0^*, g/\rho^*)$ maps, each for a particular corrected speed, N_c, and which demarcate the boundaries corresponding to various levels of critical pressure ratio, π_{cr}.

For each dashed boundary, the points on the upper right of the boundary corresponded to cases in which the critical pressure ratio at that corrected speed was higher than that labeled on the boundary. Thus, these locations in $(K_0^*, g/\rho^*)$ would be stable for the pressure ratio listed on that boundary, for the corrected speed relevant to that plot. Conversely, the points to the lower left of the dashed boundary correspond to cases in which the locations in $(K_0^*, g/\rho^*)$ would experience flutter at the pressure ratio listed on the boundary.

The series of boundaries for each corrected speed gives an indication of the coupled effects of K_0^* and g/ρ^*. The boundaries tend to curve downward, being flatter for lower K_0^* and lower g/ρ^*, but steeper for higher K_0^* and higher g/ρ^*.

The curvature in the boundaries indicates that the sensitivity changes as one moves in the parameter space. It should also be recognized that the flatter boundaries are at lower pressure ratios as well. Therefore, the changes in boundary slope may be a result of considering the boundary for a different corrected performance point, besides being at a different $(K_0^*, g/\rho^*)$ location.

Irrespective of the mechanism, the sensitivity of the relevant stability boundary changes for large changes in K_0^* or in g/ρ^*. From inspection of the plots, we can roughly say that changes in K_0^* of 5% (from 0.68 to 0.72) and changes in $(g/\rho^*)_{\text{rel}}$ of about 20% (from 0.95 to 0.75) can change the sensitivities with respect to K_0^* and g/ρ^*. We therefore restrict applicability of the sensitivity estimates at a given point to patches of these limited ranges.

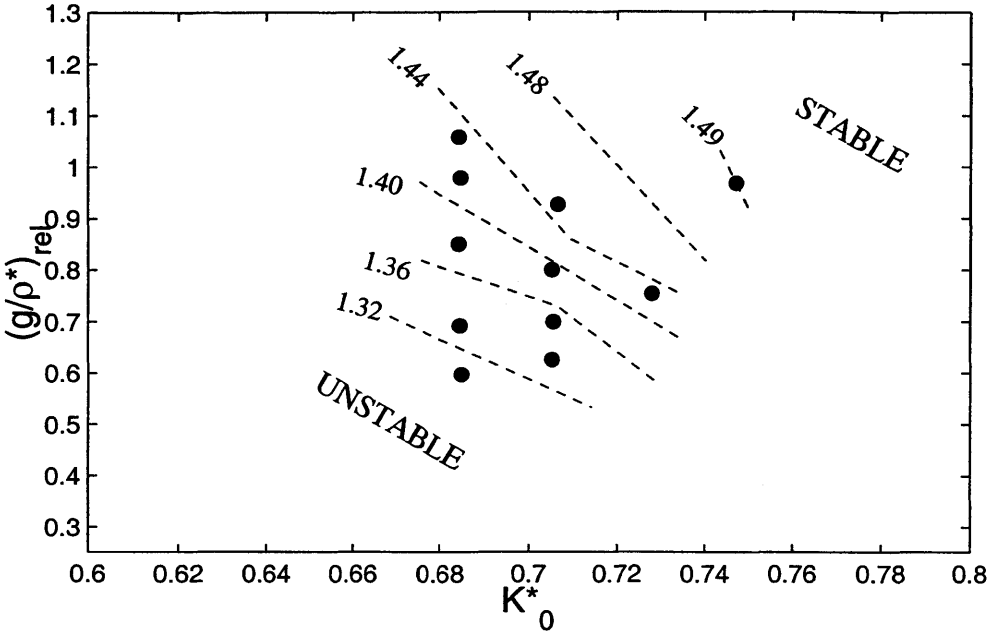

Figure 6-14: Family of flutter boundaries on $(K_0^*, g/\rho^*)$ map, for 63% corrected speed. Dashed lines indicate flutter boundary location for the labeled values of π_{cr}.

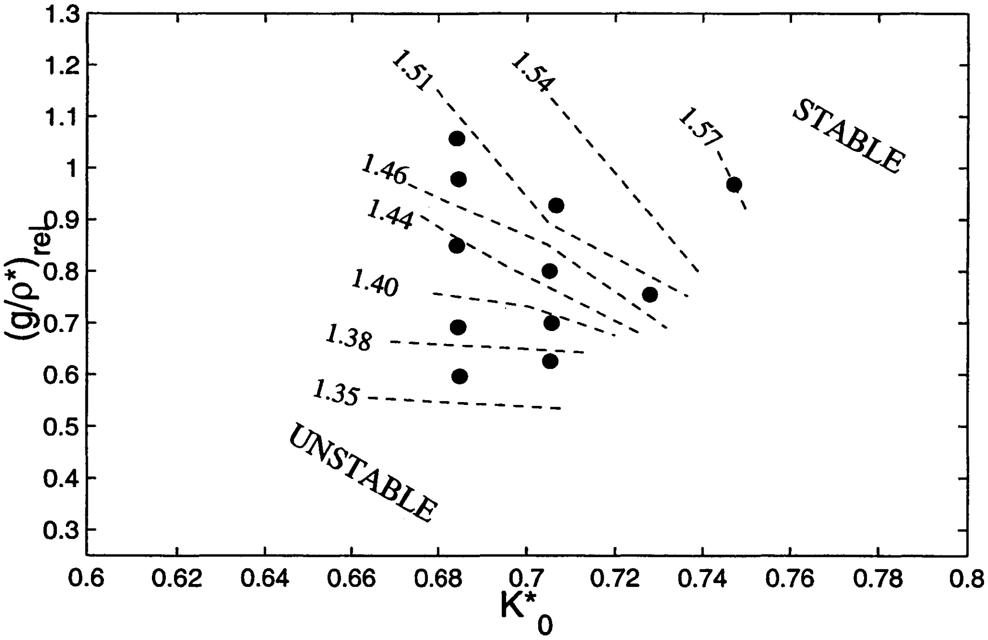

Figure 6-15: Family of flutter boundaries on $(K_0^*, g/\rho^*)$ map, for 70% corrected speed. Dashed lines indicate flutter boundary location for the labeled values of π_{cr}.

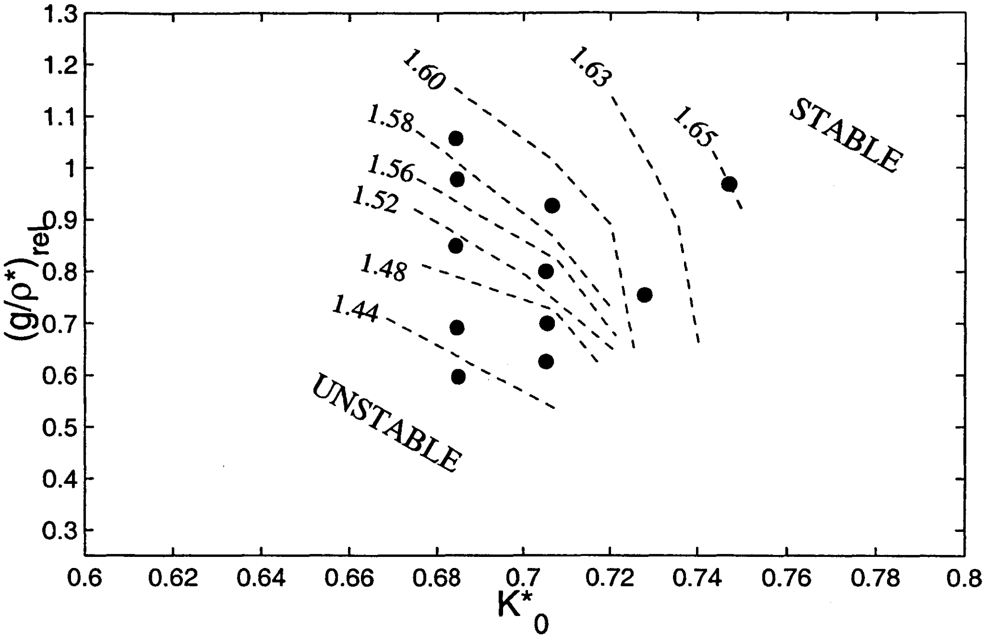

Figure 6-16: Family of flutter boundaries on $(K_0^*, g/\rho^*)$ map, for 74% corrected speed. Dashed lines indicate flutter boundary location for the labeled values of π_{cr}.

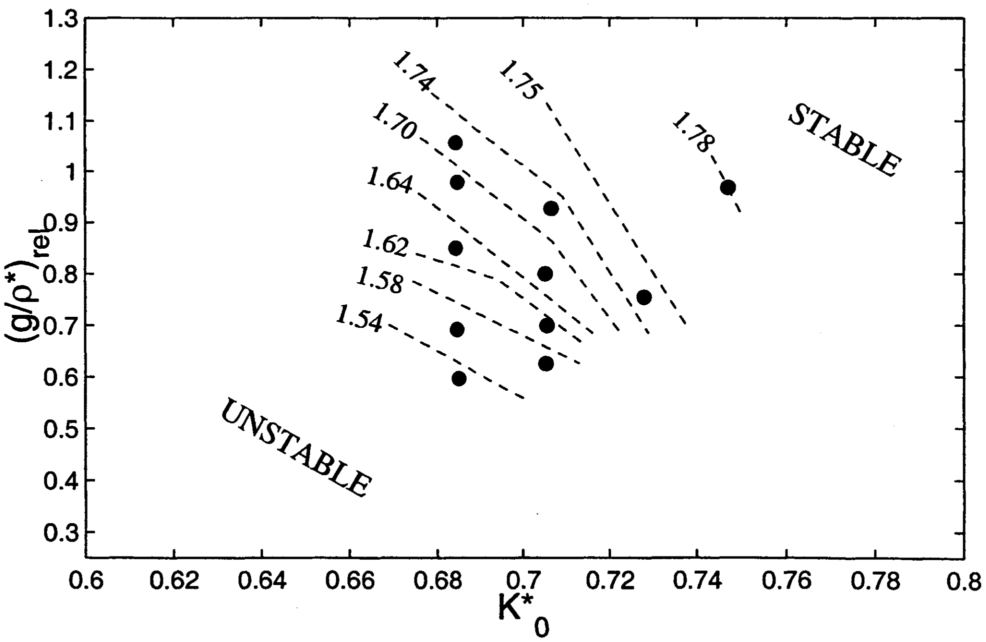

Figure 6-17: Family of flutter boundaries on $(K_0^*, g/\rho^*)$ map, for 78% corrected speed. Dashed lines indicate flutter boundary location for the labeled values of π_{cr}.

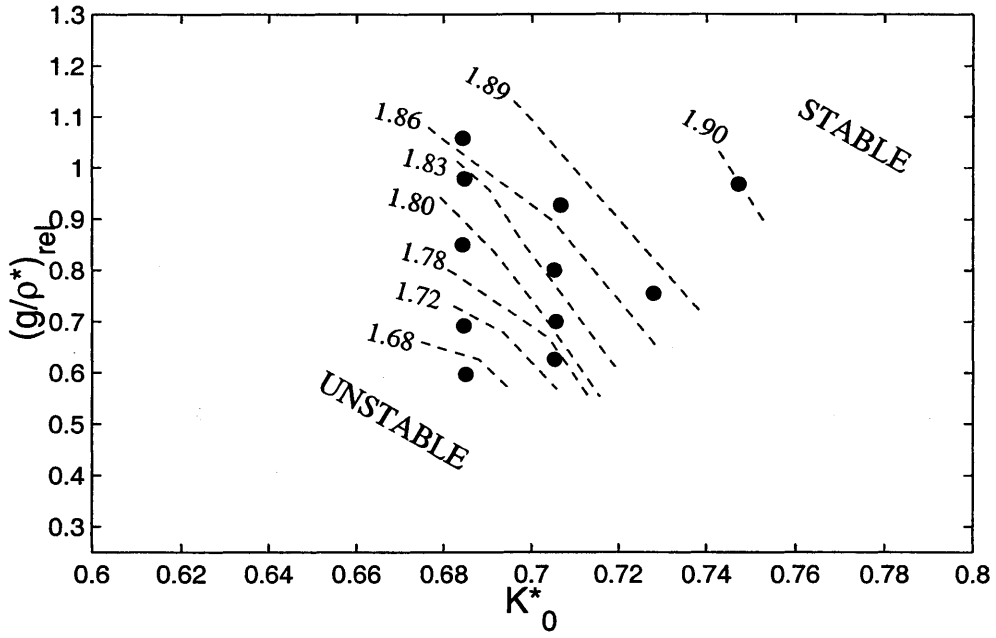

Figure 6-18: Family of flutter boundaries on $(K_0^*, g/\rho^*)$ map, for 83% corrected speed. Dashed lines indicate flutter boundary location for the labeled values of π_{cr}.

6.5 Summary

The data from the Volvo rig was analyzed using the procedure from Chapter 5 with the following main results

- The effects of increasing K_0^* and g/ρ^* were significant and were stabilizing.
- At constant inlet pressure, there was a measureable effect of inlet temperature. The inlet pressure is not the only flight condition effect upon flutter stability.
- Sensitivities of the flutter boundary (e.g. in terms of a critical pressure ratio) with respect to K_0^*, g/ρ^* and N_c are valid locally, but may change for large movements. Sensitivity estimates at a point are applicable in a local patch of roughly 5% in K_0^*, 5% in N_c, and 20% in g/ρ^*.
- Viewing the flutter boundaries, for a specific (N_c, π), on the map of (K_0^*, g/ρ^*) is useful in assessing the combined effects of K_0^* and g/ρ^*.

Chapter 7

Flutter Clearance

Flutter clearance refers to the testing procedure performed to ensure that the engine blades will not flutter throughout the engine's intended operating regime. In this chapter, we discuss the requirements of such a testing procedure in terms of the set of similarity variables ($\dot{m}_c$, N_c, K^*, g/ρ^*) introduced in this thesis. We then describe a methodology for designing such tests. An example of flight regime assessment is given using the Volvo data previously discussed in Chapters 5 and 6.

7.1 Design of Experimental Tests

The testing environment for aeroengine flutter is harsh on the measurement equipment and the machine being tested. It is desireable to minimize the test time, especially that spent in flutter to avoid accruing too many fatigue cycles. However, unlike compression instabilities such as surge which are likely to compromise the engine integrity if not immediately mitigated, it is possible to run an engine at low levels of cyclical stress during testing.

In the data discussed in Chapters 5 and 6, many data points were taken in flutter at low stress levels. In this case, the strain gages were placed in the location of maximum stress for the mode of interest. If the sensor is located in a different location, such considerations should be based on an estimate of the maximum stress. Such an estimate could be made by picking the appropriate mode (using the vibrational frequency), and applying an appropriate amplification factor based on the modeshape. It is important to place the sensor(s) in a location where there is measureable strain for each relevant vibrational mode.

In this section we focus upon the design of an experimental test from the standpoint of sampling the appropriate region of parameter space to ensure that the engine is free of flutter. Other aspects of flutter testing, including instrumentation, data acquisition, and testing procedures are beyond the current focus, but are discussed in existing literature (Mehalic et. al. 1977, Stargardter, 1979, Jutras et. al. 1982, Stargardter, 1987).

Even in absence of instabilities, it is important to efficiently sample the space. Sensor degradation is an issue when running the machine, even under stable conditions. For example, during the NASA flutter tests which followed the F100 engine development (Mehalic et. al., 1977), testing was conducted at various inlet densities and rotor speeds at progressively higher temperatures. Flutter was only observed at the highest temperature tested, but at the point when this temperature was reached in testing, many of the stress sensors were broken from previous testing! This limited the number of points which could be usefully sampled to learn about the flutter instability. Sensing technology has improved significantly, but the main point remains of efficiently planning the tests to get the necessary information for a low testing cost.

The design of a flutter test, can be framed in terms of the general theory of "Design of experiments." An introductory reference to this subject may be found in Mongomery (1976). The basic procedure is to identify the factors which determine the phenomenon, and to design a *test matrix*, or a testing schedule, to span these factors. In this case, the factors are given by the similarity variables developed in Chapter 3: $(\dot{m}_c, N_c, K^*, g/\rho^*)$.

Flutter testing (and stability testing in general) is non-standard in that the results are binary, rather than a real number. That is, at each condition sampled, one ultimately finds out only whether or not the machine is stable, but does not have a quantitative estimate of the system damping[1].

Binary data makes it a non-standard problem to interpolate between points in parameter space, and impossible to meaningfully extrapolate without outside information. The problem of interpolation is addressed by the SVM technique described in Appendix C. Furthermore, we can use some of the principles developed earlier in the thesis to extrapolate data and simplify the test matrix.

---

[1] There is active research in the area of measuring the total damping, but this has not yet been developed to the point of giving accurate damping estimates for use in flutter clearance.

7.1.1 Requirements for Flutter Clearance

In Chapter 2, it was shown that, for a given blade vibrational mode, four non-dimensional parameters span the operating space of a machine.

The requirement for flutter clearance is that *the machine must be stable for every combination of factors, ($\dot{m}_c$, N_c, K^*, g/ρ^*), that it is designed to encounter.* Testing every permutation of factors is performed in a so-called "full factorial" test. Such a test was performed on an idealized, computational model in the parameter study of Chapter 4, in which the increment of each factor was small enough to resolve the details.

Although this would satisfy the requirement, it is neither practical nor essential for flutter clearance. Using the concept that flutter stability increases with increases in K^* and g/ρ^*, the test matrix can be simplified. This trend with K^* and g/ρ^* was discussed in Chapter 3 in general terms which are based upon established trends, and was further evident in the data analysis as well.

We, therefore, use the stabilizing trend of increasing K^* and g/ρ^*, similarly to the data analysis technique depicted in Figure 5-8. In this case, however, we focus upon sampling data on the (K^*, g/ρ^*) map in the most effective locations for flutter clearance. At a given (K^*, g/ρ^*) location, a stable measurement also holds for higher values of (K^*, g/ρ^*), and an unstable measurement is relevant for lower values of (K^*, g/ρ^*). This principle is outlined in Figure 7-1.

Using this trend, we can modify the above stability requirement in the following manner: *for every performance point of operation, ($\dot{m}_c$, N_c), the machine is stable at* ($\min K^*$, $\min(g/\rho^*)$)*, where* min *denotes the minimum value encountered for the given ($\dot{m}_c$, N_c).* The behavior at this minimum (K^*, g/ρ^*) pair must estimated by some reliable means, the most straightforward of which is to take experimental measurements there.

7.1.2 Mission Requirements

Two parts of the requirement for flutter stability depend, not upon the physical characteristics of the machine, but rather upon how the machine is to be used. First, one must specify what is "every performance point of operation." Second, one must specify what the values of K^* and g/ρ^* are to be encountered. These specifications come from an analysis of the mission requirements.

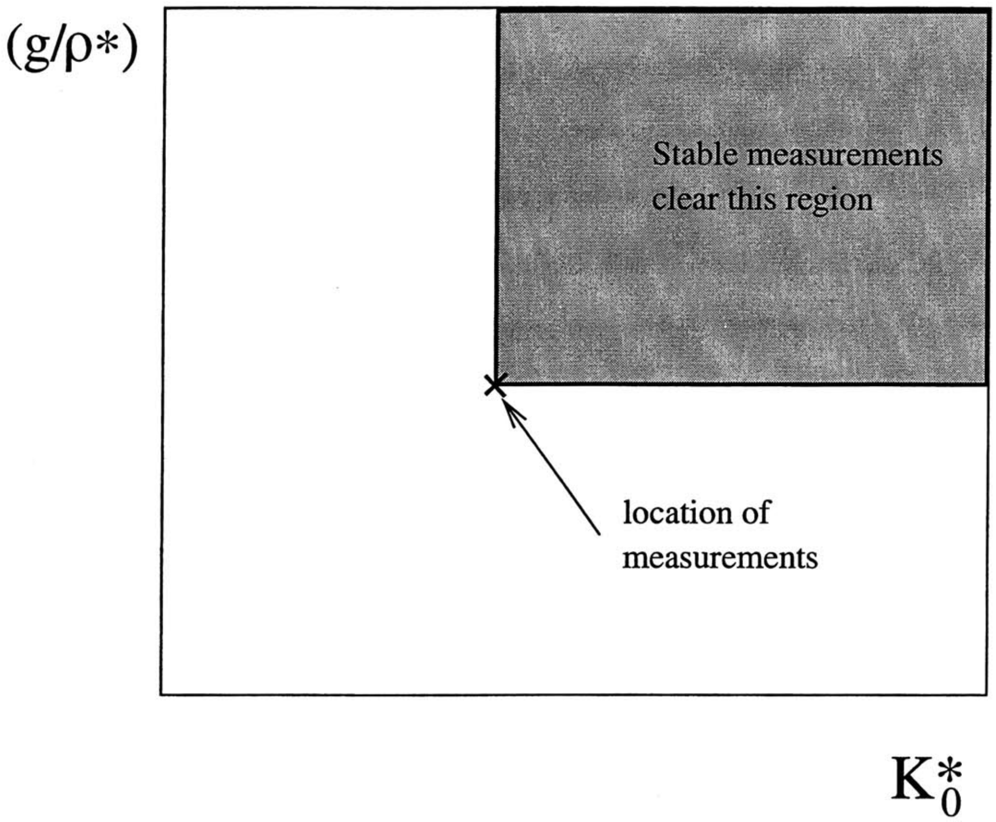

Figure 7-1: Schematic of data sampling rule on K^*, (g/ρ^*) map.

In the case of a front stage compressor or fan, and for constant structural parmeters, the flight envelope (in terms of expected altitude and flight Mach number) can determine the range of K^* and g/ρ^* seen. The increases in static pressure and temperature, from upstream stages can also influence these parameters. An example of the expected range on the (K^*,g/ρ^*) map is given in Figure 3-14.

The range of operation on the performance map is specified by a desired operating line, which gives the pressure ratio, π, requirements for every corrected speed, N_c. It could also be specified, if desired, in terms of the corrected mass flow, $\dot{m}_c$ instead of the pressure ratio. On top of the nominal operation, one specifies "margins" for performance. This can be done in terms a margin (e.g. 5%) in pressure ratio, π, at each corrected speed. To protect the operating line fully, one may also specify a margin at the maximum N_c in terms of N_c itself. This is depicted in Figure 3-15.

In some cases, the mission requirements may not be available, or may be *determined* by the flutter stability. The requirements and limitations which are considered in determining the flight envelope include the intended use of the airplane, the available power, and airframe/engine instabilities. Such analyses are discussed in McCormick (1995). Before testing, one should at least construct minimally sufficient requirements, as well as optimal requirements, so that testing can be planned accordingly. The results of the testing can then be used to decide if any modifications are needed in the design, or if the planned flight envelope need be restricted, perhaps based on a cost-benefit analysis.

7.2 Examples

To illustrate the testing design concepts discussed in the previous section, we present two flutter clearance examples. These are fictitous examples meant only to demonstrate the flutter clearance methodology, rather than to simulate a specific application.

For simplicity, we make the following assumptions in the examples:

- The mechanical damping does not vary significantly during the operation of the machine.
- The relevant modeshape, frequency, and Southwell coefficient have been identified.

In an actual case, experimental testing can check all the modes simultaneously. Also, the properties of the mechanical damping may differ for different modes, and may be dependent upon other factors (e.g. temperature and force of contact). If such variations are expected to be significant, one can account for this by assuming that the damping does not significantly vary from that tested, but requiring flutter clearance at an appropriately lower value of $\min g/\rho^*$.

We consider a machine with the same stability characteristics as that of the Volvo engine studied in Chapters 5 and 6. Simulated experimental tests in the examples are taken from the Volvo data analysis, in particular Figures 6-14 through 6-18. For a given corrected speed, N_c, we consult the appropriate figure and use the critical pressure ratio based on the K_0^* and $(g/\rho^*)_{\text{rel}}$ point.

Two cases are considered. In the first case, it is assumed that estimates are available (perhaps from a previous development program) regarding the K^* and g/ρ^* sensitivity of the flutter boundary. This case is that of a subsonic transport in which the sea level static (SLS) condition is close to the worst case. Sensitivities are used to extend SLS testing to the worst case (at a little lower K_0^* and g/ρ^* than for SLS), and thus clear the engine using only SLS tests. In the second case, it is assumed that no information is known about the machine beforehand. The objective in the second case is to clear the operating line for high speed flight.

7.2.1 Case 1: Low Speed Aircraft

In this case, we consider a fan for use in a powerplant for a subsonic transport. We assume that the SLS condition corresponds to a value of $K_0^* = 0.75$. Thus, the point at $(K_0^*, (g/\rho^*)_{\text{rel}}) = (0.75, 1)$ is relevant to this condition. The flutter boundary under these conditions is shown as a solid curve on the performance map of Figure 7-2. On this map, the desired operating line is also shown as a solid line.

We also require a range of flight conditions for this subsonic aircraft. We consider a typical case, in which the lowest K_0^* and lowest g/ρ^* occur at sea level at a Mach number of $M = 0.6$, as in the dashed curve of Figure 3-12. The corresponding minimum values are $K_0^* = 0.735$ and $g/\rho^* = 0.90$.

Since there is only a small percentage change in this minimum condition from the sea level static condition, we use the sensitivities estimated in Chapter 6 to estimate the position of the flutter boundary at the worst case location. This is done at each corrected speed on the map. For example, at 74% corrected

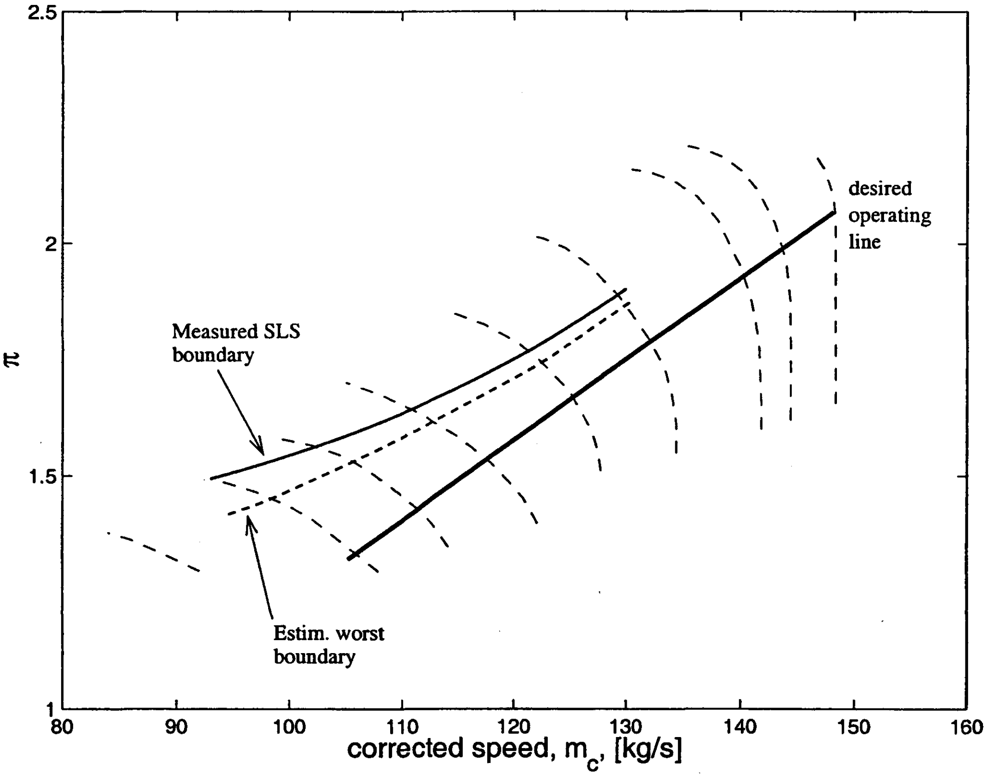

Figure 7-2: SLS Flutter boundary, estimated minimum stability boundary, and desired operating line for Case 1

speed, the difference between sea level static and sea level at $M = 0.6$ is estimated to lead to an change (decrease) in the critical pressure ratio of $\Delta\pi_{\rm cr} = -0.027$, which is computed in the following manner

$$\Delta\pi_{\rm cr} = \left(\frac{\partial\pi_{\rm cr}}{\partial K_0^*}\right) |(K_0^*)_{\rm SLS} - (K_0^*)_{\rm min}| + \left(\frac{\partial\pi_{\rm cr}}{\partial(g/\rho^*)}\right) |(g/\rho^*)_{\rm SLS} - (g/\rho^*)_{\rm min}|$$

The estimated boundary is shown as a dashed line on Figure 7-2 next to the solid SLS boundary. In this case, there is a flutter margin between the worst-case boundary and the desired operating line, indicating that the engine would be flutter-free. The necessary margin is based at least partially upon the expected transient behavior of the engine; however, for the purposes of these examples, we neglect such concerns and consider an engine cleared if the flutter boundary does not penetrate the specified operating line.

7.2.2 Case 2: High Speed Aircraft

In the second example, we consider a front stage fan of a high-speed (i.e. supersonic) aircraft. For this case, we assume that the structural design is such that the value of $K_0^* = 0.8$ at sea level static (SLS) conditions, and that the mechanical damping is taken to be the same as in the Volvo data (which leads to the same values of $(g/\rho^*)_{\rm rel}$). Furthermore, we assume that SLS testing does not exhibit flutter.

The minimal region on the $(K^*,g/\rho^*)$ map depends upon the mission requirments. Typically, the mission requirements of a high-speed aircraft are quite sophisticated, and are based upon accomplishing specific scenarios. Such an analysis is well beyond the scope of this current example, and we limit the current discussion to the simplified requirements depicted in Figure 7-3a. Minimum required Mach numbers are specified for low altitude (take-off and climb), and for higher altitudes (cruise and supersonic dash). There are two critical points for the purposes of flutter, labeled 2' and 2", respectively. The corresponding region on the $(K^*,g/\rho^*)$ map is shown in Figure 7-3b.

Since the clearance region specified in Figure 7-3b is relatively large, estimating flutter boundary using sensitivities may not be accurate. The analysis of Chapter 6 shows that the sensitivities themselves change with the changes in K^* and g/ρ^*. In any case, we presume that in this case such information is unavailable.

It is proposed to test the engine successively at the numbered points: 1, 2, and 3 on the $(K_0^*,\ g/\rho^*)$

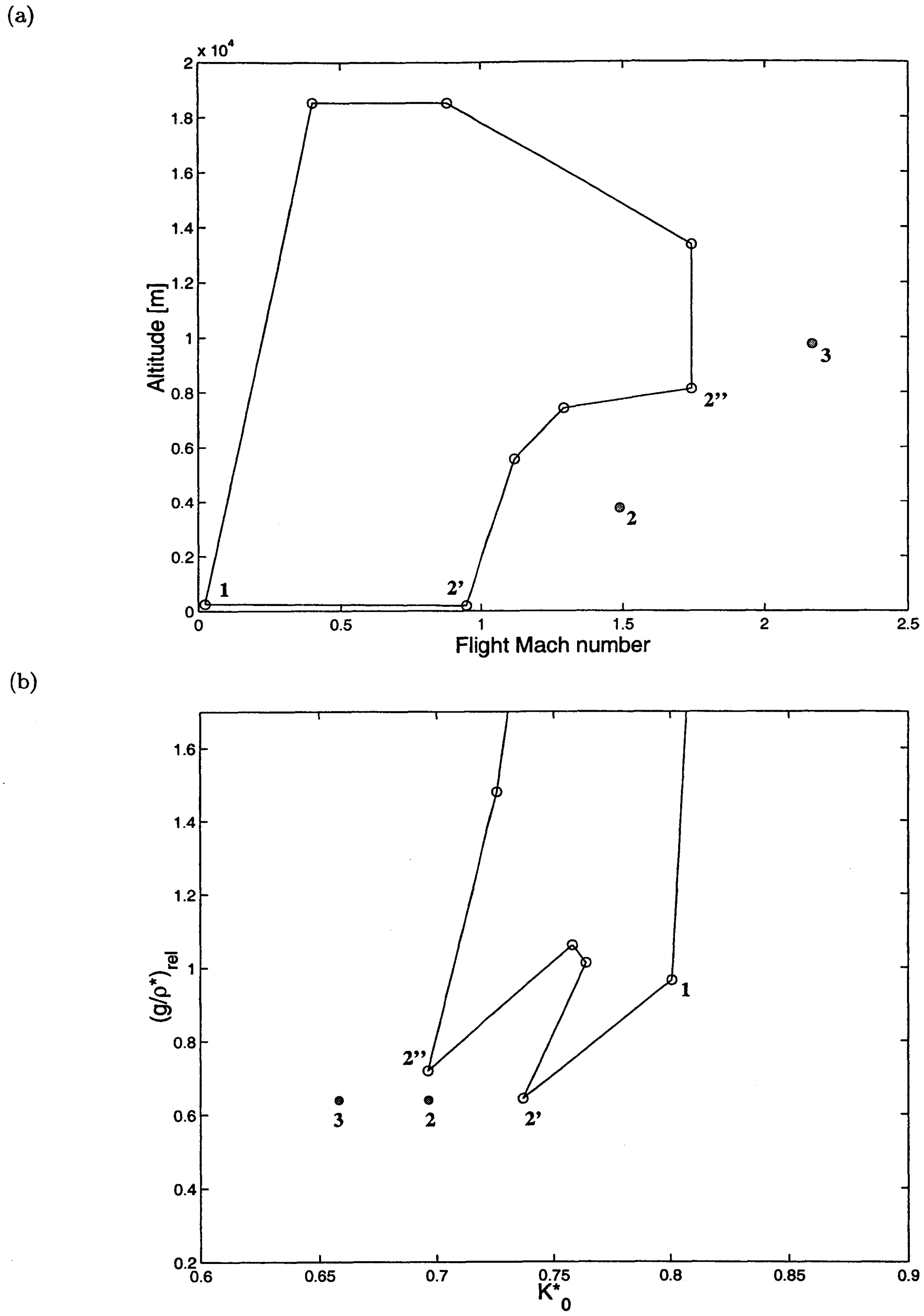

Figure 7-3: Flight requirements in terms of Mach number vs. altitude (a) and minimal clearance region on $(K_0^*, (g/\rho^*)_{\text{rel}}$ map (b). The sea level static condition is assumed to be at $(K_0^*, g/\rho^*) = (0.8, 1)$. The critical points, 2' and 2" are labeled on both plots.

map, depicted on Figure 7-3b. At each point, the engine should be run along the operating line to check for possible intersections with the flutter boundary. This type of testing requires the capability to adjust the values of K_0^* and g/ρ^*, the most straightforward method of this being to set the temperature and the pressure of the inlet flow to achieve the desired K_0^* and g/ρ^*.

Using the principle shown in Figure 7-1, it can be shown that clearing the engine at point 2 is sufficient to clear the entire minimal region. However, if a flutter event is found at point 2, then the minimal region may be cleared by clearing points 2' and 2". Using these three points, further measurements (off the operating line) can provide sensitivities, relevant to the critical region.

If points 1 and 2 are both clear, then it is useful to determine the flutter limits of the engine. This would entail testing towards point 3, which would clear a region beyond the minimal requirement. This may be useful in higher-performance extentions of the current application, or for use of the engine in different aircraft.

In the case of our example with the Volvo data, the relationship between the flutter boundary and the operating line is depicted in Figure 7-4. Although the information at point 1 (the SLS point) lies beyond the measurements, we presume that it does not exhibit flutter. However, point 2 would show a flutter event on the operating line. Further testing at points 2' and 2", however, would reveal that the operating line is clear throughout the minimally acceptable range of flight conditions, but that extensions beyond this minimally acceptable range (i.e. to point 2) can lead to a flutter event.

7.3 Summary

The application of flutter clearance testing is discussed in the context of design of experiments. The trend that K^* and g/ρ^* are stabilizing can be used to reduce the testing from all the operating points to 'critical' points.

Two hypothetical examples of clearance testing were discussed. For small changes in K^* and g/ρ^*, as might be experienced over the flight regime of a subsonic transport, the use of estimated sensitivities is appropriate as in the first example. For larger changes in K^* and g/ρ^*, relevant to high-speed aircraft, direct testing is preferable.

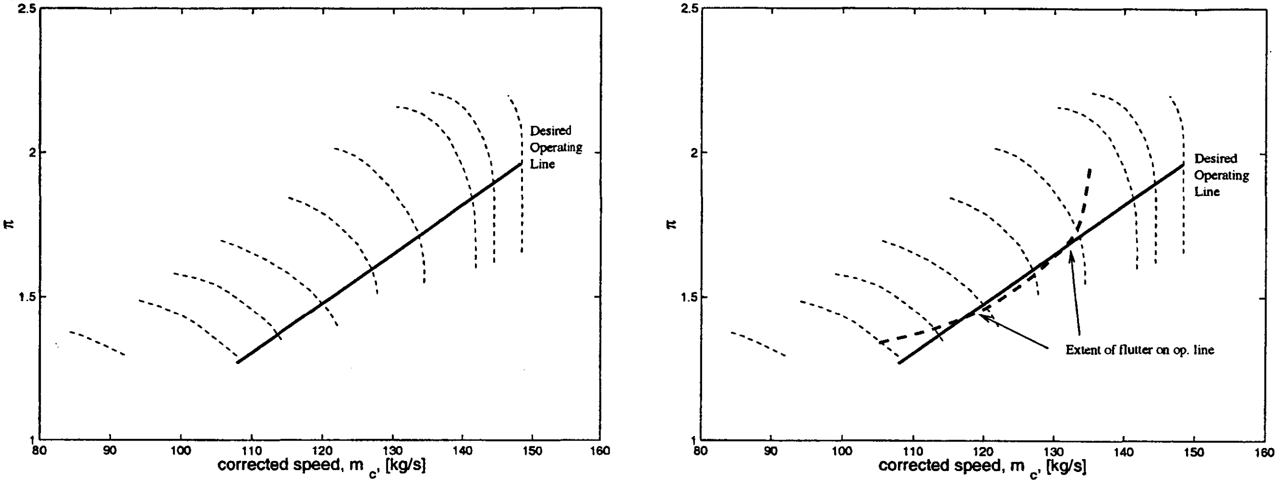
(a) Point 1

(b) Point 2

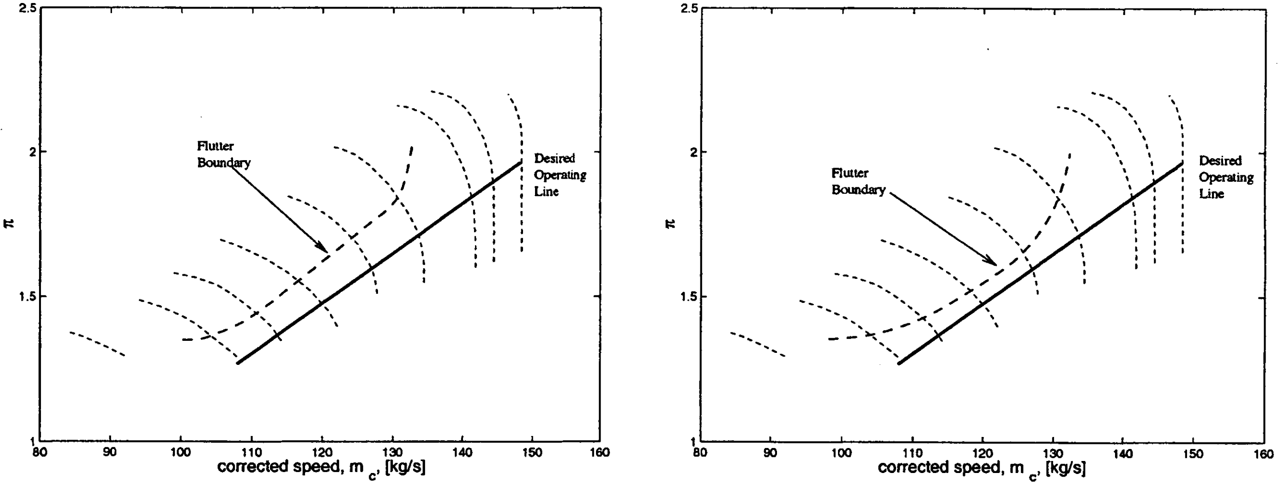
(a) Point 2'

(b) Point 2"

Figure 7-4: Flutter boundaries for various points in Case 2. The tests are performed by running the engine up and down an operating line at four points: first, at sea level static (point 1), then at point 2, where a flutter occurs on the operating line, then at points 2' and 2", which establish that the minimally acceptable envelope is clear, but is close to a flutter event at point 2.

Chapter 8

Conclusions

8.1 Thesis Summary

This thesis addresses the influence of system parameters upon aeroengine blade flutter stability, and the problem of ensuring flutter-free operation of the blades throughout the range of operation.

The study is composed of three parts: a theoretical development of parameters, a computational parameter study, and the analysis of full-scale test data. The results of these studies are then applied to the problem of flutter clearance testing.

The theoretical development is addressed in Chapters 2 and 3. A set of parameters is constructed which is necessary and sufficient for flutter stability assessment for a given design. These parameters are derived based upon the assumption of linear structural dynamics and a fluid operator based upon the full Navier-Stokes equations, with boundary conditions appropriate for the general case of turbomachinery blading, some discussion of which is contained in Appendix A. Of the relevant system parameters, some of which can be eliminated based upon approximations which are relevant in the case of aeroengines (e.g. high Reynolds number). The condition for linear stability is developed, and it is shown that four parameters are sufficient for the description of flutter stability. This requires the introduction of a new parameter, g/ρ^*, the reduced damping, which combines the blade mechanical damping, g, and the fluid inertia parameter, ρ^*, (i.e. ratio of effective fluid mass to structural mode mass) into a single parameter. Although g, and ρ^*

are individually small, their ratio, g/ρ^*, is order 1 in the typical case of inserted blades, which indicates that the effects of mechanical damping upon flutter stability can be significant.

Among the possibilities of four parameters to represent the system, there are many choices. We base our choice on the following requirements: (a) two parameters can be used to specify the position on the performance map in terms of corrected mass flow, $\dot{m}_c$, and corrected speed, N_c, (b) for constant structural properties, the other two parameters specify the flight condition in terms of the inlet thermodynamic state, and (c) that the unsteady aerodynamics problem is dependent upon only three of the four parameters. It is shown in Appendix B that a particular four parameter set, ($\dot{m}_c$, N_c, K^*, g/ρ^*), uniquely satisfies these requirements. This representation introduces another new parameter, the compressible reduced frequency, $K^* = M \cdot k$, where M is the blade relative Mach number, and k is the classical reduced frequency. A straightforward generalization can be made to the case of centrifugal stiffening, in which the structural parameters vary during operation, by replacing K^* with a centrifugally-corrected form, K_0^*. These new parameters can be thought of as decoupling the performance effects from the flight condition effects in terms of their influence upon flutter stability. This is discussed in more detail in Chapter 3.

The properties of the new parameters, g/ρ^*, and K^*, are discussed in the context of flutter stability. Increasing g/ρ^* has a stabilizing effect on flutter, a trend which is based in the analytical form of the stability criterion. The trend of increasing K^* is also stabilizing, and can be understood in terms of the effects of K^* on the fluid force phase. Although this trend has been shown to hold in a variety of idealized cases, the support for it is ultimately empirical. We take both of these trends as general principles, upon which we build further results. A representation of flutter boundaries using the full four-parameter set is established, using a technique which extends the viewpoint of the corrected performance map for aeroelastic behavior.

To quantitatively explore the parameter space, a computational study was performed using a two-dimensional, linearized unsteady, potential flow model of a vibrating rotor, as described in Chapter 4. Using the critical reduced damping, $(g/\rho^*)_{\mathrm{cr}}$, as a stability metric in unsteady flow computations appears to have some advantages over the work-per-cycle as normally defined, since its magnitude can be directly interpreted.

The computational results exhibited instability in both bending and torsion. The bending instability only occured at extremely low reduced frequency, about an order of magnitude less than the reduced frequency of torsion. In both cases, the predominant instability mechanism was local in the sense that the unsteady forces upon a given blade were determined by that blade and its neighbors. Non-local effects could be attributed the effects of "acoustic resonance," whose physical viability is controversial (experimental studies have not found acoustic resonances as a flutter mechanism). A technique of separating the results associated with acoustic resonance and those associated with the local effects was formulated, and the local effects were studied in detail for the case of torsion.

The effect of increasing K^* was stabilizing in the case of bending and for the main instability of torsion. Further study of the main instability in torsion, showed that the combined effects of reduced frequency and Mach number upon the phase of fluid forces could be summarized by a single parameter, $k/(1 - M^2)$, to a good approximation. This trend holds for a range of inlet flow angles, and for several cascade geometries. This collapse has not been recognized previously in the literature, and is not obviously related to previous analyses of the unsteady, compressible, cascade flow problem. However, it appears that the full unsteady aerodynamic operator (magnitude and phase) must be described in terms of three similarity parameters (e.g. N_c, $\dot{m}_c$, and K^*).

Fully-scaled experimental test data provides information directly applicable to aeroengine components. In Chapters 5 and 6, the technique of analysis and the results from such data, which spans the full four dimensional parameter space, is presented. The data indicate whether or not the machine was in flutter, at various operating conditions. A novel algorithmic procedure utilizing Support Vector Machines (SVM) was developed for estimating the stability boundaries, as described in Appendix C. Further, to alleviate the problem of data sparcity, the trend that increasing g/ρ^* and K_0^* is stabilizing was used to develop a rule for generating subsets of data relevant to a particular (K_0^*, g/ρ^*). This rule, along with the SVM boundary-fitting procedure, makes it possible to find stability boundaries directly from data, rather than visually estimating the location of the boundary. In Appendix D, the stability boundary is plotted on the performance map, with error estimates as well as the relevant measured data, for various cases of (K_0^*, g/ρ^*).

The results of the experimental data analysis quantify the trends with K_0^* and g/ρ^* upon flutter stability, and discuss the effect of inlet pressure, for constant structural properties. It was shown that inlet pressure effects alone were not sufficient to account for the changes in flutter stability, since at a constant inlet pressure, the effects of temperature upon flutter stability were present. This underscores the necessity of considering all four non-dimensional parameters.

Trends were assessed for constant K_0^*, at two locations, and at constant g/ρ^*. These were framed in terms of intersections between the flutter boundary on the performance map, for a particular $(K_0^*, g/\rho^*)$ and lines of constant corrected speed, N_c. For each corrected speed, the sensitivity of the flutter boundary, with respect to K^* and g/ρ^*, was estimated in terms of the critical pressure ratio, π_{cr}, at that corrected speed, and in terms of the critical corrected mass flow, $(\dot{m}_c)_{\mathrm{cr}}$, at that corrected speed. Besides the sensitivity analysis, flutter boundaries were found on the $(K_0^*, g/\rho^*)$ map, for a specific (N_c, π_{cr}) pair. This view shows that the sensitivities with respect to K_0^* and g/ρ^* can vary, depending upon the value of N_c, K_0^*, and g/ρ^*.

Chapter 7 discusses the application of these concepts to the problem of flutter clearance testing. The basic requirement that the machine must be confirmed to be stable at every point of operation, can be simplified by utilizing the trend that increasing K^* and g/ρ^* is stabilizing. This trend is founded in the physical arguments and the results of previous investigators, as discussed in Chapter 3, as well as the computational and experimental results in Chapters 4 and 6. It can be used to identify critical points in the required operating regime for clearance testing. Two examples are shown, based upon data from the Volvo rig discussed in Chapters 5 and 6. These indicate that the use of sensitvities can extend the flutter boundary for relatively small changes in inlet conditions as might be experienced in a subsonic transport applications. However, since the sensitivities vary with flight condition, it may be necessary to test applications with a wide range of flight conditions, such as a supersonic aircraft.

8.2 Conclusions

- For a given geometry, four parameters are necessary and sufficient to assess flutter stability, under broad, specified conditions. The unsteady aerodynamics can be framed in terms of three parameters. In particular, the parameter set, $(\dot{m}_c, N_c, K_0^*, g/\rho^*)$, is uniquely well-suited to flutter operability assessment in the general case.

- A new parameter, the reduced damping, g/ρ^*, collapses the combined effects of mechanical damping, modal mass, and air density. In the typical case of inserted blades, it is order 1 and impacts flutter stability. Further, the critical reduced damping, $(g/\rho^*)_{\mathrm{cr}}$, is a useful metric for aeroelastic computations.

- The effect of increasing g/ρ^* for a constant $\dot{m}_c$, N_c, and K_0^* is stabilizing, which is a consequence of the criterion for flutter stability. Further, the effect of increasing K_0^* at constant $\dot{m}_c$, N_c, and g/ρ^* is also stabilizing. This ultimately has an empirical basis, but unifies separately observed trends in the literature of the stabilizing effect of increasing frequency and the destabilizing effect of increasing inlet temperature.

- A data analysis procedure was developed which makes it possible to estimate flutter boundaries in the full 4D space using steady-state rig data. This procedure incorporates a novel, generic boundary-fitting procedure for binary data, based upon a classification algorithm. The procedure was applied to the analysis of data from full-scale engine tests.

- The full-scale test data indicated that the inlet condition effects upon flutter stability can not be solely attributed to the effects of inlet pressure. In general, a single parameter can not capture the effects of flight condition upon flutter stability.

- A rational procedure for flutter testing has been developed. Since increasing K_0^* and g/ρ^* has a stabilizing effect, clearance at minimum values of K_0^* and g/ρ^* is sufficient.

8.3 Future Work

The work described in this thesis may be further developed in a number of different directions.

- Although the focus in the current work has been upon flutter stability, the non-dimensional parameters developed are generally applicable to general aeroelastic properties of the blades. In particular, the effects of flight condition upon *forced vibration* could be expressed in the same terms, using the parameter set $(\dot{m}_c, N_c, K_0^*, g/\rho^*)$. This parameter set could be coupled with the parameters which govern the forcing to construct a unified view parameter dependence of forced vibrations.

- The clearance methodology has not been used in planning of engine testing à priori. It would be useful to apply the metholology under such circumstances to develop a practical testing protocol, based upon this methodology.

- The current work addresses the problem of characterizing the operational parameters for a given engine design. A useful extension of this work for use in preliminary design would be to account for at least some of the changes between different designs. In particular, the effects of the blade structural modeshape are known to have significant effects.

- The investigation of stall flutter using the 2D, invisicid, compressible model revealed a highly suggestive relationship between the fluid force phase and the quantity $k/(1-M^2)$ for a variety of Mach numbers, reduced frequencies, which held for several different cascade geometries, and flow angles. This gives a clue as to the proper combination of acoustic and inertial time scales for the flutter mechanism. This could be the starting point for work to elucidate, on a physical basis, the flutter mechanism in this idealized case of compressible, potential flow. Ultimately, such work could recast the vibration-induced fluid forces, $l\,(M, \alpha, K^*)$, into a more specific form motivated by the flutter mechanism.

Appendix A

Derivation of the Non-dimensional Fluid Operator

In this appendix, the conditions associated with the form for the vibration-induced fluid forces, (2.3),

$$F_j = c\rho U^2 \, l_j(\bar{\eta}_1, \ldots, \bar{\eta}_n; M, \alpha, \tilde{K}^*)$$

are delineated. For the general problem, one needs to include the compressible Navier-Stokes equations and boundary conditions from all the blades. The solution to these equations is the fluid pressure field, p. The generalized force for blade j is a weighted integral over the unsteady pressure field, written as

$$F_j = -\int_{\mathbf{blade}_j} p\,(\phi \cdot d\mathbf{A}) \tag{A.1}$$

where ϕ is the modeshape, and $d\mathbf{A}$ is the (outward) directed differential area.

A.1 Equations for the pressure field

The non-dimensional pressure, p', is defined in terms of the inlet pressure, p_0. Thus,

Quantity	expression	units
blade chord	c	length
inlet density	ρ_0	mass/(length)^3
inlet temperature	T_0	temperature
inlet sonic speed	$\sqrt{\gamma R T_0}$	length / time

Table A.1: List of fundamental fluid dynamic scales. R is the gas constant and γ is the ratio of specific heats.

$$p = \gamma p_0 p' = \rho_0(\gamma R T_0)p' \tag{A.2}$$

The fundamental flow scales are listed in Table A.1. Using these same scalings, the mass, momentum, and energy balances for a compressible, viscous fluid in the rotating coordinate frame of the blades become

$$\frac{D\rho'}{Dt'} + \rho'\nabla' \cdot \mathbf{U}' = 0 \tag{A.3}$$

$$\rho'\frac{D\mathbf{U}'}{Dt'} = -\nabla' p' + \frac{M}{Re}\nabla'\boldsymbol{\tau}' - 2\rho'\Omega'^2 r'\hat{\mathbf{r}} - \rho'\Omega'(\hat{\mathbf{z}} \times \mathbf{U}'), \tag{A.4}$$

$$\frac{1}{\gamma(\gamma-1)}\rho'\frac{DT'}{Dt'} = \frac{1}{\gamma-1}\frac{M}{Pr\ Re}\nabla' \cdot (k'\nabla' T') - \frac{M}{Re}(\boldsymbol{\tau}' : \nabla'\mathbf{U}') - p'\nabla' \cdot \mathbf{U}' \tag{A.5}$$

where primed quantities are non-dimensional, with definitions listed in Table A.1. These field equations bring several non-dimensional parameters into the problem including the characteristic blade relative Mach number, M, the characteristic Reynolds number, Re, the rotation (Rossby) number, Ω', and the Prandtl number. Not all of these turn out to be necessary. Before discussing simplifications based on the flow regime of interest, we first introduce the extra parameters from the boundaries.

Quantity	value	description
p'	$p/\gamma R\rho_0 T_0$	non-dimensional pressure
ρ'	ρ/ρ_0	non-dimensional density
$\mathbf{x}'$	$\mathbf{x}/c$	non-dimensional position
$\mathbf{U}'$	$\mathbf{U}/\sqrt{\gamma R T_0}$	non-dimensional velocity
t'	$t\sqrt{\gamma R T_0}/c$	non-dimensional time
T'	T/T_0	non-dimensional Temperature
∇'	$c\nabla$	non-dimensional 'del' operator
$\boldsymbol{\tau}'$	$\boldsymbol{\tau}/\gamma R\rho_0 T_0$	non-dimensional shear stress
k'	k/k_0	non-dimensional heat conductivity coefficient

Table A.2: List of non-dimensional flow variables. These are defined in terms of the scales in Table A.1. k_0 is the heat conductivity at the inlet.

A.1.1 Boundary Conditions

The boundaries of the flow problem can be categorized into two parts: (1) the upstream, and downstream fluid boundaries, and (2) the rigid (hub and casing) and flexible (blades) solid boundaries. Therefore, we organize the domain boundary as follows:

$$\partial D = \partial D_u \cup \partial D_d \cup \partial D_r \cup \partial D_{b_1} \cup \ldots \cup \partial D_{b_n} \tag{A.6}$$

where the terms on the right hand side denote the upstream (∂D_u), downstream (∂D_d), rigid (∂D_r), and the blade boundaries (of the form ∂D_{b_j}). For the present purposes, only the parameter dependencies of the boundary conditions are of interest. In particular, we seek to find what other parameters (besides those in the previous description) are necessary in the flow problem description.

Since there are 5 equations in the field (conservation of mass, three components of momentum equation, and the energy equation), it is clear that 5 variables must somehow be accounted on each boundary. Although the number of explicit conditions is at most 5, for the purposes of parameter dependencies, only those explicit conditions which require outside information are relevant. A general discussion concerning boundary conditions in this problem can be found in Verdon (1993).

Upstream and Downstream Boundaries

We specify conditions at the inlet: in particular, the steady-state values of $\mathbf{U}'$, T', and ρ'. By definition, $T' = \rho' = 1$ at the inlet, which does not require outside parameters. Furthermore, the $\mathbf{U}'$ distribution is assumed to be specified by two parameters: (a) a characteristic Mach number, M, and (b) a characteristic flow angle, α. The assumption that these two quantities specify the inlet velocity is equivalent to specifying that the inlet swirl distribution is fixed by operating point and is axi-symmetric.

Using information only at the inlet raises the issue of *well-posedness* of the boundary conditions. The downstream boundary can not be deduced from the inlet conditions (and the field equations) in the case of "unique incidence." In our case of ***stall flutter***, the compressor operating point typically lies outside the unique incidence region, in which lines of corrected speed are vertical on the performance map (see Figure A-1). Therefore, specifying conditions (M, α) at the inlet is sufficient to specify the operating point

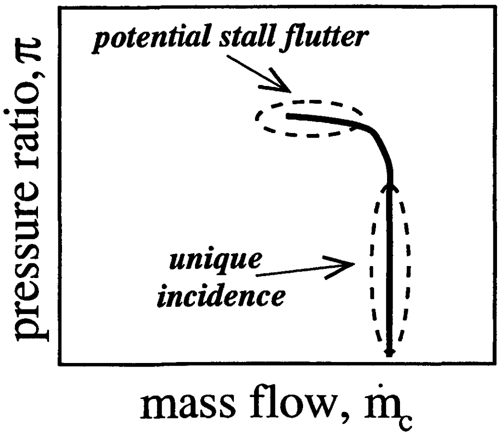

Figure A-1: Typical compressor performance at constant corrected speed, N_c.

for conditions relevant to stall flutter.

So far, we have described the boundary conditions (on ∂D_u and ∂D_d) for steady flow. With vibrating blades, however, it is important to make sure the boundary does not artificially reflect unsteady waves. Such non-reflective boundary conditions are relatively sophisticated, but do not require outside physical parameters. See Giles (1988) for further discussion on non-reflective conditions.

Solid boundaries

The conditions for the rigid surfaces (∂D_r) can be specified by the no-slip condition for the three velocities, and by an adiabatic condition for the temperature, which is reasonable for fans and compressors. The hub velocity is zero in the rotating frame, and the casing non-dimensional velocity depends upon Ω', which was identified in the discussion of the momentum equation.

At flexible boundaries, ∂D_{b_j}, the no-slip condition also holds. The blade vibration is manifested in both the location of the boundary as well as the value of the velocity at that location. If we label $B'_j(x')$ as the unperturbed location and $\bar{\eta}_j \phi_j(x') e^{i\omega t}$ as the pertubation (where ϕ_j is the modeshape and η is the modal coordinate), we can write the boundary condition for blade j as

$$\mathbf{U}'(\mathbf{x}', t)|_{\mathbf{x}' \in \partial D_{b_j}} = \frac{\partial}{\partial t'} \left(\bar{\eta}_j \phi(\mathbf{x}') e^{i\omega t} \right). \tag{A.7}$$

Here, we assume that the frequency and modeshape are effectively the same for each blade, but that they may vibrate out of phase, according to the complex argument of $\bar{\eta}$. Since the boundary ∂D_{b_j} itself is moving, it is more explicit to write

$$\mathbf{U}'(B'_j(\mathbf{x}') + \bar{\eta}_j \phi(\mathbf{x}') e^{i\omega t}, t') = \bar{\eta}_j \phi(\mathbf{x}') \frac{\partial}{\partial t'} e^{i\omega t}. \tag{A.8}$$

Note that there are two time variables in (A.8), the dimensional time, t, and the dimensionless time, t' (from Table A.1). We can relate these timescales using the parameter, K^*

$$\tilde{K}^* = \frac{c \ \mathrm{Re}(\omega)}{\sqrt{\gamma R T_0}} = \frac{t' \mathrm{Re}(\omega)}{t}. \tag{A.9}$$

Here the $\approx$ indicates that we are using the "actual" frequency, $\mathrm{Re}(\omega)$, rather than the natural frequency, ω_0.

The relevant flow at neutral stability has $\mathrm{Im}(\omega) = 0$, or zero growth/decay. In this instance, the condition for blade j, (A.8), becomes

$$\mathbf{U}'(B'_j(\mathbf{x}') + \bar{\eta}_j \phi(\mathbf{x}') e^{i\tilde{K}^* t'}, t') = \bar{\eta}_j \phi(\mathbf{x}') \tilde{K}^* e^{i\tilde{K}^* t'}. \tag{A.10}$$

From the standpoint of the parameter dependence, the details of equation (A.10) are not relevant, other than the fact that it introduces non-dimensional parameters not included in the field equations. Since there are boundaries for each blade, the complex blade amplitudes, $\bar{\eta}_j$, for $j = 1 \ldots n$, are necessary (where n is the number of blades), as is the compressible reduced frequency K^*, as defined in equation (A.9).

A.1.2 Summary of Dependence

The non-dimensional pressure field, p', is completely specified by equations (A.3), (A.4), (A.5), and the above mentioned boundary conditions, including (A.10). This introduces a number of non-dimensional parameters, and entails several assumptions as well.

We outline the assumptions up to this point, and apply some conditions to reduce the number of non-dimensional parameters. The foregoing assumptions are:

- (a) fixed, nominal flowpath geometry
  (b) single blade mode, ϕ, with modal parameters (m_0, g, ω)
  (c) adiabatic blades
- Inlet flow boundary conditions are sufficient to specify the steady flow problem.
- Inlet flow is axisymmetric and has a radial swirl distribution which is specified by Mach number, M, and flow angle, α.

The first condition is relevant to the solid boundary conditions, including (A.10), and in relating the pressure field with the generalized fluid forces, (A.1). The second and third conditions are relevant to the upstream and downstream boundary conditions. The field equations used are the compressible Navier-Stokes equations in a rotating frame.

At this point there are several non-dimensional variables in the problem.

$$Re,\ M,\ \Omega',\ Pr,\ \alpha,\ \tilde{K}^*,\ \bar{\eta}_1, \ldots, \bar{\eta}_n$$

However, three of these can be eliminated from consideration due to the flow regime and the above assumptions. The flow regime in aeroengines is typically very high Reynolds number, $O(10^6)$, and has a Prandtl number, $Pr \approx 1$. Adding this as an assumption eliminates the effects of Reynolds number and Prandtl number. The viscous and heat conduction effects that they are typically associated with are important; however, the changes in values of Re and Pr keep the flow in the same regime with respect to these effects and does not significantly change the results. For example, Isomura (1997), found that changes in Reynolds number by a factor of 2 did not significantly affect his viscous flow computations of aeroengine flutter (which had $Re = 10^6$).

Second, the rotation number, Ω', can be defined in terms of the corrected speed, N_c, as follows:

$$\Omega' = \frac{2\pi c N_c}{\sqrt{\gamma R T_r}}$$

where T_r is a (constant) reference temperature. Since, we are considering a fixed, nominal flowpath geometry, c is constant, and N_c can be expressed in terms of M and α, which are already included as non-dimensional parameters. Therefore, we can consider Ω' to be a *dependent* parameter.

Form for the generalized fluid force

Thus, the pressure operator becomes

$$p' = p'(\bar{\eta}_1, \ldots, \bar{\eta}_n, M, \alpha, \tilde{K}^*). \tag{A.11}$$

The generalized fluid force, F_j, can then be expressed

$$F_j = \rho U^2 l_j(\bar{\eta}_1, \ldots, \bar{\eta}_n, M, \alpha, \tilde{K}^*) \tag{A.12}$$

as required. The only additional conditions beyond those identified above are those of (a) high Reynolds number, Re, and (b) Prandtl number near unity, both of which are present for aircraft engine applications.

Periodic Side Boundaries

With the additional condition of linearized, unsteady dynamics it has been shown by Lane (1954), that one does not actually need all the complex amplitudes for all the blades, $\bar{\eta}_j$ for $j = 1 \ldots n$. Rather, it suffices to assume that the *interblade phase*, the phase difference between the complex amplitudes of adjacent blades, is fixed. The inter-blade phase, σ, can take on n possible values: $\sigma_j = (2\pi j/n)$. Thus, we can write the force coefficient as

$$l_j(\bar{\eta}_1, \ldots, \bar{\eta}_n, M, \alpha, \tilde{K}^*) = l_j(\bar{\eta}_1 e^{i\sigma}, \bar{\eta}_1 e^{2i\sigma}, \ldots, \bar{\eta}_1, M, \alpha, \tilde{K}^*) = l_j(\bar{\eta}_1, M, \alpha, \tilde{K}^*, \sigma). \tag{A.13}$$

Since, we furthermore, have assumed that l_j is linear with $\bar{\eta}$, we can further simplify this as follows:

$$l_j(\bar{\eta}_1, M, \alpha, \tilde{K}^*, \sigma) = l(M, \alpha, \tilde{K}^*, \sigma)\bar{\eta}_j = l_\sigma(M, \alpha, \tilde{K}^*)\bar{\eta}_j \tag{A.14}$$

where l_σ is a notation used to signify the σ dependence upon l. Ultimately, for stability purposes, all possible motions are considered (either in terms of individual blades, η_j, or in terms of interblade phase, σ), and only the worst case is selected. However, it is helpful to consider the parameter reduction using the inter-blade phase angle in the expression for the fluid forces, since this is the form used in nearly all computational solutions.

A.2 Alternate, equivalent formulation

Consider the following variation on the definition of the non-dimensional pressure:

$$p'_2 = M^2 p' = \frac{p}{\rho U^2}$$

Using p'_2 instead of p', the fluid forces become

$$F_j = \rho_0 U^2 l'_j(\bar{\eta}_1, \ldots, \bar{\eta}_n, M, \alpha, K^*)$$

where l'_j is defined as

$$l'_j = \frac{l_j}{M^2} \tag{A.15}$$

Furthermore we can make the substitution $k = K^*/M$ for K^* in the parameter dependence of l'_j, since M is available as a independent parameter. Thus, we can write

$$F_j = \rho_0 U^2 l'_j(\bar{\eta}_1, \ldots, \bar{\eta}_n, M, \alpha, k). \tag{A.16}$$

as an equivalent formulation (in the sense of parametric dependence).

Appendix B

Uniqueness of operability parameters

The purpose of this appendix is to demonstrate that under a particular set of operability requirements, one set of variables uniquely specifies the 4-D parameter space, in some sense. In particular, this motivates the use of the compressible reduced frequency, K^*, instead of the classical reduced frequency, k, for operability purposes. We also discuss a generalization to the case of centrifugal stiffening, in which it is helpful to use a centrifugally-corrected frequency parameter, K_0^*.

The parameter space is constructed in Chapter 2, and may be spanned by the four variables: (M, α, k, g/ρ^*), where M is the blade relative mach number, α is the inlet flow angle, and g/ρ^* is the reduced damping. Typically, the choice of variables to span this non-dimensional space from deduction from the basic physical scales of the problem. However, in the types of stall flutter which are of interest, there are several competing physical effects, and it is not obvious which choice of scales is most appropriate. We approach this question from the standpoint of selecting the parameters most useful for assessing operability limits. The requirements that we impose are, for a fixed geometry (i.e. chord),

1. The four parameters must span the whole parameter space.
2. Two of the parameters specify the corrected performance map.
3. The other two parameters, for constant structural properties, specify the flight condition in terms of inlet temperature and density.
4. The vibration induced fluid force coefficent, l, is independent of (at least) one of the parameters.

The first requirement is obvious.

The second requirement is in keeping with current practice in assessing steady-state aerodynamic effects for such devices, since the corrected performance map alone is sufficient for these purposes. The purpose of these corrected variables (corrected mass flow, $\dot{m}_c$, and corrected speed, N_c) is to "correct" for the effects of changing inlet stagnation pressure, which scales out of the purely aerodynamic problem.

The third requirement places, for constant structural properties, the inlet conditions in terms of the other two variables in the parameter space. These other parameters can be thought of as the factors which are "corrected out" of the corrected performance parameters. This will be made mathematically precise later in this appendix.

The fourth requirement serves to "simplify" the problem. Since the unsteady aerodynamics is the most complicated part of the problem, structuring the parameters such they do not depend upon it makes things as "simple" as possible. It turns out that this can only be done with the reduced damping, g/ρ^*.

B.1 Primitive Variables

The non-dimensional parameter space must be defined, ultimately, in terms of primitive dimensional variables. The primitive variables in this problem are as follows, grouped by category:

flight condition	T_0, ρ_0
flow vars.	U, α
structural vars.	ω_0, m, g
geometry	c

here T_0 and ρ_0 are inlet temperature and density, respectively, U is the inlet relative velocity, and α is the characteristic flow angle, and ω_0, m and g are the modal frequency, mass, and damping, respectively. In what follows, we consider a fixed geometry, such that c is fixed.

B.2 Derivation of the Parameter Set

By the second requirement, two of the variables in the parameter space must span the corrected performance map. This is accomplished in terms of the primitive variables by the corrected speed, N_c, and the corrected mass flow, $\dot{m}_c$. Although the correced speed and corrected mass flow are technically dimensional parameters, they are composed of a non-dimensional parameter times a dimensional constant. Therefore, we treat them as non-dimensional parameters. From their definitions, it can be shown that for constant geometry as specified, the pair, $(\dot{m}_c, N_c)$ is equivalent to the Mach number and flow angle (M, α) (see Kerrebrock, 1992).

The comment in Appendix A concerning the case of "unique incidence" is relevant here. In this case, the Mach number and flow angle are dependent. The remedy is to use the pressure ratio, π, as a non-dimensional parameter, replacing either the corrected mass, or the corrected speed in the final set of parameters (which are framed in terms of the above parameters) with the pressure ratio. Such a remedy does not alter any of the conditions above. Strictly speaking, this can be thought of as "non-unique" since we can choose whether to use the pressure ratio or to use the corrected speed, for example. In practice, however, the performance map is well understood in turbomachinery aerodynamics, and it is reasonable to consider the parameter space "unique" even in the face of this ambiguity.

Theorem:
Given the above definitions of primitive variables (for a fixed chord), and a parameter set, $(\dot{m}_c,\ N_c,\ x,\ y)$, which spans the parameter space of $(M,\ \alpha,\ k,\ g/\rho^*)$. The requirements

- For const. structural vars., flight condition is a smooth, one-to-one function of x and y
- Vibration induced force coef., $l\,(\dot{m}_c, N_c, x)$ is independent of y.

imply that,

$$\begin{aligned} x &= \mathrm{fn}\,(K^*), \text{and,} \\ y &= \mathrm{fn}\,(g/\rho^*) \end{aligned}$$

where fn means "a smooth, one-to-one function of" (i.e. a diffeomorphism).

Proof For the first condition to hold, we must be able to express the temperature and density in terms of unknown, smooth, monotone, functions f_1 and f_2 as follows:

$$T_0 = f_1(x, y; \omega_0, m, g, c, \gamma R), \text{and,} \tag{B.1}$$

$$\rho_0 = f_2(x, y; \omega_0, m, g, c, \gamma R). \tag{B.2}$$

In this case, the flight condition in terms of the thermodynamic state (inlet temperature, T_0, and density, ρ_0), can be expressed as a one-to-one function of the unknown parameters x and y for constant structural properties (ω_0, m, and g).

By the implicit function theorem, we can use these combine these relations to solve for the functional form of x and y. Since the functions f_1 and f_2 are diffeomorphisms with respect to x and y, the result is global. Thus,

$$x = f_3(y, T_0, \rho_0, \omega_0, m, g, c, \gamma R), \text{and,} \tag{B.3}$$

$$y = f_4(x, T_0, \rho_0, \omega_0, m, g, c, \gamma R). \tag{B.4}$$

we can further substitute one relation in to another and solve to obtain

$$x = f_5(T_0, \rho_0, \omega_0, m, g, c, \gamma R), \text{and,} \tag{B.5}$$

$$y = f_6(T_0, \rho_0, \omega_0, m, g, c, \gamma R), \tag{B.6}$$

again invoking the implicit function theorem.

At this point, the principle of similarity is applied (Buckingham, 1914). There are five variables and two constants (c and γR) in f_5 and f_6. These have the following units:

T_0	ρ_0	ω_0	m	g	c	γR
temp	mass/length^3	1/time	mass	-	length	length^2 / time^2 / temp

Since there are seven variables and four fundamental units, we expect to see 3 non-dimensional Π groups.

Three groups which incorporate the parameters are (K^*, g, ρ^*) where

$$\begin{aligned} K^* &= \frac{\omega_0 c}{\sqrt{\gamma R T_0}}, \text{and,} \\ \rho^* &= \frac{\rho_0 c^3}{m} \end{aligned}$$

Thus, we can write

$$\begin{aligned} x &= f_7(K^*, g, \rho^*), \text{and,} & \text{(B.7)} \\ y &= f_8(K^*, g, \rho^*). & \text{(B.8)} \end{aligned}$$

Now, the second condition that l_σ is independent of y and is a function of $\dot{m}_c$, N_c, and x. As discussed previously, ($\dot{m}_c$, N_c) is equivalent to (M, α). Thus, we can say that the second condition requires that there exists a diffeomorphism between (M, α, k), and (M, α, x). This is true if we can say that there exists a diffeomorphism h_1 such that

$$x = h_1(M, \alpha, k) \tag{B.9}$$

However, we also have another expression (B.8) for x. We can make the following deductions:

$$\begin{aligned} \frac{\partial x}{\partial g} = \frac{\partial h_1}{\partial g} = 0 \\ \frac{\partial x}{\partial \rho^*} = \frac{\partial h_1}{\partial \rho^*} = 0 \end{aligned}$$

we can therefore drop the g and ρ^* dependences in (B.8) and write

$$x = f_9(K^*). \tag{B.10}$$

where f_9 is a diffeomorphism.

Also, the independence of l_σ from y implies the following:

$$\frac{\partial l_\sigma(M,\alpha,k)}{\partial y} = \frac{\partial l_\sigma}{\partial M}\frac{\partial M}{\partial y} + \frac{\partial l_\sigma}{\partial \alpha}\frac{\partial \alpha}{\partial y} + \frac{\partial l_\sigma}{\partial k}\frac{\partial k}{\partial y} = 0$$

Thus,

$$\frac{\partial M}{\partial y} = \frac{\partial \alpha}{\partial y} = \frac{\partial k}{\partial y} = 0. \tag{B.11}$$

This implies that y can not have any dependence upon K^*, otherwise there would be a Mach number or reduced frequency dependence. Hence,

$$y = f_{10}(g, \rho^*).$$

To complete the space, y must take the following form

$$y = f_{11}(g/\rho^*).$$

where f_{11} is a diffeomorphism. This proves the theorem.

B.3 Generalization to the Case of Centrifugal Stiffening

We can extend these results to the case in which the structural parameters vary during the operation of the machine due to centrifugal stiffening. In this case, the vibrational frequency becomes

$$\omega_0 = \left(\omega_{\text{rest}}^2 + sN_{\text{raw}}^2\right)^{\frac{1}{2}}. \tag{B.12}$$

The extension to the compressible reduced frequency, K^*, is the centrifugally corrected form, K_0^*, as defined in equations (5.5), and (5.6),

$$K^* = \left((K_0^*)^2 + \frac{sc^2}{\sqrt{\gamma RT_{\text{ref}}}} N_c^2\right)^{\frac{1}{2}}.$$

where

$$K_0^* = \frac{\omega_{\text{rest}} c}{\sqrt{\gamma RT}}.$$

If we modify the third condition such that it holds not for constant structural parameters (i.e. $s = 0$ in equation B.12), but rather for a specified, non-zero s, then we can satisfy the conditions by using the parameter set: ($\dot{m}_c$, N_c, K_0^*, g/ρ^*).

This result follows from the same proof as above, but by modifying the primitive variables used, replacing ω with ω_0. In this case, the parameter set which emerges includes K_0^*.

Since, for $s = 0$, we retain the original case of constant structural parameters, the parameter set: ($\dot{m}_c$, N_c, K_0^*, g/ρ^*), is, in fact, a generalization rather than a special case.

Appendix C

Boundary fitting using Support Vector Machines

This report describes a data-abstraction technique based upon an algorithm called a Support Vector Machine (SVM), which has been previously applied to the problem of optimally classifying binary data (Vapnik, 1995, Burges, 1998). Given two types of data points situated in a multi-dimensional space, the current procedure can estimate the equations of curved surfaces (from a specified function class) which separate the two types of data. This is somewhat different from the usual formulation of classification using Support Vector Machines which does not explicitly construct the boundary surface. The extension to generating the equation of the bounding surface is novel.

This general technique is applied to the problem of fitting flutter stability boundaries in parameter space. We first describe the stability boundary fitting problem and how the current technique might be used in this context. Then, the boundary fitting technique is derived, including the description of a Support Vector Machine. Finally, some test cases are presented to show the performance of the procedure.

Although we discuss the SVM boundary-fitting technique in the context of fitting boundaries to stability data, it should be clear that the technique is general, and may be applied towards boundary-fitting of any sort of data.

C.1 Description of Aeroelastic Stability Data

The experimental aeroelastic data taken from aeroengine tests typically lists the operating points (as well as modeshape and frequency) of flutter points encountered when testing a given machine. From this raw information, we would like to deduce the stability boundary. Before describing the boundary-fitting, we first discuss the general context of linear stability.

With the assumption that the flutter instability obeys linear dynamics, the stability can be determined by a scalar: the system damping, δ. For positive values of δ, the system is stable, while for negative values, the system is unstable. The stability boundary is defined by the equation $\delta = 0$.

The overall damping is governed by the most unstable vibrational mode. Figure C.1 schematically shows a stability curves in an operating space, $\mathcal{V}$. The particular curve which corresponds to zero damping separates the stable region from the unstable region.

The ith experimental data point can be represented as an ordered pair, $(\mathbf{v}_i, s_i)$, where $\mathbf{v}_i$ is the location in the operating space and s_i is 1 for stable points and -1 for unstable points. In our case, the sampling of the data in the parameter space is relatively sparse. From these sparse data, we need to estimate the shape of the stability surface which is defined as the region where $\delta(\mathbf{v}) = 0$ is satisfied.

Usually, the stability data lies close to the stability boundary. Sometimes, however, points in "deep" flutter are tested. Also, stable data can also help define the boundary, by applying the criterion that the boundary should not penetrate into the region of stable points. Finding the boundary is similar to the mathematical problem of "classification": based on training points associated with 2 groups, determine the regions of parameter space associated with each group. This is distinct from the problem of regression (fitting a curve through points). Recent techniques (Vapnik, 1995) of Support Vector Machines (SVM) allow this classification to be done automatically, optimally, and for high dimensional data.

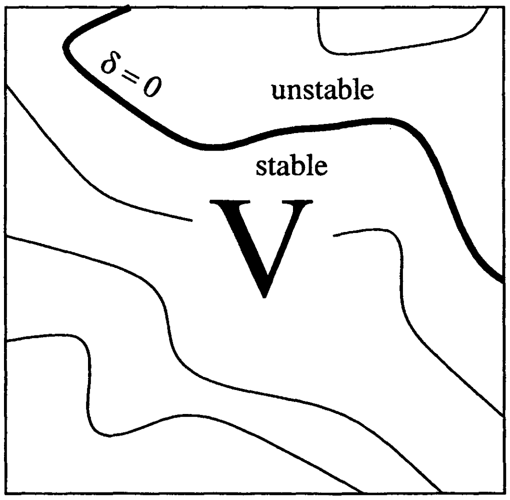

Figure C-1: Picture of abstract operating space, $\mathcal{V}$, with lines of constant damping, δ.

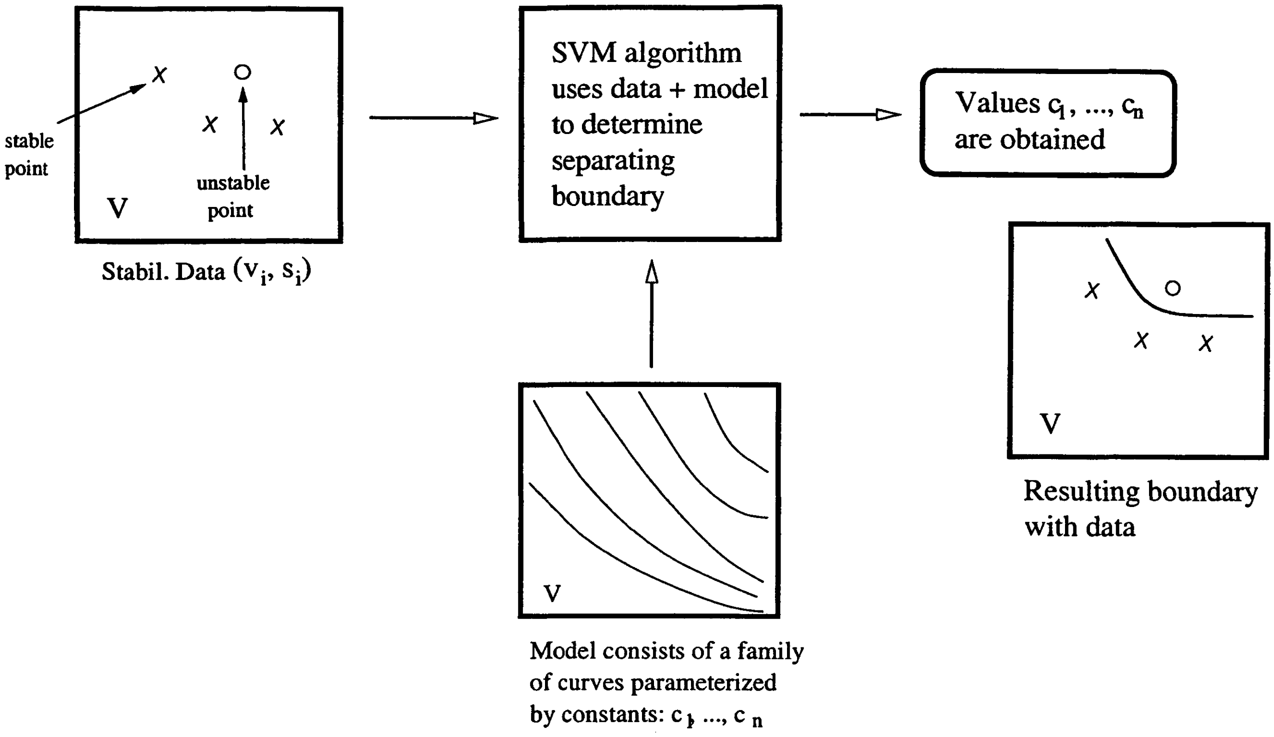

Figure C-2: Schematic of boundary fitting procedure. The binary experimental data is run through a classification algorithm which selects the best among a class of boundaries. For a specific damping model, this specifies the free constants in the model.

A model for the parameter dependence upon damping (for a given mode) takes the form $\delta_1(\mathbf{v}; c_1 \ldots c_l)$, where $\mathbf{v}$ is the point in the operating space, and $c_1 \ldots c_l$ are constants which specify the model. Such a model can be helpful in data analysis by parameterizing the boundary in terms of the c's. The equation,

$$\delta_1(\mathbf{v}; c_1 \ldots c_l) = 0,$$

defines a class of boundaries in $\mathcal{V}$, parameterized by the c's. By restricting to this model for boundaries, one can use SVM classification to select the most appropriate values for the c's on the basis of the data. This begs the question: in what sense is this selection of the c's "most appropriate"? As will be further discussed, the SVM picks the c's with a minimium in expected *generalization error* by maximizing the distance the boundary lies from each group of points.

The overall process is shown schematically in Figure C-2.

C.2 Data Classification using Support Vector Machines

Applications using support vector machines (SVM) for classification and regression are recent (for a review see Burges(1998)). The general idea for SVM has been around longer than the applications and was originated by V. Vapnik (Vapnik, 1979). It has a mathematical foundation in statistical learning theory, and there is an extensive theory concerning bounds of the expected performance of proposed boundaries (see Vapnik (1995)). Here, instead a formal treatment of the general principles, a specific implementation of a Support Vector Machine is derived. More extensive explanations of SVM Classification may be found in Burges (1998), Schölkopf et. al. (1999), and Vapnik (1998).

C.2.1 Optimal Separating Hyperplane

Support Vector Machines are founded upon the derivation of the *optimal separating hyperplane* between two groups of points. A hyperplane in an n dimensional space is defined as an $n-1$ dimensional linear subspace. For example, in 2D this is a line, and in 3D this is a plane.

The hyperplane is optimal in the sense that it maximizes the distance to the closest point in each group of data. Since the hyperplane is also supposed to separate the two groups, it is useful to use the *directed* distance from the plane. Then, for a hyperplane which lies between the two groups, the distance to points in one group is negative, while the distance to points in the other group is positive.

The pair $(\mathbf{v}_i, s_i)$ describes a data point, where $\mathbf{v}_i$ is the location parameter space, $\mathcal{V}$, and s_i is -1 for points in the first group and 1 for points in the second group. We label n as the number of data points and m as the dimension of $\mathcal{V}$. The hyperplane is defined by the equation

$$\mathbf{w} \cdot \mathbf{v} + b = 0 \tag{C.1}$$

where $\mathbf{w} \in \mathcal{V}$ is the directed normal of the hyperplane, and $|b|/||\mathbf{w}||$ is its distance from the origin. The distance from the hyperplane to a given data point is given by

$$d_{\mathbf{v}_i} = \frac{\mathbf{w} \cdot \mathbf{v}_i + b}{||\mathbf{w}||}.$$

Since the hyperplane should separate the data, we would like $d_{\mathbf{v}_i}$ to be positive for data points in one group and negative for those in another group. Or,

$$\begin{aligned} d_{\mathbf{v}_i} &\geq \epsilon \quad \text{for } s_i = 1 \\ d_{\mathbf{v}_i} &\leq -\epsilon \quad \text{for } s_i = -1 \end{aligned}$$

for some $\epsilon > 0$. If such an ϵ exists, the data are considered *linearly separable.* The case of linearly inseparable data will be treated later in this section. The above separability constraints do not uniquely define the hyperplane, however. Without loss of generality, we consider only $\mathbf{w}$'s for which $\epsilon||\mathbf{w}|| \geq 1$. The separability condition becomes

$$\begin{aligned} \mathbf{w} \cdot \mathbf{v}_i + b &\geq 1 \qquad \text{for } s_i = 1 \\ \mathbf{w} \cdot \mathbf{v}_i + b &\leq -1 \qquad \text{for } s_i = -1. \end{aligned}$$

Which can be more compactly written

$$s_i \left(\mathbf{w} \cdot \mathbf{v}_i + b \right) \geq 1. \tag{C.2}$$

Among all of the hyperplanes which satisfy the separating condition, (C.2), the *optimal* hyperplane is that one which maximizes its minimum distance from the data. For each group, the minimum distance satisfies

$$|d_{\mathbf{v}_i}| = \frac{|\mathbf{w} \cdot \mathbf{v}_i + b|}{||\mathbf{w}||} \geq \frac{1}{||\mathbf{w}||}.$$

The optimal separating hyperplane (i.e. the one that maximizes $|d_{\mathbf{v}_i}|$ to each group) is the one which minimizes $||\mathbf{w}||^2$. Figure C-3 shows graphically the effect of selecting the hyperplane with the largest minimum distance. The problem of finding the optimal hyperplane $(\mathbf{w}, b)$ for linearly separable data can be framed in terms of minimizing

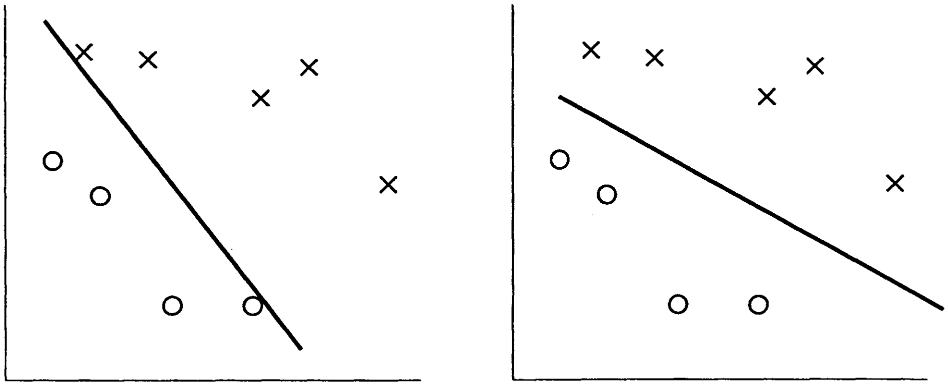

(a) (b)

Figure C-3: Distinction between separating hyperplanes which (a) do not maximize distance to groups of data, represented by × and ∘ symbols, and (b) which do. The boundary in (b) is expected to have better generalization capabilities.

$$F(\mathbf{w}) = \frac{1}{2}||\mathbf{w}||^2 = \frac{1}{2}(\mathbf{w} \cdot \mathbf{w}) \tag{C.3}$$

subject to the constraints

$$s_i\left(\mathbf{w} \cdot \mathbf{v}_i + b\right) \geq 1, i = 1 \ldots n \tag{C.4}$$

There are various algorithms available to solve this constrained optimization problem, known as a *quadratic programming* (QP) problem, since the objective function, F, is quadratic in $\mathbf{w}$, and the constraints are linear.

The constraints on the solution, (C.4), require that the separating hyperplanes must be at least a unit distance away from each of the data points. For the optimal solution, this constraint is pushed to an equality, for at least one point in each group. We can thus consider the hyperplanes parallel to the optimal, which are a unit distance on each side. These "touch" the data on either side, or in mathematical terms, they "support" the data on either side of the optimal hyperplane. A diagram of these *supporting hyperplanes* in relation to the optimal is shown in Figure C-4. The data which lie on the supporting hyperplanes are called "support vectors." For the current application to boundary fitting, it is useful to note that the region between the support vectors contains no data in the separable case (in the non-separable case, penalties

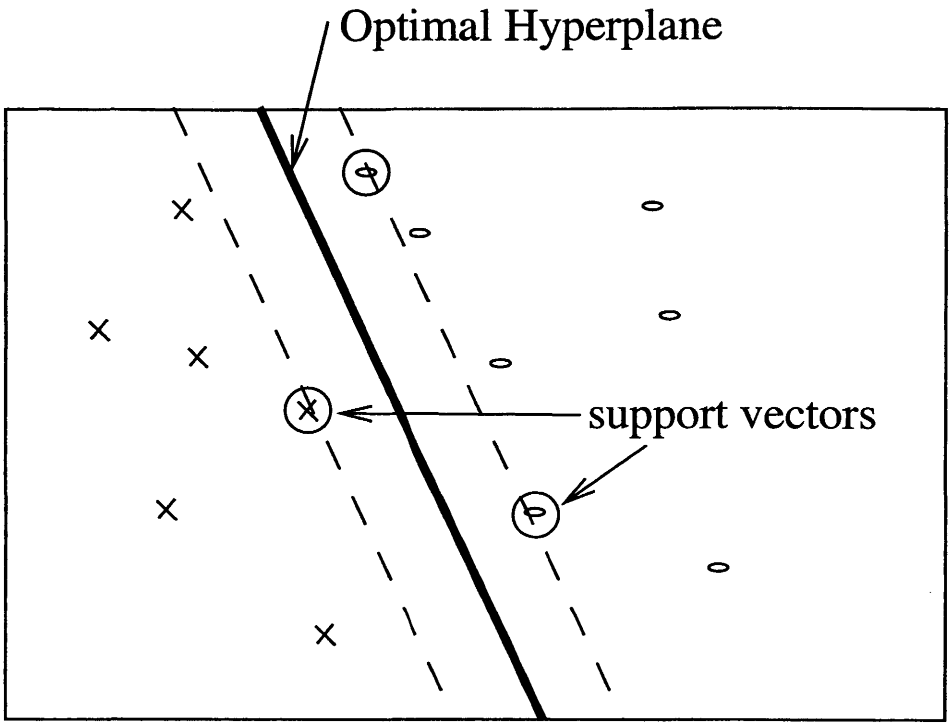

Figure C-4: The optimal hyperplane, solid line, lies between the supporting hyperplanes of each group, dashed lines. The points which lie on the supporting hyperplanes are called "support vectors." In the context of boundary fitting, the range between the supporting hyperplanes can be interpreted as the range of uncertainty in fitting the boundary.

widen this region). Thus, the supporting hyperplanes can be used as bounds of uncertainty for which the optimal hyperplane represents the most probable estimate. Even in the case of non-separable data, which is addressed in the next section, this scaling of a range a unit distance from the optimal hyperplane forms a useful uncertainty estimate.

C.2.2 Extension to non-separable data

Unfortunately, the data may not be separable. To handle this case, Cortes and Vapnik (1995) introduced the idea of *slack variables*,

$$\mathbf{e} = (\xi_1, \ldots, \xi_n)$$

which relax the constraints for certain points, but which contribute as a penalty to the objective function in the optimization. In this case, the optimization problem, as defined by (C.3) and (C.4), becomes

$$Q(\mathbf{w}, \mathbf{e}) = \frac{1}{2}||\mathbf{w}||^2 + C\sum_{i=1}^{n} \xi_i \tag{C.5}$$

subject to the constraints

$$\begin{aligned} s_i(\mathbf{w} \cdot \mathbf{v}_i + b) &\geq 1 - \xi_i, \quad i = 1 \dots n \\ \xi_i &\geq 0, \qquad\quad i = 1 \dots n \end{aligned} \tag{C.6}$$

Instead of solving this optimization problem directly, it turns to be more effective to solve its *dual problem*, which can be shown to have the same solution. Briefly, the dual problem optimizes a different function, whose solutions produces the Lagrange multipliers of the original (primal) problem. For more details on duality theory in optimization, see Bertsekas (1995). The derivation of the corresponding dual problem for the current case follows.

First, the QP problem of (C.5) and (C.6) should be written in terms of a Lagrangian, as follows:

$$L(\mathbf{w}, b, \mathbf{e}, \mathbf{a}, \mathbf{b}) = \frac{1}{2}(\mathbf{w} \cdot \mathbf{w}) + C\sum_{i=1}^{n} \xi_i - \sum_{i=1}^{n} \alpha_i (s_i(\mathbf{w} \cdot \mathbf{v}_i + b) - 1 + \xi_i) - \sum_{i=1}^{n} \beta_i \xi_i \tag{C.7}$$

where $\mathbf{a} = (\alpha_1 \dots \alpha_n)$ and $\mathbf{b} = (\beta_1 \dots \beta_n)$ are the non-negative Lagrange multipliers associated with the constraints in (C.6). For such a quadratic programming problem, the following Kuhn-Tucker conditions (see Bertsekas, 1995, for details) are necessary and sufficient to guarantee optimality:

$$\left.\begin{aligned} \frac{\partial L}{\partial \mathbf{w}_i} &= 0 \\ \frac{\partial L}{\partial b} &= 0 \\ \frac{\partial L}{\partial \xi_i} &= 0 \end{aligned}\right\} \tag{C.8}$$

$$\left.\begin{aligned} s_i(\mathbf{w} \cdot \mathbf{v}_i + b) &\geq 1 - \xi_i \\ \xi_i &\geq 0 \end{aligned}\right\} \tag{C.9}$$

$$\left.\begin{aligned} \alpha_i &\geq 0 \\ \beta_i &\geq 0 \end{aligned}\right\} \tag{C.10}$$

$$\left.\begin{array}{rcl}\alpha_i\left(s_i\left(\mathbf{w}\cdot\mathbf{v}_i+b\right)-1+\xi_i\right) & = & 0\\ \beta_i\xi_i & = & 0\end{array}\right\}\qquad\text{(C.11)}$$

where $i = 1 \ldots n$. This set of conditions can be categorized into four groups. The equations specified in (C.8) state that the partial derivatives of the Lagrangian are zero for the variables to be optimized. The conditions (C.9) are the original constraints from the QP problem. The positivity of the Lagrange multipliers is reflected in (C.10). Finally, (C.11) are the *complementarity* conditions. In each equation of (C.11) there are two factors, a Lagrange multiplier factor and a constraint factor. From (C.9) and (C.10) one can observe that both factors are non-negative. Therefore, the linear complementarity conditions (C.11) imply that *either the constraint factor or the Lagrange multiplier is zero* for each i.

By plugging in the Lagrangian, (C.7), the derivative conditions, (C.8) become

$$\left.\begin{array}{rcll}(w_i)^* & = & \sum_{k=1}^{n}\alpha_k s_k (v_i)_k, & i=1\ldots n\\ \sum_{k=1}^{n}\alpha_k s_k & = & 0 & \\ \beta_i & = & C-\alpha_i, & i=1\ldots n\end{array}\right\}\qquad\text{(C.12)}$$

which holds at the optimal point, $(\mathbf{w}^*, b^*)$. To derive the dual problem, one plugs in the conditions for the optimal solution (C.12) into the Lagrangian (C.7) to derive a new quadratic form, Q_d, in terms of the Lagrange multipliers, $\mathbf{a}$ and $\mathbf{b}$. The *dual* problem is to maximize this quadratic form, Q_d, with respect to the conditions upon the Lagrange multipliers from (C.10) and (C.12).

Equations (C.12) and (C.7) can be combined to find Q_d, as follows

$$\begin{aligned}Q_d(\mathbf{a},\mathbf{b},\mathbf{e}) &= \frac{1}{2}(\mathbf{w}^*\cdot\mathbf{w}^*)+C\sum_{i=1}^{n}\xi_i-\mathbf{w}^*\cdot\left(\sum_{i=1}^{n}\alpha_i s_i\mathbf{v}_i\right)+b\left(\sum_{i=1}^{n}\alpha_i s_i\right)+\sum_{i=1}^{n}\alpha_i-\sum_{i=1}^{n}\alpha_i\xi_i-\sum_{i=1}^{n}\beta_i\xi_i\\ &= -\frac{1}{2}(\mathbf{w}^*\cdot\mathbf{w})+\sum_{i=1}^{n}\alpha_i+\sum_{i=1}^{n}(C-\alpha_i-\beta_i)\xi_i+b\sum_{i=1}^{n}\alpha_i s_i\\ &= -\frac{1}{2}\sum_{i=1}^{n}\sum_{j=1}^{n}(\alpha_i\alpha_j s_i s_j(\mathbf{v}_i\cdot\mathbf{v}_j))+\sum_{i=1}^{n}\alpha_i\end{aligned}$$

This Q_d is considerably simpler than the Q of the primal problem, (C.5), because it depends only upon a and the slack variables, $\mathbf{e}$, and $\mathbf{b}$ drop out. The dual optimization problem, then, is to *maximize*

$$Q_d(\mathbf{a}) = -\frac{1}{2}\mathbf{a}^T\mathbf{H}\mathbf{a} + \mathbf{p}\cdot\mathbf{a} \tag{C.13}$$

where $\mathbf{H}$ and $\mathbf{p}$ are defined by

$$H_{ij} \;=\; s_i s_j(\mathbf{v}_i\cdot\mathbf{v}_j) \tag{C.14}$$

$$\mathbf{p} \;=\; (1,\ldots,1) \tag{C.15}$$

subject to the constraints (combining (C.10) and (C.12)),

$$\begin{array}{l} 0 \le \alpha_i \le C \\ \sum_{i=1}^{n} \alpha_i s_i = 0. \end{array} \tag{C.16}$$

The penalty condition from the slack variables comes in the dual formulation as a limitation on the size of α_i. Once an optimal $\mathbf{a}^*$ for this quadratic program, the hyperplane can be found by

$$\mathbf{w} = \sum_{k=1}^{n} \alpha_k s_k \mathbf{v}_k \tag{C.17}$$

Typically, many of the points in the data set have $\alpha_i = 0$. Those points for which $\alpha_i \neq 0$ are called ***support vectors.*** These are the data that contribute to the shape of the boundary. Using the ***complementarity*** conditions on the support vectors, (C.11), b can be determined. Typically, one averages the results over the correctly classified support vectors (i.e. $0 < \alpha_i < C$).

$$b = \overset{\text{mean}}{\{j|0<\alpha_j<C\}} \left(s_j - \mathbf{w}^*\cdot\mathbf{v}_j\right) \tag{C.18}$$

C.2.3 Non-linear boundary characterization

For many types of input data, a linear boundary may not be sufficient. However, an extension to non-linear classifiers is relatively straightforward in the dual formulation (C.13). The only place the input data appears

$K(\mathbf{x},\mathbf{y})$	Class of Functions
$\mathbf{x}\cdot\mathbf{y}$	Linear
$(1+\mathbf{x}\cdot\mathbf{y})^n$	Polynomials of degree n
$\exp\left(-\|\mathbf{x}-\mathbf{y}\|^2\right)$	Gaussian Radial Basis Functions
$\exp\left(-\|\mathbf{x}-\mathbf{y}\|\right)$	Exponential Radial Basis Functions

Table C.1: Listing of some commonly used Kernels and the function classes to which they refer

is in a dot product in (C.15), a matrix associated with the quadratic term in Q_d. It can be shown (as in Vapnik, 1995) that non-linear function classes can be obtained by generalizing the dot product into a kernel function. Then,

$$H_{ij} = s_i s_j K(\mathbf{v}_i, \mathbf{v}_j) \tag{C.19}$$

where K is a positive definite kernel function. Table C.1 shows several common kernels and the classes of functions to which they correspond. One should note that these function classes are valid for *any dimension* of input data.

The boundary surface, which was defined as (C.1) in the linear case becomes

$$\sum_{i=1}^{n} \alpha_i s_i K(\mathbf{v}_i, \mathbf{v}) \ + b = 0.$$

Since only the support vectors have $\alpha_i \neq 0$, this can also be written

$$\sum_{j\in SV} \alpha_j s_j K(\mathbf{v}_j, \mathbf{v}) \ + b^* = 0. \tag{C.20}$$

where SV is the set of support vectors. Unfortunately, the form of this expression is highly dependant upon the data. For example, the number of terms is equal to the number of support vectors. For classification purposes, when one is only interested in numerically computing the LHS of (C.20) to classify locations of $\mathcal{V}$, this is sufficient. However, if the purpose is to characterize the boundary with an equation, then this formulation (C.20) of the boundary is too cumbersome to be useful.

To proceed further, however, we need a *model* for the boundary, a specific equation whose solution set designates the boundary. The SVM can be used to find the coefficients in this equation in an optimal manner. Consider a boundary of the following form:

$$c_1 f_1(\mathbf{v}) + c_2 f_2(\mathbf{v}) + c_3 f_3(\mathbf{v}) + \ldots + c_l f_l(\mathbf{v}) = 0 \tag{C.21}$$

where $\mathbf{v}$ is a point in $\mathcal{V}$, f_i are scalar fields (not necessarily linear) over $\mathbf{v}$, and the c_i's are linearly independent coefficients to be determined by the optimization.

Although it represents a non-linear surface in the space of data, (C.21) represents a hyperplane in the appropriate space obtained by placing the data, $\mathbf{v}$ through the non-linear map,

$$\Phi : \mathbf{v} \mapsto (f_1(\mathbf{v}), f_2(\mathbf{v}), \ldots, f_l(\mathbf{v})) \tag{C.22}$$

which allows equation (C.21) to be rewritten as

$$\mathbf{c} \cdot \Phi(\mathbf{v}) = 0 \tag{C.23}$$

where $\mathbf{c} = (c_1 \ldots c_l)$. This boundary is similar to equation (C.1), but it lacks an offset term b. The dual optimization problem changes in this case, with the only difference that the constraints (C.16) are replaced by

$$0 \leq \alpha_i \leq C. \tag{C.24}$$

By setting f_1 to a constant value, the offset can be *implicitly* computed by the coefficient c_1. The appropriate kernel function to replace the dot product between vectors is

$$K(\mathbf{v}_i, \mathbf{v}_j) = \Phi(\mathbf{v}_i) \cdot \Phi(\mathbf{v}_j) \tag{C.25}$$

which is used in computing $\mathbf{H}$ as in (C.19). The coefficients, c_i, to (C.21) can be found from the solution to the α_k's as follows:

$$c_i = \sum_{k \in SV} s_k \alpha_k f_i(x_k) \tag{C.26}$$

The coefficients c_i can be numerically computed on the basis of the data, and using the model (C.21), the boundary corresponding to a specific data set can be characterized by its c_i's.

A useful further extension of this method lies in adjusting the value of the penalty weights associated with boundary errors for different data points. This is very easy to implement by changing (C.24) to

$$0 \leq \alpha_i \leq C_i \tag{C.27}$$

where C_i, the error penalty, is selected differently for each data point. This allows for a weighted classification without any additional computational cost.

The final form of the procedure derived fits boundaries to a non-linear model for non-separable data, and can accomodate independant weights for each data point. To summarize, one finds the coefficients to a model of the type (C.21) from the data using (C.26) where the α's associated with each data point are the solution to the quadratic program which minimizes

$$G(\mathbf{a}) = \frac{1}{2}\mathbf{a}^T\mathbf{H}\mathbf{a} - \mathbf{p} \cdot \mathbf{a} \tag{C.28}$$

where

$$\begin{aligned} H_{ij} &= s_i s_j \sum_{k=1}^{l} f_k(\mathbf{v}_i) f_k(\mathbf{v}_j) && \text{(C.29)} \\ \mathbf{p} &= (1, \ldots, 1) && \text{(C.30)} \end{aligned}$$

subject to (C.24). (n.b. the dual maximization problem is converted to a minimization problem here by taking the negative of the objective function).

C.3 Performance of Procedure on Test Cases

The boundary fitting procedure described in the previous section is constructed to minimize the expected *generalization error.* That is, to minimize the probability that, following the fitting based upon a given (training) set of data, the grouping information of a new data point is correctly predicted. Typically, one might assess error in this context by measuring rates of erroneous classification. However, in the current context of stall flutter stability, the data are scarce, so all of it is needed to construct the boundary. In this section, we use some test examples to characterize the performance of the boundary fitting procedure. The results from the test examples can provide some insight into the performance of the procedure.

In particular, we look at randomly sampled points in a segment of a parameter space, whose group information has an underlying stability surface which is a conic section (a paraboloid in 3D). With the test examples, the effects of data sparsity can be addressed directly.

The reason that random data are sampled is to avoid the effects of bias within the sampling domain. The position of the envelope of data samping is also moved in the case of the 3D paraboloid. For the intended application of stability boundaries, we expect the data to be nearer to the boundary than in the cases studied here. However, the point here is to study the general performance of the method in a well-defined test case, rather than to simulate the case of flutter stability data.

C.3.1 3D Paraboloid

The example boundary is a paraboloid in 3D. The data are sampled in a cylinder which cuts the paraboloid, as schematically shown in Figure C-5. The paraboloid is special in the sense that it is oriented along the z-axis. However, its location is arbitrary. This restricts the relevant equation for the 3D paraboloid from 16 terms (the general case), to only five terms as follows:

$$c_1(x^2+y^2)+c_2x+c_3y+c_4z+c_5=0$$

where the c_i are the unknown coefficients. Furthermore, we can normalize this equation so that the value of c_5 is constant. We pick a single paraboloid, and two different cylinders. The equation of the test paraboloid

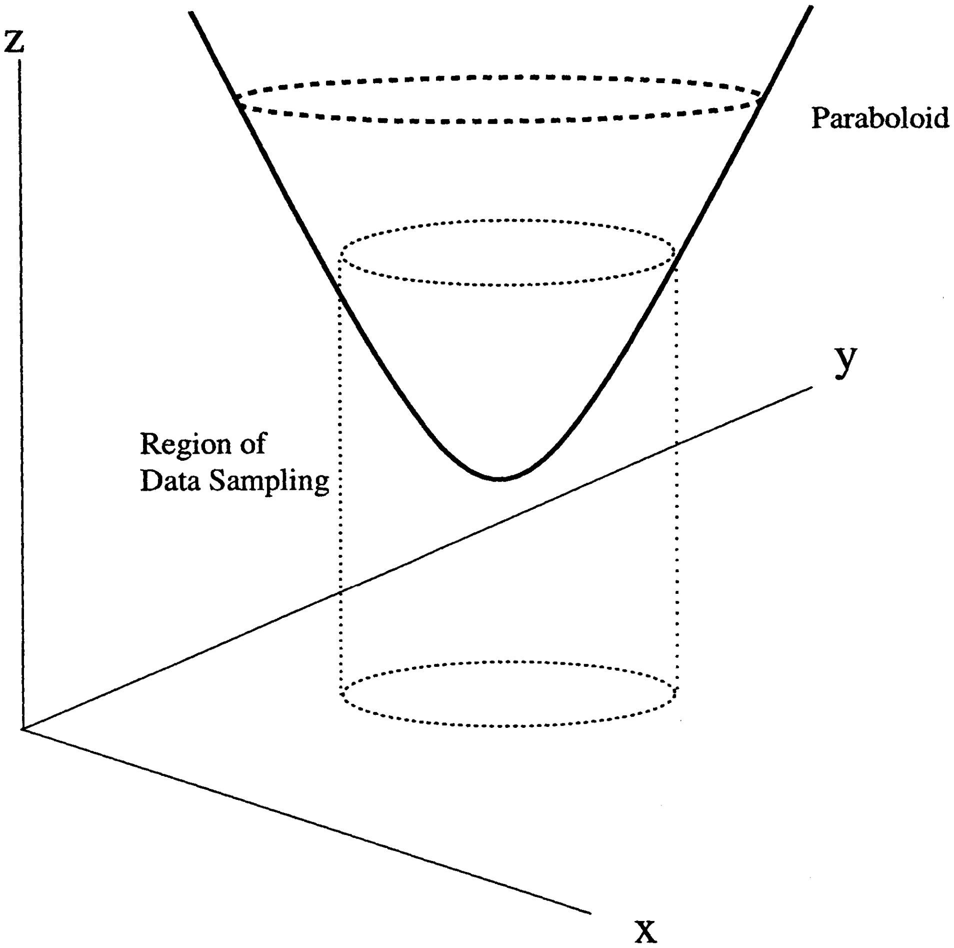

Figure C-5: Diagram of paraboloid oriented on z-axis. Randomly selected points from the dotted cylindrical region are ascribed a group based on their location with respect to the paraboloid. The boundary fitting technique aims to recover the paraboloid from the data

corresponds to the equation

$$z = 2 + (x^2 + y^2) \tag{C.31}$$

which describes a paraboloid with a minimum at (0,0,2) and which is concave upwards (towards $+z$). The normalization of c_5 was selected to be $c_5 = 2$. Therefore, the equation corresponds to $(c_1,c_2,c_3,c_4) = (1, 0, 0, -1)$. Two cylinders were selected: "Cylinder A" with a center at $(x,y) = (0,0)$, a radius of 2, and a z range from 0 to 8, and "Cylinder B" centered at $(x,y) = (1,1)$, a radius of 1, and a z-range from 0 to 8.

Since, in this case, the model for the boundary is coincident with the actual equation for the boundary, the error is measured in terms of how well the coefficients match. These results are shown in Table C.2.

Cyl	N_{pts}	N_{trials}	mean, c_1	std, c_1	mean, c_2	std, c_2	mean, c_3	std, c_3	mean, c_4	std, c_4
Actual			1		0		0		-1	
A	10	125	1.3422	5.2448	-0.3943	3.4025	0.1427	3.2067	-1.0623	3.5915
A	30	40	1.1865	0.5842	-0.0269	0.0274	0.7157	0.5096	-1.1084	0.2801
A	50	40	1.0134	0.3090	-0.0457	0.3708	-0.0318	0.3054	-1.0260	0.1252
A	100	40	1.0044	0.1214	0.0413	0.1669	-0.0087	0.1214	-1.0020	0.0478
B	10	125	0.8446	1.5035	0.0225	1.1579	0.2057	1.4796	-0.9877	1.0237
B	30	40	1.3596	1.1607	0.0829	1.0110	0.0395	0.6998	-1.0609	0.2224
B	50	40	0.9013	0.7923	0.0362	0.5898	0.1468	0.4636	-1.0053	0.1357
B	100	40	0.9379	0.3576	-0.0506	0.3158	-0.0813	0.3171	-1.0089	0.0584

Table C.2: Results from boundary fitting of paraboloid test case. The first line, labeled "actual" gives the coefficients of the underlying paraboloid. Otherwise, the mean and standard deviation are given of each set of trials.

For each entry, the mean and standard deviation of independent trials are listed.

C.3.2 2D Ellipse

We now address a 2D ellipse as a test case. This is also a conic section, just as the 3D paraboloid. A schematic of the general situation is shown in Figure C-6.

In this case, the ellipse is selected such that its axes are oriented along the x and y axes, but its location is arbitrary. The equation describing such a conic section is

$$c_1 x^2 + c_2 y^2 + c_3 x + c_4 y + c_5 = 0.$$

depending upon the values of the c's, this equation may describe a parabola, a hyperbola or an ellipse. Note that this equation has the same number of undetermined coefficients as the 3-D paraboloid. However, the data are situated in only two dimensions (only x and y) rather than three. Again, the coefficient c_5 is a free parameter and can be normalized. We choose the following ellipse for the tests:

$$4x^2 + y^2 - 8x - 2y + 4 = 0 \tag{C.32}$$

this corresponds to an ellipse centered at (1,1) with the major axis aligned with the y-axis. The major axis length is 2 and the minor axis length is 1. Accordingly, the c_5 parameter is normalized to be 4. Random

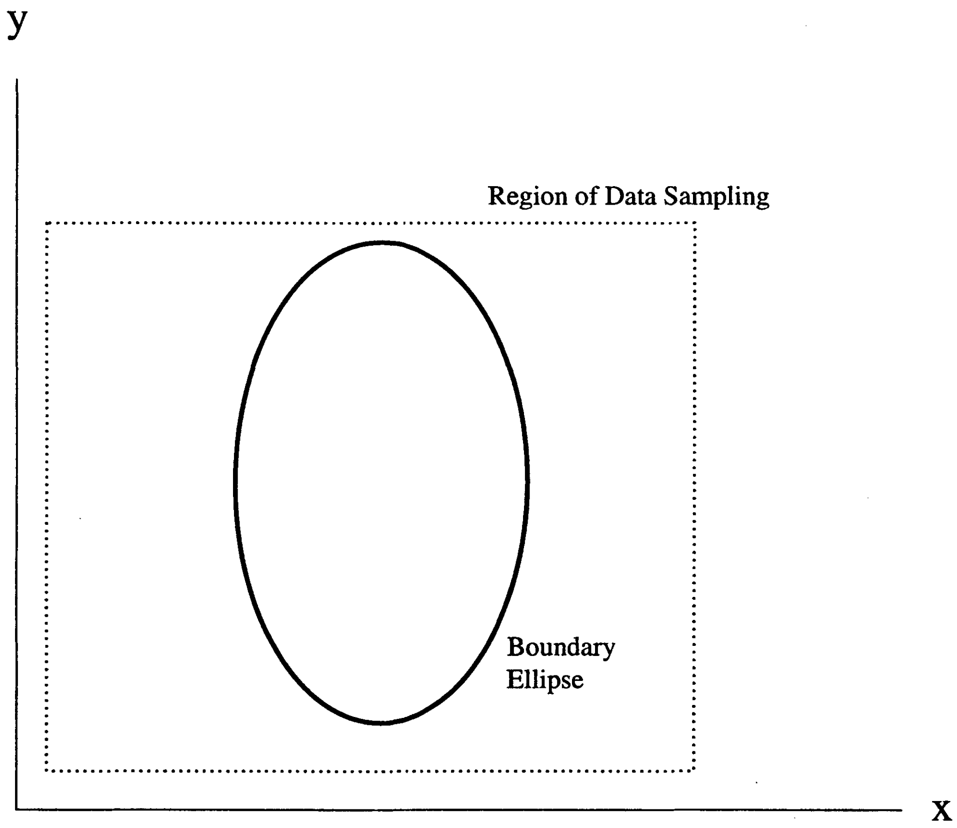

Figure C-6: Schematic of an ellipse in the plane. Randomly selected points from the boxed region are used as test data in characterizing SVM performance.

	N_{pts}	N_{trials}	mean, c_1	std, c_1	mean, c_2	std, c_2	mean, c_3	std, c_3	mean, c_4	std, c_4
Actual			4		1		-8		-2	
	10	125	6.6342	30.8235	2.1193	13.4280	-11.0047	38.6501	-4.4621	23.2327
	30	40	4.1787	0.4874	0.8905	0.5654	-8.2679	0.7765	-1.8591	0.9830
	50	40	4.0574	0.3454	0.9652	0.2823	-8.1325	0.5621	-1.9179	0.4670
	100	40	4.0091	0.1935	1.0149	0.1394	-8.0020	0.2952	-2.0303	0.2691

Table C.3: Results from boundary fitting of 2D ellipse test case. The first line, labeled "actual" gives the coefficients of the underlying ellipse. Otherwise, the mean and standard deviation are given of each set of trials.

points were selected from the box with corners at (0,0) and (2,2). The results from fitting tests are shown in Table C.3.

Appendix D

Flutter boundary fits

This appendix contains figures of the flutter boundaries on the performance map for the Volvo rig discussed in Chapters 5 and 6.

Each plot has the same format. The x-axis is the corrected mass flow, and the y-axis is the pressure ratio. The performance curves at constant corrected speed are shown as dashed lines. An inset plot shows the (K_0^*, g/ρ^*) location associated with the boundary as a boxed area, and star ($*$) which shows the median location of points on the boundary. Open circles ($\circ$) indicate unstable points measured inside the box, and stars ($*$) indicate stable points measured inside the box. Open triangles ($\triangleright$) indicate unstable points taken at a higher K_0^* and g/ρ^*, which are presumed to be unstable inside the box as well, and the plusses ($+$) indicate the stable points taken at locations with a lower K_0^* and g/ρ^* than the box. The solid line is the boundary curve fit using the Support Vector algorithm described in Appendix C. The dashed lines give an uncertainty range for each boundary.

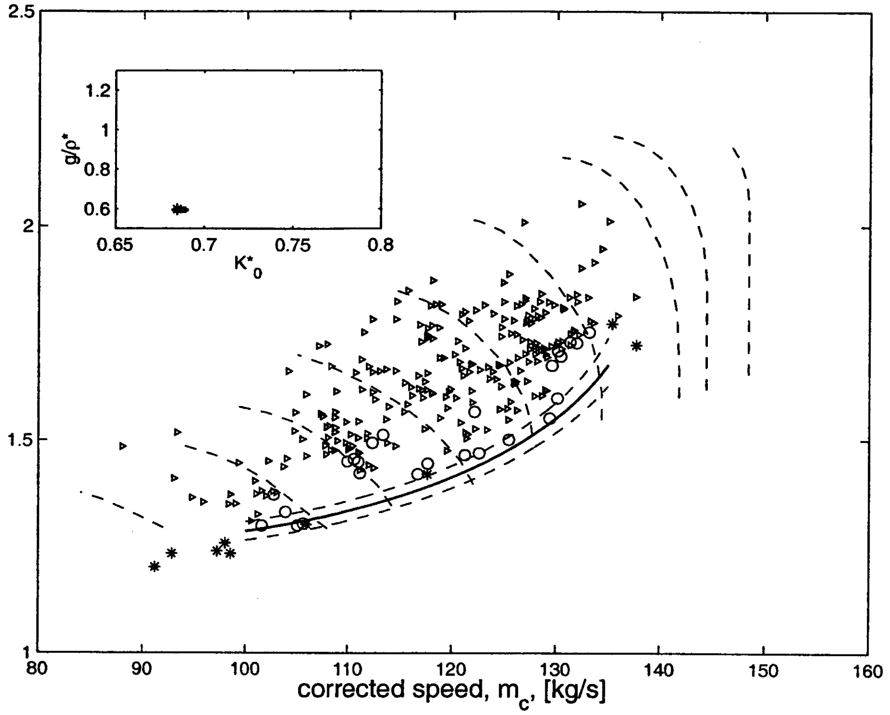

Figure D-1: Flutter boundary on performance map, for $K_0^* = 0.685$ and $(g/\rho^*)_{\text{rel}} = 0.60$

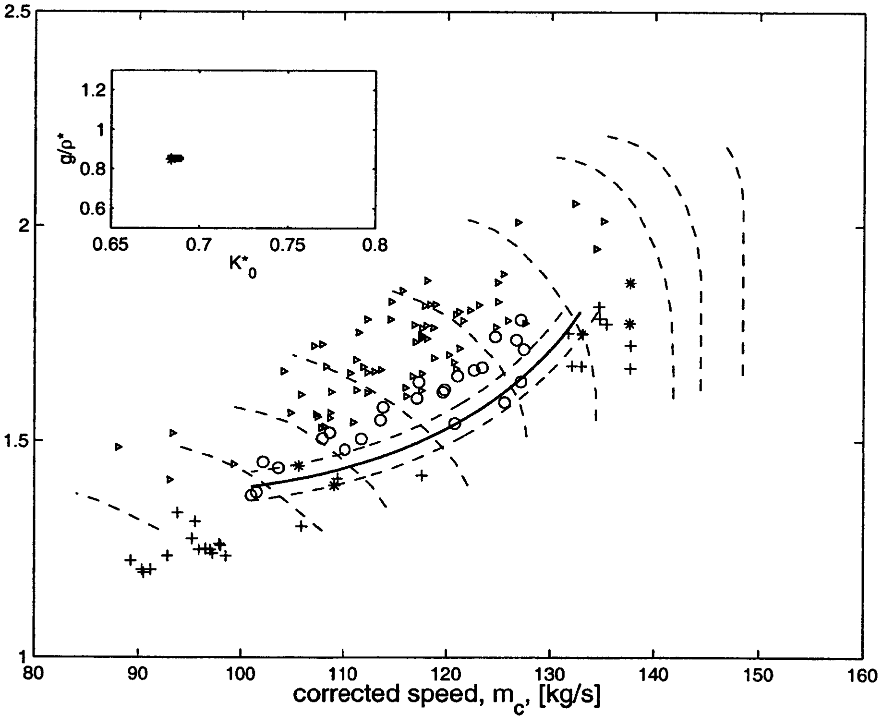

Figure D-2: Flutter boundary on performance map, for $K_0^* = 0.684$ and $(g/\rho^*)_{\text{rel}} = 0.85$

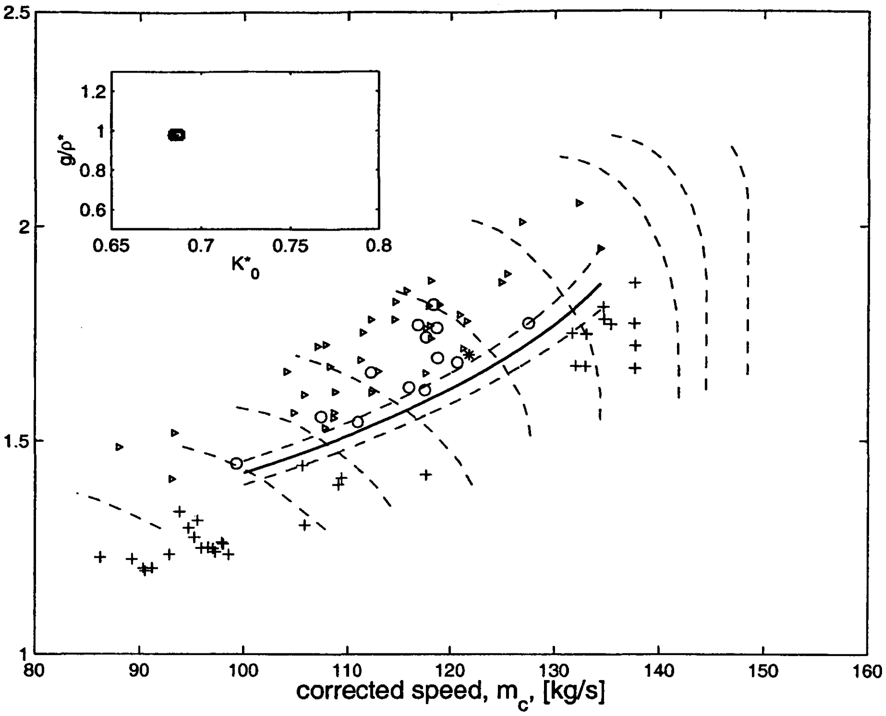

Figure D-3: Flutter boundary on performance map, for $K_0^* = 0.685$ and $(g/\rho^*)_{\rm rel} = 0.98$

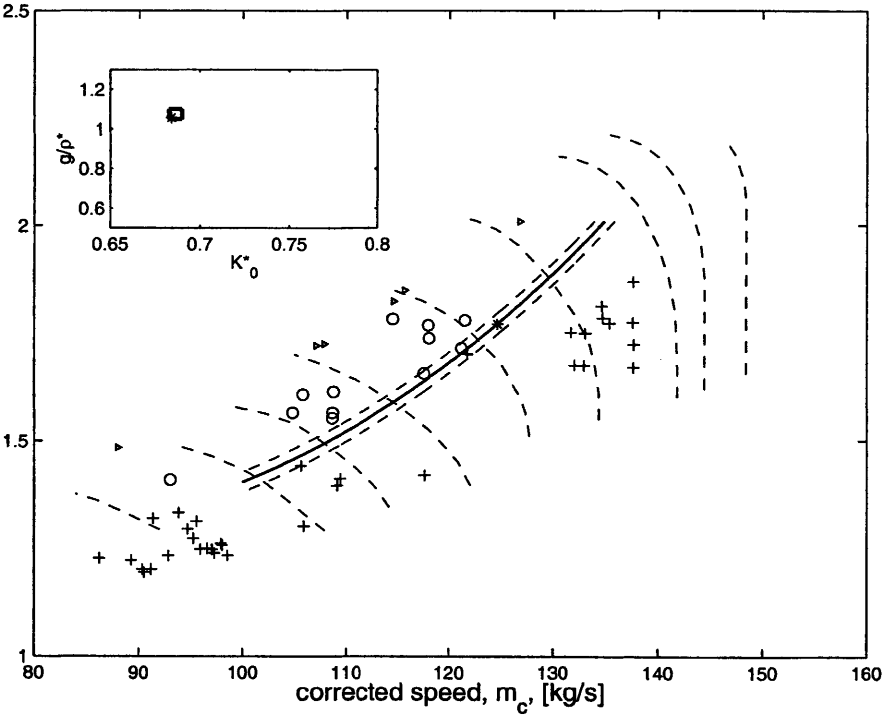

Figure D-4: Flutter boundary on performance map, for $K_0^* = 0.684$ and $(g/\rho^*)_{\rm rel} = 1.06$

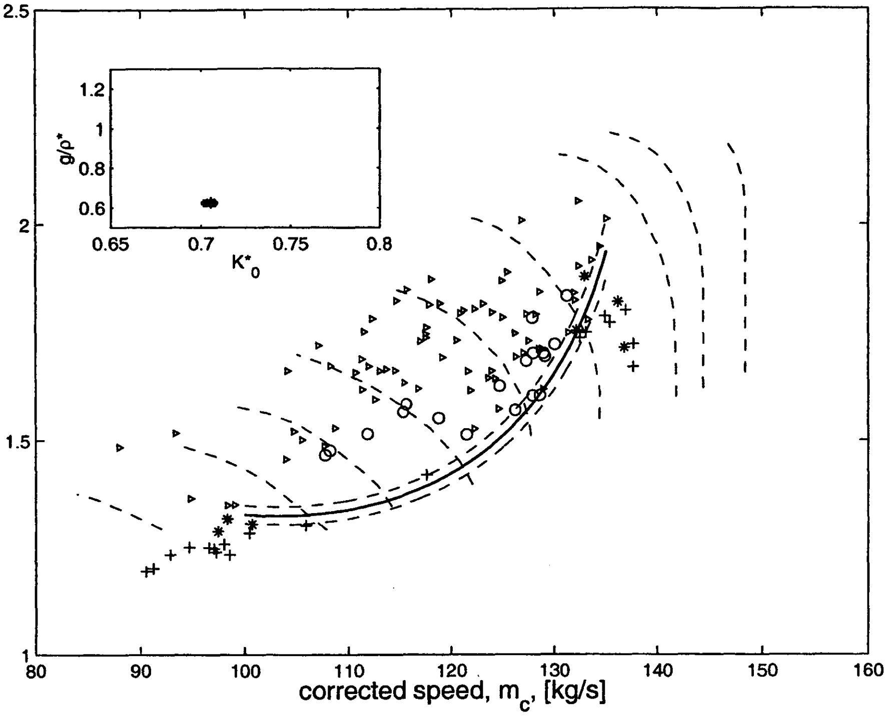

Figure D-5: Flutter boundary on performance map, for $K_0^* = 0.705$ and $(g/\rho^*)_{\text{rel}} = 0.63$

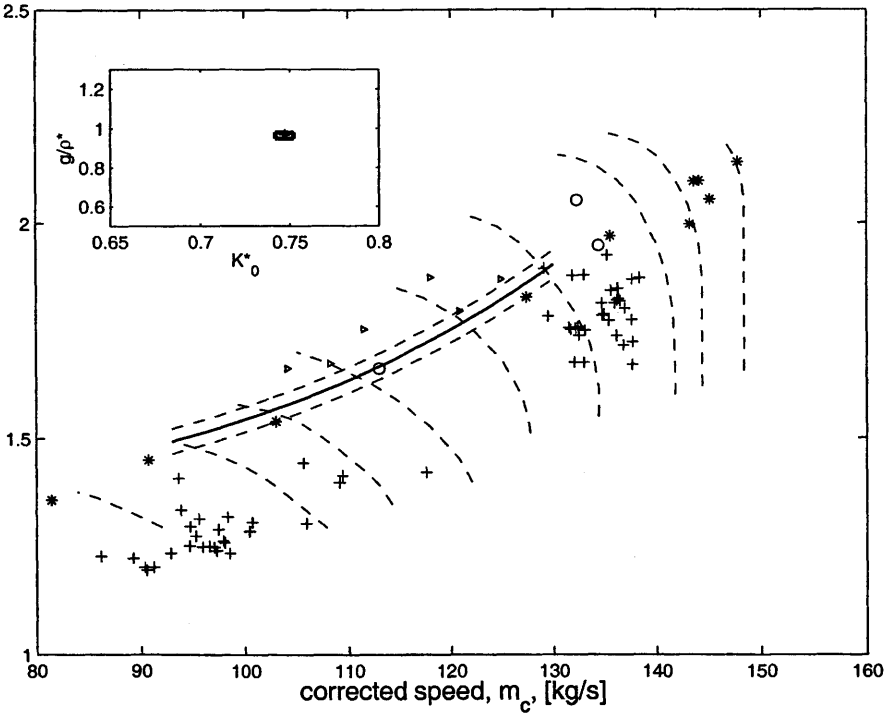

Figure D-6: Flutter boundary on performance map, for $K_0^* = 0.747$ and $(g/\rho^*)_{\text{rel}} = 0.97$

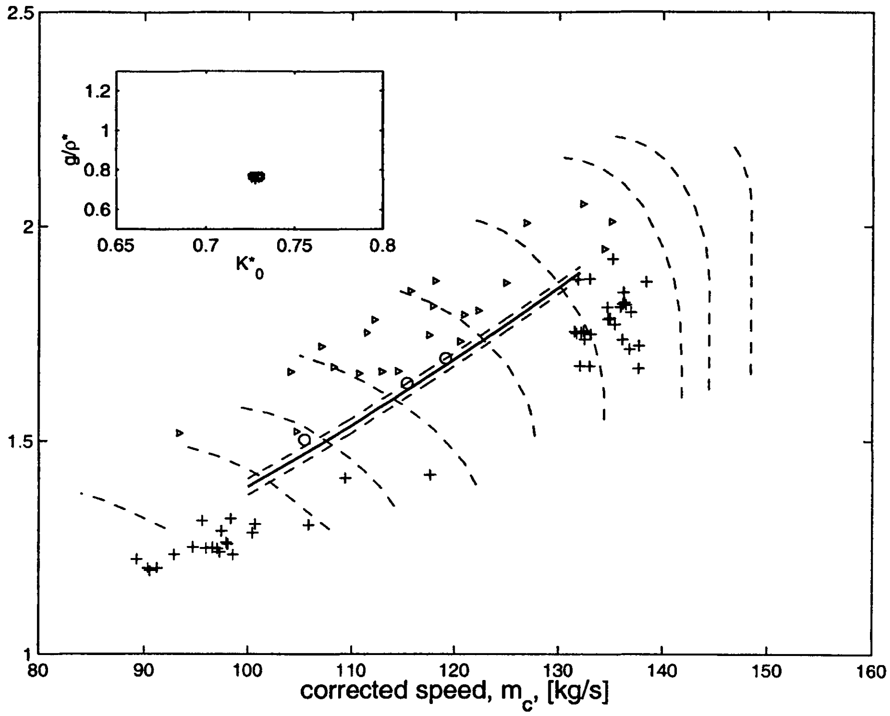

Figure D-7: Flutter boundary on performance map, for $K_0^* = 0.728$ and $(g/\rho^*)_{\text{rel}} = 0.75$

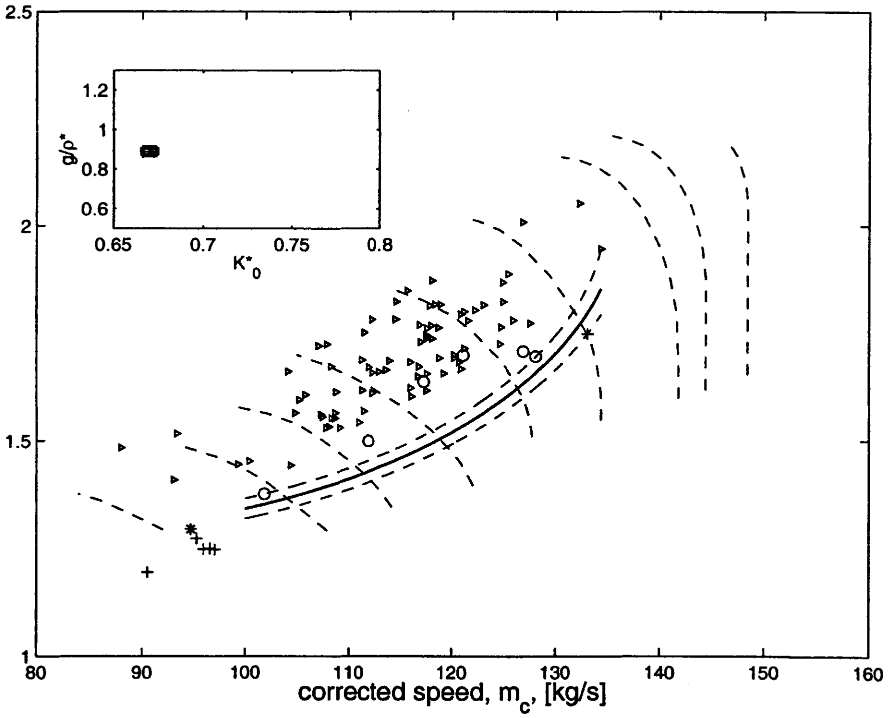

Figure D-8: Flutter boundary on performance map, for $K_0^* = 0.671$ and $(g/\rho^*)_{\text{rel}} = 0.89$

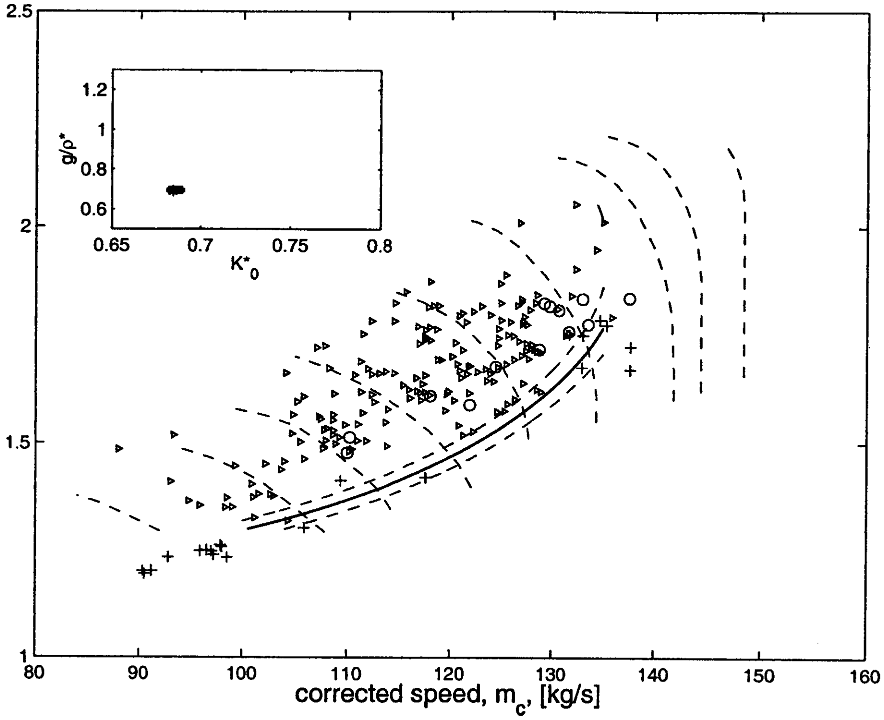

Figure D-9: Flutter boundary on performance map, for $K_0^* = 0.685$ and $(g/\rho^*)_{\rm rel} = 0.69$

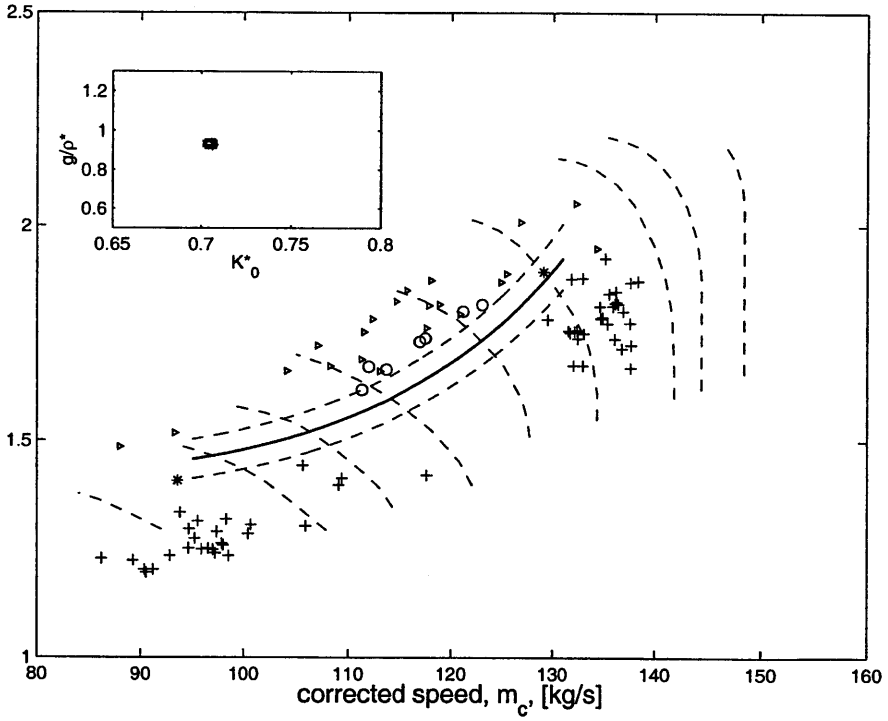

Figure D-10: Flutter boundary on performance map, for $K_0^* = 0.706$ and $(g/\rho^*)_{\rm rel} = 0.93$

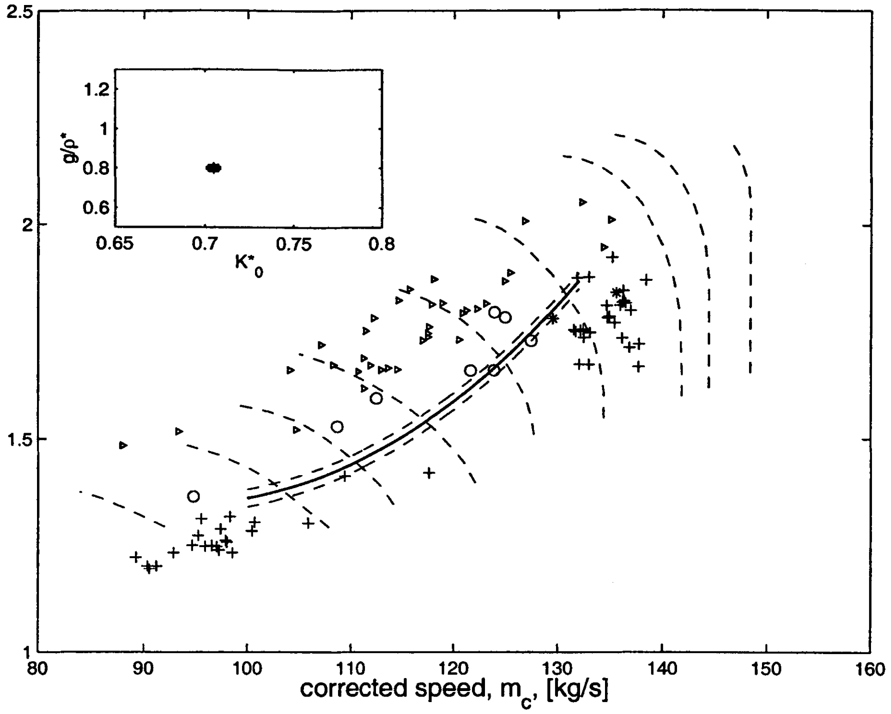

Figure D-11: Flutter boundary on performance map, for $K_0^* = 0.705$ and $(g/\rho^*)_{\rm rel} = 0.80$

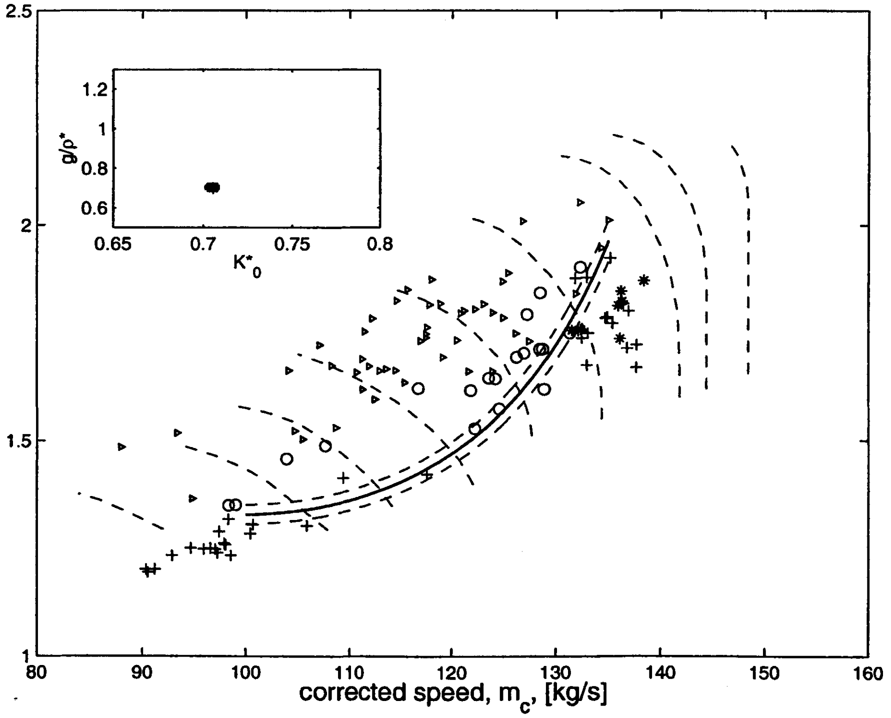

Figure D-12: Flutter boundary on performance map, for $K_0^* = 0.706$ and $(g/\rho^*)_{\rm rel} = 0.70$

Bibliography

[1] A. Abdel-Rahim, F. Sisto, and S. Thangam. Computational study of stall flutter in linear cascades. *ASME Journal of Turbomachinery*, 115:157–166, 1993.

[2] R.S. Abhari and M. Giles. A navier-stokes analysis of airfoils in oscillating transonic cascades for the prediction of aerodynamic damping. *ASME Journal of Turbomachinery*, 119:77–84, 1997.

[3] J.J. Adamczyk. Analysis of supersonic stall bending flutter in axial-flow compressor by actuator disk theory. Technical report, NASA, 1978. NASA Technical Paper 1345.

[4] H. Atassi and T.J. Akai. Aerodynamic and aeroelastic characteristics of oscillating loaded cascades at low mach number, part 1: Pressure distribution, forces, and moments. *ASME Journal of Engineering for Power*, 102:344–351, 1980.

[5] T.C. Ayer and J.M. Verdon. Validation of a nonlinear unsteady aerodynamic simulator for vibrating blade rows. *ASME Journal of Turbomachinery*, 120:112–121, 1988.

[6] O.O. Bendiksen. Role of shocks in transonic/supersonic compressor rotor flutter. *AIAA Journal*, 24:1179–1186, 1986.

[7] O.O. Bendiksen. Recent developments in flutter suppression techniques for turbomachinery rotors. *AIAA Journal of Propulsion and Power*, 4:164–171, 1988.

[8] O.O. Bendiksen. *Flight Vehicle Materials, Structures and Dynamics—Assessment and Future Directions*, volume 5, chapter 5, Aeroelastic Problems in Turbomachines, pages 241–297. ASME Publications, 1993.

[9] D. Bertsekas. *Nonlinear Programming.* Athena Scientific, Belmont MA, 1995.

[10] R.L. Bisplinghoff, H. Ashley, and R.L. Halfman. *Aeroelasticity.* Addison Wesley, 1955.

[11] A. Bölcs and T.H. Fransson. Aeroelasticity in turbomachines: Comparison of theoretical and experimental cascade results. Technical report, Ecole Polytechnique Fédérale de Lausanne, Switzerland, 1986.

[12] M.J. Brooker and D.G. Halliwell. A comparison of measured and predicted unsteady pressure on a fan blade in unstalled supersonic flutter. In *3rd International Symposium on Aeroelasticity in Turbomachines*, Cambridge, U.K., September 1984.

[13] E. Buckingham. On physically similar systems: Illustrations of the use of dimensional equations. *Physical Review*, 4:345–376, 1914.

[14] D.H. Buffum and S. Fleeter. The aerodynamics of an oscillating cascade in a compressible flow field. *ASME Journal of Turbomachinery*, 112:759–767, 1990.

[15] C.J.C. Burges. A tutorial on support vector machines for pattern recognition. *Data Mining and Knowledge Discovery*, 2:121–167, 1998.

[16] T.R. Camp. A study of acoustic resonance in a low-speed multistage compressor. *ASME Journal of Turbomachinery*, 121:36–43, 1999.

[17] V.R. Capece and Y.M. El-Aini. Stall flutter prediction techniques for fan and compressor blades. *AIAA Journal for Propuslsion and Power*, 12:800–806, 1996.

[18] F.O. Carta. *AGARD Manual on Aeroelasticity in Axial-Flow Turbomachines Volume 2*, chapter Chapter 18, Aeroelastic Coupling – An Elementary Approach. AGARDograph No. 298, 1988.

[19] R.M. Chi. Unsteady aerodynamics in stalled cascade and stall flutter prediction, 1980. ASME Paper 80-C2/Aero-1.

[20] R.M. Chi. An unsteady lifting surface theory for ducted fan blades. *ASME Journal of Turbomachinery*, 115:175–188, 1993.

[21] H.D. Chiang and S. Fleeter. Oscillating incompressible aerodynamics of a loaded airfoil cascade. *AIAA Journal*, 27:446–454, 1989.

[22] W.S. Clark and K.C. Hall. A time-linearized navier-stokes analysis of stall flutter, 1999. ASME Paper 99-GT-383.

[23] W.S. Cleveland. *Visualizing Data.* Hobart Press, Summit NJ, 1993.

[24] C. Cortes and V. Vapnik. Support vector networks. *Machine Learning*, 20:273–297, 1995.

[25] E.F. Crawley. *AGARD Manual on Aeroelasticity in Axial-Flow Turbomachines Volume 2*, chapter Chapter 19, Aeroelastic Formulations for Tuned and Mistuned Rotors. AGARDograph No. 298, 1988.

[26] N.A. Cumpsty. *Compressor Aerodynamics.* Wiley, 1989.

[27] E.H. Dowell (ed.), E.F. Crawley, H.C. Curtiss Jr., D.A. Peters, R.H. Scanlan, and F. Sisto. *A Modern Course in Aeroelasticity.* Kluwer Academic, 1995.

[28] Y.M. El-Aini. Friction damping of hollow airfoils, parts 1 and 2, 1996. ASME Paper 96-GT-109/110.

[29] Y.M. El-Aini, H.R. Bankhead, and C.E. Meece. Subsonic/transonic stall flutter investigation of an advanced low pressure compressor, 1986. ASME Paper 86-GT-90.

[30] S. Fleeter. Aeroelasticity research for turbomachine applications. *AIAA Journal of Aircraft*, 16:320–326, 1979.

[31] H. Förschíng. Aeroelastic stability of cascades in turbomachinery. *Progress in Aerospace Sciences*, 30:213–266, 1994.

[32] H. Försching. A parametric study of the flutter stability characteristics of turbomachinery cascades, 1996. ASME Paper 96-GT-260.

[33] T.H. Fransson and J.M. Verdon. Panel discussion on standard configurations for unsteady flow through vibrating axial-flow turbomachine cascades. In Atassi, editor, *Unsteady Aerodynamics, Aeroacoustics, and Aeroelaticity of Turbomachines and Propellers.* Springer-Verlag, 1993.

[34] Y.C. Fung. *An Introduction to the Theory of Aeroelasticity.* Wiley and Sons, 1955.

[35] G.A. Gerolymos. Coupled three-dimensional aeroelastic stability analysis of bladed disks. *ASME Journal of Turbomachinery*, 115:791–799, 1993.

[36] M. Giles. Non-reflecting boundary conditions for Euler equation calculations. *AIAA Journal*, 28:2050–2058, 1990.

[37] S.I. Ginzburg. Calculation of the boundary of excitation of flexural flutter of a homogeneous array in a quasistationary approximation. *Strength of Materials (translation of Problemy Prochnosti)*, pages 956–962, 1974.

[38] M.E. Goldstein. Cascade with subsonic leading-edge locus. *AIAA Journal*, pages 1117–1119, August 1975.

[39] M.E. Goldstein, W. Braun, and J.J. Adamczyk. Unsteady flow in a supersonic cascade with strong in-passage shocks. *Journal of Fluid Mechanics*, 83:569–604, 1977.

[40] R.W. Gordon and J.J. Hollkamp. An internal damping treatment for gas turbine blades. In *38th AIAA/ASME/ASCE/AHS/ASC Structures, Structural Dynamics, and Materials Conference and Exhibit, Kissimmee FL*, pages 1295–1303, 1997. also AIAA Paper 97-1154.

[41] J. Griffin. Friction damping of resonant stresses in gas turbine engine airfoils, 1979. ASME Paper 79-GT-109.

[42] S. Gunn. Support vector machines for classification and regression. Technical report, Image Speech and Intelligent Systems Group, University of Southhampton, 1998.

[43] D.L. Gysling and M.R. Myers. A framework for analyzing the dynamics of flexibly-bladed turbomachines, 1996. ASME Paper 96-GT-440.

[44] K.C. Hall. Deforming grid variational principle for unsteady small disturbance flows in cascades. *AIAA Journal*, 31:777–787, 1993.

[45] K.C. Hall. Linearized euler predictions of unsteady aerodynamic loads in cascades. *AIAA Journal*, 31:540–550, 1993.

[46] K.C. Hall and P.D. Silkowski. The influence of neighboring blade rows on the unsteady aerodynamic response of cascades. *ASME Journal of Turbomachinery*, 119:85–93, 1997.

[47] D.G. Halliwell. Some aerodynamic considerations in the prediction of unstalled supersonic flutter in transsonic fans. In *3rd International Symposium on Aeroelasticity in Turbomachines*, Cambridge, U.K., September 1984.

[48] L. He. An euler solution for unsteady flows around oscillating blades. *ASME Journal of Turbomachinery*, 112:714–722, 1990.

[49] L. He and J.D. Denton. Inviscid-viscous coupled solution for unsteady flows through vibrating blades: Part 2–computational results. *ASME Journal of Turbomachinery*, 115:101–109, 1993.

[50] K. Isomura. A numerical investigation of flutter in a transonic fan. Technical report, MIT Gas Turbine Laboratory, 1996. GTL Report 223.

[51] K. Isomura. On the effect of single mode bending/torsion coupling on the flutter behavior in a transonic fan, 1998. ASME Paper 98-GT-570.

[52] J.D. Jeffers. *AGARD Manual on Aeroelasticity in Axial-Flow Turbomachines Volume 2*, chapter Chapter 21, Aeroelastic Thermal Effects. AGARDograph No. 298, 1988.

[53] J.D. Jeffers and C.E. Meece. F100 fan stall flutter problem review and solution. *Journal of Aircraft*, 12:350–357, 1975.

[54] R.R. Jutras, R.B. Fost, R.M. Chi, and B.F. Beacher. Subsonic/transonic stall flutter investigation of a rotating rig. Technical report, NASA, 1983. NASA CR-174625.

[55] R.R. Jutras, M.J. Stallone, and H.R. Bankhead. Experimental investigation of flutter in mid-stage compressor designs, 1980. AIAA Paper 80-0786.

[56] K.R.V. Kaza and R.E. Kielb. Flutter of turbofan rotors with mistuned blades. *AIAA Journal*, 22:1618–1625, 1984.

[57] N.H. Kemp and W.R. Sears. Aerodynamic interference between moving blade rows. *Journal of the Aerospace Sciences*, 20(9):585–597, 1953.

[58] J. L. Kerrebrock. *Aircraft Engines and Gas Turbines.* MIT Press, 1992.

[59] R.E. Kielb and J.K. Ramsey. Flutter of a fan blade in supersonic axial flow. *ASME Journal of Turbomachinery*, 111:462–467, 1989.

[60] H. Kobayashi. Effects of shock waves on aerodynamic instability of annular cascade oscillation in a transonic flow. *ASME Journal of Turbomachinery*, 111:222–230, 1989.

[61] J.B. Kosmatka and O. Mehmed. Experimental spin testing of integrally damped composite blades. In *39th AIAA/ASME/ASCE/AHS/ASC Structures, Structural Dynamics, and Materials Conference and Exhibit, Long Beach CA*, pages 1295–1303, 1998. also AIAA Paper 98-1847.

[62] F. Lane. System mode shapes in the flutter of compressor blade rows. *Journal of the Aerospace Sciences*, pages 54–66, January 1956.

[63] C.C. Lin and L.A. Segal. *Mathematics Applied to Deterministic Problems in the Natural Sciences.* Macmillian, 1974.

[64] C.B. Lorence and K.C. Hall. Sensitivity analysis of unsteady aerodynamic loads in cascades. *AIAA Journal*, 33(9):1604–1610, 1995.

[65] J.G Marshall and M. Imregun. A review of aeroelasticity methods with emphasis on turbomachinery applications. *Journal of Fluids and Structures*, 10:237–267, 1996.

[66] J.D. Mattingly. *Elements of Gas Turbine Propulsion.* McGraw Hill, 1996.

[67] B. McCormick. *Aerodynamics, Aeronautics, and Flight Mechanics.* Wiley, 1995.

[68] C.M. Mehalic, H.G. Hurrel, J.H. Dicus, J.F. Lubomski, A.P. Kurkov, and D.G. Evans. Experimental results and data format of preliminary fan flutter investigation using YF100 engine. Technical Report NASA TM SX-3444, NASA, 1977.

[69] A.A. Mikolajczak, R.A. Arnoldi, L.E. Snyder, and H. Stargardter. Advances in fan and compressor blade flutter analysis and prediction. *AIAA Journal of Aircraft*, 12:325–332, 1975.

[70] D.C. Montgomery. *Design and Analysis of Experiments.* John Wiley and Sons, 1976.

[71] M. Namba. Subsonic cascade flutter with finite mean lift. *AIAA Journal*, pages 586–593, 1975.

[72] M. Nowinski and J. Panovsky. Flutter mechanisms in low pressure turbine blades, 1998. ASME Paper 98-GT-573.

[73] E. Osuna. *Support Vector Machines: Training and Applications.* PhD thesis, M.I.T., 1998.

[74] P. Ott, A. Bölcs, and T.H. Fransson. Experimental and numerical study of the time-dependent pressure response of a shock wave oscillating in a nozzle. *ASME Journal of Turbomachinery*, 117:106–114, 1995.

[75] J. Panovsky and R. Kielb. A flutter design technique for low pressure turbine blades, 1998. ASME Paper 98-GT-573.

[76] W.J. Rakowski, D.H. Ellis, and H.R. Bankhead. A research program for the experimental analysis of blade instability. In *AIAA/SAE 14th Joint Propulsion Conference*, 1978.

[77] K.Y. Sanliturk, D.J. Ewins, and A.B. Stanbridge. Underplatform dampers for turbine blades: Theoretical modelling, analysis and comparison with experimental data. ASME Paper 99-GT-335.

[78] B. Scholkopf, C.J.C. Burges, and A.J. Smola (ed.). *Advances in Kernel Methods: Support Vector Learning.* MIT Press, 1999.

[79] C. Scruton. On the wind-excited oscillations of towers, stacks, and masts. In *Proceedings of the Symposium on Wind Effects on Buildings and Structures*, pages 798–836, London, 1965. Her Majesty's Stationary Office.

[80] L.A. Segal. *Mathematics Applied to Continuum Mechanics.* Dover, 1987.

[81] J. Shioiri. Non-stall normal mode flutter in annular cascades, part 1 theoretical study. *Japan Society of Aeronautical Engineering*, 1:26–35, 1958.

[82] J. Shioiri. Non-stall normal mode flutter in annular cascades, part 2 experimental study. *Japan Society of Aeronautical Engineering*, 1:36–45, 1958.

[83] F. Sisto. Unsteady aerodynamic reactions on airfoils in cascade. *Journal of Aerospace Sciences*, 22:297–302, 1955.

[84] R. Skop and O. Griffin. An heuristic model for determining flow-induced vibrations of offshore structures. In *5th Offshore Technology Conference*, page OTC Paper 1843, Houston, TX, 1973.

[85] T.E. Smith and J.R. Kadambi. The effect of steady aerodynamic loading on the flutter stability of turbomachine blading. *ASME Journal of Turbomachinery*, 115:167–174, 1993.

[86] L.E. Snyder and D.W. Burns. *AGARD Manual on Aeroelasticity in Axial-Flow Turbomachines Volume 2*, chapter Chapter 22, Forced Vibration and Flutter Design Methodology. AGARDograph No. 298, 1988.

[87] A.V. Srinivasan. Flutter and resonant vibration characteristics of engine blades. *ASME Journal of Engineering for Gas Turbines and Power*, 119:742–775, 1997.

[88] A.V. Srinivasan, D.G. Cutts, and S. Sridhar. Turbojet engine blade damping. Technical report, NASA, 1981. Contractor Report, No. 165406.

[89] A.V. Srinivasan and J.A. Fabunmi. Cascade flutter analysis of cantilevered blades. *ASME Journal of Turbomachinery*, 106:34–43, 1984.

[90] H. Stargardter. Subsonic/transonic stall flutter study. Technical report, NASA, 1979. NASA CR-165356.

[91] H. Stargardter. *AGARD Manual on Aeroelasticity in Axial-Flow Turbomachines Volume 2*, chapter Chapter 20, Fan Flutter Test. AGARDograph No. 298, 1988.

[92] J.W. Tukey. *Exploratory Data Analysis.* Addison-Wesley, 1977.

[93] V. Vapnik. *Estimation of Dependences Based on Empirical Data [in Russian].* Nauka, Moscow, 1979.

[94] V. Vapnik. *The Nature of Statistical Learning Theory.* Springer Verlag, 1995.

[95] J.M. Verdon. Review of unsteady aerodynamic methods for turbomachinery aeroelastic and aeroacoustic applications. *AIAA Journal*, 31:235–250, 1993.

[96] J.M. Verdon and J.R. Caspar. Development of a linear unsteady aerodynamic analysis for finite-deflection subsonic cascades. *AIAA Journal*, 20:1259–1267, 1983.

[97] B.J. Vickery and R.D. Watkins. Flow-induced vibrations of cylindrical structures. In R. Silvester, editor, *Proceedings of the First Austrailian Conference on Hydraulics and Fluid Mechanics.* Pergamon Press, 1964.

[98] D.S. Whitehead. Force and moment coefficients for aerofoils vibrating in cascade. Technical Report R.&M. 3254, British A.R.C., 1960.

[99] D.S. Whitehead. Bending flutter of unstalled cascade blades at finite deflection. Technical Report R.&M. 3386, British A.R.C., 1962.

[100] D.S. Whitehead. Vibration and sound generation in a cascade of flat plates in a subsonic flow. Technical Report R.&M. 3685, British A.R.C., 1970.

[101] D.S. Whitehead. *AGARD Manual on Aeroelasticity in Axial-Flow Turbomachines Volume 1*, chapter Chapter 3, Classical Two-Dimensional Methods. AGARDograph No. 298, 1987.

[102] M. Wong. System modeling and control studies of flutter in turbomachinery. Master's thesis, Massachusetts Institute of Technology, 1997.

[103] S. Yashima and H. Tanaka. Torsional flutter in stalled cascades, 1977. ASME Paper 77-GT-72.